Quantum circuits and the superconductor-insulator transition in a disordered superconductor

Thibault Charpentier

THÈSE

Pour obtenir le grade de

DOCTEUR DE L'UNIVERSITÉ GRENOBLE ALPES

École doctorale : PHYS - Physique
Spécialité : Physique appliquée
Unité de recherche : Institut Néel

Circuits quantiques et la transition supraconducteur-isolant dans un supraconducteur désordonné

Quantum circuits and the superconductor-insulator transition in a disordered superconductor

Présentée par :

Thibault CHARPENTIER

Direction de thèse :

Olivier BUISSON — Directeur de thèse
DIRECTEUR DE RECHERCHE, CNRS DELEGATION ALPES

Thierry GRENET — Co-encadrant de thèse
CNRS

Rapporteurs :

NICOLAS BERGEAL
MAITRE DE CONFERENCES HDR, ESPCI PARIS
CHRISTOPH STRUNK
FULL PROFESSOR, UNIVERSITÄT REGENSBURG

Thèse soutenue publiquement le **10 octobre 2023**, devant le jury composé de :

CHRISTOPH STRUNK FULL PROFESSOR, UNIVERSITÄT REGENSBURG	Rapporteur
THIERRY KLEIN PROFESSEUR DES UNIVERSITES, UNIVERSITE GRENOBLE ALPES	Président
IOAN POP FULL PROFESSOR, KARLSRUHE INSTITUT FÜR TECHNOLOGIE	Examinateur
MANUEL HOUZET DIRECTEUR DE RECHERCHE, CEA CENTRE DE GRENOBLE	Examinateur
TRISTAN CREN DIRECTEUR DE RECHERCHE, CNRS DELEGATION PARIS CENTRE	Examinateur

Abstract

English Strongly disordered materials present unique and puzzling features; while disorder tends to localize electrons and hinder their transport properties, a superconducting state characterized by long-range order and a dissipationless flow of current can still be observed. By decreasing the disorder level one can induce a transition from an insulator to a superconductor, as observed in a large body of experimental works. This Superconductor-Insulator Transition (SIT) is a prototypical quantum phase transition between two very different states of matter. Its hallmark is a second-order, continuous suppression of the order parameter at the quantum critical point. Recent studies however blurred the line between insulating and superconducting states: the observation of localized, preformed Cooper pairs uncorrelated with superconductivity raised new questions about the nature of the SIT. By combining transport and microwave resonator measurements we show in this thesis that amorphous indium oxide thin films exhibit an unexpected first-order transition characterized by an abrupt drop of superfluid stiffness and critical temperature at the critical disorder. We further find that, for high enough disorder, the critical temperature of our films is no longer related to the pairing amplitude but is equal to the superfluid stiffness, as expected for the pseudogap regime of preformed Cooper pairs. Such a bosonic transition driven by phase fluctuations is accompanied with both large kinetic inductance and anomalous intrinsic microwave dissipation. Our findings raise fundamental new questions on the mechanism leading to the breakdown of superconductivity, and have implications for the use of strongly disordered superconductors in microwave quantum circuits.

Français Les matériaux fortement désordonnés présentent des caractéristiques uniques et déroutantes. Alors que le désordre tend à localiser les électrons et à entraver leur transport, un état supraconducteur caractérisé par un ordre à longue distance et un courant sans dissipation est parfois observé. En diminuant le niveau de désordre une transition d'un état isolant à un état supraconducteur peut être induite comme le démontre un grand nombre de travaux expérimentaux. Cette transition supraconducteur-isolant (SIT) est un exemple typique de transition de phase quantique du second ordre, caractérisée par une suppression continue du paramètre d'ordre au point critique. Des études récentes ont toutefois brouillé la frontière entre isolant et supraconducteur : l'observation de paires de Cooper localisées et préformées, non corrélées avec la supraconductivité, a soulevé de nouvelles questions sur la nature de la SIT. En combinant des mesures de transport et de résonateurs micro-ondes, nous montrons dans cette thèse que les films minces d'oxyde d'indium amorphes présentent une transition du premier ordre caractérisée par une chute abrupte de la rigidité superfluide et de la température critique au désordre critique. Nous constatons en outre que, pour un désordre suffisamment élevé, la température critique de nos films n'est plus liée à l'amplitude d'appariement des électrons mais est égale à la rigidité superfluide, comme prévu pour le régime de pseudogap des paires de Cooper préformées. Une telle transition bosonique entraînée par les fluctuations de la phase supraconductrice s'accompagne à la fois d'une grande inductance cinétique et d'une dissipation micro-onde intrinsèque inhabituelle. Nos résultats soulèvent de nouvelles questions fondamentales à propos du mécanisme conduisant à la destruction de l'état supraconducteur et ont des implications concernant l'emploi de supraconducteurs fortement désordonnés dans les circuits quantiques.

Acknowledgements

My first acknowledgements go to the members of the jury. I want to thank Nicolas Bergeal and Christoph Strunk for their very positive comments on the manuscript, as well as Thierry Klein, Ioan Pop, Manuel Houzet and Tristan Cren for attending the defense. I am grateful for their feedbacks and comments during and after the questions session.

Then, I want to express my deepest gratitude to my supervisors. I can boast of having been trained by not only one or two, like is usually the case, but four amazing physicists throughout this PhD. Olivier and Thierry G. drew on their long experience of condensed matter physics to always provide helpful and wise advices when I needed them. Then comes the pair formed by Nicolas and Benjamin, who lured me into the world of strongly disordered superconductors and guided me through it. Their complementary expertise and their enthousiasm actually made my work very easy; I was genuinely happy to go the lab in the morning and learn something new every day. I can say that I am proud of having worked with them.

This work could not have been achieved without the tremendous support, both theoretical and technical, provided by our collaborators. I am thankful to Denis Basko, Lev Ioffe and Anton Khvalyuk for invaluables discussions about theory. I am especially grateful to Mikhail Feigel'man who dedicated a large amount of his time to the interpretation of our data, and was always eager to answer my questions (even the most stupid ones). I feel truly blessed for these collaborations and hope they will go on in the future.
On the technical side I was lucky to be helped on every aspects of my work. Starting from sample fabrication, where the Nanofab team and especially Thierry Crozes were always there to assist. Everytime the cryostat broke down I could count on Éric Eyraud to come to the rescue and work his magic, and if the experiments in F building were successful it is in great part thanks to Frédéric Gay and Florent Blondelle. I am most grateful to Sébastien for his patience in teaching me all I needed to know during my master internship, and to Kazi and Arpit for their constant help. Thank you guys for your assistance and your kindness. I also benefited from the expertise of Corentin who basically lived in cleanroom for a while (I hope he is now recovering from his addiction to isopropanol).

Life at the lab was made much more cheerful by the presence of all the amazing collegues and friends at Néel Institute, first in the QuantECA group with Vladimir, Farshad, Luca, Jovian, Karthik, Dorian, Samuel, Seddik ... and the newest members of this evergrowing team. Then in the QuNES team with David, Wenmin, Bilal and, of course, the inhabitants of the mad house we called an office. In this crowded broom cupboard of the D building where I spent so much time lately I always enjoyed the discussions with Corentin, Marco, Alexis (aka Léodagan) and Hadrien with sometimes a thundering visit by Guilliam. To everyone: I enjoyed the years in your company and wish you all the best for the future.
Et pour finir, à mes parents: cette thèse est un peu la vôtre, merci pour tout ce que vous avez fait pour moi! And Marcela, your loving presence helped me carrying on the writing of this manuscript, so *muchas gracias corazón*.

Contents

Part I

From Insulator to Superconductor : The emergence of Superconductivity in Disordered Materials

CHAPTER 1

Introduction: Breakdown of Superconductivity

It is customary to assume that formation of Cooper pairs (bound states of two electrons of opposite momenta and spins) in a normal metal precipitates the long-range order characterizing superconductivity. This is indeed the case in the framework of the very successful BCS theory. The superconducting transition is modelled within the Ginzburg-Landau theory by defining a complex order parameter

$$\Psi = |\Psi| e^{i\varphi(\mathbf{r})}$$

that describes the superconducting ordered state, and vanishes at T_c to restore the "disordered", normal state.

While the simultaneity of Cooper pairing and apparition of superconducting order is well established in a broad range of metals, there exists materials which evade this classification. It is possible for the two phenomena to occur separately: pairing can develop at higher temperature than superconductivity. This implies the existence of an intermediate temperature range above T_c where Cooper pairs are preformed but not condensed.
In other words, this corresponds to a state where the amplitude $|\Psi|$ of the order parameter is large, but the phase $\varphi(\mathbf{r})$ varies strongly throughout the sample, preventing superconducting order to set in. Superconductivity then happens at a lower temperature when phase coherence is developped over the whole sample.
Such superconductors are anomalously sensitive to phase fluctuations compared to the usual BCS superconductors, and we will show that they are characterized by a low *superfluid density*, that is the number of condensed Cooper pairs is small.

1.1 | Breakdown of superconductivity

Two classes of fluctuations are responsible for altering the ground state of a superconductor: amplitude fluctuations of the order parameter (related to pair breaking), or phase fluctuations (related to current of Cooper pairs).[1]

The pairing strength, in BCS theory, is related to the superconducting gap Δ_0 (via $\Delta_0 \propto e^{-1/\lambda}$ where λ describes the attraction between electrons generated by electron-phonon interactions). The mean-field critical temperature T_{c0} is related to Δ_0 via $\Delta_0 = 1.76\, k_B T_{c0}$. Above T_{c0} the pairs break and long-range order vanishes simultaneously.

We can construct another typical energy scale as follows: divide the sample into blocks of linear size of the order of the coherence length ξ_0 and ask how much energy it would cost to change the value of the complex order parameter at the center of one block. As long as the

[1] This section is inspired from [Carlson et al., 2002].

amplitude remains constant over this lengthscale, the cheapest way to do so is to twist the phase of the order parameter.
Applying the same translation of the phase $\varphi(\mathbf{r}) \to \varphi(\mathbf{r}) + 2\theta$ uniformly to all blocks does not change the free energy.[2]. This is similar to a solid whose constituting atoms are all translated together in space: there is no deformation.
On the other hand changing the phase by a different amount from block to block *i.e.* inducing a spatial variation of the phase, hence a gradient $\nabla\varphi$ requires energy. The simplest expression that satisfies the required symmetries and describes the elastic energy cost to change the phase of the whole sample is the *phase only* functional [M. E. Fisher et al., 1973]:

$$U(\varphi) = \frac{1}{2}\Theta \int d^d\mathbf{r}\, |\nabla\varphi|^2 \tag{1.1}$$

in dimension d, where the proportionality constant Θ is called the *superfluid stiffness* and has the dimension of energy in 2D.

The meaning of Θ is quite obvious: a non-zero Θ means that it costs energy to twist the phase of the order parameter. This quantity describes the rigidity of a superconductor against phase fluctuations, hence the name of *stiffness*.
Note that a formally equivalent energy scale describes the deformation of solids, the spin stiffness of magnets... An expression equivalent to Eq. (1.1) can in fact be derived for any type of symmetry breaking, where some *elastic* energy opposes to distortions. For instance in crystals the broken translational order introduces a rigidity to shear deformations. In magnets the broken rotational symmetry (all spins are aligned in the same direction) induces a stiffness against single-spin rotations [Chaikin et al., 1995].

When the superfluid stiffness is low, phase fluctuations become energetically favorable. The superconductor becomes increasingly sensitive to quantum and thermal fluctuations of the phase. **When the temperature is comparable to Θ, thermal agitation will produce random phase changes from block to block, and hence destroy long-range order.**

1.1.1 Relation with the superfluid density

The 2D superfluid stiffness can be related to the superfluid density *i.e.* the density of condensed Cooper pairs n_s as [M. E. Fisher et al., 1973]:

$$\Theta = \frac{\hbar^2 n_s}{m^*} \tag{1.2}$$

where n_s is the density of Cooper pairs per unit area and $m^* = 2m$ is the effective mass of a Cooper pair.
The 3D superfluid stiffness is then just Θ/a where a is some short lengthscale (usually the thickness d of the film).
This equation can seem surprising at first glance: indeed it suggests that the superfluid density n_s is not just a property of the bulk that describes the number of superconducting charge carriers. It is also intimely related to the response of a superconductor to external perturbations (and even to topological defects as we shall see later in relation to the BKT transition).
Importantly this means that superconductors with low superfluid density are less

[2] It can be shown [Schrieffer, 1999] (page 225) that charge conservation implies gauge invariance. Choosing a different gauge (and therefore inducing a rotation of the order parameter by the angle θ) is arbitrary and corresponds to an equivalent description of the same physical state [Poniatowski, 2019]

resilient to phase fluctuations.

Writing the velocity of the superflow[3]

$$\mathbf{v_s} = \frac{\hbar}{m^*}\langle\nabla\varphi\rangle \tag{1.3}$$

one sees that Eq. (1.1) can be rewritten

$$U = \int \frac{1}{2} m^* v_s^2 \, n_s \, d\mathbf{r} \tag{1.4}$$

which is nothing more than the kinetic energy of the superfluid. Therefore classical phase fluctuations correspond to the thermally induced current of Cooper pairs.

1.1.2 What zero-T properties of a superconductor allow to predict T_c ?

We have defined two energy scales leading to the thermal breakdown of superconductivity: the pairing temperature T_{c0}, and the superfluid stiffness Θ. These two quantities are of course upper bounds on the real, experimentally measurable critical temperature T_c.
As a result, the critical temperature of a superconductor must obey the following inequality:

$$T_c \leq \min\left(T_{c0}, \Theta\right) \tag{1.5}$$

where $T_{c0} = \Delta_0/1.76$ is the mean-field critical temperature, governed by the BCS superconducting gap. When $T_{c0} \ll \Theta$, phase fluctuations can be safely neglected and $T_c \leq T_{c0}$. This is the case for BCS superconductors, where the upper bound is reached.

If $T_{c0} \gg \Theta$ the superconducting state is suppressed by phase fluctuations: $T_c \leq \Theta$. As a result the number of Cooper pairs remains non-zero above T_c: this opens many interesting questions which will be treated later.
The case where none of the two mechanisms above can be neglected is also relevant in some materials, and the suppression of order parameter occurs by suppressing both phase coherence and pairing amplitude.

1.1.3 Quantum breakdown of superconductivity

In order to completely suppress superconductivity one then has two options: either reduce the amplitude of the pairing energy ($T_{c0} \to 0$) or destroy the phase coherence by lowering the superfluid stiffness ($\Theta \to 0$). By the inequality Eq. (1.5) this means destroying superconductivity by pushing down the critical temperature to zero.

One efficient way to reduce either T_{c0} or Θ at, and hence T_c, is to increase the disorder of the sample. Without giving a precise definition of disorder for the moment (this is the object of the entire Appendix A), one can say on general grounds that a very disordered sample has a strongly suppressed normal-state conductance compared to its clean counterpart.

[3] This relation comes from the properties of waves in quantum mechanics: considering a normalized wavefunction $\psi(\mathbf{r}) = e^{i\mathbf{k}\cdot\mathbf{r}}\psi_0$, with a phase $\varphi(\mathbf{r}) = \mathbf{k}\cdot\mathbf{r} = \nabla\varphi\cdot\mathbf{r}$ defines the gradient $\nabla\varphi$. From the momentum $\mathbf{p} = \hbar\mathbf{k} = -i\hbar\nabla = m\mathbf{v}$ this describes a wavepacket moving with velocity $\mathbf{v} = \langle\psi|\,\mathbf{p}/m\,|\psi\rangle = -i\hbar/m\int\psi^*(\mathbf{r})\nabla\psi(\mathbf{r})\,d\mathbf{r} = (\hbar/m)\langle\nabla\varphi\rangle$.

The effect of disorder is to *localize* charge carriers because of the presence of defects. This has consequences on interactions between electrons, and notably is expected to reduce the pairing strength.
Additionally the presence of impurities enhances the role of phase fluctuations. This important fact has its roots in quantum mechanics: superconducting phase and number of Cooper pairs are quantum canonically conjuguate (*i.e.* their operators do not commute) and must obey Heisenberg uncertainty principle. Localization of electrons reduces the uncertainty of their spatial position and consequently enhances the uncertainty in the superconducting phase, leading to fluctuations.
With disorder, metals become dangerously close to an insulating state upon increase of impurity level. The resulting insulating state (the *Anderson insulator* described in Appendix A) presents a large variety of features, some of which compete with superconductivity and lead to its destruction.

An important question that arises concerns the nature of the state terminating superconductivity. For instance, driving T_{c0} to zero corresponds to breaking all available Cooper pairs, and the resulting system is made out of free electrons: it resembles a metal. On the other hand setting Θ to zero suppresses the phase coherence of Cooper pairs without altering the attractive interaction responsible for pairing. The resulting state would then be made of incoherent pairs of electrons.

Experimentally, a large body of works shows that, right after the suppression of the superconducting state the system enters an insulating state with diverging resistance at low temperatures. The nature of this Superconductor-Insulator Transition (SIT) has been the subject of numerous theoretical and experimental studies, and has seen the emergence of several different paradigms [Goldman and Marković, 1998; Benjamin Sacépé, Mikhail Feigel'man, et al., 2020].

In the following sections we first describe how disorder can suppress T_{c0}, and therefore superconductivity through was is known as the *fermionic mechanism*. We then give an important example of system in which superconductivity is suppressed by classical phase fluctuations through the Berezinskii-Kosterlitz-Thouless Transition (BKT).
Finally we describe a similar situation in which the SIT is induced by quantum phase fluctuations at $T = 0$ (known as the *bosonic scenario*).

These two pathways for the Quantum Breakdown of Superconductivity (QBS) will be the main reference points for the experimental investigation of the SIT in disordered amorphous indium oxide which is the subject of this thesis.

1.2 | Fermionic suppression of critical temperature with disorder

In homogeneously disordered films with $\Theta \gg \Delta_0$ Coulomb repulsion between electrons can lead to the suppression of superconductivity, as we discuss now [Maekawa et al., 1982; P. W. Anderson et al., 1983].
In disordered samples electronic diffusion is slowed by impurities, in turn reducing the effect of screening of Coulomb interactions. When these repulsive interactions become of significant

importance they compete with the attractive electron-electron interactions at the origin of superconducting pairing, therefore reducing the Cooper attraction strength λ at energy ε as

$$\lambda(\varepsilon) = \lambda_0 - \frac{1}{3\pi g} \ln \frac{1}{\tau_e \varepsilon} \tag{1.6}$$

where $g = h/(e^2 R_\square)$ is the dimensionless conductance and λ_0 is the bare Cooper attraction constant. τ_e is the scattering time related to the mean free path l_e.
The dimensionless conductance g is of fundamental importance to describe the effects of disorder on electronic transport, and will be discussed in details in chapter A. It is inversely proportional to the sample resistance, and as such decreases upon increase of disorder.
Eq. (1.6) describes the reduction of pairing upon increase of disorder-enhanced Coulomb repulsion, often called the *fermionic mechanism*.

Using the renormalization group Finkel'stein obtained an analytical formula describing the complete evolution of critical temperature with disorder [Finkel'stein, 1986]:

$$\frac{T_c}{T_{c0}} = e^{-1/\gamma} \left[\left(1 + \frac{\sqrt{t/2}}{\gamma - t/4} \right) \times \left(1 - \frac{\sqrt{t/2}}{\gamma - t/4} \right)^{-1} \right]^{1/\sqrt{2t}} \tag{1.7}$$

where $\gamma = \ln 1/\left(T_{c0}\tau_e\right)$ and $t = e^2/(2\pi^2\hbar)R_\square = 1/(\pi g)$. Here T_{c0} is the bulk critical temperature.

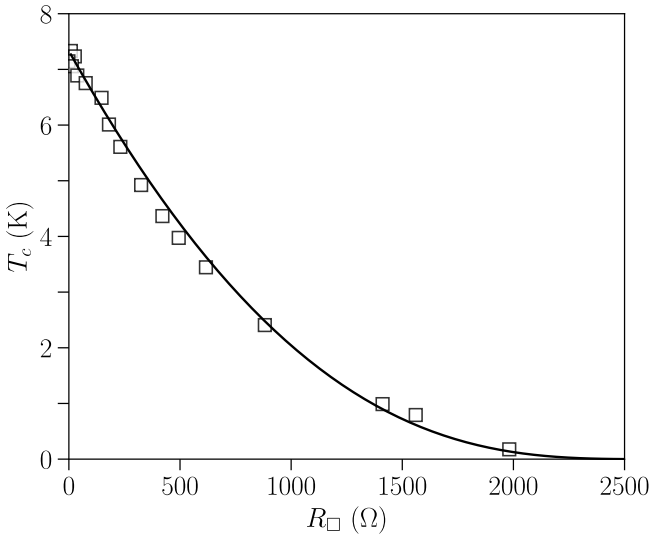

Fig. 1.1. Suppression of T_c via the fermionic mechanism. Squares are data on thin amorphous MoGe from [Graybeal et al., 1984], and solid line is a fit using Eq. (1.7) with parameter $\gamma = -0.12$. Reproduction from [Finkel'stein, 1986].

As shown in Fig. 1.1 the model of Eq. (1.7) is able to reproduce the reduction of T_c in homogeneous, amorphous MoGe samples measured by [Graybeal et al., 1984]. T_c decreases continuously down to zero at a critical conductance g_c.
In this theory Cooper pairs are progressively broken by Coulomb repulsion between electrons, leaving a state of unpaired quasiparticles.

1.3 | An example of system ruled by phase fluctuations: The Berezinskii-Kosterlitz-Thouless transition in 2D

Another characteristic energy scale of a superconductor is the phase stiffness Θ. If $\Theta \ll T_{c0}$ then phase fluctuations can become strong enough to suppress the order parameter. In this section we discuss briefly how **thermal** (classical) phase fluctuations can drive the superconductor into a disordered, non-superconducting state in two dimensions.[4]

It is well known that two-dimensional systems cannot have long-range order [Chaikin et al., 1995][5]. True 2D systems are then said to have *quasi-long-range order*.
[Berezinsky, 1971; Kosterlitz et al., 1973] demonstrated that at high enough temperature such quasi-order could be broken by topological defects of the order parameter, the *vortices*.
The presence of a vortex deforms locally the phase field which winds around the defect. A vortex core is a normal metal and can dissipate energy through its motion. In some specific configurations the effect produced by a single vortex on the phase field can be compensated by an *anti-vortex* of opposite topological charge. Thus a state with such a pair of vortices is topologically equivalent to a uniform state.
Below a critical temperature T_c^{BKT} quasi-long-range order is preserved by the formation of such vortex-antivortex pairs (see Fig. 1.2 left panel).

Above T_c^{BKT} pairs of vortices break apart and single vortices start to proliferate in the superconductor, suppressing abruptly the superconducting quasi-order (see Fig. 1.2 right panel). At this temperature the correlation function decays exponentially.[6]

Discovered by [Berezinsky, 1971; Kosterlitz et al., 1973], this transition (later known as the Berezinskii-Kosterlitz-Thouless (BKT) transition) is expected to occur in a wide range of different 2D systems and is quite universal. [Beasley et al., 1979] showed that two-dimensional superconductors present a BKT transition.

Thus the BKT transition is characterized by a change in the behavior of the correlation function close to T_c^{BKT}: at this temperature the superfluid stiffness drops to zero sharply, as illustrated in Fig. 1.3. In all system in which a BKT transition exists, the superfluid density has a *universal*

[4] This section is inspired by the book [Chaikin et al., 1995] and the review [Goldman and Wolf, 1984] (chapters by Mooij and Minnhagen).

[5] That is, if one defines the spatial correlation function as

$$G(\mathbf{r}) = \langle \Psi^*(\mathbf{r})\Psi(0)\rangle = |\Psi(\mathbf{r})|^2 \langle e^{-i\varphi(\mathbf{r})} e^{i\varphi(0)}\rangle \tag{1.8}$$

then a true long-range order defined by the condition $\lim_{|\mathbf{r}|\to\infty} G(\mathbf{r}) \neq 0$ cannot exist for any finite temperature. Instead the correlation function decays to zero algebraically at finite temperatures. This can be shown directly using a gaussian model. Assuming a gaussian distribution one finds $G(r) \sim \left(\frac{a}{r}\right)^{\eta(T)}$ where $a \ll r$ is a microscopic cutoff length, of the order of the coherence length for instance, and the temperature-dependent exponent is given by $\eta(T) = \frac{k_B T}{2\pi\Theta}$. This important result demonstrates that, indeed, for a finite temperature $T > 0$ true long-range order cannot develop, as $G(r)$ decays to zero at infinity.

[6] Close to T_c^{BKT} the correlation function becomes $G(r) \sim e^{-r/\xi(T)}$ where the correlation length $\xi(T)$ (the typical distance above which the effective interaction between two vortices vanishes) is $\xi(T) \sim e^{-b|T-T_c^{\mathrm{BKT}}|^{-1/2}}$.

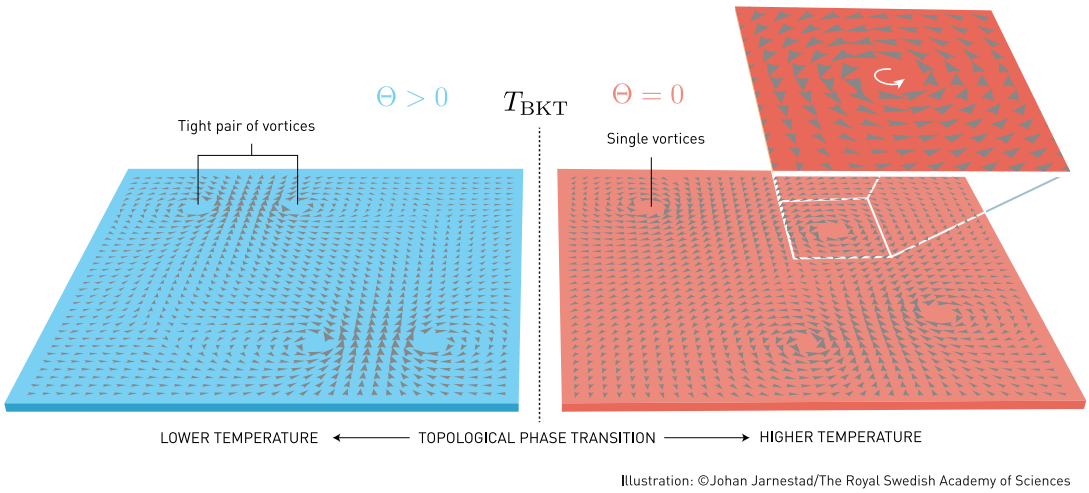

Fig. 1.2. Berezinskii-Kosterlitz-Thouless transition. At low temperatures vortices are scarce and can only appear in pairs (with opposite winding numbers), interacting logarithmically over the distance separating them. At the critical temperature T_c^{BKT} pairs of vortices unbind abruptly, leaving single vortices that dissipate and drive the quasi-long-range order into a disordered phase. The superfluid stiffness Θ drops sharply to zero. Adapted from [The Royal Swedish Academy of Sciences, 2016].

jump of size [Nelson et al., 1977]

$$\frac{\Theta(T_c^{\mathrm{BKT}})}{T_c^{\mathrm{BKT}}} = \frac{2}{\pi} \tag{1.9}$$

in the limit of infinite sample size.

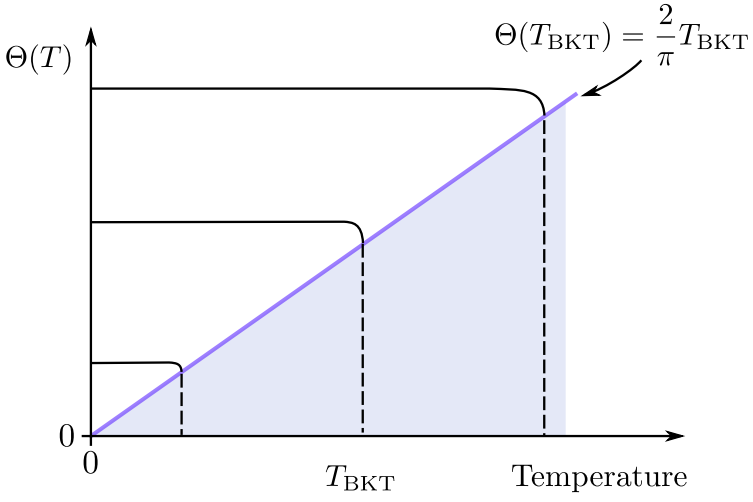

Fig. 1.3. Superfluid jump at the BKT transition temperature. Sketch of the abrupt drop of superfluid stiffness Θ at T_c^{BKT} for different values of zero temperature stiffness $\Theta(0)$. Blue line represents the relation of Eq. (1.9). One sees that the critical temperature is ruled by the value of superfluid stiffness at $T = 0$: $T_c^{\mathrm{BKT}} \sim \Theta(0)$. Upon decrease of $\Theta(0)$ the critical temperature decreases accordingly.

Importantly, T_c^{BKT} defines the *real*, experimentally measurable critical temperature T_c of the system below which the material has non-zero superfluid density and supercurrent. It is smaller than the mean-field prediction T_{c0} for a clean bulk superconductor. To quantify the difference between these two energy scales the *Ginzburg-Levanyuk number* G_i is often used as a description of the temperature range where thermal fluctuations are strong. The relative spacing between the BKT temperature T_c and the mean-field T_{c0} is [Larkin, 1999]

$$\frac{T_{c0} - T_c}{T_c} = 4G_i \tag{1.10}$$

where $G_i \propto 1/g$. Here $g = h/(e^2 R_\square)$ is the normal-state dimensionless conductance: a small g signals a strongly disordered system.

Eq. (1.10) states that the shift of critical temperature with classical fluctuations increases with increasing disorder: $\delta T_c/T_c \propto 1/g$ (we recall that an enhancement of disorder strength reduces the dimensionless conductance g). That is, in theory, by reaching a strong enough disorder one should be able to see a clear reduction of T_c with disorder due to BKT mechanism, while the pairing temperature T_{c0} remains unaffected [Beasley et al., 1979]. We shall give a more quantitative analysis of this fact later.

Preformation of Cooper pairs As seen from Eq. (1.10) two distinct energy scales increasingly separate with disorder. First the mean-field critical temperature T_{c0}, below which Cooper pairs form, and a critical temperature T_c^{BKT} above which superconductivity breaks down.
This opens a temperature range $T_c^{\mathrm{BKT}} < T < T_{c0}$ in which Cooper pairs have formed ($T < T_{c0}$) but the superconducting state is destroyed by the proliferation of vortices ($T > T_c^{\mathrm{BKT}}$), as illustrated in Fig. 1.4.
Thus the BKT transition in presence of disorder implies the preformation of incoherent electron pairs in the normal state.

Upon increase of disorder the enhancement of phase fluctuations results in a suppression of the superfluid stiffness Θ. Because of the BKT relation $T_c^{\mathrm{BKT}} \sim \Theta(0)$ this also leads to a reduction of the BKT temperature T_c^{BKT}. At very large disorders one can drive T_c^{BKT} to zero, breaking down superconductivity following the *bosonic* pathway.

1.4 | Bosonic pathway

For sufficiently strong disorder the picture above leads to a state where $T_c^{\mathrm{BKT}} = 0$ (phase coherence is destroyed at $T = 0$) but $T_{c0} \neq 0$: Cooper pairs are preformed and remain bound. This situation is represented in Fig. 1.4.
This leads to the important conclusion that, **at the critical disorder $1/g_c$ one has a quantum phase transition (i.e. a phase transition at $T = 0$) above which superconductivity breaks down.**

Therefore, in two dimensions a strong disorder induces the Quantum Breakdown of Superconductivity.
Starting from this simple observation M. Fisher developed a quantum critical theory of the *dirty boson model* [M. P. A. Fisher, 1990]. It consists in modelling Cooper pairs by hard-core charge-$2e$ bosons interacting through Coulomb repulsion in presence of disorder and vortices.

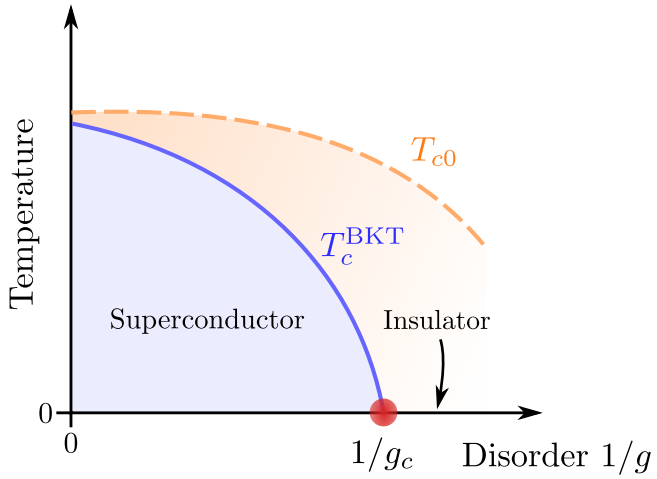

Fig. 1.4. Bosonic pathway of superconductivity. Upon increase of disorder $1/g$ the mean-field critical temperature T_{c0} (below which Cooper pairs form) is reduced by the fermionic mechanism (disorder-enhanced repulsion of electrons). For a 2D superconductor the BKT mechanism predicts the existence of another energy scale, the BKT critical temperature T_c^{BKT} above which quasi-long-range order breaks down by the proliferation of free vortices. $T_c^{\mathrm{BKT}} \sim \Theta(0)$ is suppressed by the increasingly strong phase fluctuations, down to the quantum critical point (QCP) $1/g_c$ where $T_c^{\mathrm{BKT}} = 0$ but T_{c0} remains finite (*i.e.* Cooper pairs are not destroyed). In the temperature range $T_c^{\mathrm{BKT}} < T < T_{c0}$ (orange area) Cooper pairs are preformed but superconducting order does not set in because of the presence of free vortices. At the QCP the 2D material is a combination of incoherent Cooper pairs and free vortices.

1.4.1 Charge-vortex duality

In a system of bosons at $T = 0$, phase fluctuations do not originate from thermal excitation. Instead they are related to fundamental properties of quantum mechanics: the boson density operator $\hat{n}$ (related to the number of Cooper pairs) and the superconducting phase order parameter $\hat{\varphi}$ are conjuguate variables, and do not commute:

$$[\hat{\varphi}, \hat{n}] = i\hbar \tag{1.11}$$

which results in the well known Heisenberg uncertainty relation

$$\sigma_\varphi \sigma_n \geq \frac{\hbar}{2} \tag{1.12}$$

where $\sigma_{\mathcal{O}} = \sqrt{\langle \hat{\mathcal{O}}^2 \rangle - \langle \hat{\mathcal{O}} \rangle^2}$ is the standard deviation of the Hermitian operator $\hat{\mathcal{O}}$.

Therefore fixing locally the number of charges n (*i.e.* setting $\sigma_n \to 0$) enhances the local fluctuations of the phase φ. This is (in a handwaving approach) what localization of bosons does to the system.
Near the quantum critical point the system sees the competition of kinetic energy of Cooper pairs (which tries to delocalize the particles and hence reduce phase fluctuations) and the combination of interactions and disorder which try to localize the particles (and hence reduce the number density fluctuations).

M. Fisher demonstrated that the 2D problem of interacting bosons in a random potential could be represented either by involving the order parameter phase, or by an effective magnetic

field $\mathbf{B} = \nabla \times \mathbf{A}$ (where $\mathbf{A}$ is a gauge field) which plays the role of the boson density n. These two fundamentally different descriptions of the same Hamiltonian lead to the concept of duality between bosons in 2D (and at $T = 0$) and a bulk superconductor in an applied random magnetic field [M. P. A. Fisher and D. H. Lee, 1989].
This mapping has many important consequences, as it allows to relate the ground state ($T = 0$) properties of bosons with the thermodynamic characteristics of a classical superconductor. In particular vortices and bosons play a dual role (see Fig. 1.5).[7]

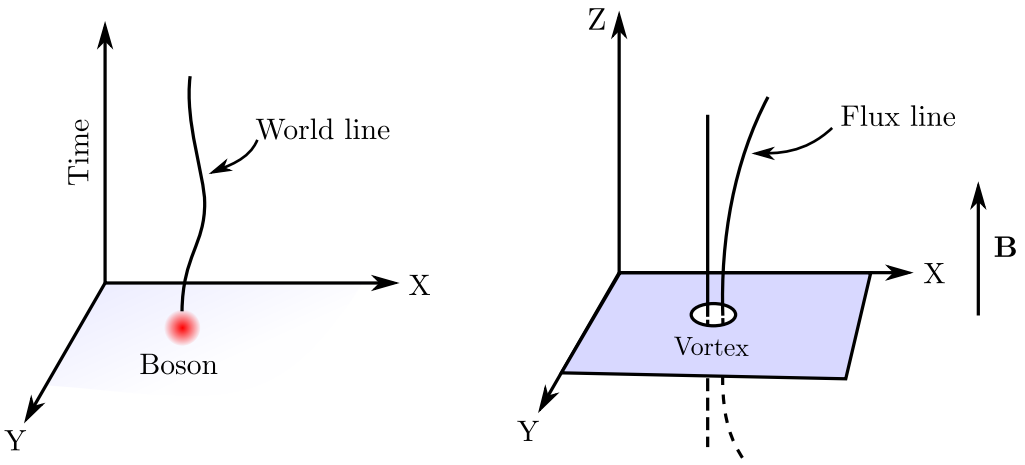

Fig. 1.5. Boson-vortex duality. The world line of a particle (here a boson) represents its 'history' in a $(d+1)$-dimensional spacetime. M. Fisher states that it is equivalent (the models are isomorphic) to the flux line piercing a superconductor under the influence of an effective (ficticious) magnetic field. In this representation bosons (modelling Cooper pairs) at $T = 0$ and vortices in a superconductor under magnetic field (and $T \neq 0$) are dual quantities [M. P. A. Fisher and D. H. Lee, 1989].

We have mentioned that the disordered state terminating the quasi-long-range order at the BKT transition is made of unpaired, free vortices. They become mobile under the application of a current and drift under the influence of a Magnus force. It can be shown that when such a free vortex crosses a sample along its width it induces a change of the phase by 2π between the two extremities (phase slip). By the Josephson relation $\Delta V = (\hbar/2e)(\Delta\dot{\varphi})$ where ΔV is the voltage drop along the sample and $\Delta\varphi$ is the overall phase difference, one sees that a phase slip generates a voltage drop, and therefore dissipation. Such resistivity can be written [Halperin et al., 1979]:

$$\rho = \left(\frac{\hbar}{2e}\right)^2 n_v \mu \tag{1.13}$$

where n_v is the density of free vortices and μ is the vortex mobility (related to the resistance of the material and other microscopic parameters).
The resistivity ρ is the *real* dissipation by proliferation of vortices in a 2D system above T_c^{BKT}. Note that if one identifies the flux quantum $\hbar/(2e)$ to a *vortex charge* and recalls the Einstein relation for conductivity $\sigma_v = q^2 n_v \mu$ for the charge q one can identify the resistivity

[7] Vortices were treated as bosons, which is a rather strong approximation.

of Eq. (1.13) to a vortex conductivity σ_v as

$$\rho \sim \sigma_v \tag{1.14}$$

which is one consequence of vortex-boson duality.

1.4.2 Disordered and ordered phases

We now come back to the $T = 0$ quantum phase transition. First we describe a state below the critical disorder $1/g < 1/g_c$.
The effect of disorder and repulsive interactions on a 2D system of condensed bosons is to localize vortices. They are pinned at definite positions of the lattice and do not contribute to the sample conductivity. By the relation Eq. (1.14) this implies no dissipation in the boson system: $\rho \sim \sigma_v = 0$. The superconducting state is therefore the combination of Bose condensed charge-$2e$ particles and localized vortices.

On the other side of the quantum phase transition ($1/g > 1/g_c$) bosons tend to be localized by the cumulated effects of repulsive interactions and disorder. Deep in the insulating state they are localized over short distances and do not contribute to conduction: the dual version of Eq. (1.14) imposes the vanishing resistivity of free vortices ρ_v, as $\rho_v \sim \sigma = 0$ where σ is the conductivity of bosonic particles. The zero-dissipation state of free (mobile) vortices is assured by a Bose condensation of these vortices. The resulting system is an insulator made of localized bosons, and delocalized, Bose condensed vortices, called a *Bose glass*. It can be seen as an ordered, 'superconducting' state with respect to the vortex condensate, and simultaneously corresponds to the disordered, insulating state for bosons.

Interestingly, this picture implies that at the critical disorder $1/g_c$ where the transition between superconductor and Bose glass occurs both Cooper pairs and vortices should be mobile and dissipate. This leads to the prediction of a *universal* sample resistance at the critical resistance R_c [M. P. A. Fisher, Grinstein, et al., 1990; Cha et al., 1991]

$$R_c \sim \frac{h}{(2e)^2} \tag{1.15}$$

where the prefactor is unity in the case of exact self-duality (for each Cooper pair flowing in the sample one vortex crosses and induces a 2π phase slip). The value of this prefactor has been largely studied in various situations.
Another important consequence is the universal scaling of resistance with temperature and distance to the critical point [M. P. A. Fisher, Weichman, et al., 1989; M. P. A. Fisher, Grinstein, et al., 1990].
Unfortunately extensive experimental studies of various systems have shown quite different value of critical resistance R_c and scaling exponents. Some theorists have concluded the necessity to develop an ad hoc microscopic description for each system, allowing to study short-wavelength phase fluctuations which were not taken into account in the model presented above [Benjamin Sacépé, Mikhail Feigel'man, et al., 2020].

Conclusion

A complex superconducting order parameter of the form $\Psi = \Delta e^{i\varphi}$ must vanish when superconductivity breaks down. Beyond the usual mechanism where Cooper pairs break and $\Delta \to 0$, the superconducting state can be destroyed by loss of phase coherence. This second scenario becomes predominant in superconductors with low density of carriers ($n_s \propto \Theta \ll \Delta$). Classical phase fluctuations rule the superconducting order and suppress the real critical temperature $T_c \sim \Theta$ through the BKT mechanism. The increase of microscopic disorder tends to localize Cooper pairs, in turn enhancing phase fluctuations and suppressing further long-range order.

At a critical disorder level Cooper pairs become so localized, and phase fluctuations so strong, that the superconducting state gets destroyed at $T = 0$. This is a quantum phase transition to an insulator made of localized bosons. This pathway, related to the loss of phase coherence is known as the *bosonic scenario*.
Another effect of disorder is to localize single electrons and affect their interactions: disorder can enhance the Coulomb repulsion of electrons forming a Cooper pair, therefore driving the pairing strength to zero, leaving a state composed of single electrons. This mechanism is known as the *fermionic scenario*.

To describe theoretically the bosonic QBS M. Fisher and collaborators predicted *universal* features of disordered superconductors, but this universality has been contested experimentally by a large body of works.
More recent theories put forward the idea that microscopic (short scale) properties of a material must be taken into account in the description of a SIT.
In this thesis we draw our attention to a particular amorphous material, indium oxide, which can be tuned from a superconductor to an insulator at $T = 0$. Recent theories suggest that superconductivity in this material *originates* from the microscopic properties of the underlying insulator. To precise this point (and give some meaning to the notions of *disorder* and *dimensionless conductance* g used in this chapter without explanation) the reader can find some details in Appendix A where Anderson localization is introduced.
In chapter 2 we discuss how localization and superconductivity, two seemingly opposite concepts, can coexist and intertwine. We will mention recent theoretical works that introduce the idea that Cooper pairs naturally emerge from the Anderson insulator microscopic structure.

These exciting features motivated us to study the disorder-driven Superconductor-Insulator Transition in amorphous indium oxide, the result of which are shown in this thesis.

CHAPTER 2

Disordered Superconductors: a state of the art

In this chapter we show, based on both theoretical and experimental arguments, how a seemingly purely insulating material can host superconductivity. While most of the discussion can be applied to a variety of disordered amorphous materials, we put a specific accent on amorphous indium oxide which is the subject of this thesis.
The puzzling superconducting state emerging from an insulating background has some particularities which we discuss in the light of recent theoretical advances.

2.1 | Indium oxide: Anderson insulator or superconductor ?

A popular semiconductor

The material investigated in this thesis is rather well known and popular for industrial applications: when mixed with tin, indium oxide becomes indium tin oxide (ITO), one of the most widely used Transparent Conducting Oxide (TCO) materials.
Its high electrical conductivity and transparency make it a perfect coating for touch-screen devices and various types of displays[1].

Pure indium oxide comes in two main phases, crystalline or amorphous, depending mostly on the deposition temperature: an amorphous to crystalline transition can be obtained by gradually increasing the deposition temperature, as shown in [Buchholz et al., 2014]. A deposition below 0°C displays a vanishingly small crystalline fraction.
Post-deposition annealing of indium oxide samples also differs for amorphous and crystalline phases: it is found that the room temperature resistance of the crystalline version increased upon heating the samples (up to 400°C), but is a reversible process (repeating the annealing and cooling it down slowly could recover the initial resistance).
On the other hand, the resistance of *amorphous* indium oxide samples only decreases upon annealing (at temperatures below 60°C to prevent crystallization). Room temperature aging also reduces the resistance of amorphous films [Ovadyahu, 1986; Zvi Ovadyahu, 2019].

On the nature of disorder in a:InO It is customary to relate a material's disorder to its resistance (measured at room temperature or at lower temperature depending on the convention). An increasingly large resistance means an enhancement of the sample's disorder level. Microscopically this can be understood as a decrease of the carrier density.

[1] It is very likely that the reader's smartphone is coated with ITO. The material is also used for solar cells and numerous types of applications that require transparency and good electrical properties [Nagata, 2019]

In the case of indium oxide it is believed that disorder is related to the local concentration of oxygen vacancies [Z. Ovadyahu, 2022b; Z. Ovadyahu, Ovryn, et al., 1983]. Such vacancies correspond to the ponctual removal of an oxygen atom from its matrix, leading to a local redistribution of charge.
The existence of oxygen vacancies is favored by the deposition process: by evaporating indium oxide and quench-condense its vapor phase onto a cold substrate results in a 'spongy' structure full of microvoids [Z. Ovadyahu, 2022b; Medvedeva et al., 2017]. Oxygen atoms liberated by this process diffuse within the sample or in and out of the material, changing the stoechiometry.[2]

Therefore the carrier density (and consequently disorder) can be tuned by controlling the oxygen to indium ratio during fabrication. This is done in practice by leaking a small volume of pure oxygen in the evaporation chamber: the higher the oxygen partial pressure the higher the disorder.

The indium oxide films studied in this thesis were deposited by electron-beam evaporation (with $2\ \text{Å}/\text{s}$ rate) of a high-purity 99.99% In_2O_3 pellet on a cold silicon substrate in a high vacuum chamber[3] with a controlled O_2 partial pressure. The low temperature evaporation allows to obtain fully amorphous samples, with an oxygen content tuned at will during the process.[4]

2.1.1 Experimental evidence of Anderson localization

Anderson Metal-Insulator Transition Important features of the theory of localization are reminded with more details in Appendix A.4. In this section we only define some key concepts needed for the understanding of what follows.

In presence of disorder, quantum interference between electronic waves in a metal are strongly enhanced. With a large disorder (strong density of impurities) these electronic waves can interfere destructively. This translates into a decrease of the sample conductivity, of purely quantum origin [B. Altshuler et al., 1985]. Importantly these electronic wavefunction, although strongly altered by the presence of disorder, are still *extended*, that is they spread in the entire available space.
Above a critical disorder strength Anderson showed that a drastic change occurs: the electron occupies only an exponentially small volume of space $|\Psi(\mathbf{r})|^2 \propto \frac{1}{\xi_{\text{loc}}^d} e^{-\mathbf{r}/\xi_{\text{loc}}}$ where the *localization length* ξ_{loc} is the typical size of an electron wavepacket [P. W. Anderson, 1958a].

The electron becomes *localized*, and the metal's transport properties change completely: at strictly $T = 0$ conduction along the sample is blocked and the metal becomes an insulator.
To describe this Metal-Insulator Transition (MIT) in three dimensional systems, Mott [S. N. Mott, 1978; N. Mott, 1987] defined an energy scale called the *mobility edge* E_c marking

[2] When the [O]/[In] ratio is reduced compared to the perfectly stoechiometric case ($= 1.5$), some In atoms have a smaller coordination with oxygen. As a result the polyhedra formed by an In atom surrounded by oxygen atoms distort locally, leading to an under-sharing of these In/O structures. In such region where under-coordinate In atoms concentrate, an oxygen-depleted area forms, acting like an oxygen vacancy. [Medvedeva et al., 2017]

[3] In addition to turbo-pumping, the chamber pressure is further reduced by circulating cold water and a nitrogen tank. This provides a pressure before deposition of about $6\,10^{-7}$ mbar. The sample substrate also benefits from the cooling, and probably has a temperature of a few degrees Celsius.

[4] Oxygen pressure is in the range $1 - 8\ 10^{-5}$ mbar, from relatively clean to strongly disordered superconductors.

the frontier between extended and localized states: when the Fermi energy E_F exceeds the mobility edge ($E_F > E_c$) states are extended and the sample is metallic. On the other hand when $E_F < E_c$ electrons are localized and the sample is an insulator.
Thermal activation allows hopping from one localized state to the other, providing a non-zero conductivity which can be be measured as we will discuss below. The models for such activated behavior can be found in Appendix A.4.

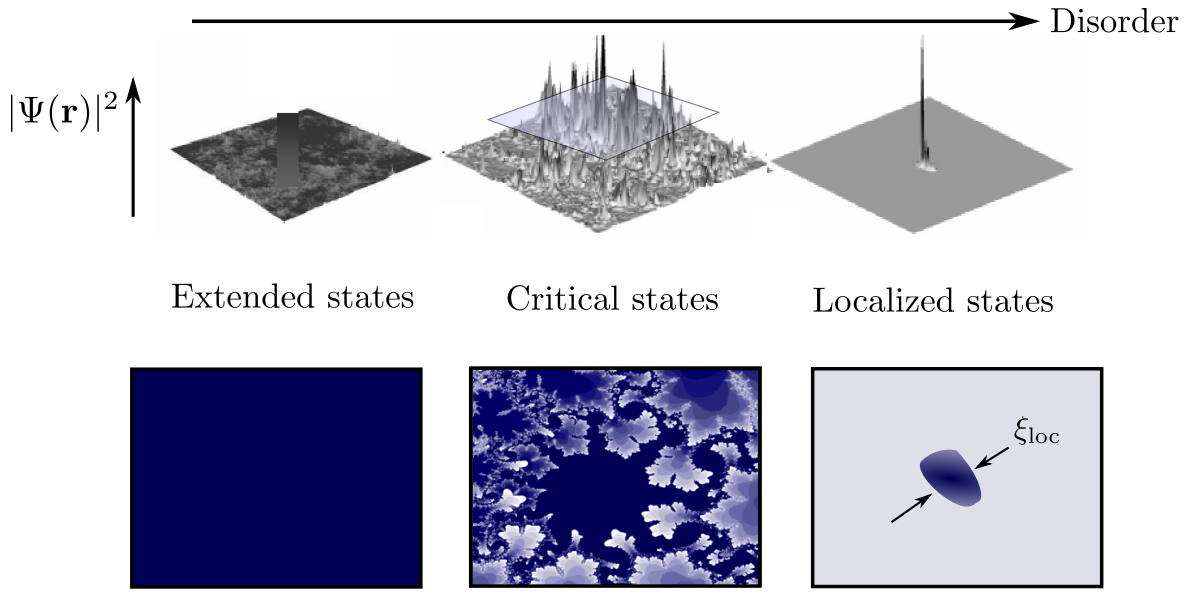

Fig. 2.1. Fractal wavefunctions across the Metal-Insulator Transition. The wavefunction intensity $|\Psi(\mathbf{r})|^2$ is shown in 3D space (top) and along a horizontal cut (bottom). Darker blue corresponds to larger intensity. **Left:** At low disorder wavefunctions are extended and their intensity is uniform (they occupy all available space). **Center:** At critical disorder $E_F = E_c$ wavefunctions present a multifractal structure. They occupy a smaller volume L^{D_2} where $D_2 < 3$ is the fractal dimension. **Right:** For localized states ($E_F \ll E_c$) wavefunctions are exponentially suppressed and occupy the small volume ξ_{loc}^d. Adapted from [Cuevas et al., 2007].

One additional note regarding critically disordered metals at the MIT: electronic wavefunctions present a unusual fractal distribution in space for $E_F \sim E_c$, as illustrated in Fig. 2.1 [Cohen et al., 1983; Castellani et al., 1986; A. Mirlin, 2000]. At criticality electrons are neither extended in the whole sample, nor fully localized, and the volume they occupy in a box of lateral size L is not L^3 but the smaller L^{D_2} where $D_2 = 1.3 < 3$ [A. Mirlin, 2000] is some fractal dimension.
Further, [Cuevas et al., 2007] showed that electron fractality survives relatively far from the MIT in both metallic and insulating states, with fractal features comprised in shells of decreasing size $\sim \xi_{\mathrm{loc}}$.
Later on in this chapter fractality near the Anderson Metal-Insulator Transition will be used to link insulators and disordered superconductors.

Experimental works on amorphous indium oxide Early experimental works have focused on determining whether or not amorphous indium oxide displayed the expected signatures of an Anderson insulator.
Measurements of the evolution of sample resistance with temperature (thermally activated

transport in Anderson insulators is briefly reminded in Appendix A.4) have shown the usual weak localization scalings at moderately low temperatures, and a Mott variable range hopping at lowest temperatures [Zvi Ovadyahu and Imry, 1981; Ovadyahu, 1986]. This observation is consistent with a picture of weakly interacting Anderson insulator. A crossover between Mott and Efros-Shklovskii variable range hoppings was evidenced by [Rosenbaum, 1991], therefore demonstrating the existence of a Coulomb gap and the role of Coulomb repulsion on the insulating state.

Another property of strongly disordered Anderson insulators is non-ergodic transport: when excited from equilibrium the sample conductance increases, and the excess conductance ΔG relaxes back to normal extremely slowly $\Delta G(t) \propto \ln(t)$. Related memory effects were also observed [Vaknin et al., 2002; Z. Ovadyahu and Pollak, 2003] and suggest that deeply insulating indium oxide is an electron glass, *i.e.* a strongly interacting system dominated by Coulomb repulsion [Z. Ovadyahu, 2022a].

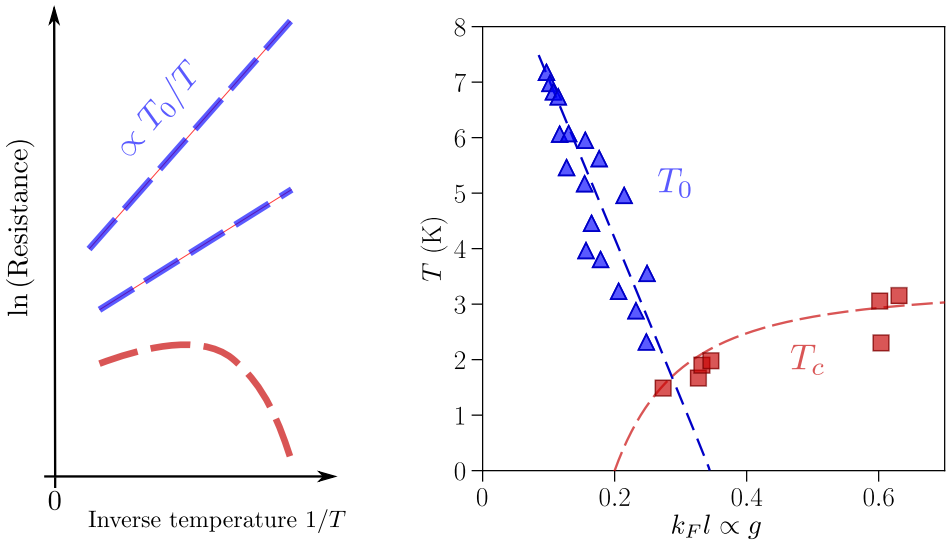

Fig. 2.2. SIT in transport. Left: Evolution of resistance with temperature for insulating (blue) and superconducting samples (red). **Right:** Activation energy T_0 (insulating samples) and critical temperature T_c (superconducting samples) across the SIT. Data adapted from [Shahar et al., 1992].

Measurements for less disordered samples closer to the Metal-Insulator Transition showed an unexpected feature however: the resistance followed the activated (or Arrhenius) law $R \propto \exp\left(T_0/T\right)$ [Shahar et al., 1992; Shammass et al., 2012; Givan et al., 2012].
The temperature T_0, determined from the slope of the $\ln(R)$ versus T^{-1} curves, decreases upon approaching the MIT (see blue triangles on Fig. 2.2 Right panel).

Then [Shahar et al., 1992] observed a striking new feature: by lowering disorder further the system changes drastically; it becomes a superconductor. In this new state the sample resistance drops to zero below a critical temperature T_c and T_0 cannot be defined.
This leads to the conclusion that **amorphous indium oxide experiences a Superconductor-Insulator Transition (SIT) driven by disorder.**

Numerous works confirmed the SIT in this material [Shahar et al., 1992; Kowal et al., 2008; Mitra et al., 2016], all displaying the transition between a thermally activated insulator and

a superconductor. Fig. 2.2 displays the gradual suppression of T_0 upon decrease of disorder (blue curves), and the sudden apparition of superconductivity (red curves).

A surprising relation of superconductor and insulator In the thermally activated Anderson insulator typical energy separation between two localized states in dimension d is $\delta_{\mathrm{loc}} \sim \left[\nu \xi_{\mathrm{loc}}^d\right]^{-1}$[5] Transport occurs by hopping to the nearest neighbour by thermal activation above δ_{loc}, as $\sigma(T) \propto \exp\left(-\delta_{\mathrm{loc}}/k_B T\right)$.

The experimental work of [Shahar et al., 1992] suggests that the activation energy $k_B T_0 \sim \delta_{\mathrm{loc}}$ becomes nearly equal to T_c at the SIT. This can be seen from Fig. 2.2, where T_c and T_0 curves meet at the transition.
Therefore one could argue that the activation energy, by essence related to electronic localization, is also related to superconducting energy scales.
This observation triggered intense theoretical works trying to reconcile strongly localized insulators and superconductors.

As we shall see now, other experimental works further blurred the line separating insulator and superconductor in indium oxide.

2.1.2 Experimental demonstration of the interplay of insulator and superconductor

A different and very instructive experimental approach consisted in probing the *local* properties of **superconducting** disordered indium oxide films using a Scanning Tunneling Microscoscope (STM) via the local measurement of the tunneling conductance G that can be directly related to the density of states. This method therefore allows for the measurement of the local value of the superconducting gap (noted E_g in the following, and not Δ as will become clearer soon).

Fig. 2.3 shows such tunneling spectroscopy for two disordered indium oxide samples performed by [Benjamin Sacépé, Dubouchet, et al., 2011]. At lowest temperatures (blue curve on panel **a**) the density of states (DoS) presents a typical result compatible with BCS theory: below E_g the DoS is suppressed, while it increases sharply at the edges of the gap, forming what are known as *coherence peaks*. These features are expected in BCS theory as they host the missing spectral weight below the gap.

The surprising discovery of [Benjamin Sacépé, Dubouchet, et al., 2011] is made at higher temperatures, above the critical temperature T_c for which superconductivity should break down, and therefore the gap should close. What can be seen in Fig. 2.3 is strikingly different: the tunneling gap remains large above T_c, while the coherence peaks smear out (see panel **c**). Measurements on an even more strongly disordered sample (panels **b-d**) show that, for some positions of the STM tip on the sample coherence peaks could vanish even at lowest temperature, evidencing strong spatial fluctuations of the tunneling gap.

Using this technique similar results we obtained on several disordered superconductors such as TiN [B. Sacépé, C. Chapelier, et al., 2008; Benjamin Sacépé, Claude Chapelier, et al., 2010] and NbN [Chand et al., 2012; Kamlapure, Das, et al., 2013; Noat et al., 2013; Lemarié et al.,

[5] For a density of states ν the number of states in a localization volume ξ_{loc}^d on d dimensions is $\nu \xi_{\mathrm{loc}}^d$.

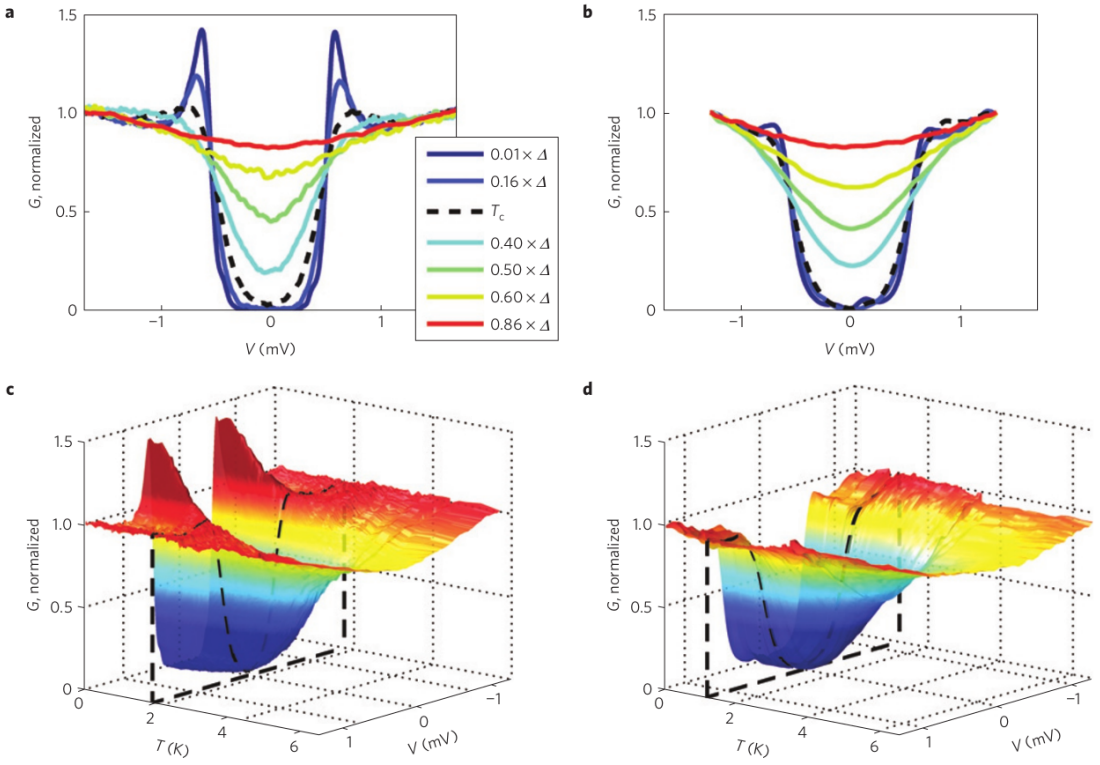

Fig. 2.3. Observation of the pseudogap in indium oxide by local tunneling spectroscopy. Local tunneling conductance G was measured as a function of bias voltage V and temperature in two indium oxide samples of different disorder (**a-c** correspond to a low-disorder sample while sample **b-d** was strongly disordered). The tunneling conductance is proportional to the local density of states and provides a measure of the spectral gap, which survives at temperatures above T_c (denoted by the black dashed line). The superconducting state is destroyed at T_c, as evidenced by the vanishing coherence peaks. From [Benjamin Sacépé, Dubouchet, et al., 2011]

2013; Carbillet et al., 2020], where a strong spatial inhomogeneity of the gap was found. Fig. 2.4 shows such gap spatial inhomogeneities measured in disorded TiN by [B. Sacépé, C. Chapelier, et al., 2008]. Similar results were found in indium oxide but not published [B. Sacépé, Private communications]

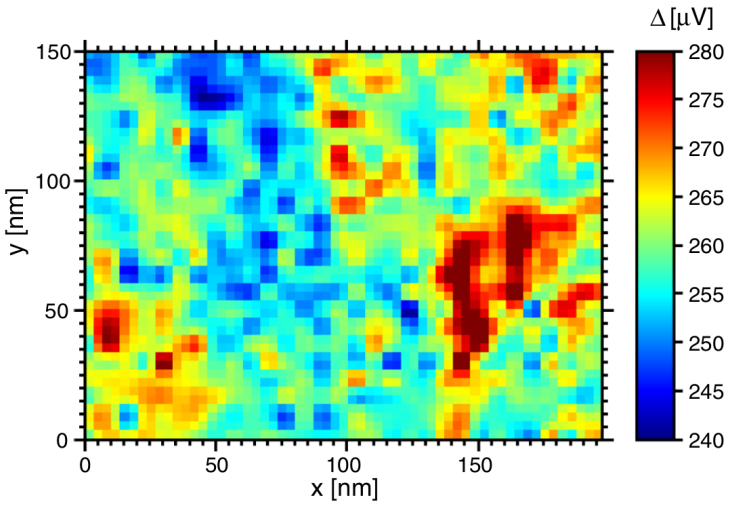

Fig. 2.4. Gap spatial inhomogeneities in TiN. The gap amplitude measured by STM in disordered titanium nitride fluctuates strongly, forming regions where the tunneling gap remains large, and regions where it is suppressed. From [B. Sacépé, C. Chapelier, et al., 2008]

These findings suggest an unusual mechanism for the formation of superconductivity: the presence of a superconducting gap above T_c (but without coherence peaks) seems to indicate that formation of Cooper pairs and long-range superconducting state do not occur simultaneously. One could say that pairs of electrons *pre-form* at temperatures well above T_c, and finally condense at the critical temperature into the superconducting state.
This scenario is quite different from the standard BCS mechanism for which the opening of a gap Δ is concomittant with the superconducting state. The unexpected spectral gap that survives above T_c is then often called a *pseudogap*.

Further, these observations can be made only for relatively disordered films. For clean samples the local DoS behaves according to BCS theory, suggesting that the dissociation of pairing and condensation energy scales is induced by disorder.

By controlling the point-contact conductance of a scanning tip microscope on a superconducting indium oxide sample, [Dubouchet et al., 2018] were able to probe not only single electron tunneling, but also tunneling of Cooper pairs (charge $2e$), allowing to clearly identify a new energy scale, called the collective gap Δ_{coll} (see right graph of Fig. 2.5). This energy related to Cooper pairs is of the order $\sim T_c$, further suggesting that Δ_{coll} is related to the superconducting state, while E_g is independent of it. This measurement clearly shows the dissociation of pairing (energy $\sim E_g$) and condensation ($\sim \Delta_{\text{coll}}$) energy scales in strongly disordered films.

A final, clear-cut evidence is found in the work of [D. Sherman et al., 2012; Daniel Sherman, Gorshunov, et al., 2014], who demonstrate that the **pseudogap also survives in the insulating state**.
This time, a planar tunneling junction is used to probe the superconducting gap of two indium oxide samples, one is superconducting (blue curve in Left graph of Fig. 2.5) and behaves like a superconductor both from resistance measurements and tunneling spectroscopy (with coherence peaks), and an insulating sample (diverging resistance at low temperature) that still shows a large tunneling gap (orange curve).

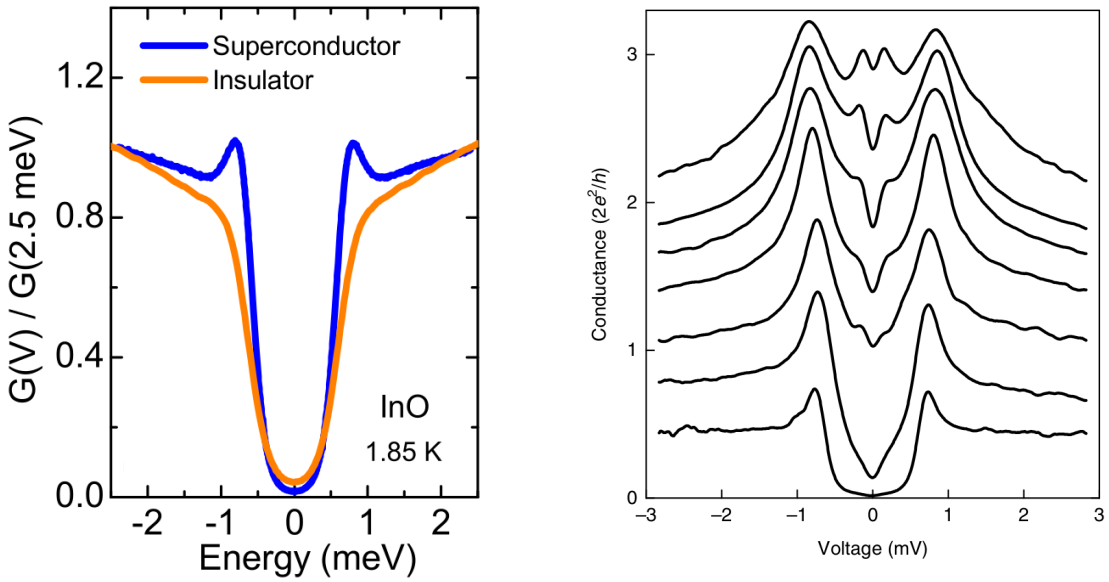

Fig. 2.5. Pseudogap in the insulator and collective gap. Left: Measurement of the pseudogap in insulating (as checked in transport) and superconducting indium oxide at finite temperature $T = 1.85$ K. E_g is comparable in both cases but coherence peaks vanish in the insulator. From [Daniel Sherman, Gorshunov, et al., 2014]. **Right:** STM measurement of a superconducting indium oxide sample. By varying the point-contact conductance between the STM tip and the film [Dubouchet et al., 2018] were able to probe single electron tunneling (measuring E_g, lowest curves) and Cooper pair tunneling by Andreev spectroscopy (upper curves). In the Andreev regime a gap of size Δ_{coll} appears within the single particle gap.

To conclude, it has been demonstrated experimentally that the insulating indium oxide (characteristic energy scale T_0) could turn into a superconductor by lowering disorder (with typical energy $\sim T_c$). Also, a gap in the single particle density of states, called the pseudogap, survives across the superconducting transition ($T > T_c$) and the Superconductor-Insulator Transition (above a critical disorder).
These intriguing facts could actually be related: is the activation energy T_0 related to the pseudogap ? How can we understand the preformation of Cooper pairs in the insulating state ? To try to answer these questions we now briefly summarize recent theoretical models dealing with the interplay of superconductivity and disorder.

2.2 | From Anderson insulator to fractal superconductor

The question of the fate of superconductivity in presence of strong disorder was raised by P.W. Anderson shortly after the development of BCS theory. He demonstrated that conventional superconductors are robust with respect to disorder, *i.e* the critical temperature T_c remains unaffected by impurities [P. Anderson, 1959]. While this general statement holds for a large variety of dirty superconductors it has become clear that this *Anderson theorem* does not apply at stronger disorder levels, especially close to a SIT.

The effect of Anderson localization on superconductivity and T_c has been studied extensively on theoretical ground [Takagi et al., 1982; Ma et al., 1985] but remains a relevant subject for theoretical and experimental developments.

2.2.1 Extension of Anderson theorem

The interplay of localization and superconductivity is a difficult and complex theoretical problem. Adding to it interactions (attractive or repulsive) between electrons and between pairs of electrons (such as Coulomb repulsion) makes the system even more difficult to solve. In the literature many models have neglected interactions between electrons, in the line of Anderson's model.
In the first part of this section we use the same simplification and neglect interactions between electrons. We consider only the combination of superconductivity (with the possibility for electron pairs) and the localization of single electrons. We discuss the case of systems for which the disorder can be assumed 3D (and therefore with the existence of a mobility edge).

[Ma et al., 1985] showed the important result that superconductivity could survive deeper in the insulating regime than predicted by the Anderson theorem. Their new criterion introduces an other energy scale, related to the confinement of electronic wavefunctions in a localization volume:

$$\delta_{\mathrm{loc}} = \frac{1}{\nu_0 \xi_{\mathrm{loc}}^3} \tag{2.1}$$

where ν_0 is the average density of states at the Fermi level, ξ_{loc} is the localization length and therefore ξ_{loc}^3 is the typical volume occupied by a strongly localized wavefunction.
δ_{loc} has the meaning of the mean spacing between (discrete) energy levels in the volume occupied by a localized wavefunction.
The criterion of [Ma et al., 1985] for the survival of superconductivity reads

$$\Delta \gg \delta_{\mathrm{loc}} \tag{2.2}$$

where Δ is the average superconducting gap.
Eq. (2.2) can be understood as the fact that superconductivity is favorable when more than two energy levels of localized electrons are included in the energy interval of order $\sim \Delta$.
Equivalently this relation can be written as a condition on characteristic lengths:[6] $\xi_{\mathrm{loc}} \gg \xi$ where ξ is the superconducting coherence length (that is, the typical size of a Cooper pair must be comprised in a localization volume). Both interpretations are pictured in Fig. 2.6.

2.2.2 Attractive Bose-Hubbard model

There is an obvious theoretical interest in allowing *attractive* electron-electron interactions (which could be mediated by the coupling to phonons, or other processes). In this section we describe the numerical works of [Ghosal et al., 2001; Bouadim et al., 2011] in which attraction between single electrons is added to an Anderson insulator, and we show that this simple assumption has very peculiar and important consequences on the emergence of a superconducting state.

The works of [Ghosal et al., 2001; Bouadim et al., 2011] consider the simplest Hamiltonian that accounts for both Anderson localization and interactions between electrons in a two-dimensional system. Attraction is described by the potential U entering the interaction Hamiltonian H_{int}.

[6] Close to the metal-insulator transition $g_c \sim 1$ and ξ_{loc} diverges which leads in 3D (see section A.3.2) $\nu_0 \xi_{\mathrm{loc}} \sim (\hbar D)^{-1}$. Using the dirty limit BCS relation for the coherence length $\xi^2 \sim \hbar D/\Delta$ Eq. (2.2) finally reduces to $\xi_{\mathrm{loc}} \gg \xi$.

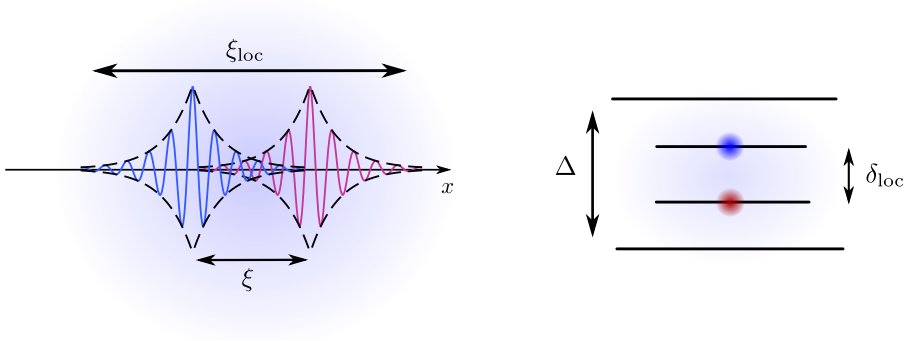

Fig. 2.6. Extension of Anderson's theorem. [Ma et al., 1985] showed that superconductivity survives localization until $\Delta \gg \delta_{\rm loc}$ (right), or equivalently $\xi_{\rm loc} \gg \xi$ (left).

The resulting model is then the sum of two terms: $H = H_0 + H_{\rm int}$ where

$$H_0 = -t \sum_{\langle ij \rangle \sigma} \left(c^\dagger_{i\sigma} c_{j\sigma} + \text{h.c} \right) + \sum_{i\sigma} \left(V_i - \mu \right) n_{i\sigma} \tag{2.3}$$

$$H_{\rm int} = -|U| \sum_i n_{i\uparrow} n_{i\downarrow} \tag{2.4}$$

where $c^\dagger_{i\sigma}$ ($c_{i\sigma}$) is the fermionic creation (annihilation) operator with spin σ on site $\mathbf{r_i}$ of a square lattice. t is the nearest-neighbour hopping constant, i, j are nearest neighbour sites and $|U|$ is the pairing interaction. $n_{i\sigma} = c^\dagger_{i\sigma} c_{i\sigma}$ and μ is the chemical potential. Disorder is represented by the random variable V_i uniformly distributed over $[-V, V]$ at each site $\mathbf{r_i}$.

In this model all interactions between electrons are neglected except for the attraction $|U|$. In particular it does not consider Coulomb interactions, a contribution that should be added later on to describe a real system. It is a minimal model containing both localization (setting $|U| = 0$ one recovers the Anderson problem) and a BCS-like description of paired electrons on the same site giving rise to superconductivity (for $V = 0$). This Hamiltonian is often refered to as the *negative-U (or attractive) Hubbard model*.

By treating the problem using a mean-field Bogoliubov-de-Gennes method the authors demonstrate the existence of a pairing order parameter $\Delta_{\rm OP}$, similar to the usual BCS gap in a conventional superconductor. When this quantity is non-zero pairs of electrons can be found in the system. Below a critical temperature $T_c \propto \Delta_{\rm OP}$ and for low disorders the system behaves like a superconductor.

Inhomogeneous order parameter

The first important result of [Ghosal et al., 2001] is the demonstration of the strong spatial variations of the local order parameter mean values $\Delta_{\rm OP}(\mathbf{r_i})$, the result of which is shown in Fig. 2.7.
Upon increase of disorder the order parameter amplitude vanishes locally, forming an electronically *granular* structure of superconducting islands with large pairing amplitude embedded in an insulating matrix with $\Delta_{\rm OP}(\mathbf{r_i}) \approx 0$. It is crucial to note here that the initial disorder potential $V(\mathbf{r})$ is randomly distributed, without intrinsic granularity.
Therefore the simulations show that order parameter granularity emerges naturally from homogeneous disorder.

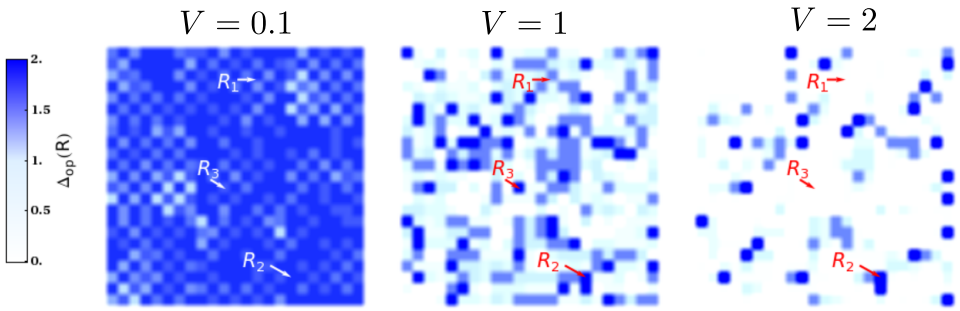

Fig. 2.7. Inhomogeneous local order parameter for three disorder strengths $V = 0.1, 1, 2$**.** The BdG mean-field treatment of the attractive Bose-Hubbard model carried out by [Ghosal et al., 2001; Bouadim et al., 2011] shows the strong inhomogeneity of the local value of the order parameter $\Delta_{\mathrm{OP}}(\mathbf{r})$ as disorder is increased. The intensity of blue signals the value of the order parameter, with a deep blue corresponding to larger values and white signaling lowest values. As disorder is increased regions with vanishingly small amplitudes appear, forming a *granular* structure of superconducting islands at the scale of the coherence length ξ immersed in an insulating matrix. From [Bouadim et al., 2011].

A pseudogap predicted by numerical simulations

The authors then combine the BdG approach to Quantum Monte Carlo (QMC) simulations, which have the advantage of considering thermal and quantum fluctuations of the superconducting phase as well as the spatial fluctuations of the order parameter amplitude. In particular they were able to simulate the single-particle density of states $N(\omega)$ as displayed in Fig. 2.8 for different disorder realizations.

Their main findings are the following:

- A gap in the single-particle density of states is present below T_c, accompanied with coherence peaks. However, in the non-superconducting state for temperatures above T_c the DoS remains suppressed (forming a *pseudogap*) and the coherence peaks vanish (see panels **C**-**D** of Fig. 2.8)
- At $T = 0$ the gap in the single-electron density of states E_g survives in the insulating state. Its value remains finite in the insulator, and even increases with disorder (panels **A**-**B** of Fig. 2.8). The pseudogap in the insulator even remains upon increase of temperature (panels **E**-**F** of Fig. 2.8)

Therefore these simulations evidence the increasing deviation from standard BCS theory with disorder. The existence of a gap E_g in the single-particle density of states becomes unrelated with the long-range order characterizing superconductivity, the latter being related to the order parameter Δ_{OP}. As seen in Fig. 2.9 (Left) these two energy scales coincide at low disorder $V \ll 1$ where BCS theory is expected to hold, but separate upon increase of disorder (green shaded area). The missing energy $\Delta_{\mathrm{P}} = E_g - \Delta_{\mathrm{OP}}$ is called a *pseudogap* and persists in the normal and insulating states.

An energy scale ω_{pair}, defined as the energy cost to add a pair of electrons to the insulator, increases with disorder (see Right panel of Fig. 2.9). This two-particle energy gap is nearly zero close to the SIT (since there is no cost to add a pair to the superconducting condensate),

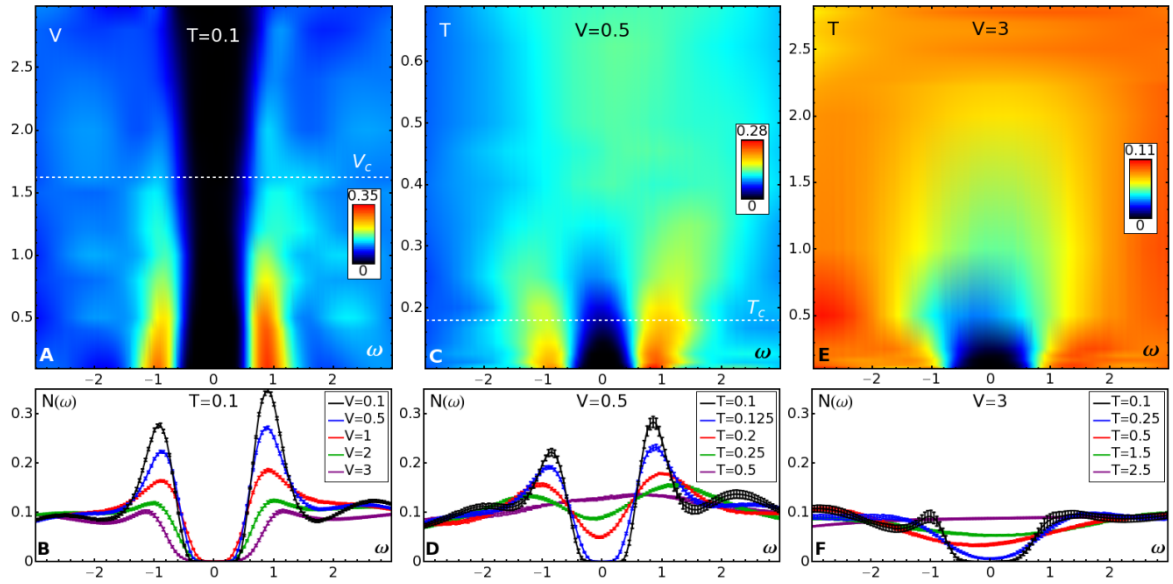

Fig. 2.8. Single-particle density of states. Top graphs shows the density of states $N(\omega)$ and bottom plots displays the corresponding spectra. **Left (A,B)**: disorder dependence of $N(\omega)$ for a fixed low temperature $T = 0.1$ (in dimensionless units). A hard gap (black region) persists for all disorders V below and above the SIT (at disorder $V_c = 1.6$ shown by the horizontal dashed line) but the coherence peaks (red regions) exist only in the SC state and not in the insulator. **Center (C,D)**: T-dependence of $N(\omega)$ for the superconductor ($V < V_c$). The coherence peaks (red) visible in the SC state (for temperatures below T_c, shown by the horizontal dashed line), vanish for $T \geq T_c$. A *disorder-induced pseudo-gap* persists well above T_c. **Right (E,F)**: T-dependence of $N(\omega)$ for the insulator at strong disorder ($V > V_c$). A pseudogap without coherence peaks is observed in a broad range of temperatures in the insulating state. From [Bouadim et al., 2011].

but going deeper into the insulator this quantity increases. Note the intriguing similarity between this theoretical phase diagram, where T_c decreases on the superconducting side and ω_{pair} increases on the insulating side, and the experimental phase diagram shown in Fig. 2.2 in which the decrease of T_c on the SC side is mirrored by the increase of the activation energy T_0 on the insulating side.
We shall discuss later the relation between T_0 and the two-particle energy scale.

The apparent increase of E_g upon approaching the SIT is rather surprising. For a standard superconductor one would expect all energy gaps to close, thence allowing all single electrons near the Fermi level to contribute to conduction, in a metallic state. Here E_g not only remains large but also increases when entering the insulating state. [Ghosal et al., 2001] showed that this behavior comes from properties of Anderson insulators, as we briefly discuss now.

From a mean-field treatment of the attractive Bose-Hubbard Hamiltonian Eq. (2.4), it is possible to show that at small disorders the gap is identical to the order parameter: $E_g = \Delta_{\text{OP}}$, as expected from standard BCS theory in a clean system.
Looking now at the strong disorder limit, where eigenstates of the non-interacting system are exponentially localized and weakly overlap in space, the single particle gap scales as

$$E_g \sim \frac{|U|}{2\xi_{\text{loc}}^2} \tag{2.5}$$

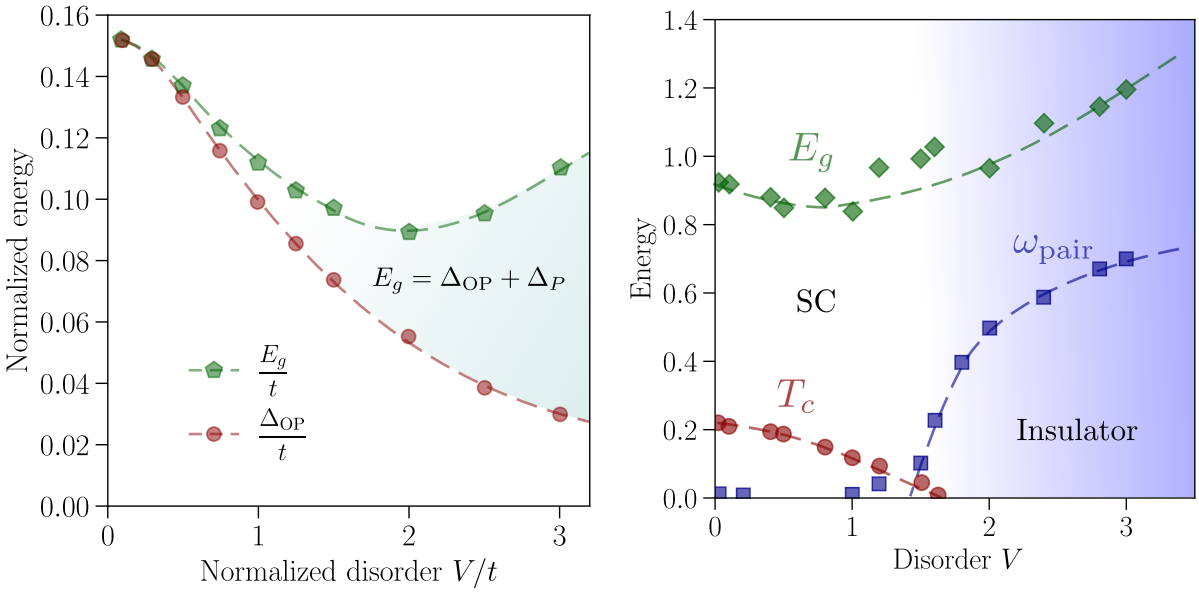

Fig. 2.9. Energy scales predicted by simulation of the attractive Bose-Hubbard model. Left: Numerical simulations of spectral (E_g) and superconducting ($\Delta_{\rm OP}$) gaps using the Bogoliubov-de Gennes approach. The disorder strength is caracterized by the impurity potential V. For $V \ll 1$ spectral gap E_g and order parameter $\Delta_{\rm OP}$ are the same, as expected for a BCS s-wave superconductor. Upon increase of V towards the SIT the two energy scales separate, with an enhancement of E_g and a suppression of $\Delta_{\rm OP}$. The missing energy scale is the pseudogap $\Delta_{\rm P}$. Adapted from [Ghosal et al., 2001]. **Right:** Reproduction of the phase diagram proposed in [Bouadim et al., 2011] using the QMC method. Critical temperature T_c, spectral gap E_g and two-particle gap $\omega_{\rm pair}$ are shown on both sides of the SIT. The QMC approach accounts for phase fluctuations in addition to spatial inhomogeneity.

where $\xi_{\rm loc}$ is the localization length of the Anderson problem and $|U|$ is the attractive potential responsible for pairing.
This calculation is approximate and expected to hold only for localized states with negligible overlap (thus deep in the insulating regime). The authors have however checked numerically that diagonal matrix elements are indeed the dominant contribution.

Therefore the survival and enhancement of the spectral gap E_g across the disorder-driven SIT can be explained by Anderson localization effects. The decrease of localization length $\xi_{\rm loc}$ when going deeper in the insulating regime and further from the mobility edge[7] leads to an increase of the spectral gap E_g with disorder.

The existence of the gap E_g in the single-particle density of states above T_c and in the insulating state suggests the presence of paired electrons in these phases (with pairing energy $\sim E_g/2$). [Bouadim et al., 2011] put forward the possibility that local attraction between electrons is enhanced because of their confinement in the small localized volume $\xi_{\rm loc}^d$. In this picture Cooper pairs are formed thanks to localization of electrons. However these electron pairs do not necessarily provide a superconducting state.

One then has a system formed of non-interacting electron pairs (remember that the system considered here neglects any other interaction than the potential for bound pairs $|U|$), which

[7] The localization length scales with the distance to the mobility edge as $\xi_{\rm loc} \sim |E - E_c|^{-\nu}$.

can be either in a global superconducting state, or on the contrary in an insulating state. We now discuss the mechanism that the authors propose for the suppression of the superconducting state, using the criterion developped in [Scalapino et al., 1993].

Superconductivity is ruled by phase fluctuations

[Ghosal et al., 2001; Bouadim et al., 2011] estimate the zero-T superfluid stiffness $\Theta(0)$ of the superconducting state via the current-current correlators [Scalapino et al., 1993]. They observe a decrease of Θ with disorder, reaching zero at a critical disorder V_c marking the transition between superconducting and insulating states.[8]

Since the system under study is two-dimensional, it should be in the BKT-class (see section 1.3) and therefore have a superconducting state ruled by classical phase fluctuations. This allows to estimate the critical temperature from the superfluid stiffness as $T_c \sim \Theta(0)$ [Emery et al., 1995]. The resulting evolution of $T_c \sim \Theta(0)$ estimated from these simulations is shown in the phase diagram of Fig. 2.9.

The criterion that determines whether the system is in a superconducting or insulating state is now the superfluid stiffness Θ ($\sim T_c$), irrespective of the value of single particle gap E_g: a non-zero superfluid stiffness signals superconducting long-range order, and the critical disorder at which Θ goes to zero determines the SIT. At low disorder the BCS relation $E_g \propto T_c \propto \Delta_{\mathrm{BCS}}$ holds, signaling that the spectral gap is still related to the BCS gap. The latter simultaneously quantifies local pairing attraction and long-range order. Upon increase of disorder E_g and T_c become unrelated, and Θ governs the superconducting state.

In [Seibold et al., 2012] it was demonstrated (again using the BdG treatment of the attractive Bose-Hubbard model) that upon increase of disorder quantum phase fluctuations were enhanced, as evidenced by a strong reduction of the superfluid stiffness, eventually leading to destruction of superconductivity.
In this picture current follows a quasi one-dimensional percolative path along the "good" superconducting regions with large local order parameter $\Delta(\mathbf{r_i})$. Concurrently local superconducting phase gradients $\nabla\varphi(\mathbf{r_i})$ are larger in weakly superconducting regions, leading to smaller local stiffnesses. The 'macroscopic' phase stiffness Θ vanishes when no percolative path exists along the sample.

2.3 | Theory of pseudogap

While the numerical works presented in section 2.2.2 give an important qualitative glimpse at the properties of paired insulators, with the intriguing predictions of pseudogap, spatial gap fluctuations and SIT, they do not provide a quantitative description of a real material defined by intrinsic parameters such as Cooper pairing constant λ, distance to the mobility edge $|E_F - E_c|$ or microscopic details of disorder. Importantly the simulations are performed for a 2D system with strong coupling U while real experimental realizations involve most frequently weak coupling. Also, these numerical simulations do not explain the origin of pairing in an Anderson insulator. Finally a consistent theory of disordered superconductors should be able to provide an interpretation of the experimentally measured activation energy T_0.

[8] In [Ghosal et al., 2001] the BdG method was used and fluctuations could not be taken into account. They found that the phase stiffness did not go to zero. When adding quantum and thermal fluctuations with the QMC approach in [Bouadim et al., 2011] such issue was solved.

We now present the theory of pseudogapped superconductors developped my Mikhail Feigel'man and collaborators and published in an on-going series of paper [M. V. Feigel'man, Ioffe, Kravtsov, et al., 2007; M.V. Feigel'man et al., 2010; M. V. Feigel'man, Ioffe, and Mézard, 2010].

The starting assumption of this theory is that local pairing of electrons originates from the fractal nature of electronic wavefunctions close to criticality in Anderson insulators. A reminder of the properties of fractals and their relation with electronic wavefunctions in the Anderson problem can be found in Appendix A.3.5.
Due to their fractal spatial extension on short scales smaller than the localization length $r < \xi_{\rm loc}$, localized electron wavefunctions occupy a smaller volume in space which enhances the phonon-mediated attraction leading to pairing. In this picture Cooper pairs naturally emerge from the insulating or metallic state as pairs of incoherent spatially localized electrons.

2.3.1 On the origin of local pairing in the insulator

Following the calculations of M. Feigel'man we explain in this section why preformed pairs of electrons should develop in the Anderson insulator, in **some** materials, and especially in amorphous indium oxide. The two conditions for this are: low carrier density ($n \sim 10^{21}\ \mathrm{cm}^{-3}$ for indium oxide) and high dielectric constant of the insulating matrix. Conduction electrons interact via this insulating matrix, notably through repulsive Coulomb interactions and phonon-mediated electron-electron attraction. We show that attractive interactions can overcome Coulomb repulsion, leading to preformed pairs.

One must keep in mind at this point that the dielectric constant of Anderson insulators is actually not a constant *per se*, but rather a function of the length-scale involved. Therefore one has significantly different values of dielectric constant depending on the spatial range of the interaction of interest.
For instance it was demonstrated in [M V Feigel'man et al., 2018] that the major contribution to the *macroscopic* dielectric constant κ comes from large spatial scales $\sim (5-10)\,\xi_{\rm loc}$. This is the value of κ that enters the expression of *long-range* Coulomb interactions between electrons (or between electron pairs).
The relevant dielectric constant for this discussion, however, concerns very short range interactions: Coulomb repulsion between two electrons localized within the same localization volume have a range $r \leq \xi_{\rm loc}$. Here the dielectric constant has a value of the order of $\kappa_1 \approx 50$.[9]

The key difference between the two types of interactions between electrons in the insulator (phonon-induced attraction and Coulomb repulsion) is that the first one is local (with typical length-scale of lattice constant), while the second one is long-range, $V_C(r) = e^2/\kappa_1 r$ with $r \leq \xi_{\rm loc}$. It can be shown that the fractal nature of electron wavefunctions enhances the former, leading to an overall slightly larger local attraction between electrons than their repulsion.[10]

[9] The value $\kappa_1 = 30$ is known for insulating crystalline indium oxide. [Ovadyahu, Private communications].

[10] The goal is to estimate the average matrix elements of the interaction $V(\mathbf{r})$ for localized electron wavefunctions Ψ:

$$\overline{U} = \int d\mathbf{r}\, d\mathbf{r}'\, V(\mathbf{r}-\mathbf{r}')\overline{\Psi^2(\mathbf{r})\Psi^2(\mathbf{r}')} \tag{2.6}$$

for the two competing interactions.

The local phonon-mediated attraction is of the form $V_{\rm e-ph}(\mathbf{r}-\mathbf{r}') = -g_{\rm e-ph}\delta(\mathbf{r}-\mathbf{r}')l^3$ where $g_{\rm e-ph}$ is a coupling constant with dimension of energy and l is a short-scale cutoff of the order of the lattice constant. The Coulomb potential is $V_C(r) = e^2/\kappa_1 r$ with $r \leq \xi_{\rm loc}$.
Using the properties of multifractal wavefunctions [M. Feigel'man, Private communications] estimates the

Therefore local Coulomb repulsion between electrons can be overcome by phonon-induced local attraction, leading to preformed pairs.

2.3.2 Pseudo-gap in fractal insulators

We start by studying the effects of performed Cooper pairs in the insulating state predicted by [M.V. Feigel'man et al., 2010].

Let us consider a BCS-like ground state in the basis of localized single-electrons $\{\Psi_i\}$.

$$H = \sum_{j\sigma} \varepsilon_j c^\dagger_{j\sigma} c_{j\sigma} - \frac{\lambda}{\nu_0} \sum_{jk} M_{jk} c^\dagger_{j\uparrow} c^\dagger_{j\downarrow} c_{k\downarrow} c_{k\uparrow} \tag{2.9}$$

$$M_{jk} = \int \Psi_j^2(\mathbf{r}) \Psi_k^2(\mathbf{r}) d\mathbf{r} \tag{2.10}$$

where $\varepsilon_j = E_j - E_F$ is the single-particle energy of the eigenstate j counted from the Fermi energy, $c^\dagger_{j\sigma}$ is the associated creation operator for spin σ and ν_0 is the density of states. λ is the dimensionless Cooper coupling constant, which is assumed small. This assumption is an important difference from the numerical works above.
This Hamiltonian is the minimal model containing localization of electrons at sites j, k as well as pairing between these localized electrons.

Looking at the diagonal matrix elements M_{jj} one recognizes the inverse participation ratio (IPR) discussed in section A.3.5, with typical scaling with system size $\bar{M} \propto L^{-D_2}$, and fractal dimension $D_2 \approx 1.3$. Using the short-scale cutoff for fractals structures L_0 (energy E_0) leads to the typical value of matrix element near the mobility edge

$$\bar{M} \approx L_0^{-3} \left(\frac{\xi_{\text{loc}}}{L_0} \right)^{-D_2} = \nu_0 E_0 \left(\frac{L_0}{\xi_{\text{loc}}} \right)^{D_2} \tag{2.11}$$

In the insulating phase, the authors demonstrate that the energy cost to break a preformed pair of localized electrons in the same orbital is $2\Delta_P \approx \lambda / \nu_0 \bar{M}$. The energy scale Δ_P is the *parity gap* first introduced by [Matveev et al., 1997] in ultra small superconducting grains. The parity effect states that the energy of a system of preformed pairs is lower for an *even* number of electrons than for the nearest *odd* number of electrons. These considerations lead to an estimation of the parity gap Δ_P as

---

ratio of attractive and repulsive interactions as

$$\frac{|\overline{U_{\text{e-ph}}}|}{\overline{U_C}} = g_{\text{e-ph}} \left(\frac{l}{\xi_{\text{loc}}} \right)^{D_2} \frac{\pi \kappa_1 \xi_{\text{loc}}}{e^2 J_c} \tag{2.7}$$

where $D_2 = 1.3$ is the fractal dimension at criticality and $J_c \approx 120$ is related to the wavefunction overlap. The consequence of the fractal nature of wavefunctions resides in the factor $(l/\xi_{\text{loc}})^{D_2}$: this term is significantly enhanced compared to the bare value obtained usually by taking $d = 3$.

Using physically relevant estimates for the constants entering Eq. (2.7) gives

$$\frac{|\overline{U_{\text{e-ph}}}|}{\overline{U_C}} \approx 8\lambda_0 > 1 \tag{2.8}$$

where $\lambda_0 = g_{\text{e-ph}} l^3 \nu_0$ is the dimensionless Cooper attraction constant. Using the approximate value $\lambda_0 \approx 0.128$ from [Benjamin Sacépé, Dubouchet, et al., 2011] gives $8\lambda_0 = 1.024 > 1$.
Despite the fact that $\lambda_0 < 1$, Cooper instability occurs for arbitrary small attraction strength, provided it overcomes Coulomb repulsion.

$$\Delta_P = \frac{\lambda}{2} E_0 \left(\frac{L_0}{\xi_{\rm loc}} \right)^{D_2} \propto (E_c - E_F)^{\nu D_2} \tag{2.12}$$

where last equality originates from the scaling of the localization length as $\xi_{\rm loc} \approx L_0 \left[E_0/(E_c - E_F) \right]^{\nu}$ with the scaling exponent $\nu \approx 1.6$.
The result $\Delta_P \propto \lambda \xi_{\rm loc}^{-D_2}$ given by Eq. (2.12) is to be compared with the estimation $E_g \propto |U| \xi_{\rm loc}^{-d}$ obtained from numerical simulations in Eq. (2.5). The results are qualitatively the same, with the major difference that the parity gap model accounts for the fractal structures of electronic wavefunctions (with dimension $D_2 < d$), which further enhances the spectral gap in the insulator. Fig. 2.10 shows an illustration of the parity gap.

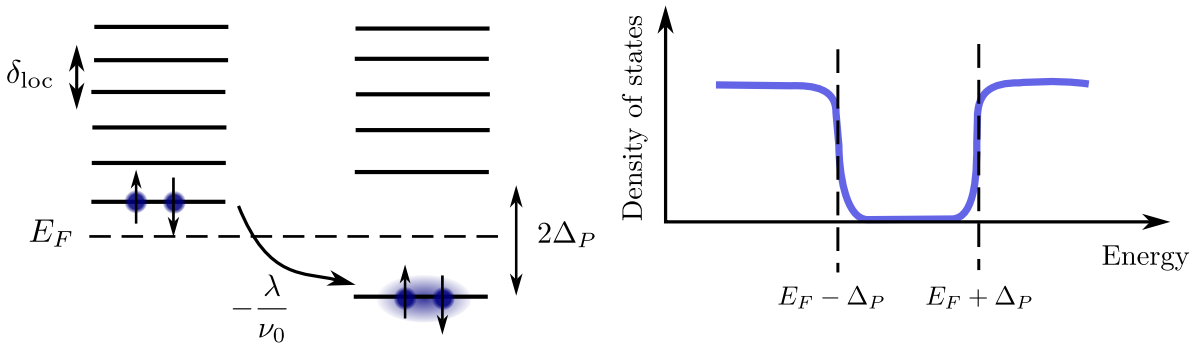

Fig. 2.10. Parity gap. In the insulator for $\Delta < \delta_{\rm loc}$ switching on attractive interactions between electrons within the same localized volume opens a parity gap Δ_P in the single-electron density of states. The latter is of intrinsically different origin from the usual BCS gap and is not accompanied with coherence peaks.

Note that this gap induced by parity effects is intrinsically different from the usual BCS gap that originates from many-body correlations of electrons with energy within $\sim \Delta_{\rm BCS}$ from the Fermi level. Here all states occupied by a bound pair of localized electrons are shifted down in energy with respect to the Fermi level by the quantity Δ_P, leading to a DoS of the form $\nu(\varepsilon) = \theta(\varepsilon - \Delta_P)$ where θ is a step function and $\varepsilon = E - E_F$. Therefore the condition for the conservation of the total number of states does not require the apparition of coherence peaks at the border of the gap, unlike the usual BCS mechanism. The parity gap bears some qualitative resemblance with the Coulomb gap discussed in section A.4.
Therefore one should note that this picture of locally preformed pairs is **not** equivalent to a model of incoherent superconducting puddles embedded in an insulating matrix and connected by Josephson coupling between islands. Indeed in this picture local spectroscopy of the DoS should show coherence peaks in the good superconducting regions, which is not required here.

[M.V. Feigel'man et al., 2010] suggest that the parity gap can be identified with the pseudogap experimentally observed in disordered superconductors.
This theory also gives an interpretation to the activation energy T_0 observed in the temperature evolution of resistance for insulating indium oxide samples. Δ_P is the energy scale that enters the thermally activated conductivity of strongly disordered insulators by hopping of single localized electrons $\sigma(T) \propto \exp\left[-(T_0/T)\right]$ close to the mobility edge, with the activation energy:

$$T_0 \sim 0.25 \Delta_P \propto |\sigma - \sigma_c|^{\nu D_2} \tag{2.13}$$

where σ is the high temperature conductivity and σ_c is the critical conductivity at the Anderson metal-insulator transition[11].

2.4 | Fractal superconductivity

Decreasing the disorder eventually leads to $\Delta > \delta_{\rm loc}$ for which superconducting correlations develop between localized preformed pairs. Transport then happens by coherent hopping of localized Cooper pairs from site to site.

Close to the SIT all the energy scales of the problem (notably T_c and Δ) are much smaller than the pseudogap Δ_P. Therefore the system can be understood by the Anderson pseudo-spin model (first introduced in [P. W. Anderson, 1958b] as a reformulation of BCS theory) which describes hopping of the preformed pairs between localized single particle states:

$$H = -\sum_i 2\xi_i S_i^z - \sum_{\langle ij \rangle} \left(J_{ij} S_i^+ S_j^- + \text{h.c} \right) \tag{2.14}$$

where S_i^+ / S_i^- is the creation / annihilation operator for a pair at site i. They are derived from fermionic operators as $2S_i^z = a_{i\downarrow}^\dagger a_{i\downarrow} + a_{i\uparrow}^\dagger a_{i\uparrow} - 1$, $S_i^+ = a_{i\uparrow}^\dagger a_{i\downarrow}^\dagger$ and $S_i^- = a_{i\downarrow} a_{i\uparrow}$.
$S_i^z = +\frac{1}{2} / -\frac{1}{2}$ corresponds to occupied (resp. unoccupied) Cooper pair at site i. The matrix elements J_{ij} for the hopping between single-electron wavefunctions localized at sites i and j is given by

$$J_{ij} = g \int \Psi_i^2(\mathbf{r}) \Psi_j^2(\mathbf{r})\, d\mathbf{r} \tag{2.15}$$

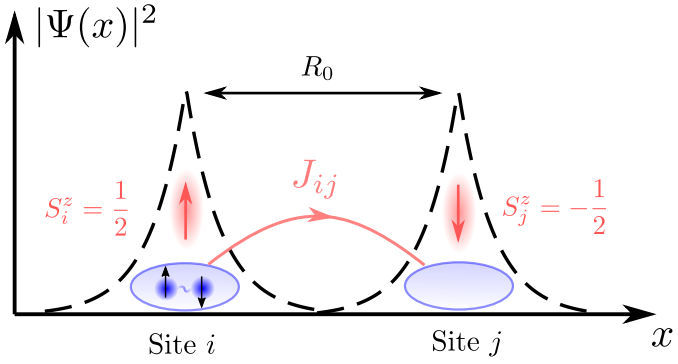

Fig. 2.11. Anderson pseudospins and Cooper pair hopping. Schematic representation of the pair-hopping process between localized single electron states described by the Hamiltonian (2.14).

Second term of Eq. (2.14) describes pair-hopping, and competes with the first term that describes random on-site potential. The preformed pairs are hard-core bosons (they cannot occupy the same quantum state) and therefore the pair operators are equivalent to spin-$\frac{1}{2}$ operators $\mathbf{S}$. A schematic illustration is displayed in Fig. 2.11.

In the superconducting state pair-hopping occurs, *i.e.* the quantum-statistical average values $\Delta_i = \sum_j J_{ij} \langle S_j^- \rangle$ are non-zero. In the opposite limit where $\Delta_i = 0$ Cooper pairs are localized.

[11] We used $(E_c - E_F) \propto (\sigma_c - \sigma)$

The quantity of interest is the effective coupling constant $J \sim J_{ij}Z$ where Z is the average number of connections per pseudo-spin *i.e* the effective number of neighbours of a site i on an interaction graph. Upon increase of disorder (thus reduction of electron density) the number of neighbours Z decreases, leading to a weakening of the effective coupling strength J.
At a given critical coupling J_c the system undergoes a superconductor-insulator transition at $T = 0$.

The model presented above was used by [M.V. Feigel'man et al., 2010] to demonstrate analytically the qualitative observations made from numerical simulations of the attractive Bose-Hubbard model, amongst which strong local inhomogeneity of the superconducting order parameter and persistence of a pseudogap. Especially the distribution of the order parameter amplitude is found to be extremely broad [A. V. Khvalyuk et al., 2021].

2.5 | Some properties of disordered superconductors

2.5.1 BKT transition in indium oxide

Experimental studies of the superfluid density suppression at finite temperatures in amorphous indium oxide films were carried out in [Fiory et al., 1983; R. Crane et al., 2007; R. W. Crane et al., 2007; Liu, Kim, et al., 2011; Liu, Pan, et al., 2013; Misra et al., 2013], observing a deviation from BCS theory near T_c with a qualitative agreement to a BKT transition.

Both low-frequency measurements of [Fiory et al., 1983] (see Fig. 2.12 Left panel) and studies in the gigahertz range (Fig. 2.12 Right panel) suggest a quantitative aggreement with the universal BKT relation $T_c^{\mathrm{BKT}} = (\pi/2)\Theta(T_c^{\mathrm{BKT}})$ in amorphous indium oxide. With one subtlety however: at large frequencies superconducting correlations survive above T_c, and the (non-zero) superfluid stiffness becomes strongly frequency-dependent.

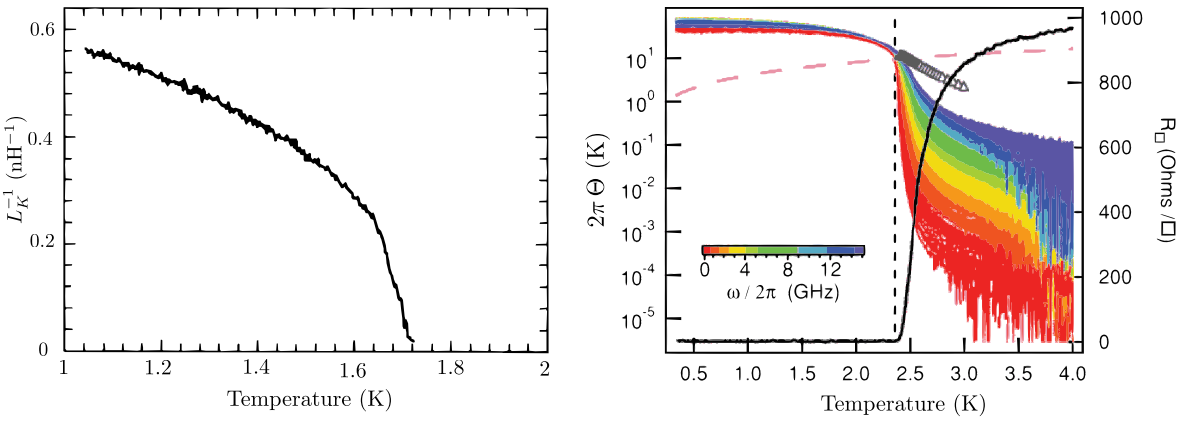

Fig. 2.12. BKT transition in amorphous indium oxide. **Left:** Drop of inverse kinetic inductance $L_K^{-1} \propto \Theta$ near T_c at low frequency $f \sim 150$ Hz. From [Fiory et al., 1983]. **Right:** Suppression of Θ with temperature measured at frequencies $f \in [0.2, 15]$ GHz from [Liu, Kim, et al., 2011]. The universal relation $T_c^{\mathrm{BKT}} = (\pi/2)\Theta(T_c^{\mathrm{BKT}})$ is shown by the dashed pink line. T_{BKT} (corresponding to the vertical dashed line) is the temperature at which the superfluid stiffness becomes frequency-dependent and the sample sheet resistance simultaneously drops to zero.

This is expected, as the sharp, universal BKT superfluid jump to zero actually occurs in the zero-frequency limit only (corresponding to infinite length scale). Therefore a macroscopic sample will have a vanishing resistance whenever the superconducting phase is ordered over its entire length only.

Superconductivity on short scales is not necessarily destroyed still. This is what a high-frequency measurement can demonstrate: $\Theta(\omega)$ measures the superfluid stiffness on length scales set by the probing frequency ω.[12] Above T_c the size of phase-coherent regions decreases with increasing frequency: a large measurement frequency will probe smaller regions in which superconducting correlations remain, leading to an overall larger superfluid stiffness. Pushing this argument further, this suggests that at lower frequencies one must inevitably average over 'bad' superconducting regions, which reduces the superfluid stiffness.

Such frequency-dependent behavior can be seen from Fig. 2.12, where superfluid stiffness curves separate upon increasing frequency above T_{BKT}. It was further demonstrated in [R. W. Crane et al., 2007] that at higher frequencies $\sim 100\ \mathrm{GHz}$ the superfluid stiffness' dependence with temperature approaches the usual BCS prediction. The temperature at which Θ becomes frequency-dependent can be associated with T_{BKT}, as is further confirmed by the vanishing of DC resistance at this temperature.

2.5.2 Survival of superconducting correlations across the SIT at $T = 0$

Recent works have focused on the AC response of amorphous indium oxide in a perpendicular magnetic field, driving the superconductor into an insulating state and probing the frequency-dependent superfluid stiffness across the transition [R. Crane et al., 2007; Liu, Pan, et al., 2013; Misra et al., 2013]. These works, which are the first finite frequency studies of the (field-tuned) SIT in indium oxide, further confirm the existence of short-scale superconducting correlations in the insulating state.

[Liu, Pan, et al., 2013] observe a strong frequency dependence of the zero-T Θ for high magnetic fields, where the DC resistance signals an insulator, while low-B measurements show a frequency independent superfluid stiffness. Similar measurements performed on a more disordered indium oxide sample [R. Crane et al., 2007] show a persistence of short-scale superconducting correlations at even larger fields.
These observations have been interpreted as an additional experimental demonstration of the presence of localized preformed pairs in the insulating state of indium oxide near criticality: it is insulating on long length scales but shows signatures of superconductivity on the local scale.

2.5.3 Electrodynamics of disordered superconductors

We have already mentioned the low-frequency experimental evidences for a pseudogap and order parameter inhomogeneities in amorphous indium oxide, but also in TiN [B. Sacépé, C. Chapelier, et al., 2008; Benjamin Sacépé, Claude Chapelier, et al., 2010] and in NbN [Chand et al., 2012;

[12] This length is proportional to the vortex diffusion length during one radiation cycle (which scales with frequency f as $\propto (D/f)^{1/2}$) [Liu, Kim, et al., 2011], and is potentially shorter than the average inter-vortex distance. In these regions the superconducting phase is virtually unaffected by the presence of free vortices, leading to local 'good' superconducting islands which preserve phase coherence. Then the superfluid stiffness goes continuously to zero as the number of free vortices increases. This process varies with frequency, leading to a clear separation of the $\Theta(T)$ curves above T_c.

Kamlapure, Das, et al., 2013; Noat et al., 2013; Lemarié et al., 2013]. Other amorphous materials display similar physics, such as NbSi [Pourret et al., 2006] or MoGe [Mandal et al., 2020]. We want to stress out that these materials show properties that could be compared to some high-T_c superconductors (namely pseudogap, inhomogeneities and low superfluid density), but that a further analogy is hard to establish. The s-wave superconductivity discussed here might have a quite different origin from that of the cuprates, and this question remains of great interest for future theoretical works.

We have shown previously that finite frequency measurements probe the phase coherence on shorter lengthscale, providing new insight on the local preformation of Cooper pairs (above T_c or in the insulating state). This technique can also be used at low temperatures (~ 20 mK, well below T_c) and in the superconducting state (where the phase is coherent over the whole sample) to measure the superfluid stiffness and gain important knowledge about the role of phase fluctuations in these systems.

To achieve this goal several experimental techniques have been developed, such as the *two-coil measurement*[13] [Kamlapure, Mondal, et al., 2010; Yong et al., 2013; Misra et al., 2013; Mandal et al., 2020] allowing the measurement of the surface impedance at moderately low frequencies ($f \sim 1$ kHz $- 100$ MHz) and its evolution with temperature, or the *THz spectroscopy* that enables a direct measurement of the superconducting gap [Pracht, Scheffler, et al., 2012; Daniel Sherman, Pracht, et al., 2015; Levy-Bertrand et al., 2019].
Another powerful technique consists in probing the reflection coefficient of a superconducting sample terminating a coaxial transmission line: by sending a microwave signal ($f = 0.1 - 20$ GHz) on the sample and measuring the reflected wave with a commercial vector network analyzer (VNA), one is able to get the sample surface impedance and consequently its complex conductivity $\sigma(\omega)$. This method is sometimes referred to as *Corbino microwave spectrometer* [Liu, Kim, et al., 2011; Mondal, Kamlapure, et al., 2013; Liu, Pan, et al., 2013].

An example using this method is shown in Fig. 2.13, where three distincts measurements techniques (STM tunneling conductance, DC resistance and Corbino microwave spectroscopy) are combined to obtain a phase diagram of NbN samples as a function of disorder. A pseudogap ($\Delta_P = k_B T^*$) opens with increasing disorder as evidenced by the STM data and separates from the critical temperature T_c. Similar films were studied in transport (resistance versus temperature curves on right panel), providing the critical temperature, and at microwave frequencies giving the frequency-dependent conductivity $\sigma(\omega) = \sigma'(\omega) + i\sigma''(\omega)$ and superfluid stiffness $\Theta(\omega)$ (see right panel where two samples are shown, one weakly disordered and one strongly disordered). $\Theta(\omega, T)$ survives just above T_c and vanishes at a temperature T_m^* comparable to the pseudogap T^*. Plotting these data alltogether leads to a phase diagram, clearly demonstrating the influence of the pseudogap on strongly disordered niobium nitride.

[13] This ingenious technique was introduced by [Hebard et al., 1980] to demonstrate the BKT transition in thin aluminum films. The sample is placed in between two coaxial coils, the first of which is fed by a low-frequency ac current ($f \sim 1$ kHz $- 100$ MHz typically), and the second coil measures the induced pick up voltage. The surface currents induced in the superconducting film perturb the mutual signal, and the contribution of the film's kinetic inductance can be extracted. This method is relative by essence (one must remove the background generated by the electromagnetic environment) but later works demonstrated an *absolute* determination of the London penetration length λ with very little uncertainty [Turneaure, Ulm, et al., 1996; Turneaure, Pesetski, et al., 1998]

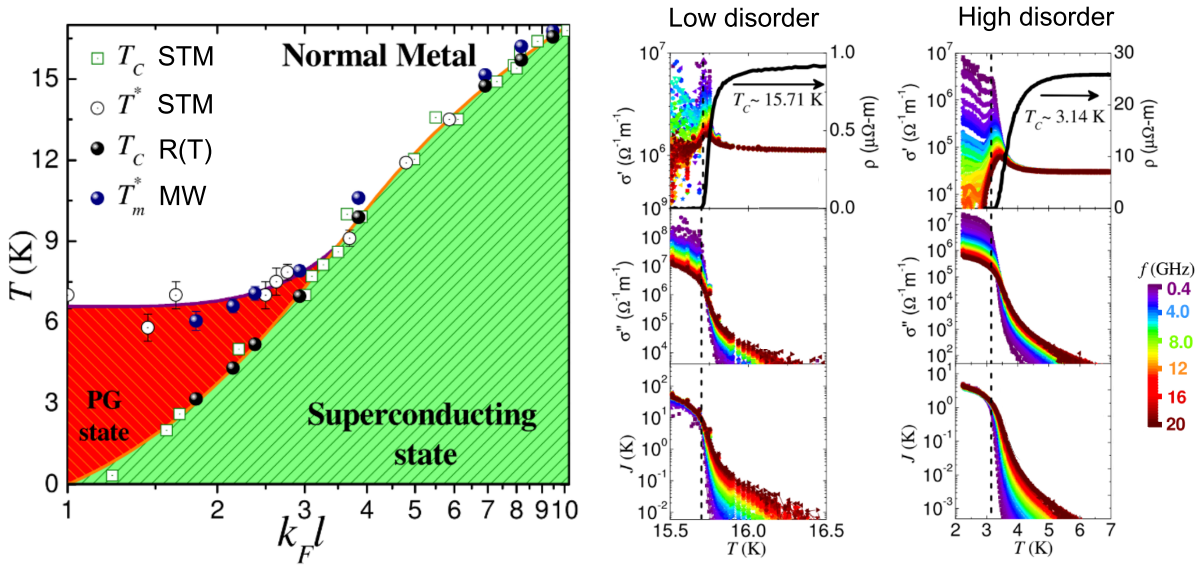

Fig. 2.13. Phase diagram of disordered NbN and complex conductivity. The work of [Mondal, Kamlapure, et al., 2013] combines STM measurements (providing the pseudogap temperature T^* and the critical temperature T_c), resistivity versus temperature and microwave spectroscopy. The latter allows the determination of the complex conductivity $\sigma(\omega) = \sigma'(\omega) + i\sigma''(\omega)$ and the superfluid stiffness Θ, noted J in this work (see right panel). T_m^* is defined as the temperature above which the finite frequency superfluid stiffness $\Theta(f, T)$ drops below the experimental resolution. The critical temperature T_c extracted from $R(T)$ data (dashed vertical line) is in very good agreement with the tunneling measurements, and corresponds to T_m^* for low disorder only. Strongly disordered samples show a clear separation of T_m^*, T^* and T_c in the pseudogap regime. With modifications from [Mondal, Kamlapure, et al., 2013].

Still in the GHz range, [R. Crane et al., 2007; R. W. Crane et al., 2007] used resonant cavities as a probe: by inserting a superconducting sample (amorphous indium oxide here) into a microwave cavity perturbs the TE resonant modes, whose frequency and quality factor vary with the sample's complex impedance.
This approach is powerful and relatively non-intrusive: no direct contact with the sample is needed, and the measurement is indirect (with the cavity mode as an intermediate) therefore leaving the disordered superconductor virtually unaffected by the measurement probe. This scheme is in fact at the basis of the non-demolition readout of superconducting qubits.
With the growing field of circuit quantum electrodynamics (cQED) another technique has emerged. It consists in turning slabs of superconducting material into resonators operating at microwave frequencies, the response of which can be measured using commercially available standard microwave equipment [Camarota et al., 2001; Driessen et al., 2012; N. Maleeva et al., 2018].
This is the method that we propose to exploit to gain new insight on the superfluid properties of indium oxide, and will be detailed in next chapter.[14]

As a final note, microwave spectroscopy of a disordered superconductor should allow to have a better understanding of the relation between collective excitations and dissipation.
It is known that the apparition of a superconducting long-range order is accompanied by the

[14] To our knowledge only two previous works measured microwave resonators fabricated with indium oxide [Astafiev et al., 2012; Dupré et al., 2017].

generation of collective excitations, among which the plasmons which are the subject of this thesis.
In standard BCS superconductors most low energy (long-wavelength) modes do not couple to light and cannot be excited below twice the gap 2Δ, therefore reducing optical absorption and preserving a dissipationless state at microwave frequencies.
In strongly disordered superconductors with locally varying order parameter however, such modes acquire a dipole moment and couple to light. This leads to subgap optical absorption and dissipation [Cea et al., 2014].
In pseudogapped superconductors further study of the Hamiltonian Eq. (2.14) [M. V. Feigel'man and Ioffe, 2018] leads to the observation that above a moderately large disorder short-scale bosonic collective modes should appear underneath the gap Δ.

Conclusion

In this chapter we have summarized some of the main properties of strongly disordered amorphous superconductors, and especially amorphous indium oxide. This material, which is the focus of the present thesis, is a well-known semiconductor displaying signatures of strong localization and an Anderson metal-insulator transition (MIT). Surprisingly enough this material with a tendency towards insulation can turn into a superconductor at lower disorders.

Numerous experimental and theoretical works evidence the non-trivial interplay of localization and superconductivity near criticality, putting forward the idea that electron pairs preform in the non-superconducting state (with a related energy scale called the *pseudogap*), leading to a two-step process for the onset of superconducting correlations: incoherent, localized Cooper pairs form before the apparition of superconducting long-range order.
Recent theories suggest that the origin of this pair preformation could be found in the properties of Anderson insulators near the Metal-Insulator Transition.

The strong spatial fluctuations of the order parameter with disorder are accompanied with an increasingly important role of phase fluctuations, which become the driving mechanism for the breakdown of superconductivity through the suppression of long-range phase coherence.
We have discussed how high-frequency experimental probes were adapted to determine the superfluid response of superconductors, and quantify the role of phase fluctuations via the superfluid stiffness Θ.
In next chapter we introduce a modern and powerful experimental probe operating at GHz frequencies: superconducting microwave resonators. These tools can be used to measure the superfluid response of disordered superconductors, as will be developed in this thesis, and additionally provide a way to benefit from the unusual properties of pseudogapped superconductors in future technological applications.

CHAPTER 3

Superconducting microwave resonators: a superfluid density probe

The purpose of this chapter is to introduce the low-frequency collective excitations of superconductors known as *plasmons* [Mooij and Schön, 1985]. We show an alternative and practically useful description of these modes using standard microwave engineering techniques. As a practical use we demonstrate how microwave resonators can be used to give access to the superfluid properties of disordered superconductors, which will be studied in details in next chapters.

3.1 | Finite-frequency response of a superconductor: Plasma oscillations

We have discussed in section 1.1 the importance of phase fluctuations in thin superconducting films. By relating the energy required to twist the phase of the order parameter to the kinetic energy of the superconducting charge carriers (the Cooper pairs) we have shown that phase fluctuations and motion of Cooper pairs are two faces of the same coin.
Phase gradients lead to non-zero velocity $v_s = \hbar/m^* \nabla\varphi$ of charge carriers. The latter have a mass $m^* = 2m$ and therefore accumulate kinetic energy when put in motion. Such inertia of Cooper pairs is well described by an equivalent inductive energy that represents the energy stored in the superconducting condensate:

$$E = \frac{1}{2} L_K I^2 \tag{3.1}$$

where $I \propto \nabla\varphi$ is the supercurrent, and L_K is called the *kinetic inductance*.[1]
L_K is inversely proportional to the wire cross-section $S = wd$ and to the density of charge carriers n_s, as $L_K = ml/(2n_s e^2 S)$ for a wire of length l. For samples with a narrow cross-section and low enough n_s, the effects of kinetic inductance predominate over the usual geometric inductance.

[1] We have shown in Eq. (1.4) that the energy cost for phase fluctuations was exactly the kinetic energy of Cooper pairs. Writing this kinetic energy, say, for a sample of rectangular cross section $S = wd$ (width w and thickness d) and length l: $E = \frac{1}{2} m^* v_s^2 (n_s S l)$ where v_s is the superflow velocity and n_s is the 3D superfluid density. The current of Cooper pairs in this sample is $I = -e^*(n_s S) v_s$, which allows to rewrite the kinetic energy as an *inductive* energy $E = \frac{1}{2} L_K I^2$ where the effective inductance is given by $L_K = m^* l/((e^*)^2 n_s S)$, where the mass and charge of a Cooper are related to that of single electrons by $m^* = 2m$ and $e^* = 2e$.

Alternatively, one could introduce the kinetic inductance from the imaginary part of the complex Drude conductivity as $L_K = (\sigma_s''(\omega)\omega)^{-1}$, see Appendix E.1.

A straightforward comparison between the expressions for the 2D superfluid stiffness Θ (Eq. 1.2) and the sheet kinetic inductance $L_K^{\square} = m/(2n_s e^2 d)$ shows that these two quantities are proportional[2]:

$$\Theta = \left(\frac{\hbar}{2e}\right)^2 \frac{1}{L_K^{\square}} \tag{3.2}$$

Therefore the resilience of a superconductor against phase fluctuations (quantified by the superfluid stiffness Θ) is suppressed for large kinetic inductances.

Consistently one can link inertia of the superfluid condensate (kinetic inductance L_K) with phase fluctuations of the order parameter (with energy $\sim \Theta \int (\nabla\varphi)^2\, dr$). A small density of superconducting carriers n_s (thus a large L_K) implies strong fluctuations of the superconducting phase (small Θ) that eventually break down the superconducting state (as discussed in section 1.3).
Since we are interested in the properties of superconductors, and more especially in the mechanisms that can lead to its destruction, the experimentally measurable quantity of interest here is the kinetic inductance. To measure it we drive the superconductor into a collective motion and extract L_K as we shall describe soon.

3.1.1 Plasmons

The motion of Cooper pairs is collective: the charge density varies along the wire, leaving uncompensated charges behind. The latter interact at long range via Coulomb interactions to restore a neutral charge distribution. This mechanism is at the origin of charge-density oscillations of the superconductor, known as *plasmons* in analogy with the similar collective excitations that occur at the surface of normal metals.
Plasma modes[3] in superconductors were first discussed theoretically by [Kulik, 1973] and [Mooij and Schön, 1985] and observed experimentally more recently (see for instance [Chin et al., 1992; Camarota et al., 2001]).

In the following sections we detail an equivalent description of the plasmon modes, using only classical electromagnetism provided by Maxwell's equations. Following a commonly used method in the field of superconducting quantum circuits we model the collective excitations as propagating waves in a transmission line operating at microwave frequencies. This picture allows for a simple integration of superconducting resonators into more complex schemes, such as coupling to an external environment and measurement apparatus.

3.2 | The microstrip transmission line

First developped in the 1850s following the recent formulation of Maxwell's equations, transmission lines allowed for the controlled propagation of electromagnetic waves over arbitrarily large distances. One famous and historically important use of such developments was the conception of the telegraphic transatlantic line, connecting for the first time in history two places separated by 2 500 nautical miles.
More recently the development of integrated electronics required the use of a different kind of transmission line operating over much shorter lengths (a few millimeters) that would allow the fabrication of complex printed electronic circuits. One of the most popular options for such

[2] Keeping in mind that 2D and 3D superfluid densities are related by $n_{s,2D} = d\, n_{s,3D}$.
[3] The terms of plasmons, plasma modes and collective excitations will be used indifferently in this thesis.

planar transmission lines is the *microstrip*, first described in [Grieg et al., 1952].

We give a brief description of a microstrip line and of the basic equations that describe it, quoting abundantly the microwave engineering book by David Pozar [Pozar, 2011]. The effects of dissipation and distortion are discussed, before demonstrating that an open-ended portion of a microstrip line acts as a resonator in the microwave regime.

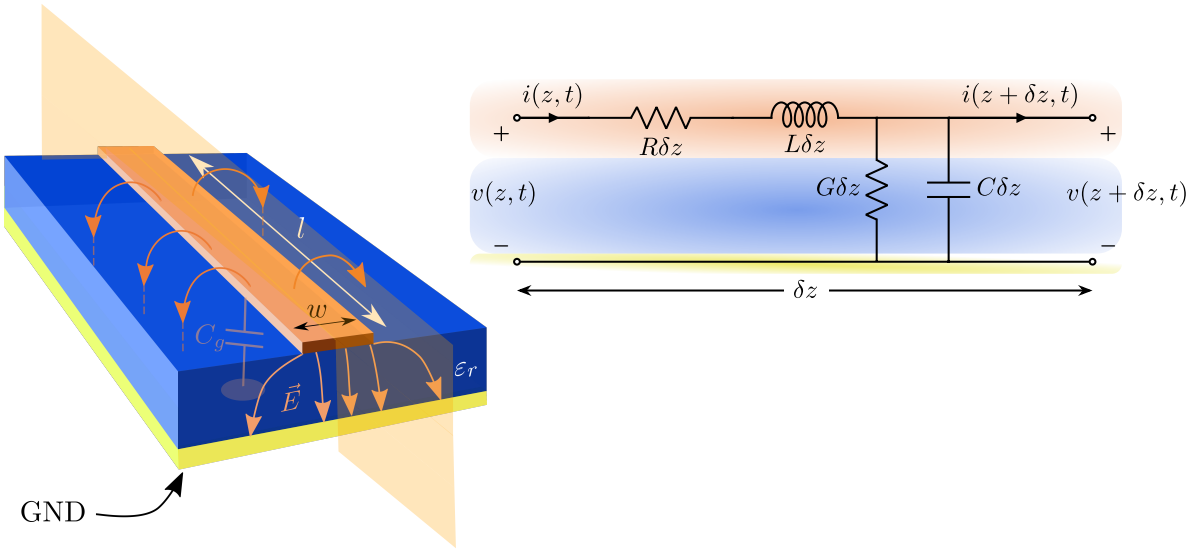

Fig. 3.1. Microstrip transmission line a) Schematic representation of a microstrip, consisting of two conductors (yellow and orange layers) separated by a dielectric (permittivity ε_r). The upper conductor is an infinitely long ($l \gg w, d$) and narrow (width w) strip surrounded by air ($\varepsilon = 1$) and the dielectric substrate. The electric field lines represented by orange arrows originate from the voltage drop introduced by the presence of the dielectric, giving rise to an effective capacitance to ground C_g. **b)** Equivalent electric circuit corresponding to a cut of the schematic in **a)** along its length, for a portion of infinitesimal length $\delta z \ll l$.

3.2.1 Telegrapher's equations

Fig. 3.1 shows a scheme of a microstrip line, composed of two conductors (orange and yellow) separated by a thick dielectric layer. The line is infinitely long ($l \gg w, d$) and narrow with width w. Realistic microstrips have a finite thickness d which will be considered small compared to the other lengths $d \ll l, w$.

Due to the presence of the dielectric layer charges accumulate in both conducting layers, giving rise to an electric field $\vec{E}$. The field is partly located in the dielectric substrate and partly in the air above the device (see figure).

The equivalent circuit of Fig. 3.1**b** can be seen as a line cut along the length of the microstrip of infinitesimal length δz but is actually very general and describes any transmission line. The total transmission line is then the cascade of such quadripoles. Each circuit portion of size δz is characterized by the dipoles:

- $L =$ series inductance per unit length for both conductors

- $C =$ capacitance to ground per unit length between the conductors
- $R =$ series resistance per unit length for both conductors of finite conductivity
- $G =$ conductance per unit length in the dielectric

Since each portion of transmission line has small size $\delta z \ll l$ one can safely consider that the quantities R, L, C, G do not vary over it, allowing to model the continuous transmission line by a series of lumped circuit elements.

Using Kirchoff's laws and assuming a sinusoidal time dependence with angular frequency ω as $v(z,t) = V(z)e^{j\omega t}$ one can write the *telegrapher's equations*:

$$\frac{d^2V(z)}{d^2z} - \gamma^2 V(z) = 0 \tag{3.3}$$

$$\frac{d^2I(z)}{d^2z} - \gamma^2 I(z) = 0 \tag{3.4}$$

that model the evolution of voltage and current along the wire with z.
We have introduced the propagation constant γ:

$$\gamma = \alpha + j\beta = \sqrt{(R + j\omega L)(G + j\omega C)} \tag{3.5}$$

The solutions for voltage and current can be written

$$V(z) = V_0^+ e^{-\gamma z} + V_0^- e^{\gamma z} \tag{3.6}$$

$$I(z) = I_0^+ e^{-\gamma z} + I_0^- e^{\gamma z} \tag{3.7}$$

corresponding to superposition of waves traveling towards positive and negative z.
One can now define a characteristic impedance Z_0 as

$$Z_0 = \frac{V_0^+}{I_0^+} = \sqrt{\frac{R + j\omega L}{G + j\omega C}} \tag{3.8}$$

The waves have velocity v and wavelength λ given by

$$\lambda = \frac{2\pi}{\beta} \tag{3.9}$$

$$v = \frac{\omega}{\beta} = \lambda f \tag{3.10}$$

Therefore the propagation of electromagnetic waves along a transmission line can be modelled in a quite general and simple way, and only require knowledge of a few per-unit-length quantities $L,\ C,\ R,\ G$. The difficulty resides in the precise determination of these quantities according to the chosen transmission line geometry.

Next we discuss the models used to estimate these parameters in the microstrip geometry.

3.2.2 Capacitance to ground

The first problem one has to solve is the exact charge distribution along the wire in order to obtain the capacitance to ground C of the microstrip. While the microstrip geometry is one of the most used transmission lines for micro-electronics, an exact model for the capacitance in

the slightly unusual case of a remote ground plane is still lacking. In the following we describe a method to account for the distributed capacitance of a long and thin strip far from its ground plane.

In the case of a thin dielectric layer (thickness $h \leq w, d$) one can see the problem locally as a parallel plates capacitance where charges accumulate in the top conductor and the bottom ground, generating an electric field mostly perpendicular to the plates. The effective capacitance to ground $C \approx \varepsilon\varepsilon_0 w/h$ is related locally to the charges and the electrostatic potential by $Q = CV$, and is uniformly distributed along the wire. Therefore for a ground plane in the close vicinity of the top conductor long-range interaction between charges can be safely neglected. A consequence is that the resulting capacitance is independent of frequency.

For a thicker dielectric however, the long-range Coulomb interactions between distant charges come into play, modifying the distribution of charges and the effective capacitance. Here we follow the method described in [Krupko et al., 2018] and calculations for the microstrip geometry [Denis Basko, Private communications].
We assume point-like charges $Q(\mathbf{r})$ and consider the long-range interactions between them using the method of image charges. The system possesses two boundary conditions for the electric field, given by the ground plane with zero potential $V = 0$ and the interface between top conductor and air ($\varepsilon = 1$). Therefore the potential must be defined in two regions, first in the dielectric of dielectric constant ε ($-h < z < 0$) where h is the dielectric thickness, and in the air above the substrate ($z > 0$). Fig. 3.2 shows a schematic view of the system.

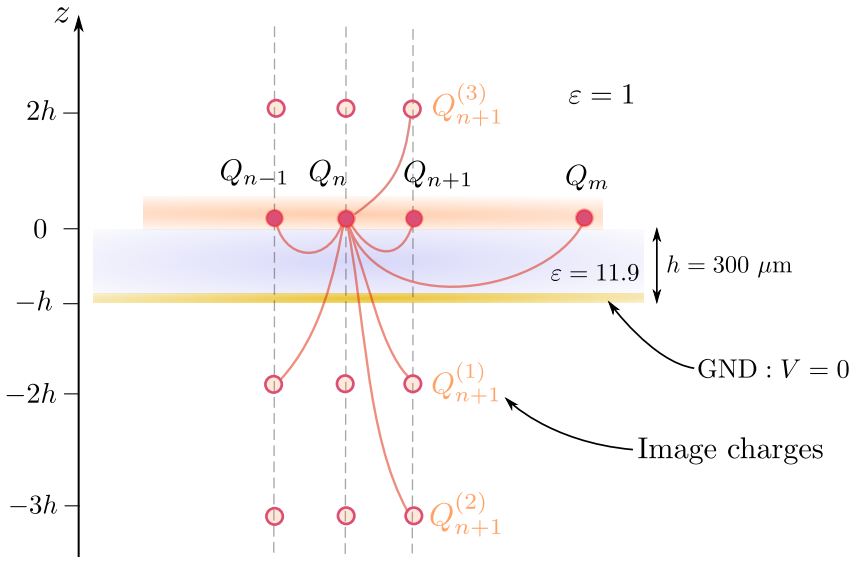

Fig. 3.2. Screening of a point-like charge Q_n by long-range Coulomb interactions. The electrostatic potential $V(\mathbf{r})$ produced by a point-like charge Q_n on top of the substrate can be calculated by introducing image charges, allowing to take into account long-range Coulomb potentials between distant charges Q_m distributed in the conductor. Image inspired from [Krupko et al., 2018].

The electrostatic potential $V(\mathbf{r})$ produced by a point charge Q_n located on top of the substrate in $(0,0,0)$ is

$$V(x,y,z>0) = \sum_{j=0}^{\infty} \frac{\zeta_j Q_n}{4\pi\varepsilon_0\sqrt{x^2+y^2+(z+2jh)^2}} \tag{3.11}$$

$$V(x,y,-h<z<0) = \sum_{j=-\infty}^{\infty} \frac{\zeta_j' Q_n}{4\pi\varepsilon_0\sqrt{x^2+y^2+(z+2jh)^2}} \tag{3.12}$$

where ζ_j' and ζ_j are coefficients that can be determined by writing the boundary condition equations for V at the system boundaries ($V=0$ at the ground plane $z=-h$ and electric field continuity at $z=0$). The infinite summation accounts for the contribution of all image charges to the total potential.
Summing over all the point like charges and taking the Fourier transform (with wave vector k along the x direction), the capacitance C_k can be obtained from

$$\frac{1}{C_k} = \frac{1}{\pi\varepsilon_0(1+\varepsilon)}\left[\mathcal{K} - \sum_{j=1}^{\infty}\zeta_j K_0(2jhk)\right] \tag{3.13}$$

where $K_0(x)$ is the modified Bessel function of the second kind, $\zeta_j = 2\varepsilon\,(1-\varepsilon)^{j-1}/\,(1+\varepsilon)^j$ and $\mathcal{K}$ accounts for charge distribution accross the strip width. The two terms under bracket separate short-range and long-range contributions of the Coulomb potential.

$\mathcal{K}$ can be evaluated as $\mathcal{K} \approx -\ln(kw) + 1.5 + 0.1(kw)^2$ but can also be estimated numerically with good precision using a Python code available in Appendix (see Fig. 3.3 for a numerical result).

Eq. (3.13) provides the result that, when long-range Coulomb interactions are taken into account the capacitance to ground acquires a frequency dependence. Here $k = \mathrm{Im}(\gamma)$ is the imaginary part of the propagation constant in the transmission line and therefore is related to frequency by $\omega = vk$, as discussed in previous section.

Fig. 3.3 displays capacitances C_k obtained from Eq. (3.13) for three different microstrip widths w on a $300\ \mu$m-thick dielectric of permittivity $\varepsilon = 11.9$. Clearly the dispersion is non-linear, demonstrating the importance of long-range Coulomb interaction for an accurate evaluation of the capacitance to ground.

The method developed by D. Basko can be seen as an amelioration of the results obtained in [Mooij and Schön, 1985]. Indeed they derived an inverse capacitance per unit length $C_k^{-1} = 2\ln\big(1/kr_0\big)/(1+\varepsilon)\varepsilon_0$, which is nothing more than the first term under bracket of Eq. (3.13). The summation over image charges provides better accuracy on the evaluation of C_k, especially at low k where the Bessel functions have their largest values.

This result is of great use for the accurate description of plasma waves described in next sections.

3.2.3 Geometric and kinetic inductances

The wire inductance L has two main contributions: the geometric inductance L_g, fixed by the strip geometry, and the kinetic inductance L_K that quantifies the motion of charge carriers in

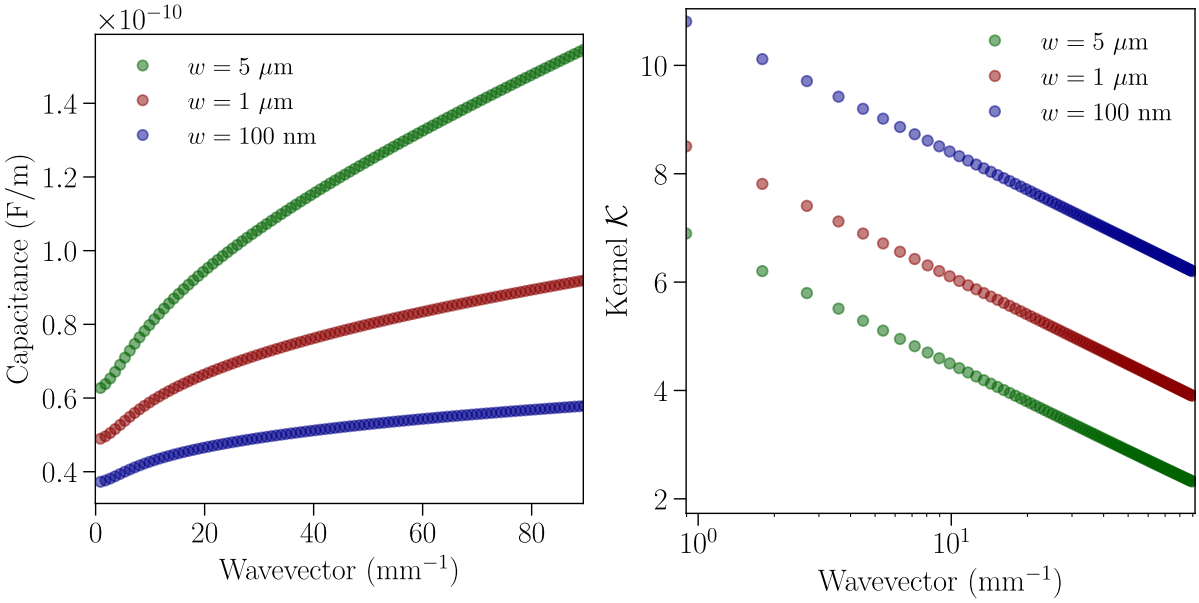

Fig. 3.3. Evolution of capacitance with frequency. Left: Capacitance to ground per unit length of an infinite microstrip line of three different widths w using Eq. (3.13). The logarithmic increase of C_k with frequency originates from the long-range Coulomb interactions due to the large distance $h = 300\ \mu\text{m}$ to ground plane. As expected an increase of strip width implies a slight enhancement of capacitance to ground. **Right:** Evaluation of the kernel $\mathcal{K}$ for three strip widths. As can be seen $\mathcal{K}$ is mostly logarithmic with k.

the film.

Geometric inductance can be calculated from approximate formulae for the impedance Z_0 (see for example [Wheeler, 1965]) and the capacitance of last section (since $L \approx CZ_0^2$). For a $1\ \mu$m-wide wire on a $300\ \mu$m-thick dielectric of permittivity $\varepsilon_r = 11.9$ this leads $L_g = 0.0018\ \text{nH}/\square$.
For the disordered superconductors considered in this thesis we show that kinetic inductance is of the order of $1\ \text{nH}/\square$ or above, much larger than geometric inductance.
Thus

$$L = L_g + L_K \approx L_K \tag{3.14}$$

3.2.4 Low loss and distortionless lines

In the practical situation of low-loss and high frequencies which is the subject of this work [4], one can safely simplify Eq. (3.5)-(3.8) by setting $R \ll \omega L$, $G \ll \omega C$ and Taylor expanding to

[4] In the case of larger loss the phase velocity v acquires a frequency dependence (see Eq. 3.10 and Eq. 3.5) which can induce signal distortion: different frequency components of the signal are transmitted with different velocities, leading to mixing of the information over long wire lengths. This was the cause of the poor performances of the first transatlantic telegraph line of 1858. The solution provided by Heaviside consists in the right choice of parameters $\frac{G}{C} = \frac{R}{L}$ which garantees a distortionless line. To match this condition the transatlantic line was loaded by a high magnetic permeability metal used to increase L and fulfill the Heaviside criterion.

obtain the real and imaginary parts of the complex propagation constant $\gamma = \alpha + j\beta$:

$$\alpha \approx \frac{1}{2}\left(\frac{R}{Z_0} + GZ_0\right) \tag{3.15}$$

$$\beta \approx \omega\sqrt{LC} \tag{3.16}$$

where $Z_0 = \sqrt{L/C}$ is the characteristic impedance.

This leads to the result that the wave phase velocity v can be expressed simply by

$$v = \frac{\omega}{\beta} = \frac{1}{\sqrt{LC}} \tag{3.17}$$

Eq. (3.17) shows that the wave velocity can be pushed down to lower values by increasing the inductance $L \approx L_K$. This observation is central in next sections as it links plasmon frequency to kinetic inductance in a simple manner.

Concerning the losses in the line (expressed by $e^{-\alpha}$ in Eq. (3.6)) it must be noted that most of discussions to come concerns superconductors well below T_c, where the top conductor loss is negligible. The bottom conducting ground plane however can be made of regular metals (and indeed it will be the case in next chapter) therefore providing a (very low) but non-zero resistance R.

In the same line of thought the dielectric substrate is chosen so that it becomes insulating at milli-Kelvin temperatures, but is not *per se* a perfect insulator, and therefore still has a finite G *i.e* a non-negligible loss tangent δ.

Analysis of Eq. (3.15) shows that for large wave impedances $Z_0 \gg R$ (*i.e* large L) the effect of residual resistance from conduction in the real part α of the propagation constant cancels out. On the contrary, large Z_0 enhances the dielectric losses GZ_0 through the substrate.

3.3 | Open-ended transmission line resonators

Let us now "cut" our transmission line into a section of length l, with open ends at each extremities as shown in Fig. 3.4. Doing so the current at each end of the wire vanishes by construction, and $I(-l) = I(0) = 0$.

Using the general expression for the current in a transmission line with propagation constant $\gamma = \alpha + j\beta$ of Eq. (3.7) and assuming a lossless line ($\alpha l \ll 1$) for simplicity one gets the condition for the propagation constant and the wire length

$$\sin(\beta l) = 0 \Rightarrow \beta l = n\pi \text{ for } n \in \mathbb{N} \tag{3.18}$$

Since the wavelength is given by $\lambda = 2\pi/\beta$ this relation leads to

$$l = n\frac{\lambda}{2} \tag{3.19}$$

Due to reflections on the open-ends of the truncated transmission line, a superposition of left and right-moving propagating waves form standing waves with the wire length being exactly an integer multiple of the half-wavelength. **The open-ended transmission line becomes**

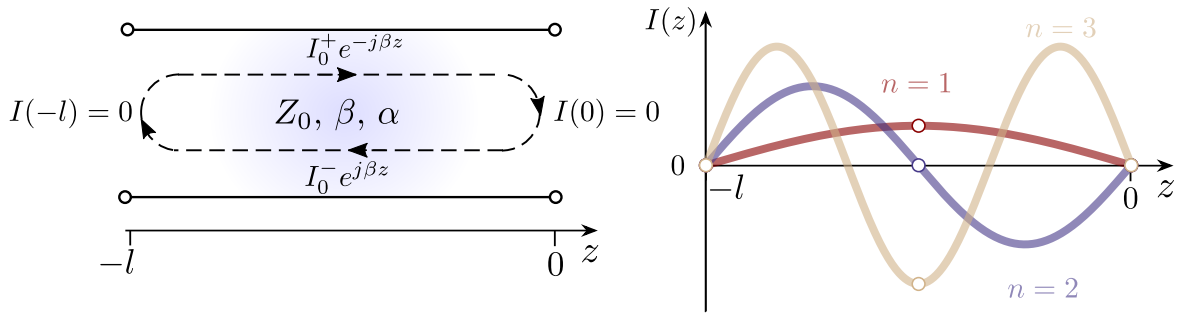

Fig. 3.4. Open-ended transmission line. By cutting a low-loss line with characteristic quantities Z_0, α, β to a finite length l, propagating waves are reflected on the boundaries and are superposed, creating standing waves. The resulting current oscillations are 0 at the extremities and are either 0 or reach their maximum value in the center of the line depending on the mode number n parity.

a microwave resonator, called a half-wavelength line.

Eq. (3.18) also gives the result that angular frequency ω (or the frequency f) are related to the wire length as

$$\omega(\beta) = v\beta = \frac{n\pi}{l}v = \frac{n\pi}{l\sqrt{LC}} \tag{3.20}$$

Therefore the 1D collective excitation spectrum in the open-ended transmission line is quantized, leading to a discrete dispersion relation $\omega_n = \beta_n v$.

From Eq. (3.20) it follows that the frequency spacing between two consecutive modes n and $n+1$ is given by

$$\omega_{n+1} - \omega_n = \frac{\pi v}{l} = \omega_1 \tag{3.21}$$

if one assumes a frequency independent phase velocity v. We have already seen that this is not the case since the capacitance C_β increases slightly with frequency, but this approximation is useful for qualitative discussion.

It becomes clear that the spacing between modes is nearly constant, and is determined by the wire length l: for instance a large l implies a small resonance frequency spacing, leading to densely packed modes. This observation will be put to good use in the experimental realization of such resonators.

Using the accurate model for the capacitance C_k given in section 3.2.2 and Eq. (3.20) one can finally obtain a precise description of the plasmon mode dispersion as

$$\boxed{\omega(k_n) = \frac{k_n}{\sqrt{LC_k}}} \tag{3.22}$$

where $k_n = n\pi/l$ is the wavenumber, L is the inductance of the line per unit length and C_k is the k-dependent capacitance per unit length given by Eq. (3.13).

Equivalent RLC circuit The open-ended transmission line with characteristic impedance Z_0 and propagation constant $\alpha + j\beta$ can be mapped to a resonant parallel RLC circuit for

frequencies close to a resonance ω_0 with equivalent parameters $\tilde{R}$, $\tilde{L}$, $\tilde{C}$ and quality factor Q_i given by [Pozar, 2011]:

$$\tilde{R} = \frac{Z_0}{\alpha l} \tag{3.23}$$

$$\tilde{C} = \frac{\pi}{2\omega_0 Z_0} \tag{3.24}$$

$$\tilde{L} = \frac{1}{\omega_0^2 \tilde{C}} \tag{3.25}$$

$$Q_i = \omega_0 \tilde{R} \tilde{C} = \frac{\beta}{2\alpha} \tag{3.26}$$

where the *unloaded* (or *internal*) quality factor Q_i is defined as the ratio of energy stored by power loss in the resonator:

$$Q_i = \omega \times \frac{\text{Energy stored}}{\text{Power loss}} \tag{3.27}$$

The quality factor measures the energy loss experienced by electromagnetic standing waves due to intrinsic dissipation in the wire, as represented by the equivalent resistance $\tilde{R}$. In the ideal case of lossless transmission line ($\alpha = 0$) one has $\tilde{R} \to \infty$, meaning that the equivalent circuit becomes a parallel LC resonator which oscillations are not damped with time. The quality factor diverges to infinity in an ideal scenario.

3.3.1 Coupling the resonator to the environment

In a realistic system however, internal losses in the resonator cannot be neglected (even though they might be small) leading to a finite value of internal quality factor Q_i. The numerous origins of such dissipation are discussed in a later chapter of the thesis. We will now introduce another contribution to the quality factor induced by the necessary coupling of the resonator to the external environment.

Any experimentally measurable system requires some coupling to the measurement apparatus, *i.e.* one must be able to excite the resonator at will and measure its response to the excitation. One common option, which will be used in most of this work, is to couple the resonator to an external feedline.

A scheme depicting the coupled system is displayed in Fig. 3.5. It consists in a long $50\ \Omega$ transmission line (called a *feedline*) matched to the standard commercial microwave equipment used for measurement, and a $\lambda/2$ transmission line resonator in its vicinity. The feedline is connected on both ends to the measurement electronics, feeding an input voltage V_{in} at one extremity and collecting the outcoming voltage V_{out} on the other end.

In this particular coupling geometry and out of resonance, most of the input signal is collected at the output, leading to a transmission close to unity. To quantify the transmission we introduce the scattering element S_{21}, as is commonly done in microwave engineering:

$$S_{21} = \frac{V_{\text{out}}}{V_{\text{in}}} \tag{3.28}$$

For a lossless feedline not coupled to an external lossy environment S_{21} is exactly 1 ($= 0$ dB) since all the microwave power is transmitted.

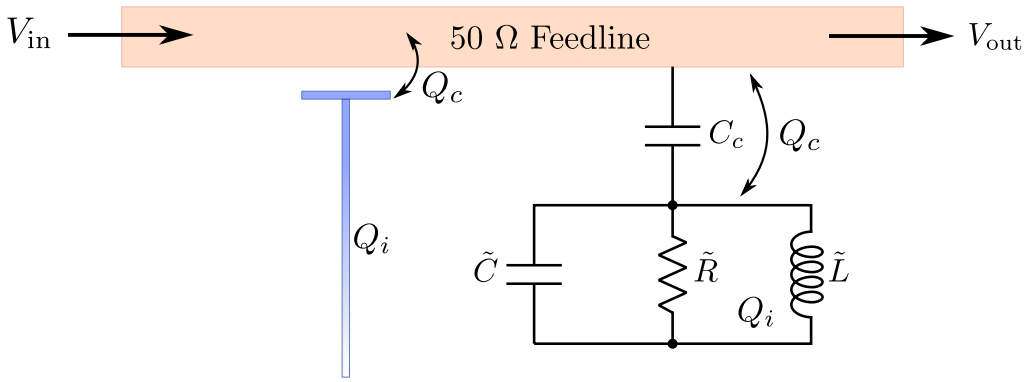

Fig. 3.5. Coupling of a resonator to the environment. A feedline made from a transmission line with characteristic impedance $50\ \Omega$ is connected at both ends to the microwave measurement setup and coupled to a resonator with coupling quality factor Q_c. **Left:** schematic representation of a $\lambda/2$ transmission line resonator. **Right:** Equivalent RLC circuit coupled to feedline via the capacitance C_c. This equivalent circuit analogy is valid close to resonance, for angular frequencies $\omega = \omega_0 + \delta\omega$ where ω_0 is a resonant mode and $\delta\omega \ll \omega_0$. The internal quality factor Q_i describes the intrinsic loss of the resonator, while Q_c is related to coupling to the environment.

Coupling capacitance To estimate the equivalent coupling capacitance C_c between the feedline and resonator one has to account for fringing fields in the air above the substrate, and in the dielectric below with permittivity ε_r (see Fig. 3.6). Since the conductors are ultra thin one neglects in first approximation the parallel plate capacitance formed by the lateral sides of the microstrips. One also neglects the capacitance to ground and the long-range Coulomb potential in this very crude estimate. Doing so the capacitance is approximately given by (see e.g [Garg, 1979]) :

$$C_c \sim l\varepsilon_0 \left(1 + \varepsilon_r\right) \frac{K(a')}{K(a)} \tag{3.29}$$

where $a = \dfrac{s}{s + 2w}$, $a' = \sqrt{1 - a^2}$ and K is a complete elliptic integral of the first kind.

Here w is the microstrip width, s is the spacing between the two lines and l is the coupling length.

Fig. 3.6 shows the evolution of C_c with spacing s for a realistic set of parameters. While this model is very crude and quite inaccurate it provides an estimation of the geometry required to achieve a given coupling capacitance: decreasing s and increasing l enhance the coupling, as intuition suggests. In practice coupling is fine tuned using electromagnetic simulations for accuracy.

Coupling quality factor The coupling quality factor Q_c is defined as the ratio of energy stored in the resonator to the power dissipated in the external environment. In a first approximation the largest dissipation comes from the $50\ \Omega$ transmission line, and therefore a strongly coupled resonator should have a smaller Q_c, since a larger amount of energy has been lost in

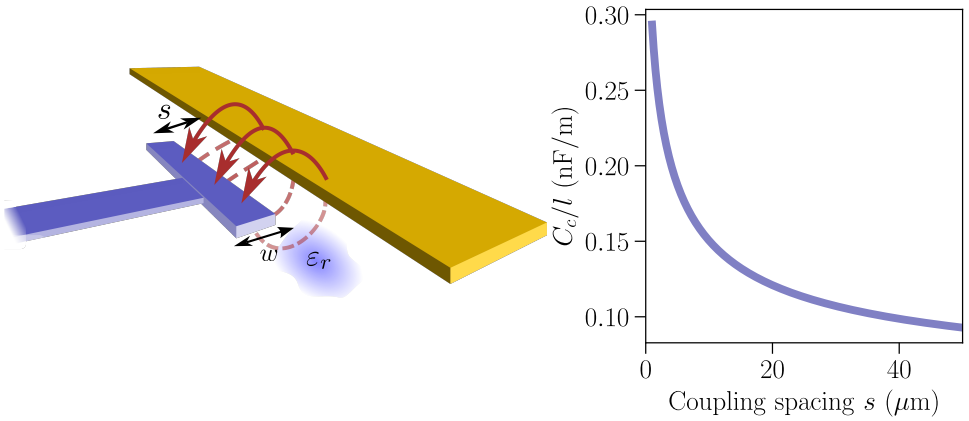

Fig. 3.6. Coupling capacitance. Schematic of the coupling between two microstrips. The fringing field is mainly situated in the air above the circuit and in the dielectric below it. The strength of the coupling mainly depends on the distance s between the two conductors and on the length l of the coupling part. **Right:** Calculated coupling per unit length versus spacing s using Eq. (3.29) for a wire of width $w = 5\ \mu\text{m}$ on a $300\ \mu\text{m}$-thick substrate.

the feedline.

Following [Pozar, 2011] and [Etienne Dumur, 2015] one can derive a relation between coupling capacitance and external quality factor Q_c:

$$Q_c \approx \frac{\pi}{2\omega_0^2 C_c^2 Z_r Z_0} = \frac{\pi}{2}\frac{C}{C_c^2 \omega_0 Z_0} \tag{3.30}$$

where $Z_0 = 50\ \Omega$ is the impedance of the feedline seen as a *load* and $Z_r = \sqrt{L/C}$ is the resonator impedance. As expected, the higher the coupling capacitance C_c the lower the Q_c.

For a typical experimental setting, $\omega_0 \sim 2\pi \times 3$ GHz, $C_c \sim 1$ fF, $Z_r \sim 1\ \text{k}\Omega$ and $Z_0 = 50\ \Omega$, leading to $Q_c \sim 10^5$.

In pratice, for design purposes one uses more generally electromagnetic simulation of a resonator in a given geometry and extract directly Q_c by fitting the transmission response, as will be detailed in the next sections.

Loaded quality factor The quality factor of the total system, called *loaded* quality factor Q_l accounts for the sum of dissipation in the resonator and in the environment:

$$\frac{1}{Q_l} = \frac{1}{Q_i} + \text{Re}\left(\frac{1}{Q_c}\right) \tag{3.31}$$

where the real part of Q_c is taken since this quantity can be complex, in the form $Q_c = |Q_c|\exp(-j\phi)$ where ϕ accounts for impedance mismatch along the line [S. Probst et al., 2015].

One sees that depending on the geometry (*i.e* the value of the coupling capacitance C_c), external loss can either lower significantly the quality factor Q_l, or not at all.

For large couplings and small internal loss for instance ($C_c^2 \gg 1/\left(\omega_0^2 Z_r\right)$), $Q_l \sim Q_c$ and the system loss is dominated by the coupling to the environment (we say that the resonator is

overcoupled).

In the other limit ($C_c^2 \ll 1/\left(\omega_0^2 Z_r\right)$), $Q_l \sim Q_i$ and the overall loss is dominated by the internal losses in the resonator (the resonator is *undercoupled*).

The intermediate case for which $Q_i \sim Q_c$ describes a *critically coupled* resonator.

Transmission measurement in the hanging geometry In the system shown in Fig. 3.5 electromagnetic field in the feedline excites plasmons in the resonator that reflect on the open ends, leading to standing waves. Interferences between waves entering the resonator and waves leaving it after being reflected at the boundaries (while acquiring a π phase shift) are destructive at resonance, resulting in an overall decrease of output microwave power for frequencies close to f_r. Therefore when monitoring the transmission S_{21} by sweeping frequencies one observes a dip in transmission amplitude around f_r (see Fig. 3.7).

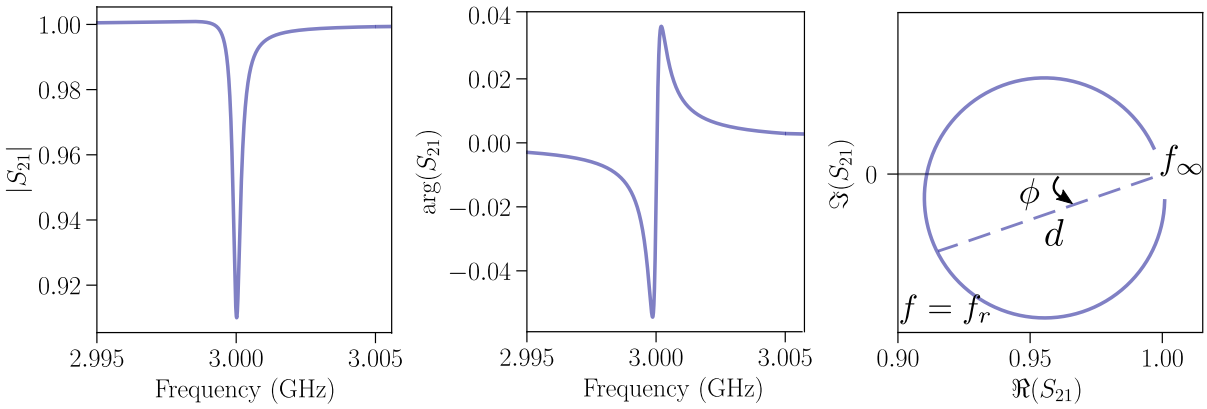

Fig. 3.7. Transmission near a resonance. Amplitude (**Left**) and phase (**Center**) of the complex transmission of Eq. (3.32) is shown for frequencies close to the resonance $f_r = 3$ GHz, with $Q_i = 10^4$ and $Q_c = 10^5$. The minimum of transmission amplitude is $\approx 1/\left(1 + Q_i/Q_c\right) \approx 0.9$ and the amplitude bandwidth at -3 dB is $\Delta f_{3\mathrm{dB}} \approx f_r/Q_i = 300$ kHz. A dephasing $\phi = 0.2$ modifies slightly the amplitude shape. **Right:** Imaginary versus real part of S_{21}, showing a circle open for frequencies far from resonance ($f = f_\infty$) at the opposite side of f_r. The circle diameter is given by $d = Q_l/|Q_c|$, and is tilted by the angle ϕ.

A general formula for the scattering coefficient $S_{21}(f)$ at frequency f close to a resonance f_r can be found in [S. Probst et al., 2015]:

$$S_{21}(f) = \underbrace{a e^{j\eta} e^{-2\pi j f \tau}}_{\text{environment}} \underbrace{\left[1 - \frac{(Q_l/|Q_c|)e^{j\phi}}{1 + 2jQ_l(f/f_r - 1)}\right]}_{\text{ideal resonator}} \tag{3.32}$$

where Q_l is the loaded quality factor, $|Q_c|$ is the absolute value of the (complex) coupling quality factor and ϕ quantifies the impedance mismatch. In addition to these parameters describing the *ideal* coupled and lossy resonator, one accounts for other losses due to the

environment by defining an amplitude a, phase shift η and electric delay τ that accounts for the finite wave velocity in a cable of finite length.

Eq. (3.32) states that for frequencies far from the resonance f_r the transmission spectrum is flat: $S_{21} = 1 = 0$ dB. At resonance $f \approx f_r$ however one has (for the ideal case with $\phi = 0$) $|S_{21}| \approx 1 - Q_l/Q_c = 1/\left(1 + Q_i/Q_c\right)$. Therefore the transmitted signal presents a dip at f_r whose shape qualitatively changes with the ratio of internal and external quality factors. For instance, for low loss resonators $Q_i \gg Q_c$ and the amplitude dip depth is $\sim Q_c/Q_i \to 0 = -\infty$ dB. In addition the dip width at 3 dB can be estimated as

$$\Delta f_{3\mathrm{dB}} = \frac{f_r}{Q_l} \tag{3.33}$$

Therefore depending on the respective values of Q_i and Q_c the resonance visibility will be modified, which suggests that some optimal parameters must be found for experimental realizations.

If one wants to accurately extract the internal quality factor Q_i from experimental data, the coupling scheme shown in Fig. 3.5 (sometimes called a *hanging resonator*) is particularly adapted. Indeed the transmission baseline far from resonance ($S_{21} = 0$ dB) acts as a reference for the amplitude dip at resonance. This geometry allows for a more accurate determination of Q_i than for other schemes for which the transmission baseline is unknown (e.g for a reflection measurement).

Real experimental data often drift from the ideal case. The amplitude and phase of the complex S_{21} can become asymmetric, resulting from impedance mismatch along the line, or from unwanted reflections between input and output. Lossy coaxial lines in the measurement setup induce some attenuation while the length of these cables introduces dephasing. As a result the transmitted signal can be strongly modified and the fitting procedure is flawed. A robust algorithmic method allowing to filter these various unwanted effects is described in [S. Probst et al., 2015] and readily usable open-source Python codes can be found in [Sebastian Probst, 2015]. Using this fitting procedure one can extract accurately Q_i, Q_c and f_r from noisy experimental data.

3.4 | Plasma modes as a pathway to superfluid density

Collective bosonic excitations of a superconductor can be used to obtain a crucial information on the superconducting state, the *superfluid stiffness* Θ which has dimension of energy and describes the resilence of the superfluid to phase fluctuations.

Using the microstrip open-ended transmission line geometry detailed previously we propose to measure the superfluid stiffness of disordered indium oxide thin films through the study of one-dimensional plasmons. We will show how Θ can be extracted from the dispersion relation of these modes, and in due course how the introduction of an external parameter such as temperature of magnetic field is expected to modify the superfluid response.

Simulations and sample designs of microstrip indium oxide resonators will be presented, in order to prepare for the thorough experimental study which is the topic of next chapter.

3.4.1 Determination of superfluid density via plasmon dispersion relation

Our method for measuring accurately the superfluid stiffness of indium oxide films follows the steps described below:

- Design of a long indium oxide wire withstanding many plasmon modes
- Measure the frequency of as many resonance modes as possible, in order to obtain the dispersion relation $\omega(k)$
- Fit the dispersion relation $\omega(k)$ with the dispersion model Eq. (3.22), by adjusting the value of kinetic inductance L_K only
- Compute the superfluid stiffness from L_K following $\Theta = \left(\frac{\hbar}{2e}\right)^2 \frac{1}{L_K}$

Electromagnetic simulation In order to assess the validity of the procedure described above we first compare to commercial electromagnetic simulation softwares. A simple design similar to Fig. 3.5 is implemented in Sonnet Software [Sonnet Software, Inc, n.d.], with a lossless $50\ \Omega$ transmission line connected to ports of the EM solver. In close vicinity is placed a long ($l = 3505\ \mu\mathrm{m}$) and narrow ($w = 1\ \mu\mathrm{m}$) wire with a kinetic inductance per square L_K, deposited on a dielectric substrate (thickness $h = 300\ \mu\mathrm{m}$, $\varepsilon = 11.9$) the bottom side of which is connected to ground. The situation is identical to the problem of capacitance to ground discussed previously (see Fig. 3.2 and related comments).

It was already mentioned that, by choosing a large wire length l, the resonance spectrum should be densely packed with a small frequency spacing. To further enhance this effect one can set a large value of kinetic inductance, therefore pushing down the first resonant mode to low frequency and reduce the spacing between modes $\Delta f \propto 1/(l\sqrt{L_K})$.

We perform two simulation runs with the exact same geometry but two distinct kinetic inductances, with $L_{K,\mathrm{sim}} = 1.35\ \mathrm{nH}/\square$ and $L_{K,\mathrm{sim}} = 0.6\ \mathrm{nH}/\square$. These values are set into the software, providing a surface impedance.

Fig. 3.8 displays the simulation results. On the left a typical transmission trace is shown for frequencies ranging from 0 to $15\ \mathrm{GHz}$. Each dip corresponds to a resonant mode f_n. The right plot shows the extracted evolution of resonance frequency with wavenumber $k_n = n\pi/l$.

It can be observed that this dispersion relation is nearly linear at high frequencies ($\omega_n \approx v k_n$) but departs slightly from this linear behavior at lower k_n. This effect originates from the frequency dependence acquired by the capacitance to ground C_k due to long-range Coulomb interaction, as discussed in Section 3.2.2.

We now use our model for the dispersion relation to fit the simulated data using Eq. (3.22). The only fitting parameter is the kinetic inductance L_K, since all other parameters are chosen by design. The resulting inductances are very close the input ones: $L_{K,\mathrm{fit}} = 1.37\ \mathrm{nH}/\square$ and $L_{K,\mathrm{fit}} = 0.62\ \mathrm{nH}/\square$, suggesting a systematic error of $\Delta L_K = 0.02\ \mathrm{nH}/\square$ which might originate from the coarse settings used to decrease the simulation time. Note that we have not substracted the contribution of geometric inductance here, leading to a slight overestimation of L_K.

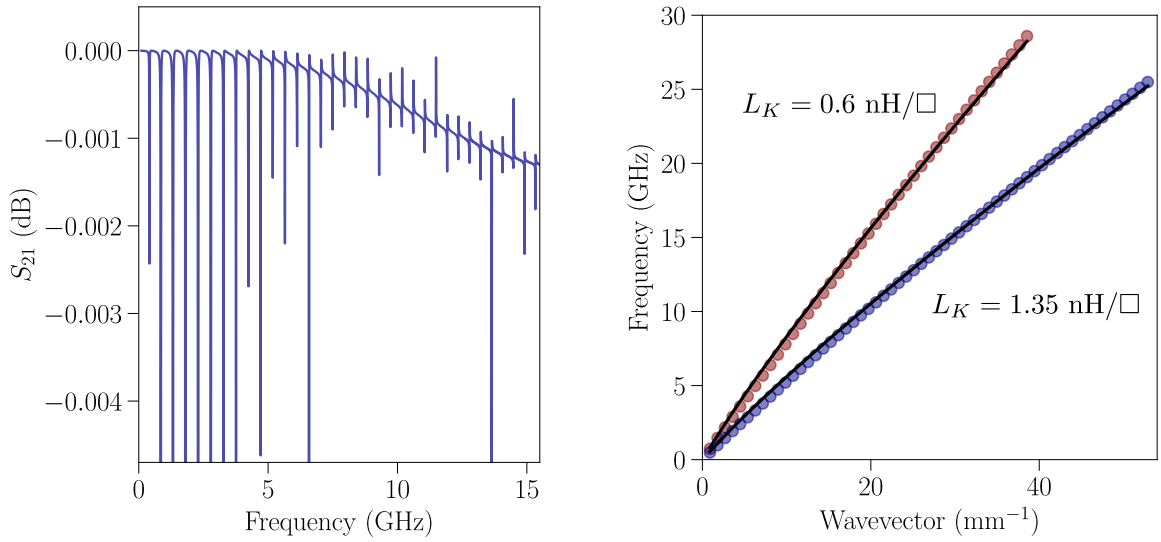

Fig. 3.8. Electromagnetic simulations of plasmon resonances. Simulated transmission using Sonnet electromagnetic solver for the geometry discussed in this section. The kinetic inductance per square L_K is fixed for two different simulations at two distinct values. The obtained dispersion relations are fitted using Eq. (3.22). The fitting parameter $L_{K,\mathrm{fit}}$ is close to the value set in the simulation within $3\ \%$.

The above simulation confirms the accuracy of our capacitance model to extract the kinetic inductance L_K, which will be used extensively throughout this thesis.

3.4.2 Two-tones measurements

We have seen how to accurately extract the kinetic inductance out of plasmon modes dispersion relation. We have not explained so far, however, how $\omega(k)$ can be obtained experimentally in a large frequency range[5]. In this section we present a technique called *two-tones spectroscopy* providing the required result [Weißl et al., 2015]. It originates from the non-linearity of plasmons that is detailed below.

Cross-Kerr non-linearity The hamiltonian for one-dimensional plasmons with weak non-linearity treated as a perturbation can be written in second-quantized form [Weißl et al., 2015; Krupko et al., 2018; A. Khvalyuk et al., 2023]

$$\hat{H} = \sum_n \hbar\omega_n \hat{a}_n^\dagger \hat{a}_n - \hbar \sum_{n,m} K_{nm} \hat{a}_n^\dagger \hat{a}_n \hat{a}_m^\dagger \hat{a}_m + (\text{higher order terms}) \tag{3.34}$$

where

$$\omega_n = \tilde{\omega}_n - \sum_m K_{nm} \tag{3.35}$$

$\hat{a}_n^\dagger$ and $\hat{a}_n$ are bosonic creation and annihilation operators respectively, describing collective modes along the wire, and K_{nm} is the cross-Kerr coefficient related to modes n and m. An estimation of K_{nm} for a disordered superconductor can be found in Appendix D.2 and in

[5] usual microwave setups have a narrow operating bandwidth due to limitations of microwave components (amplifiers, circulators, filters...). Therefore in many cases direct measurement of microwave transmission is limited to 4-12 or 4-8 GHz.

[A. Khvalyuk et al., 2023].

Eq. (3.35) states that the frequency $\tilde{\omega}_n$ of mode n is renormalized by cross-Kerr effect even when modes m are not populated, a consequence of zero-point fluctuations.

When modes m are populated with $\langle \hat{a}_m^\dagger \hat{a}_m \rangle = N_m$ photons Eq. (3.34) implies that frequency of mode n is lowered following

$$\omega_n' = \omega_n - \sum_m K_{nm} N_m \tag{3.36}$$

This frequency shift is at the root of the *two-tones spectroscopy* that will be detailed now.

Modus operandi A two-tones measurement goes as follows (see also the scheme in Fig. 3.9):

- A resonant mode n (frequency f_n) is found in the measurement bandwith. A power sweep is performed to determine the optimal operating power P_{VNA}, large enough to ensure a good signal-to-noise ratio but small enough to reach the low-power regime (negligible frequency shift of the mode with power). The frequency f_n is re-measured at the power P_{VNA}: $f_n = f_n(P_{\mathrm{VNA}})$.

- The Vector Network Analyzer (VNA) power is set to P_{VNA}, and is configured to measure at fixed frequency f_n. In transmission this corresponds to measuring the minimum of $|S_{21}|$ (at the lowest position of the dip amplitude). A second, external microwave tone is connected to the setup, with a trigger linked to the VNA: for each signal sent at a given frequency by the source, the measurement at frequency f_n is triggered on the VNA.

- The source power P_{Source} is set, and the second tone f is swept in a large range ($f \in \{100\ \mathrm{kHz}, 30\ \mathrm{GHz}\}$). Due to cross-Kerr interactions of modes f_m and f_n the VNA measurement result is influenced by the source frequency: when f matches the frequency of mode m ($f_m \sim m f_1$) the frequency f_n is lowered by cross-Kerr effect: f_n becomes $f_n' = f_n - N_m K_{nm}/(2\pi)$ where N_m is the number of photons in mode m. For sufficiently large non-linearity K_{nm} the VNA measurement at f_n does not probe the minimum of $|S_{21}|$ anymore, resulting in a sharp increase of transmission. The shape of the transmission peak is mainly dictated by the widths of mode n $\Delta f_{3\mathrm{dB}} = f_n/Q_l$ and of mode m, as well as the Kerr coefficient K_{nm}. If $N_m K_{nm}/(2\pi) > \Delta f$ the peak amplitude reaches its maximum.

- With a further increase of source frequency f far from a resonant mode the system gets back to normal, $|S_{21}|$ is back to its minimum value ($f_n' = f_n$).

- Once the whole frequency range has been swept one obtains a series of peaks, each of which corresponds to a resonance mode m, as shown in Fig. 3.9.

3.4.3 Frequency shift as a measurement of superfluid density suppression

It has been argued that, for a given resonator geometry (capacitance to ground C_g, wire dimensions and coupling to environment) the resonance frequencies are solely ruled by the kinetic inductance L_K, or equivalently by the superfluid density. If the resonator is made out of a material which superfluid response is particularly sensitive to external perturbations such as

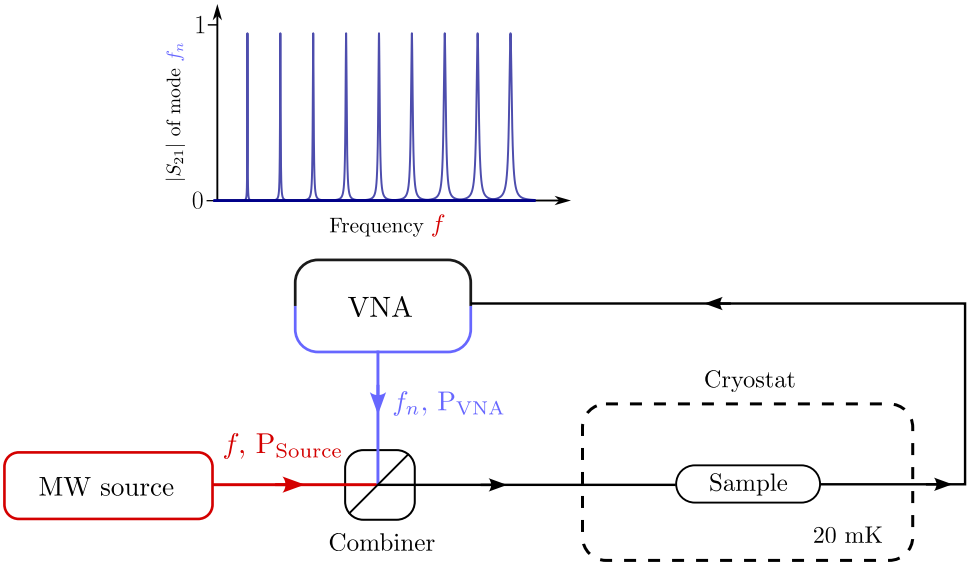

Fig. 3.9. Two-tones measurement scheme. Illustration of the two-tones measurement scheme described in the text. Details of the microwave setup are not shown and will be discussed in Appendix. **Top graph:** Typical trace of two-tones spectroscopy probed in transmission. Out of resonance the VNA transmission is minimal. Close to resonance (for any resonance mode m) transmission increases and reaches its maximum at $f = f_m$. By sweeping the probe frequency in tens of GHz range one obtains the full dispersion relation of plasma modes.

temperature, magnetic field or driving power the microwave resonator turns into a superfluid density probe. When varying an external parameter $\chi \in \{T, B, P, ...\}$ the frequency shifts by the quantity

$$\frac{\delta f(\chi)}{f} \equiv \frac{f(\chi) - f(\chi_0)}{f(\chi_0)} = \sqrt{\frac{L_K(\chi_0)}{L_K(\chi)}} - 1 = \sqrt{\frac{\Theta(\chi)}{\Theta(\chi_0)}} - 1 \tag{3.37}$$

where χ_0 is the initial value of the parameter χ, L_K and $\Theta = \left(\hbar/2e\right)^2 L_K^{-1}$ are the kinetic inductance and superfluid stiffness respectively.

For small variations of f Eq. (3.37) becomes

$$\frac{\delta f(\chi)}{f} \approx -\frac{1}{2}\frac{\delta L_K}{L_K} \approx \frac{1}{2}\frac{\delta \Theta}{\Theta} \tag{3.38}$$

In most cases the parameters mentioned above reduce the superfluid density, leading to a decrease of frequency (with a negative frequency shift). The evolution of resonance frequency with χ can easily be extracted from experiment, and, from Eq. (3.37) one obtains the relative suppression of superfluid density with parameter χ

$$\frac{L_K(\chi_0)}{L_K(\chi)} = \frac{\Theta(\chi)}{\Theta(\chi_0)} = \left(1 + \frac{\delta f(\chi)}{f}\right)^2 \tag{3.39}$$

This method only allows for a *relative* measurement of superfluid suppression, thus the value of $\Theta(\chi_0)$ must be extracted using another technique such as the fit of plasmon dispersion relation described previously.

The advantage of this type of measurement is two-fold: first it is relatively easy to perform experimentally, since it only requires to monitor the resonance frequency as a function of χ,

without significant calibration needed. Secondly it allows for a *continuous* measurement of the evolution of $\Theta(\chi)$, therefore potentially revealing non-trivial dependence of superfluid density on the external parameters (where the dispersion relation method for instance would require sampling of the χ values). By making a complementary use of both techniques (dispersion relation and frequency shift) one has a powerful tool to study the superfluid response of a superconductor.

3.4.4 Suppression of superconductivity by thermal excitation of plasmons

Amongst the usual parameters leading to a suppression of superconductivity are the magnetic field, which will be the topic of a chapter, and the temperature. We now discuss the effect of temperature on the resonator operating frequency.

In the usual BCS treatment of superconductivity at finite temperature the main mechanism opposing to superconductivity is the breaking of Cooper pairs by thermal excitation.
When the thermal energy is increased the number of quasiparticles is enhanced as [Tinkham, 1975]:

$$n_{\mathrm{QP}} = n\sqrt{\frac{2\pi\Delta}{k_B T}}\exp\left(-\frac{\Delta}{k_B T}\right) \tag{3.40}$$

This equation states that at low temperatures well below the gap the superfluid condensate remains mostly unaffected by temperature, as the number of quasiparticles is exponentially small. In this standard (BCS) situation the suppression of superconductivity is then governed by the competition of gap Δ and thermal energy $k_B T$.
In systems where superfluidity is ruled by phase fluctuations however, superfluid density is expected to be reduced at all temperatures below the gap.

This can be seen using a simple idea that we briefly summarize here and can be found in more details in Appendix D.2.4 and in [A. Khvalyuk et al., 2023].
The application of an electromagnetic drive on a superconductor gives rise to non-linear terms in the relation between current density and vector potential [Maki, 1964]. As a result bosonic collective excitations occuring in superconducting films interact with each other, due to this non-linearity. This is the Kerr effect mentioned earlier in relation to the plasmons.
These modes are bosonic and therefore are thermally populated following the Bose-Einstein distribution. A summation over these interacting thermal plasmonic excitations leads to an estimation of the superfluid density suppression by classical phase fluctuations:

$$\frac{\delta f(T)}{f} \approx \langle(\nabla\varphi)^2\rangle_T = \frac{\xi^2}{\Theta}\int d^3q \frac{\hbar\omega_q}{e^{\frac{\hbar\omega_q}{T}}-1} \approx -\left(\frac{T}{T_\varphi}\right)^2 \tag{3.41}$$

in which left hand side term is the relative shift of frequency with temperature defined as $\delta f(T)/f = \left(f(T) - f(T_{\min})\right)/f(T_{\min})$, where $T_{\min}$ is the cryostat base temperature (usually ~ 20 mK). ξ is the superconducting coherence length in the dirty limit.
Last equality is obtained after assuming a linear dispersion of one-dimensional modes $\omega_q = vq$. In theory one could also consider 2D and 3D modes in the summation.

Since disorder enhances the role of phase fluctuations, one should expect a decrease of T_φ with disorder (*i.e* an increase of the frequency shift amplitude). Indeed the model predicts

$$T_\varphi \propto \Theta^{3/4} \tag{3.42}$$

where the proportionality constant depends mostly on the sample geometry and on the way the summation is carried out (see Appendix D.2.4).

Eq. (3.41) states the important fact that phase-induced suppression of superconductivity by an increased temperature does not follow the BCS activated behavior of Eq. (3.40) which predicts an exponentially suppressed frequency shift at low T, but rather a power law decay **at all temperatures**.

3.4.5 Sample design

The sample geometry adopted for the experimental determination of the superfluid density of indium oxide comprises two measurement devices: first a microwave resonator coupled to a feedline as shown in Fig. 3.5, and secondly a four-probe resistance measurement device allowing for the in-situ determination of DC properties in the superconductor under study. Fig. 3.10 displays a typical chip used in this work. For this study we consider two distinct geometries described below.

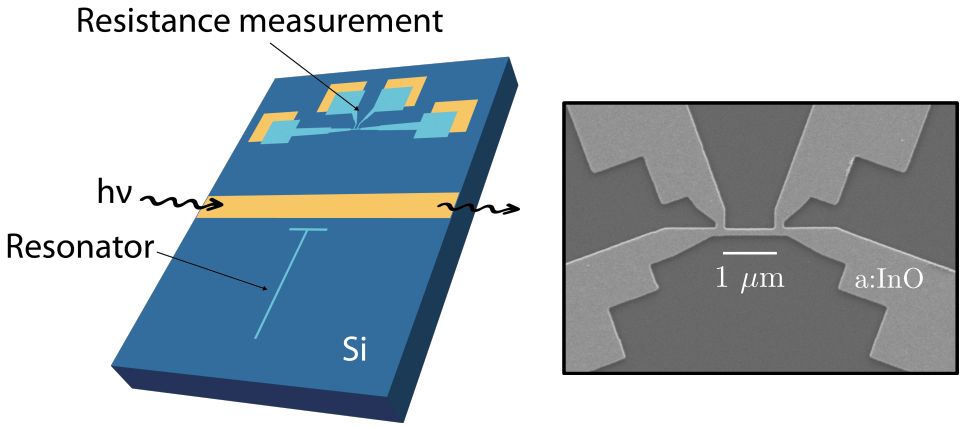

Fig. 3.10. Scheme of the chip. Left: A typical chip measured in this thesis has this form, with a gold $50\ \Omega$ transmission line in the center to which the microwave resonator is capacitively coupled. Further on the chip is designed a resistance measurement device. Light blue color represents amorphous indium oxide on this picture. **Right:** SEM image of the four contact resistance measurement device present on each sample in addition to the microwave resonator. Here the dimensions of the Indium oxide wire (center) are $1\ \mu\mathrm{m}$ by $100\ \mathrm{nm}$, for a total of 10 squares (this corresponds to the second geometry described in the text).

First geometry The first set of samples consists in $1\ \mu$m-wide and thin ($40\ \mathrm{nm}$-thick) disordered indium oxide resonators of long length $l = 3505\ \mu\mathrm{m}$ capacitively coupled to a $50\ \Omega$ feedline ($w = 240\ \mu\mathrm{m}$ for $Z_0 = 50\ \Omega$) in the hanging geometry. They are open at both extremities such that the transmission line acts as a $\lambda/2$ resonator with densely packed mode spectrum due to the long wire length.

The aimed-for kinetic inductance value is of the order of 1 to $10\ \mathrm{nH}/\square$, allowing to estimate a first mode frequency in the sub-GHz range.

Indium oxide lines are deposited on a $300\ \mu$m-thick high-resistivity silicon substrate (permittivity $\varepsilon_r = 11.9$), therefore setting the system in the domain of applicability of the long-range

Coulomb interaction model for the estimation of capacitance to ground described in section 3.2.2.

The device for the resistance measurement is a $1\ \mu\mathrm{m}$-wide and $10\ \mu\mathrm{m}$-long indium oxide wire connected to four gold lines terminated by squares of large area used for wire bonding. The resulting line is then 10 squares-long (see Fig. 3.10).

Second geometry For the second set of samples we chose identical parameters except for two major differences: a reduced wire width and length.

The resonator length is $l = 300\ \mu\mathrm{m}$ for a width $w = 100\ \mathrm{nm}$. Therefore dimensions have been divided by 10 compared to the first set of samples.

Consistently, the resistance measurement device is a $1\ \mu\mathrm{m}$-long, $100\ \mathrm{nm}$-wide strip, resulting in a 10 squares line.

Conclusion

In this chapter we have provided an accurate and experimentally simple way to access important properties of a superconductor such as the kinetic inductance L_K and the related superfluid stiffness Θ at low temperatures. The gist of the method resides in the quantitative description of plasma modes dispersion relation which allows for the extraction of L_K (being the only fitting parameter in the model). This model has been successfully confirmed by electromagnetic simulations.

We provide a measurement scheme operating at microwave frequencies based on the *two-tones measurement* that provides an experimentally relevant determination of the dispersion relation $\omega(k)$.

We present the typical sample geometries that will be studied in the coming chapters, and allow for the experimental investigation of the disorder-induced SIT in amorphous indium oxide.

Part II

Quantum Breakdown of Superconductivity across the Disorder-driven Superconductor-Insulator Transition

Chapters I and 2 gave a general overview of the physics of strongly disordered superconductors, and tried to convey the incredible complexity of such materials in which phenomena as important in physics history as Anderson localization and superconductivity are intertwined, giving rise to extremely rich states of matter.
In chapter 3 we described the measurement technique based on the tools of cQED that we propose to use to probe the superfluid response of superconducting indium oxide resonators.

In the following chapters we shall uncover some important features of strongly disordered Indium oxide thin films of increased disorder, from the superconducting state to the insulator. Each sample studied here allows for the measurement of superfluidity in amorphous indium oxide both in transport and at microwave frequencies, on the same physical chip and during the same cooldown. A chip is composed of a standard four contact device for resistance measurement and a microwave microstrip resonator made out of indium oxide, as pictured in Fig. 3.10.

We want to stress that transport and microwave measurements are performed on the same indium oxide film (fabricated in the same evaporation process) and in similar conditions (temperature, pressure, electromagnetic environment...) and therefore should describe the same physical object but at different frequencies (and different sizes). While the description of these measurements is separated in two distinct chapters (first transport properties and then results in the microwave regime) the reader should bear in mind that these two sets of measurements actually describe the same object. This is of great importance as we shall see that transport properties and superfluid density are strongly related in a non-trivial way close to the transition to insulation.

CHAPTER 4

Superconductor-Insulator Transition measured in transport

Disordered metals at low temperature display easily recognizable signatures; quantum interference between electronic trajectories lead to a number of features that can be identified via transport measurements. Study of such systems lead to numerous theoretical and experimental works on Anderson insulators and localization. A short introduction of this topic and its major consequences can be found in Appendix A.

The subject becomes more intringuing when the metal is replaced by a superconductor: the sample resistance may either vanish to zero or diverge to infinity as the temperature approaches zero [Shahar et al., 1992; Graham et al., 1998].
This quantum phase transition between superconductor and insulator is sometimes accompanied with the unusual preformation of Cooper pairs well above T_c and a pseudogap in the density of states, as shown via tunneling spectroscopy [Benjamin Sacépé, Dubouchet, et al., 2011; Daniel Sherman, Gorshunov, et al., 2014; Dubouchet et al., 2018].

Transport (low frequency) measurement techniques are well-suited to unveil unique properties of disordered superconductors. In this chapter we report on the systematic measurement of resistance in amorphous indium oxide sample of increasing disorder, driving the system from a standard superconductor to a much less trivial pseudogaped insulator.[1]

4.1 | Increase of normal-state resistance with disorder

As can be seen in Fig 4.1 the normal-state resistance of increasingly disordered Indium oxide samples (defined as the maximum of the $R(T)$ curve[2]) ranges from less than 1 to more than $16\ \mathrm{k}\Omega/\square$, well above the superconducting resistance quantum $h/(2e)^2 \sim 6.45\ \mathrm{k}\Omega$. This huge increase of resistance when cooling down signals the proximity of the mobility edge for localization. At $T = 0$ the sample would be an insulator if superconducting correlations did not arise. In presence of superconductivity the resistance goes to zero below a critical temperature T_c.

Upon further increase of disorder superconductivity eventually breaks down: the resistance does not drop to zero. Instead the low-temperature resistivity increases by orders of magnitude, evidencing the transition to an insulating state (see red curves in Fig 4.1). The SIT was already

[1] The experimental setup is described in Appendix C.

[2] Some authors consider the resistance at 4 K. This is convenient for experimentalists (since 4 K is the liquid Helium temperature) but is a rather arbitrary definition, and becomes inaccurate for nearly-critical disorder.

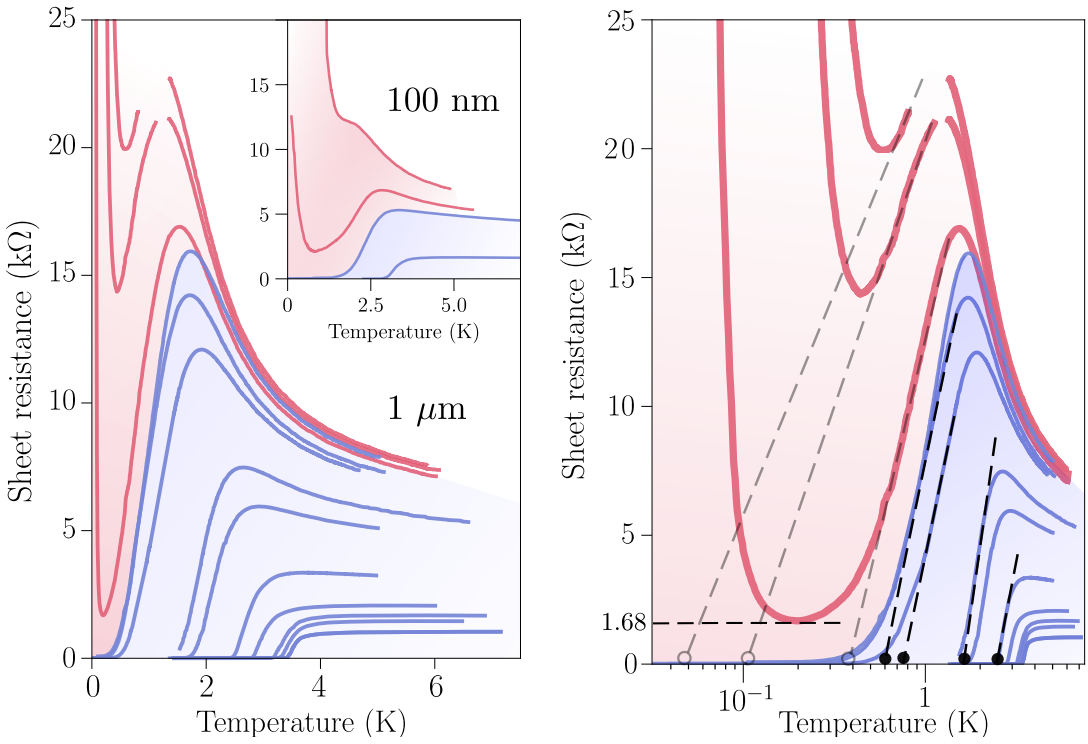

Fig. 4.1. Resistance of Indium oxide striplines versus temperature. a) Superconducting transition curves for films of various disorders. Upon increase of disorder the normal state resistance R_n increases. The normal state resistance is measured at the maximum of resistance just above the transition temperature for superconductors (shown in blue), and can become larger than the superconducting resistance quantum $h/(2e)^2 \sim 6.45\ \mathrm{k\Omega}$. Upon further disorder increase the resistance diverges at $T \to 0$ and the film becomes an insulator (red curves). **Inset:** Resistance measurements for nanowires with width $w = 100\ \mathrm{nm}$. **b) Re-entrant insulators and T_c measurement.** Just above the SIT the resistance presents a *re-entrant* behavior; upon cooling down the resistance first decreases similarly to a usual superconducting transition, but increases sharply at lower temperature before finally diverging at $T \to 0$ (red curves). The resistance minimum can be as low as $R_{\mathrm{min}} \sim 1.7\ \mathrm{k\Omega/\square}$, one order of magnitude lower than the corresponding normal state resistance $R_n \sim 16\ \mathrm{k\Omega/\square}$. Dashed lines show how the critical temperature T_c is obtained from the $R(T)$ curves; T_c is the temperature at which a linear interpolation of the resistance crosses the x-axis (black dots). The same process can be applied to re-entrant curves, providing a *would be* critical temperature "T_c" for the insulating state (grey empty dots). As can be seen from both **a)** and **b)** an increase of disorder not only enhances the normal state resistance but also strongly reduces the critical temperature.

observed in amorphous indium oxide, as presented in section 2.1.2.

It is convenient for the discussion to introduce a dimensionless normal-state conductance, defined as the ratio of the electronic resistance quantum $R_Q = h/e^2$ by the sheet normal state resistance R_n:

$$g = \frac{R_Q}{R_n}$$

The reader would have recognized the dimensionless conductance g studied in relation to the scaling theory of localization (see Appendix A.3.2).
One should however bear in mind that g is measured here at a finite temperature T_{peak} above

the transition, in contrast to the zero-T quantity considered in section A.3.2. If one could derive the complete temperature evolution of conductance $g_{\mathrm{theory}}(T)$, taking into account simultaneously effects of localization, sample effective dimensionality and paraconductivity above T_c, then the measured value would be simply $g = g_{\mathrm{theory}}(T_{\mathrm{peak}})$. Such a function is unfortunately out of reach for now.
We shall see below that this experimental g might actually be related to other properties of the material.

A crude estimation of $k_F l_e \propto g$ [3] from our measurements leads $k_F l_e < 1$, as was previously noted by [Shahar et al., 1992; Graham et al., 1998]. This has to be compared with the Ioffe-Regel criterion stating that the condition $k_F l_e \sim 1$ corresponds to the Anderson metal-Insulator transition for electrons (see Appendix A).
Therefore the indium oxide samples studied here are subject to strong localization effects reminiscent of insulator physics. Amazingly superconductivity can still take place in such systems where electrons are localized.

4.2 | Decrease of T_c with disorder

We have argued in section 1.1.2 that suppression of superconductivity could be due to fluctuations of either the order parameter amplitude, or its phase. In both case an increase of sample disorder, with a tendency to localize charge carriers, should result in a decrease of transition temperature T_c. We now compare to experimental measurements, by extracting T_c from the $R(T)$ curves.

Fig 4.2 shows the dramatic suppression of critical temperature with disorder observed in our indium oxide films. Upon increase of disorder (*i.e* decrease of g) T_c decreases by one order of magnitude, from $T_c = 3.6$ K down to $T_c = 0.4$ K close to the SIT. On this graph are also shown the *would be* critical temperatures "T_c" obtained by interpolation of the re-entrant insulating curves (empty markers).

4.2.1 Unusual T_c suppression

The decrease of T_c with decreasing conductance g can be accurately fitted by a logarithmic law:

$$T_c = T_{c_0} \ln g \tag{4.1}$$

where $T_{c_0} = 1.09$ is the only fitting parameter. By construction the critical conductance at which T_c vanishes is then $g_c = 1$. Strikingly, this critical point was never reached: at $g \leq 1.6$ the resistance diverges at low temperatures, giving rise to a re-entrant insulator. The *would be* critical temperatures "T_c" however still fall on the line defined by Eq. (4.1), before vanishing at $g = 1$.

This leads to an important observation: Close to the SIT the critical temperature reaches a finite value $T_c \sim 0.4\ \mathrm{K} \neq 0$. **As a consequence T_c drops abruptly to zero at a critical conductance $g_c = 1.6$.** This intriguing feature will be further investigated in the coming sections of the thesis.

[3] $k_F l_e = g \frac{n^{1/3}}{d(3\pi^2)^{2/3}}$ where n is the carrier density and d is the film thickness.

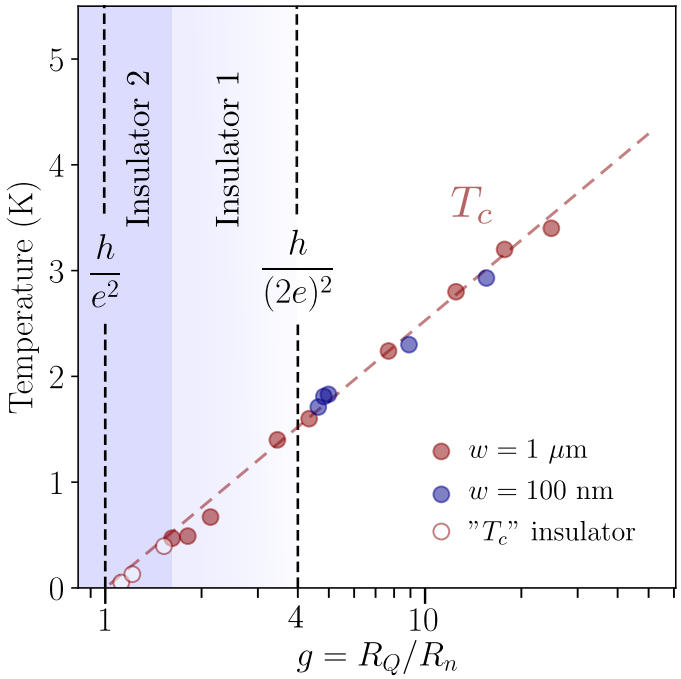

Fig. 4.2. Decrease of critical temperature with disorder. The critical temperatures of wide ($w = 1\ \mu$m, red dots) and narrow wires ($w = 100$ nm, blue dots) are shown versus the normal state conductance calculated from $g = R_Q/R_n$ where $R_Q = h/e^2$ is the electronic resistance quantum. Upon increase of disorder (*i.e* decrease of g) the critical temperature is continuously reduced. The data is nicely fitted by a simple logarithmic formula $T_c = T_{c_0} \ln g$ where $T_{c_0} \sim 1.09$. At $g \sim 4$ narrow wires become insulating (Insulator 1). Below $g_c = 1.6$ larger wires also turn into an insulator (Insulator 2). In both cases the critical temperature abruptly drops to zero at g_c. In the insulating state for $g < 1.6$ the *would be* critical temperature "T_c" denoted by empty markers also follows the logarithmic scaling, before vanishing at $g = 1$ (*i.e* $R_n = R_Q = h/e^2$).

4.2.2 Comparison with amplitude-driven pathway

It was suggested in section 1.2 that superconductivity in homogenously disordered films could be increasingly suppressed by disorder as Coulomb repulsion between electrons forming a Cooper pair becomes more effective, leading to a gradual suppression of pairing [Finkel'stein, 1994] [4].

It is worth noting here that the formula given by Finkel'stein (Eq. (1.7)) does not accurately describe the suppression of T_c in the films displayed in the present work. Figure 4.3 shows the Finkel'stein prediction for various values of the parameter γ, only fitting parameter of the theory. One cannot find a γ that fits reasonably well our indium oxide data.
This observation is actually not so surprising. Indeed this (mean-field) theory, valid up to some moderate disorder only ($g \gg 4$ in our notations) neglects the effects of phase fluctuations which are expected to become predominant at strong disorders [Larkin, 1999].

We now turn to comparison with the bosonic pathway for which phase fluctuations are the relevant mechanism.

[4] This is the *fermionic mechanism* discussed in section 1.2

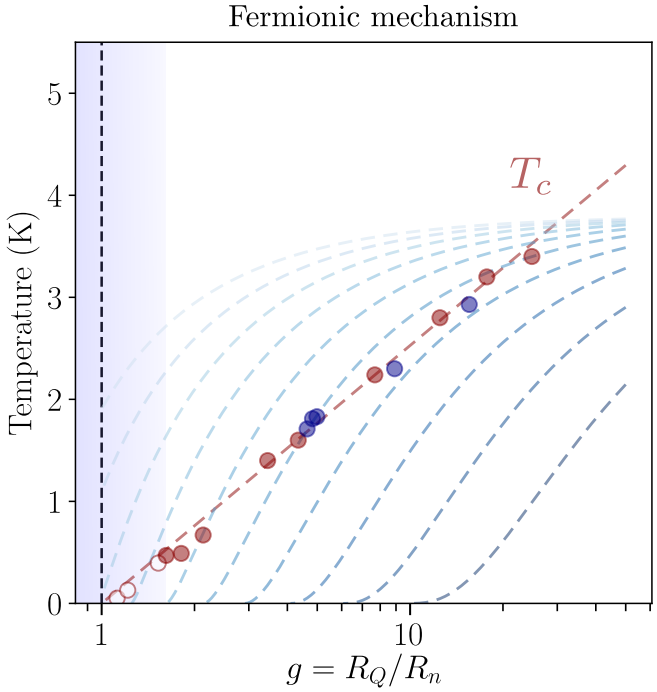

Fig. 4.3. Attempted fit with Finkelstein's formula. Predictions of fermionic mechanism given by Eq. (1.7) are plotted for several values of the parameter γ (in blue) and compared to the experimental critical temperature (in red). γ ranges from -0.38 to -0.12, and the bulk critical temperature is assumed to be $T_{c,0} = 3.8$ K.

4.2.3 Bosonic pathway

The bosonic mechanism predicts that the *real* (measurable) critical temperature is given by the BKT theory, and can be much smaller than the BCS value. This quantity is proportional to the superfluid stiffness Θ as $T_c^{\mathrm{BKT}} \propto \Theta(T_c^{\mathrm{BKT}})$. Upon increase of disorder Θ is suppressed, reducing in turn the *real* critical temperature while the mean-field T_{c0} remains unaffected. This mechanism is detailed in section 1.3.
We mentioned already that a large panel of experimental work on indium oxide demonstrates the preformation of Cooper pairs above T_c. This strongly suggests the relevance of the bosonic scenario for understanding the alteration of superconductivity in this particular material.

In next chapter (section 5.1.3) will be described how an increase of disorder $1/g$ translates into the simultaneous decrease of superfluid stiffness Θ and BKT critical temperature T_c. Using usual Mattis-Bardeen (BCS) expressions relating (measured) normal-state resistance and zero-T superfluid stiffness $\Theta(T = 0)$ in addition to the BKT superfluid jump at T_c given by $T_c = \beta\Theta(T_c)$ allowed us to estimate (grossly) the suppression of T_c with disorder. The result of this procedure is shown in Fig. 4.4 which compares our data to the expected reduction of T_c generated by phase fluctuations via the BKT mechanism. Dashed red line is the result of the numerical solving of Eq. (5.6) with $\beta \sim 0.45$ and a bulk $T_{c0} = 3.9$ K.

The chosen value of β is 2 to 3 times smaller than the expected BKT universal value $\beta = \pi/2$. It is only at this cost that our simple model fits the experimental data. This is expected, as we used only BCS expressions that might not be applicable close to the SIT, and neglected fluctuations of the order parameter amplitude (which should lead to a non-negligible additional suppression of T_c). The question of the meaning of g measured at finite temperature also

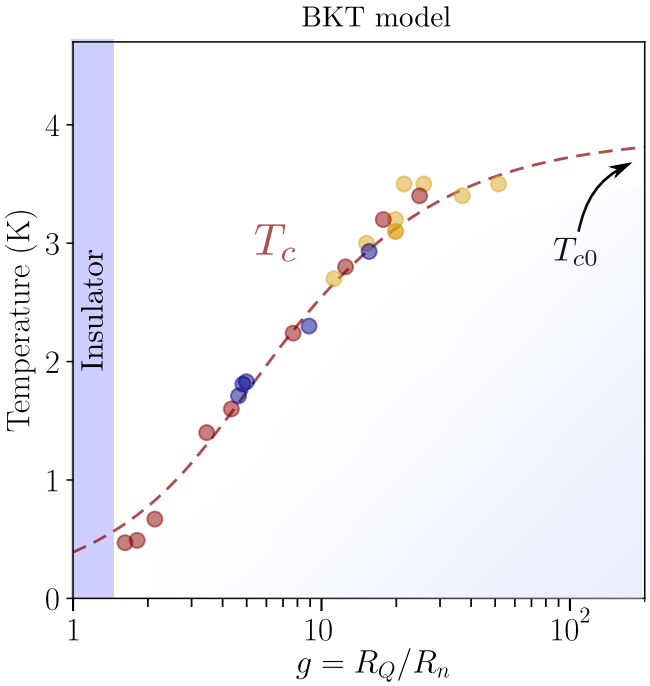

Fig. 4.4. Suppression of critical temperature by the BKT mechanism. Blue and red points are large and narrow wires, as previously. Yellow points are 60 nm-thick and tens of microns- wide films from [B. Sacépé, Seidemann, et al., 2015]. Dashed line is the BKT model described in section 5.1.3, with a bulk critical temperature $T_{c0} = 3.9$ K and assuming that the critical temperature is ruled by the BKT mechanism as $T_c = \beta\Theta(T_c)$ with $\beta \sim 0.45$. Θ is suppressed upon increase of disorder (such dependence is estimated using usual BCS formulae).

comes into play. In any case, a simplistic model such as this allows to reproduce qualitatively the nearly-logarithmic reduction of $T_c(g)$. We shall analyse this model further in next chapter.

Comparison with other superconductors with a pseudogap We now ask whether or not other disordered superconductors present a similar suppression of superconductivity with disorder.
To make sure that the comparison is fair we use the exact same procedure for the determination of T_c and g for various data found in the literature. From a $R(T)$ curve we define the T_c as the temperature at which a linear interpolation of the resistivity crosses the x-axis, as described earlier. The dimensionless conductance is found from $g = R_Q/R_n$ where R_n is the maximum of sheet resistance before the superconducting transition.[5]
Fig. 4.5 displays the suppression of critical temperature with disorder for several different materials (indium oxide, titanium nitride, niobium nitride, bismuth, niobium titanium nitride). The data is extracted from the available literature.
It is seen from Fig. 4.5 that these materials present a similar relation to the one discussed above: $T_c \propto \ln(g)$ (note the log scale on the x-axis). To my knowledge this feature was never observed or commented before: this could be a property of strongly disordered amorphous superconductors.

From the previous section it comes that this peculiar scaling of critical temperature could originate from strong phase fluctuations. A proper account of quantum fluctuations on top of

[5]To apply this procedure one must have access to the $R(T)$ curves with temperatures down to 0. This reduces the number of articles from which data could be extracted.

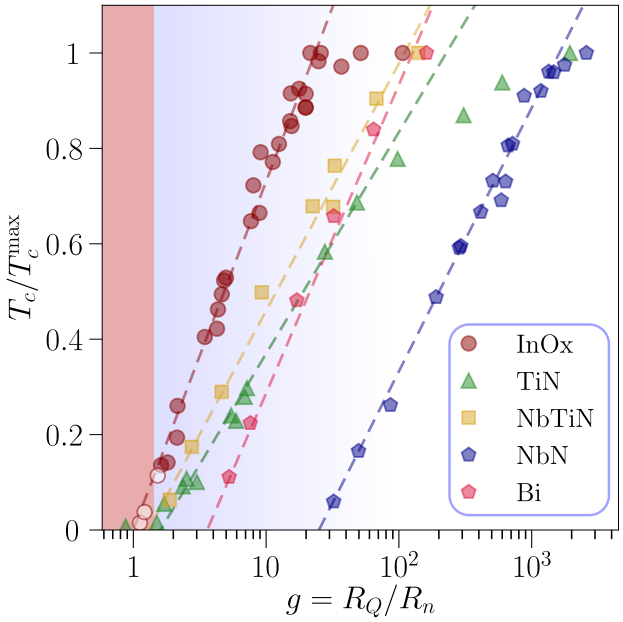

Fig. 4.5. Logarithmic suppression of T_c in pseudogap superconductors. $T_c(g)$ is shown in semi-log scale for Indium oxide (with data from the present work and B. Sacépé, Seidemann, et al., 2015), TiN (Baturina, Mironov, et al., 2007; B. Sacépé, C. Chapelier, et al., 2008; Benjamin Sacépé, Claude Chapelier, et al., 2010; Baturina, Postolova, et al., 2012; Amin et al., 2022), NbN (Chand et al., 2012; Chockalingam et al., 2008), Bismuth (Haviland et al., 1989) and NbTiN (Burdastyh et al., 2020).

BKT theory must be made however to capture the whole physics at hand here [König et al., 2015].
It is very interesting to note that these materials are known to possess a pseudogap. This is probably not a coincidence: as discussed in chapter 2 a pseudogap is most likely accompanied with strong spatial inhomogeneities of the order parameter, which in turn enhance phase fluctuations.
One could wonder if a relation between normal-state conductance g and T_c could be found theoretically for materials having a pseudogap Δ_P.

4.2.4 Critical conductance at the transition g_c

We have seen in section 1.4 that strong enough disorder could lead to a scenario where quantum and thermal phase fluctuations break superconductivity at $T = 0$. At a critical conductance g_c the superconducting state turns into an insulator made of localized Cooper pairs.

In the framework of the dual theory of M. Fisher (see section 1.4) the critical conductance at the transition is given by $g_c = 4$ (which corresponds to $R_n = h/(2e)^2 \sim 6.45\ \mathrm{k}\Omega$) if one considers self-duality between Cooper pairs and vortices. Alternatively the conductance can also be found as $g_c = \text{constant}$ where the constant is not universal in more realistic settings [Larkin, 1999].

Effect of wire dimension We now discuss the values of critical conductance found for two different sample geometries.
We studied two geometries of samples: some DC devices are $10\ \mu$m-long and $1\ \mu$m-wide, and

a second set of wires is 1 μm-long and 0.1 μm-wide. The dimensions have been chosen to keep the same aspect ratio in both configurations.
Measurement of the critical temperature for both sets of device gives the same quantitative result: T_c for both geometries lie on the same curve (the graphs shown above contain both large and narrow wires).
One observation however seems to show a qualitative difference between the two: **larger (and longer) wires seem to survive deeper in disorder than the narrowest ones.**

- $w = 1$ μm: the critical conductance at which T_c vanishes is $g_c^{\text{large}} = 1.6 \sim \pi/2$.
- $w = 100$ nm: T_c is suppressed at lower disorder, $g_c^{\text{small}} \sim 4$.

The first thing one should recall is the ill-defined character of the dimensionless conductance g. It is indeed measured at finite temperature (and therefore corresponds in part to a *failed* Anderson insulator suppressed by inelastic processes) and is of non-trivial nature, with preformed localized Cooper pairs and a possible contribution by Aslamasov-Larkin paraconductivity above T_c [Aslamasov et al., 1968]. Thus without proper theory to account for all these phenomena at once one cannot discuss quantitatively the values of dimensionless conductances g_c at criticality.

That being said, one must acknowledge the resemblance between the results for the nanowires $g_c^{\text{small}} = 4.5$ and the theoretical $g_c \approx 4$ of the bosonic scenario.
It can be noted that the longer wires (which are exactly 10 times longer and 10 times larger) have a critical conductance $g_c^{\text{large}} = 1.6$, leading to a ratio $g_c^{\text{small}}/g_c^{\text{large}} = \sqrt{10}$. This could be purely coincidental.

The effects of dimensions on transport in indium oxide have been observed and displayed a quite different trend [Kowal et al., 2008]: their longest wires were the most insulating, while the shortest ones displayed a tendency to superconductivity. All samples were prepared simultaneously, with the exact same disorder. In our case it seems that shorter (and narrower wires) are less resilient to disorder than wide, long ones.

The question becomes whether it is the decrease of length or width that drives such phenomenon. For instance it is known that ultra-narrow nanowires are more sensitive to phase-slips, leading to a dissipative quantum phase transition with a critical resistance of the order of the superconducting resistance quantum [Zaikin et al., 1997; Bezryadin et al., 2000]. The effect of wire dimensions on phase-slips will be discussed in a coming chapter.

4.2.5 On the broadening of the superconducting transition

As can be seen in Fig 4.1 strongly disordered films display a large broadening of the superconducting transition curves, compared to standard clean superconductors. One might wonder if this broadening influences our measurement of the critical temperature.

While many effects contribute to such broadening of the $R(T)$ curves near T_c (such as paraconductivity for instance), these are rather small. On the other hand the BKT transition in strongly disordered systems implies a large enhancement of the critical region: for temperatures in the window $T_c < T < T_{c0}$ free vortices proliferate and dissipate, gradually increasing the sample resistance. The size of this region increases with disorder as $\sim 4G_i \propto 1/g$ (see section 1.3).

If one chose to obtain T_c by fitting the data to some available theory, one would need to take into account the BKT broadening (like in Benfatto et al., 2009), but also the Aslamasov-Larkin

paraconductivity (Aslamasov et al., 1968) and other contributions to the conductivity (Maki and Thompson, 1989). Some of these contributions cancel each other (Stepanov et al., 2018) and would involve many fitting parameters.

In our view, it is more relevant to define the critical temperature in a systematic way for every sample, without relying on a theoretical model.
We then define the critical temperature as the temperature at which a linear interpolation of the resistance curves crosse the x-axis (see dashed lines in Fig. 4.1**b**). Conveniently this definition also allows the estimation of the *would be* critical temperature of re-entrant insulators.

4.3 | Competition of superconducting and insulating energy scales at the transition

4.3.1 Comparison of activation energy and critical temperature

We have demonstrated above that an increase of structural disorder in amorphous indium oxide films results in a significant suppression of the condensation energy T_c, down to the transition to an insulating state ($T_c = 0$).
The increase of resistivity with lowering temperature in similar insulating films has been thoroughly studied by [Shahar et al., 1992]. They observed that insulating samples close to the transition are best fitted by the thermally activated law $R \propto \exp\left(T_0/T\right)$ where T_0 is an *activation energy* with a crossover to Mott's law deeper in the insulating regime.

A reproduction of the original plot from [Shahar et al., 1992] is shown in Fig. 4.6**c**, in order to allow comparison with our data. The activation energy T_0 decreases upon approaching the SIT from the insulating side, reaching a value $T_0 \sim T_c \sim 2$ K at the SIT.
The same observation can be made for the samples presented here, by fitting the low-temperature part of re-entrant insulating resistance curves (Fig. 4.6**a**) to the activation law and extracting T_0 (Fig. 4.6**b**).
At the SIT activation energy and critical temperature are identical $T_0 = T_c \sim 0.4$ K, suggesting a puzzling relation between these two intrinsically different energy scales.

T_0 is indeed *a priori* unrelated to superconductivity as it sets the thermal energy that the system must be given in order to allow hopping between Anderson-localized electronic states, resulting in finite conductivity at non-zero temperatures. T_c on the contrary describes long-range phase ordering of electron pairs on a macroscopic scale.

The explanation for this observation comes from the theory of pseudogap in Anderson insulators close to the mobility edge.
In section 2.3 it was argued that the energy scale T_0 is related to the *parity gap* Δ_P originating from preformed Cooper pairs composed of localized electrons. Transport is thermally activated with single electrons "jumping" from one localized state to another. T_0 decreases upon approaching the transition as $T_0 \sim \Delta_P \propto |g - g_c|^{\nu D_2}$ where g_c is the conductance at which the pseudogap develops, which reproduces the experimental evolution of T_0 with disorder seen in Fig. 4.6**c**.

Experimentally it is observed that at the SIT the lowest achievable value of critical temperature is not zero: below this critical value T_c does not exist and the $T = 0$ state is an insulator. See Fig. 4.6**b** and **c**.

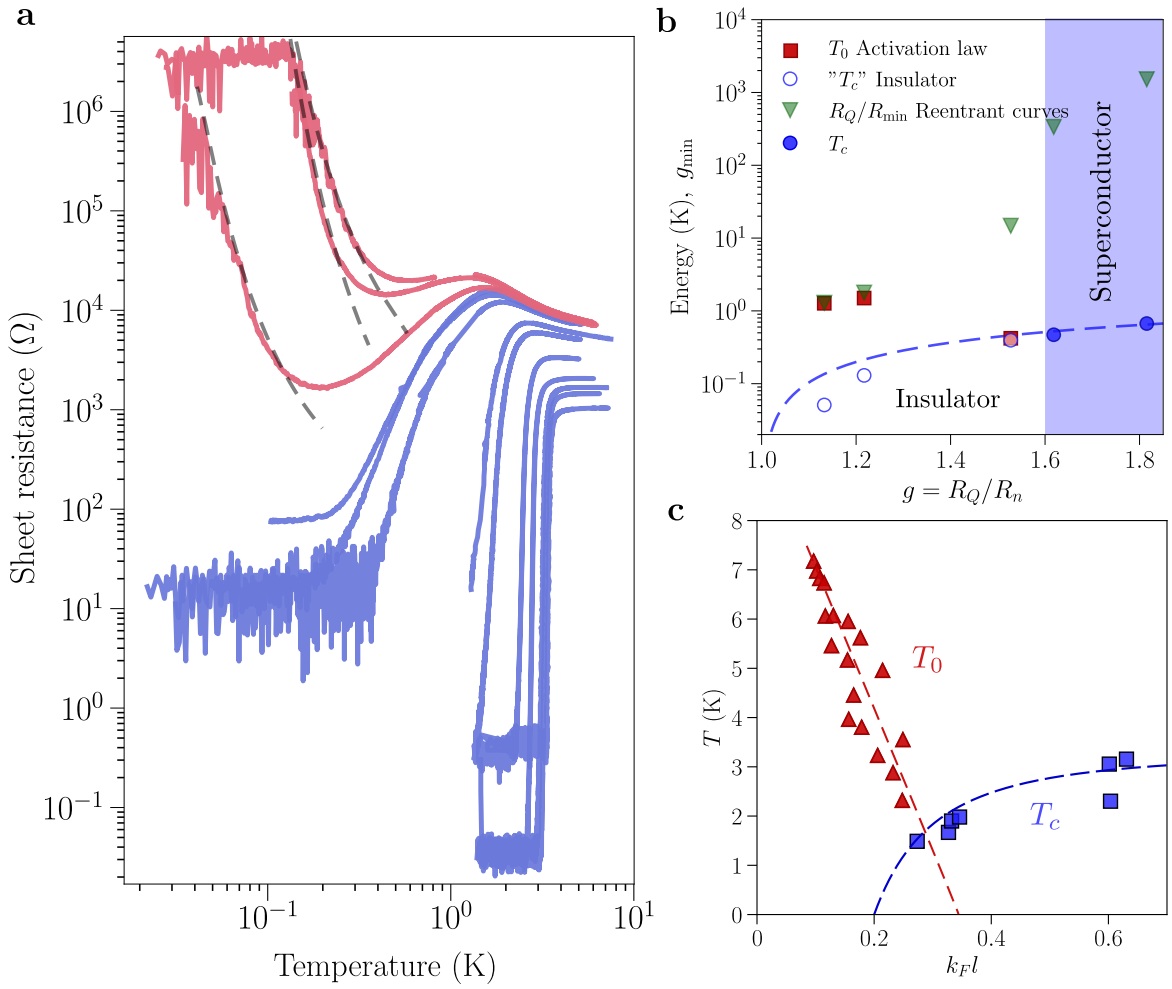

Fig. 4.6. Closer look at the re-entrant insulators. a) Transition curves in log-log scale. Close to the transition the low-resistance of superconducting samples is somewhat higher than their low-disorder counterparts, with $R_{\min} > 200\ \Omega$. The low-temperature part of re-entrant insulators can be fitted by an activation law $R \propto \exp\left(T_0/T\right)$ where T_0 is an activation energy. The fits are shown in dashed grey lines. **b) Energy scales across the SIT.** The critical temperature T_c on the superconducting side of the transition and the *would be* critical temperature "T_c" on the insulating side are shown across the SIT alongside the logarithmic formula $T_c = T_{c_0} \ln g$ (dashed line). The activation energy T_0 is obtained by fitting the re-entrant resistance, and the dimensionless conductance of the re-entrant insulators is given by $R_Q/R_{\min}$ where $R_{\min}$ is the minimum of resistance measured for near-critical samples. When crossing the SIT (*i.e* $g = 1.8 \to 1$) one first observes that the activation energy T_0 is of the order of the critical temperature : $T_0 \sim T_c$, then increasing to $T_0 \sim 2$ K upon approaching $g = 1$. Secondly one notes the decrease of the minimum conductance $R_Q/R_{\min}$ from 10^3 to $R_Q/R_{\min} \sim T_0$. **c)** The dependence of the pertinent energies at the transition T_0 for insulating samples (red triangles) and T_c for superconducting samples (blue squares) on disorder ($k_F l \propto g$) in amorphous indium oxide films. Blue dashed line follows $T_c = 3.3\left(1 - (0.2/k_F l)^2\right)$, which is mostly a guide for the eye. Reproduction from [Shahar et al., 1992].

Within the theory of pseudogap T_0 should indeed be of the order of T_c at the transition: the superconducting state develops when the criterion $\Delta \sim \Delta_P$ (discussed in section 2.2.1, where

Δ_P now replaces δ_{loc}) is verified.

STM measurements of the spectral gap [Benjamin Sacépé, Dubouchet, et al., 2011] give the estimation $E_g \sim 7$ K close to the transition. Our estimations of $\Delta \approx 2T_c \sim 1-2$ K and $\Delta_P \sim T_0 \sim 2$ K are in agreement with $E_g = \Delta + \Delta_P$ in order of magnitude.

4.4 | Re-entrant $R(T)$ curves

Insulator and superconductor are intertwined close to the SIT: localization effects are present on the superconducting side, while Cooper pairs are bound on the insulating side. The nature of the re-entrant resistance curves upon cooling down remains to be adressed.

We will show that in the framework of the theory of pseudogap **Coulomb interactions between localized pairs must be taken into account in order to explain re-entrant behavior of resistivity displayed in Figs. 4.1, 4.6 and 4.8.**
Indeed in most of the theory described in chapter 2, interactions between electrons were neglected for simplicity. In a real system interactions might become relevant, as we will show.

We have already discussed the effects of Coulomb interaction between single electrons within a localization volume, and concluded that this repulsion could be overruled by phonon-induced attraction.
There exists another Coulomb interaction occuring in a system with a pseudogap, namely the repulsion between localized *electron pairs*.

The long-range interaction between pairs (of charge $2e$) on site i and j is

$$V_{ij} = \frac{4e^2}{\kappa r_{ij}} \tag{4.2}$$

where κ is the dielectric constant.
The weakness of this interaction is due to the large dielectric constant. In an Anderson insulator *without* superconducting pairing the dielectric constant κ (in units of $4\pi\varepsilon_0$) can be estimated by [M V Feigel'man et al., 2018]:

$$\kappa \approx 40\, e^2\, \nu_0\, \xi_{\mathrm{loc}}^2 \tag{4.3}$$

where ν_0 is the density of states for electrons. For pairs the DoS is twice smaller.
This dielectric constant can be large *e.g.* $\kappa \approx 1000$ in amorphous indium oxide.[6]
Comparable values have been obtained experimentally on the insulating side of the transition by [Ebensperger, 2021].

4.4.1 Coulomb gap of preformed pairs

Similarly to the case of single electrons, the Coulomb repulsion between pairs opens a soft Coulomb gap in the density of states.
This can be demonstrated by following the derivation of the Coulomb gap presented in Appendix A.4, and replacing $e \to 2e$ to account for the repulsion of pairs. One gets the Coulomb gap of preformed pairs:

$$\Delta_C = \nu_0^{1/2} \left(\frac{4e^2}{\kappa}\right)^{3/2} \approx 0.04\, \delta_{\mathrm{loc}} \tag{4.4}$$

[6] We have used $\nu_0 = 0.5\, 10^{46}$ J^{-1}m^{-3} as measured from Hall effect [B. Sacepe et al] and a localization length of the order of the coherence length $\xi_{\mathrm{loc}} = 5$ nm.

where last equality follows from Eq. (4.3).

Estimation of the Coulomb gap for indium oxide Using the estimates for the DoS of pairs $\nu_0 = 0.5\,10^{46}\ \mathrm{J}^{-1}\mathrm{m}^{-3}$ and the dielectric constant $\kappa \approx 1000$ leads to the Coulomb gap width:

$$\Delta_C \approx 4\ \mathrm{K} \tag{4.5}$$

The estimate above demonstrates that the Coulomb gap of preformed pairs has a value comparable to that of the superconducting energy scales $\Delta \sim 2T_c$ and T_0.

Nature of the Cooper pair insulator It is suggested from experimental data that the superconducting state in a pseudogapped superconductor is terminated by a state of incoherent localized Cooper pairs. The absence of supercurrent originates from the loss of long-range phase coherence between Cooper pairs over the sample length.
The electrons of a pair remain tightly bound (one needs to bring the energy $2\Delta_P$ to break a pair) and are distant from one another by a few localization lengths.

The pairs also weakly repel each other through Coulomb interactions, which remain long-range because they are poorly screened. All Cooper pairs interact repulsively with each other forming a complex many-body localized system called *Coulomb glass* [M. Müller and Ioffe, 2004].
It is plausible that Coulomb repulsion between electron pairs and condensation of these pairs into a superconducting state are in competition. When disorder and the related phase fluctuations become strong, Coulomb repulsion between pairs can overcome and induce an insulating state. We will comment further on this mechanism later.

From a handwaving argument this interpretation gives a meaning to the *would be* critical temperature extracted from re-entrant insulating samples: that quantity describes the critical temperature that would be observed experimentally if Coulomb repulsion between localized preformed pairs could be turned off.

4.4.2 Consequence on resistance at finite temperatures

At finite temperatures the number of quasiparticles is non-zero, and increases when warming the sample up as $n_{\mathrm{qp}} \propto \exp\left(-\Delta/k_B T\right)$. It follows that a current of unbound electrons (charge e) flows in the device. It was demonstrated that these electrons could screen Coulomb interactions [M. V. Feigel'man, Korshunov, et al., 1997], and therefore reduce the amplitude of the Coulomb gap compared to its zero-T value. This mechanism could be at the origin of the re-entrant resistance observed near the SIT, as described below.[7]

[7] In disordered granular superconductors and Josephson junction arrays a re-entrant resistance with temperature is often observed, and interpreted as the competition between Coulomb repulsion (charging energy E_c) and Josephson coupling (Josephson energy E_J) [van der Zant et al., 1996]. The mechanism described in this paragraph is very similar to it, with the major difference of the microscopic properties of charges: in a granular superconductor Cooper pairs are gathered in superconducting grains, and transport occurs by coherence tunneling between grains. Therefore in a particular grain (with size typically of the order of ξ) electronic wavefunctions are extended, and form a superconducting state which present all the characteristics of a BCS superconductor (which should be seen by a local probe such as STM). For a homogeneous disordered superconductor based on an insulator, electronic wavefunctions are localized, and electron pairs are formed because of the pseudogap. These pairs are localized and transport occurs by hopping between localized states.

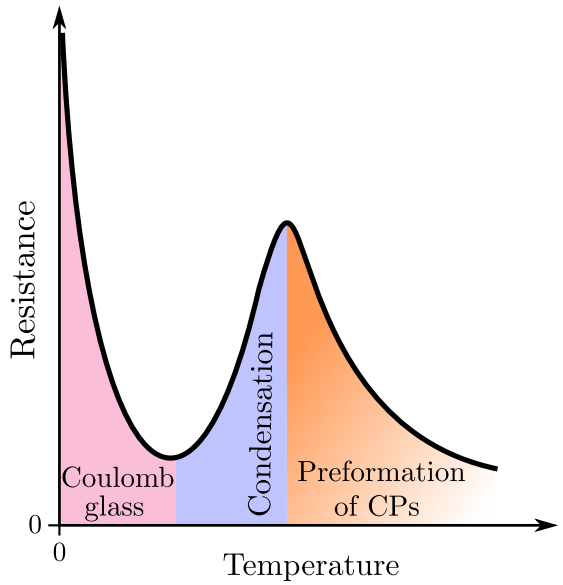

Fig. 4.7. Re-entrant resistance in pseudogapped superconductors. Critically homogeneously disordered samples close to the SIT might present a re-entrant behavior. This is due to the interplay between Coulomb repulsion of preformed pairs, condensation of these pairs, and thermally excited quasiparticles. Anderson localization of single electrons is increasingly efficient as temperature is decreased, enhancing the probability for quantum interferences. At lower temperatures pairs of electrons start to form through the localization-induced phonon-mediated attraction. At even lower temperature normal electrons (quasiparticles) screen the Coulomb interactions, favoring the condensation of pairs upon cooling down: the resistance drops. Concurrently quasiparticles get frozen out, reducing the effect of screening: Coulomb repulsion takes over and drives the sample into an insulating state made of localized Cooper pairs that repel each other at long range.

At finite temperatures $T > 0$ quasiparticles screen Coulomb interactions with increasing efficiency, consequently reducing the Coulomb gap: $\Delta_C(T) < \Delta_C(0)$. Upon cooling down the sample however, down to $T = 0$, quasiparticles are frozen, thus suppressing the screening effect and restoring the Coulomb gap to its largest value.
Re-entrant behavior of critically insulating samples can then be interpreted as a competition of the superconducting order parameter Δ and the Coulomb gap Δ_C:

$$\eta(T) = \gamma \frac{\Delta(T)}{\Delta_C(T)} \tag{4.6}$$

where γ is an unknown constant that determines the quantum critical point at $T = 0$ between the insulator dominated by repulsion of pairs and the superconductor characterized by condensation of paired electrons.

When lowering the temperature starting from the normal state, the system experiences an energy gain by condensation of Cooper pairs $-E_{sc} \propto \nu_0 \Delta^2$. Here the temperature remains high enough to screen long-range Coulomb interactions, and $\eta > 1$, favorizing superconductivity and reducing the sample resistance.
Upon further decrease of temperature quasiparticles get frozen out, leading to an increase of $\Delta_C(T)$. Eventually Coulomb interactions take over condensation energy ($\eta < 1$) and resistance increases following an activated behavior with activation energy of the order of the parity gap

Δ_P.[8] This three-step mechanism is illustrated in Fig. 4.7.

4.5 | Heating effects in critically disordered samples

We add here that special precautions must be taken when interpreting data obtained by transport measurements of disordered superconductors near the Superconductor-Insulator transition. It was indeed predicted theoretically [B. L. Altshuler et al., 2009] and observed experimentally in indium oxide films [M. Ovadia, B. Sacépé, et al., 2009; Doron et al., 2017] that strong linearity and large discontinuities of the $I-V$ characteristics could occur due to electron-phonon decoupling.

Suppose that electrons have a temperature T_{el} distinct from the phonon bath temperature. B. L. Altshuler et al., 2009 showed that T_{el} could be obtained by solving the equation

$$\frac{V^2}{R(T_{\mathrm{el}})} = \Gamma\Omega\left(T_{\mathrm{el}}^{\beta} - T_{\mathrm{ph}}^{\beta}\right) \tag{4.7}$$

where Ω is the volume of the sample and Γ is the electron-phonon coupling strength. At low enough temperatures this equation gives two solutions for T_{el}, inducing a bistability of $I-V$ curves, with a jump between a low-resistive and a highly-resistive regime. The critical temperature at which such a bistability appears decreases upon approaching the transition. The experimental consequence of electron overheating is that some systems might become impossible to measure: voltages or currents used to probe the sample need to be extremely small in order to remain in the high-resistance regime, but still above the inevitable noise threshold implied by the measurement electronics.

Fig. 4.8 focuses on a re-entrant insulator measured in a narrow indium oxide wire. $I-V$ curves obtained with a current bias show that upon increase of current $\mathrm{I_{dc}}$ the 4-probe resistance decreases, following the same evolution as the temperature decrease of resistivity. Hence currents as small as $1\ \mathrm{nA}$ are heating the sample. The question is then whether or not the measured resistance is in the high or low resistance bistable regimes.

[8] The presence of a Coulomb gap for *electron pairs* suggests an additional channel for conduction based on the Efros-Schlovskii variable range hopping of *pairs*. Very close to the SIT this conduction channel could act in parallel to the thermal activation of *electrons* above the parity gap.

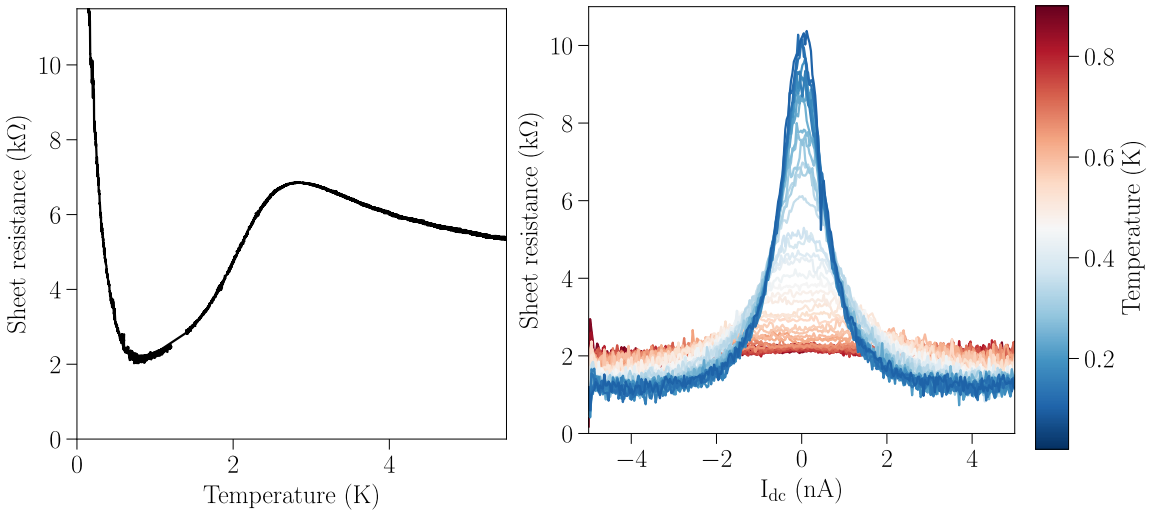

Fig. 4.8. a) Re-entrant insulating curve for a critical 100 nm-wide stripline. **b)** $I-V$ curves obtained on the same sample for various cryostat temperatures. The AC bias used here is $\mathrm{I_{ac}} = 100$ pA.

Conclusion

In this chapter we reported on the systematic transport measurements of a set of amorphous indium oxide samples with increasing disorder. Tuning the disorder level enabled us to cross the Superconductor-Insulator transition.
We demonstrate that the low-temperature superconducting state in this material is surprisingly resilient to disorder, as shown by the very low critical temperature $T_c \sim 0.4$ K and high normal-state resistance $R_\square \sim 16\ \mathrm{k\Omega}/\square$ reached at the SIT. Superconducting state survives deep in the Anderson insulator, and the interplay of the two leads to interesting features such as re-entrant resistance curves with temperature.

Finally, and most importantly, we notice that the SIT is accompanied by an abrupt suppression of T_c at a critical disorder g_c: where usual second-order transitions would require the continuous suppression of the transition temperature to zero, we observe a seemingly discontinuous *jump* of T_c. The critical disorder g_c also seems to be geometry-dependent.
We make the suggestion that the SIT in this system might be a first-order transition.
To strengthen this argument we now turn to the microwave spectroscopy of the exact same samples as the ones described in this chapter.

CHAPTER 5

Microwave frequency study of the Superconductor-Insulator Transition

Subsequently to the numerous studies of transport properties in disordered superconductors near the SIT (see also previous chapter), recent works have been focusing on finite frequency spectroscopy. Increasing the operating frequency allows for the measurement of the complex conductivity $\sigma(\omega) = \sigma_1 - j\sigma_2$, the real part of which describes dissipation and where the imaginary part $\sigma_2 = 1/L_K\omega$ is related to the kinetic energy of superfluid motion.

Along with the fastly growing field of circuit Quantum Electrodynamics (cQED), modern methods involving standard commercial microwave equipment (such as VNA, microwave amplifiers ...) were recently used to probe superconductivity via microwave resonators (in the line of the ones described in chapter 3). Several materials have already been measured using this technique, among which granular aluminum [N. Maleeva et al., 2018], heterostructures such as LaO/STO [G. Singh et al., 2018] or Josephson junction arrays [Kuzmin et al., 2019]. Amorphous indium oxide was used only twice in the making of superconducting circuits [Astafiev et al., 2012; Dupré et al., 2017], moderately far from the SIT.

In this chapter is presented the first study of the SIT in amorphous indium oxide using microwave resonators.
The samples are long (l = a few mm) and narrow ($w = 1\ \mu\mathrm{m}$) thin indium oxide wires, as pictured in Fig. 5.1. When excited by microwave radiations these wires withstand collective excitations which can be probed using the techniques presented in chapter 3.

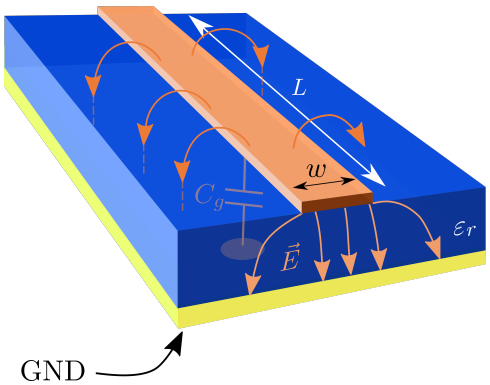

Fig. 5.1. Schematic view of a microstrip resonator used in this study. Details on the geometry and wave propagation are given in chapter 3. Here orange material is disordered amorphous indium oxide with kinetic inductance $L_K \sim 1\ \mathrm{nH}/\square$ or beyond.

5.1 | Superconductivity at $T = 0$ is Bosonic: ruled and suppressed by phase fluctuations

The reduction of superconducting pairing in amorphous indium oxide cannot be taken for the only responsible of superconductivity suppression by impurities [Benjamin Sacépé, Mikhail Feigel'man, et al., 2020]. We have mentioned an alternative scenario in which Cooper pairs gradually loose their phase coherence and form an insulating state composed of electron pairs. This idea is compatible with the experimental observations of a pseudo-gap, and is known as the *bosonic scenario of superconductivity* (presented in chapter 1).

Using the novel tools of microwave superconducting circuits introduced in chapter 3, **we will demonstrate in this chapter that the suppression of superconductivity in amorphous indium oxide follows the bosonic pathway**.
Doing so, we will show that disordered a:InO has exceptionally low superfluid density, and consequently large kinetic inductance [M. V. Feigel'man and Ioffe, 2018].

5.1.1 Microwave spectroscopy of disordered amorphous indium oxide

Typical microwave measurements of superconducting amorphous indium striplines are shown in Fig. 5.2. The adopted resonator geometry (*e.g* wire length $\sim$ few mm) allows for densely packed resonances with a typical inter-mode spacing ~ 0.4 GHz. a:InO resonators can either be probed in *single-tone* measurement, resulting in a transmission drop at the resonance frequency (Fig. 5.2**a**) or with *two-tones spectroscopy* displaying a series of transmission peaks signaling resonant modes (Fig. 5.2**b**).
Details on these spectroscopy techniques can be found in chapter 3.

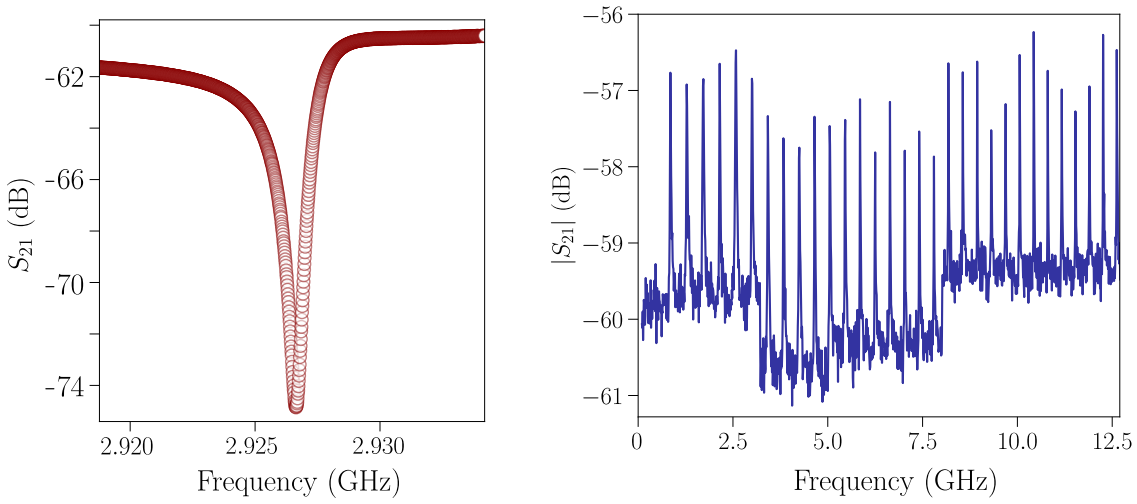

Fig. 5.2. a) Typical microwave transmission near a resonant mode of an indium oxide stripline, caracterized by a drop in amplitude. **b)** Excerpt of a typical two-tones measurement displaying a series of transmission peaks, each of which signals the existence of a resonant mode.

The kinetic inductance of indium oxide microwave resonators is accurately extracted from the dispersion relation curves shown in Fig. 5.3 for various disorders using the plasmon dispersion model given by Eq. (3.22) detailed in chapter 3.

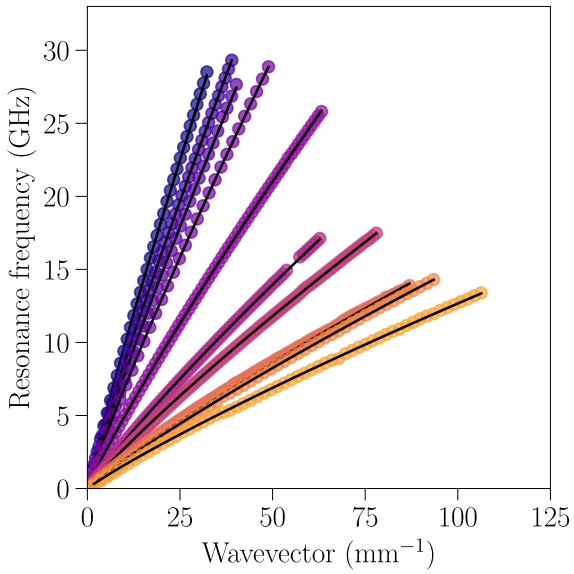

Fig. 5.3. Dispersion relations $f_n(k_n)$ obtained through two-tone spectroscopy of amorphous indium oxide resonators of increasing disorder. Black solid lines are fits following the plasmon dispersion model of Eq. (3.22), the kinetic inductance L_K being the only fitting parameter. Upon increase of disorder L_K increases, in turn decreasing the slope of the dispersion relation.

The resulting evolution of kinetic inductance with film disorder is shown in Fig. 5.4. Table 5.1 gathers both DC and microwave measurements carried out on the samples discussed in the present chapter.

By increasing the normal state resistance by one order of magnitude the kinetic inductance is enhanced by almost two orders of magnitude, reaching a maximum value of $L_K \sim 17$ nH/□ near the SIT, several times larger than the state of the art for disordered superconductors.
The increase of inductance with resistance for a dirty superconductor is given by the optical weight conservation [Mattis et al., 1958] and can be written[1]

$$L_K = \frac{\hbar R_n}{\pi \Delta} \tag{5.1}$$

where Δ is the (collective) superconducting gap and R_n is the normal-state film resistance measured above the transition temperature. Thus L_K is expected to grow linearly with normal state resistance.
Dashed line in Fig. 5.4 is the prediction of Eq. (5.1) in which the superconducting gap has been estimated as $\Delta = \alpha_S \, k_B T_c$ with $\alpha_S = 2$, corresponding to the BCS strong coupling limit. The validity of this estimation can be assessed by reasoning backwards: the coupling constant α_S is calculated from the data, as shown in Fig. 5.4**b**, demonstrating that the value of the coupling constant at low disorder is close to the BCS weak coupling $\alpha_S \sim 1.76$, then grows slowly up to $\alpha_S \sim 2.4$ at $g = 4$. At higher disorders the coupling constant diverges, evidencing the loss of validity of Eq. (5.1) close to the SIT.

Another coupling constant can be obtained from local measurement of the spectral gap via STM imaging [Benjamin Sacépé, Dubouchet, et al., 2011], as being the ratio of spectral

[1] See also an alternative derivation of this formula in Appendix E.1.

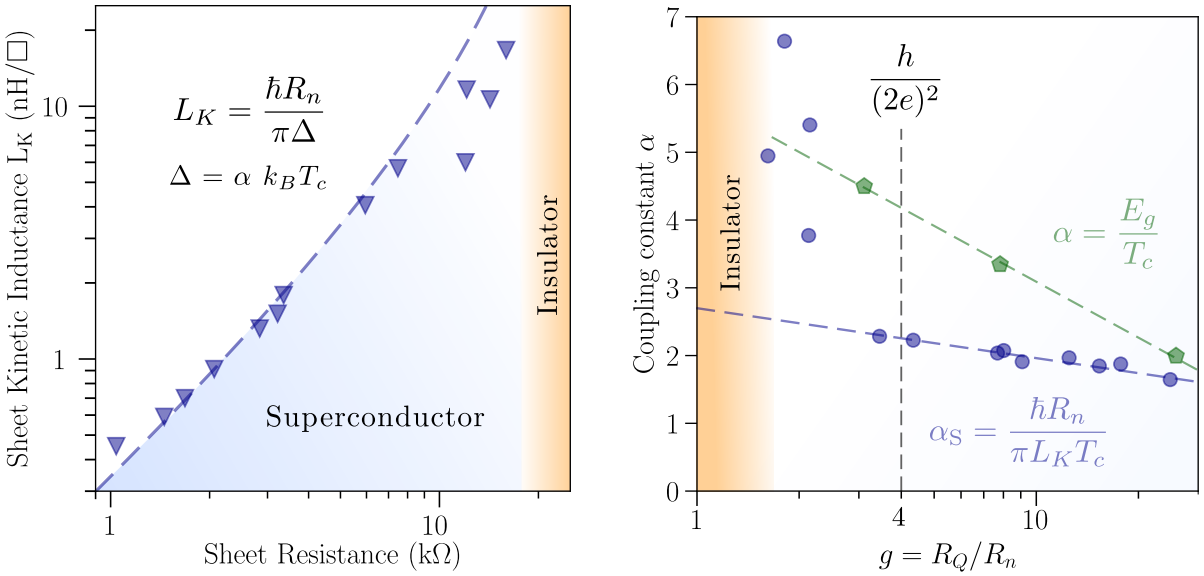

Fig. 5.4. Increase of kinetic inductance with disorder. a) Kinetic inductance versus normal state resistance. By increasing the normal state resistance by one order of magnitude the kinetic inductance is enhanced by almost two orders of magnitude, reaching a maximum value of $L_K \sim 17$ nH/□ near the SIT, several times larger than the state of the art for disordered superconductors. Dashed line is the estimation given by the optical sum rule formula $L_K = \hbar R_n/(\pi\Delta)$ where it is assumed that $\Delta = \alpha\, k_B T_c$ with $\alpha = 2$. The fit fails very close to the SIT. **b) Coupling constants** The coupling constant defined by the ratio of the superconducting gap by the critical temperature has two distinct values in a pseudo-gapped superconductor. The ratio E_g/T_c where E_g is the single particle gap measured in [Benjamin Sacépé, Dubouchet, et al., 2011] is shown in green, while the coupling constant obtained from BCS theory with $\Delta = \alpha_S T_c$ is $\alpha_S = \hbar R_n/(\pi L_K T_c)$ shown in blue. Upon increase of disorder (*i.e* $g \to 1$) α_S increases logarithmically but stays bounded : $1.76 \leq \alpha_S < 2.4$ before diverging for $g < 4$. On the other hand the single particle coupling constant α grows continuously as $E_g/T_c \propto -\ln g$.

gap E_g by the critical temperature T_c (shown in green). At low disorder α is close to the BCS value, but increases strongly upon increase of disorder (following a logarithmic evolution [2]).

The apparent divide between spectral and *collective* gap is an essential point of the theory of bosonic suppression of superconductivity (see chapter 1). Numerical simulations in presence of strong disorder predict a qualitatively similar result (see section 2.2.2): at low disorder both energy scales (single particle gap E_g and order parameter Δ) coincide, as expected for a BCS superconductor, whereas they separate increasingly with disorder, eventually reaching the SIT at which the collective gap vanishes but the single particle gap remains large. The same prediction was obtained analytically in the theory of fractal superconductors presented in section 2.3.

As suggested by Fig. 5.4**b** the opening of a pseudogap in the single particle density of states is related to a change in the coupling constant α. For Eq. (5.1) to hold, one must now put a coupling constant of the order of 5, which is the order of magnitude of the α obtained from tunneling data (green points). This observation, of course, it to be taken with a grain of salt. One might conclude that the relation Eq. (5.1) is actually more general than BCS theory alone

[2] if one is brave enough to declare that a fit based on three points is reliable.

(which can be demonstrated theoretically, see Appendix E.1), provided the superconducting gap is known. The relation $\Delta = \alpha T_c$, however, comes from BCS theory and breaks down at high disorders.

5.1.2 Phase fluctuations break down superconductivity

We have mentioned in section 2.2.2 that the order parameter inhomogeneneity induced by disorder enhances the role of superconducting phase fluctuations.
Upon increase of disorder fluctuations of the phase (quantum or classical) destroy long-range order and break down superconductivity. The relevant parameter to describe rigidity of the superconducting phase against fluctuations is the *superfluid stiffness* Θ introduced in chapter 1.
We shall now describe how superfluid stiffness evolves with disorder, and compare with transport measurements in a *phase diagram* near the SIT.

5.1.3 Phase diagram

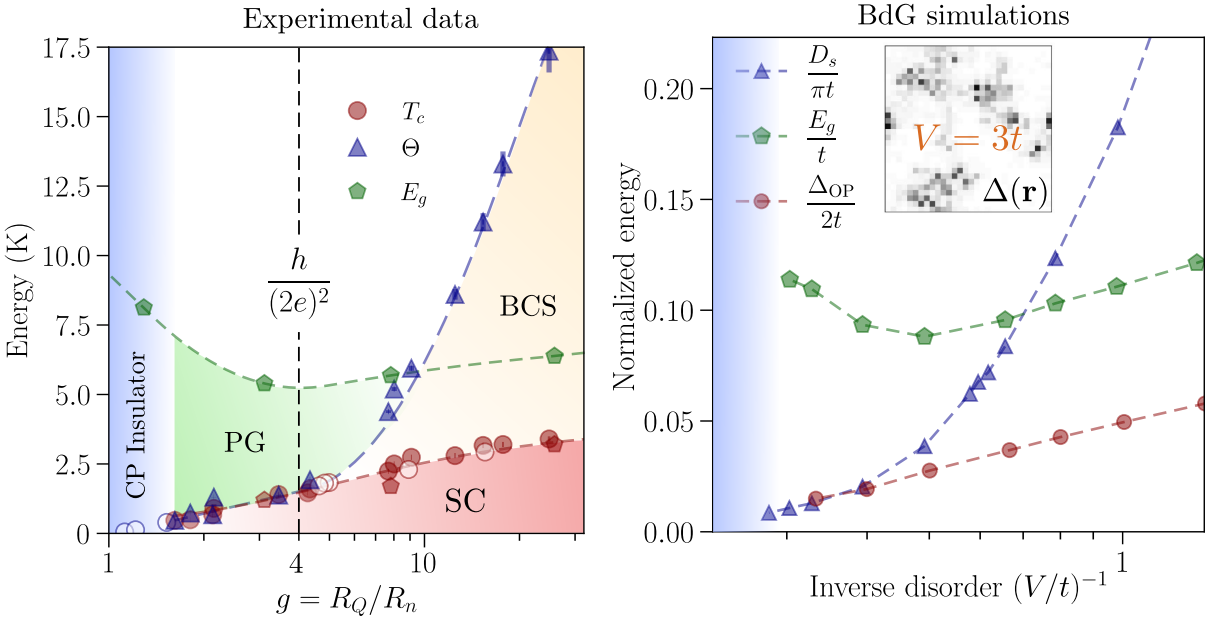

Fig. 5.5. a) Experimental phase diagram near the SIT in strongly disordered amorphous indium oxide. Both DC (T_c, g, E_g) and microwave (Θ) quantities are compared upon increase of disorder. E_g was measured by tunneling spectroscopy in [Benjamin Sacépé, Dubouchet, et al., 2011; Daniel Sherman, Gorshunov, et al., 2014] (E_g and the corresponding critical temperatures are represented by green and red pentagons respectively). When approaching the transition T_c and Θ coincide $T_c \sim \Theta$, evidencing the underlying bosonic mechanism. **b) Simulations of the attractive Bose-Hubbard model using the Bogoliubov-de Gennes approach.** The evolutions of E_g, superfluid stiffness $\Theta = D_s/\pi$ and critical temperature $2T_c = \Delta_{OP}$ are strikingly similar to experimental observations. Inset shows spatial inhomogeneity of the order parameter $\Delta(\mathbf{r})$ for strong disorder $V/t = 3$, near the SIT. Adapted from [Ghosal et al., 2001].

The superfluid stiffnesses obtained for indium oxide resonators are displayed in Fig. 5.5**a** (blue triangles) along with the related critical temperatures T_c (red dots).
Spectral gaps previously measured in indium oxide in the superconducting state [Benjamin

Sacépé, Dubouchet, et al., 2011] and in the insulating state [Daniel Sherman, Gorshunov, et al., 2014] are also added (green pentagons). This graph shows a comparison of the relevant energy scales for a disordered superconductor near the SIT, and as such we will refer to it as a phase diagram.

On the low disorder part of the diagram ($g \gg 1$) one observes the large value of Θ compared to the other energy scales. Indeed, for low disorder mean-field theories remain valid, and the role of phase fluctuations on superconductivity can be neglected. In this region the BCS proportionality between superconducting gap and T_c applies, as discussed in relation to Fig. 5.4.

Upon further increase of disorder the superfluid stiffness decreases below the gap: $\Theta < E_g$: the order parameter amplitude is increasingly inhomogeneous (as evidenced by STM measurements [B. Sacépé, C. Chapelier, et al., 2008] and numerical simulations, see section 2.2.2) and phase fluctuations become strong. The single particle gap E_g is enhanced by localization, while the critical temperature is suppressed. In this region the pseudo-gap (or *parity gap*) develops, and superconductivity becomes intertwined with Anderson localization. Around $g = 4$ (*i.e.* $R_n = h/(2e)^2$) the superfluid stiffness becomes remarkably small (a few K). Long-range order becomes controlled by the resilience of the superconducting condensate against fluctuations, *i.e.* by phase coherence.[3]
Thermal phase fluctuations destroy long-range order and lead to the relation (Emery et al., 1995):

$$T_c \sim \Theta(0) \tag{5.2}$$

Remarkably, Fig. 5.5**a** displays relation (5.2) between critical temperature and superfluid stiffness in a (relatively) large disorder range ($T_c \sim 2$ K down to $T_c = 0.4$ K). Stronger disorder drives the transition to the insulating state where both T_c and Θ are zero.

This relation is reminiscent of the Berezinskii-Kosterlitz-Thouless transition in the 2D XY model (see section 1.3). In this picture the transition temperature is ruled by the critical superfluid stiffness value at the BKT transition, while the phase stiffness itself is reduced upon increase of disorder. This results in the concomitant decrease of T_c and Θ with disorder as observed here.
The proportionality constant in Eq. (5.2) should be ≈ 0.89 for the 2D XY model, as demonstrated numerically [Olsson et al., 1991; Adler et al., 1993; Hsieh et al., 2013]. The universal BKT relation $T_c = (\pi/2)\Theta(T_c)$ is valid right at the critical temperature in the thermodynamic limit (infinite sample size), but becomes non-universal (and model-dependent) at low temperature.

Importance of phase fluctuations in superconductors with low superfluid density
Our observation of the relation $T_c \sim \Theta(0)$ for several samples of increasing disorder confirms the intuition that phase fluctuations rule superconductivity in nearly critical samples. As disorder increases the density of superconducting charge carriers n_s is reduced and, by the relation $\Theta \propto n_s$ presented in section 1.1, the resilience to phase fluctuations is suppressed. Therefore low superfluid density superconductors are expected to present the relation $T_c \sim \Theta(0)$ characteristic of a system ruled by classical phase fluctuations. This important result was discussed in [Emery et al., 1995] in relation to high-T_c superconductors.

[3] See the very thorough review article [Raychaudhuri et al., 2021] on phase fluctuations.

We now present a very simple (and naive) model to describe the evolution of T_c and $\Theta(0)$ with disorder g, incorporating both BCS theory (that should prevail at lowest disorder) and the BKT transition which dominates at strong disorder.

Evolution of T_c and $\Theta(0)$ with disorder We start by describing the evolution of Θ with disorder $1/g = R_n/R_Q$, using a simple BCS formalism (probably inaccurate for strongly disordered samples). The main point is to relate the effect of disorder (described by a measurable DC quantity such as the normal-state resistance) to the superfluid response of the superconductor.

The Mattis-Bardeen theory gives the evolution of the complex conductivity with frequency and temperature [Mattis et al., 1958]. In the limit of low frequency or high temperature ($\hbar\omega \ll k_B T$) one finds the estimation

$$\frac{\sigma_2}{\sigma_n} = \frac{\pi\Delta}{\hbar\omega}\tanh\left(\frac{\Delta}{2k_B T}\right) \tag{5.3}$$

where σ_n is the normal state conductivity given by Drude's formula.

Using the definition of kinetic inductance $L_K = (\sigma_2\omega)^{-1}$ and writing the 2D superfluid stiffness as $\Theta = (\hbar/(2e))^2 1/L_K^{\square}$ one rewrites last equation as

$$\Theta(T) = \frac{1}{8}\Delta g \tanh\left(\frac{\Delta}{2k_B T}\right) \tag{5.4}$$

We estimate (roughly) the evolution of the superconducting gap $\Delta(T)$ with temperature using a well-known interpolation formula[4] allowing us to model the suppression of $\Theta(T)$ by thermally-induced breaking of Cooper pairs. Neglecting in first approximation the dependence of Δ on disorder (we disregard the fermionic mechanism here) one sees that $\Theta(T) \propto g$ decreases upon increase of disorder.

Next we assume that the system possesses a BKT transition *i.e.* the real, measurable critical temperature T_c is given by the BKT relation $T_c = \beta\Theta(T_c)$, where $\beta = \pi/2$. Note that recent experiment in thin disordered NbN films demonstrates that, unlike some previous past observations of a broadened transition the BKT transition is in fact sharp and fits the usual RG model [Weitzel et al., 2023].
Setting $T = T_c$ in Eq. (5.4) and equating with the critical value of $\Theta(T_c)$ predicted by the BKT mechanism, one gets an equation that can be solved analytically to find the ratio $T_{c0}/T_c^{BKT}(g)$ as a function of g[5] as well as $\Theta(g)$ at zero temperature.
The result of this procedure is displayed in Fig. 5.6. Left plot illustrates the main features of the calculation: upon increase of temperature $\Theta(T)$ is suppressed by pair-breaking, and jumps

[4] The temperature evolution of Δ can be interpolated in the whole temperature range as

$$\Delta(T) \approx \Delta_0 \tanh\left(\frac{\pi}{2}\sqrt{\frac{T_{c0}}{T} - 1}\right) \tag{5.5}$$

with $\Delta_0 = \alpha k_B T_{c0}$ where $\alpha = 1.76$.

[5]

$$\frac{8}{\alpha\beta g} = X\tanh\left(\frac{\pi}{2}\sqrt{X-1}\right)\tanh\left[\frac{\alpha}{2}X\tanh\left(\frac{\pi}{2}\sqrt{X-1}\right)\right] \tag{5.6}$$

in which we have introduced the ratio of critical temperatures $X = T_{c0}/T_c$.

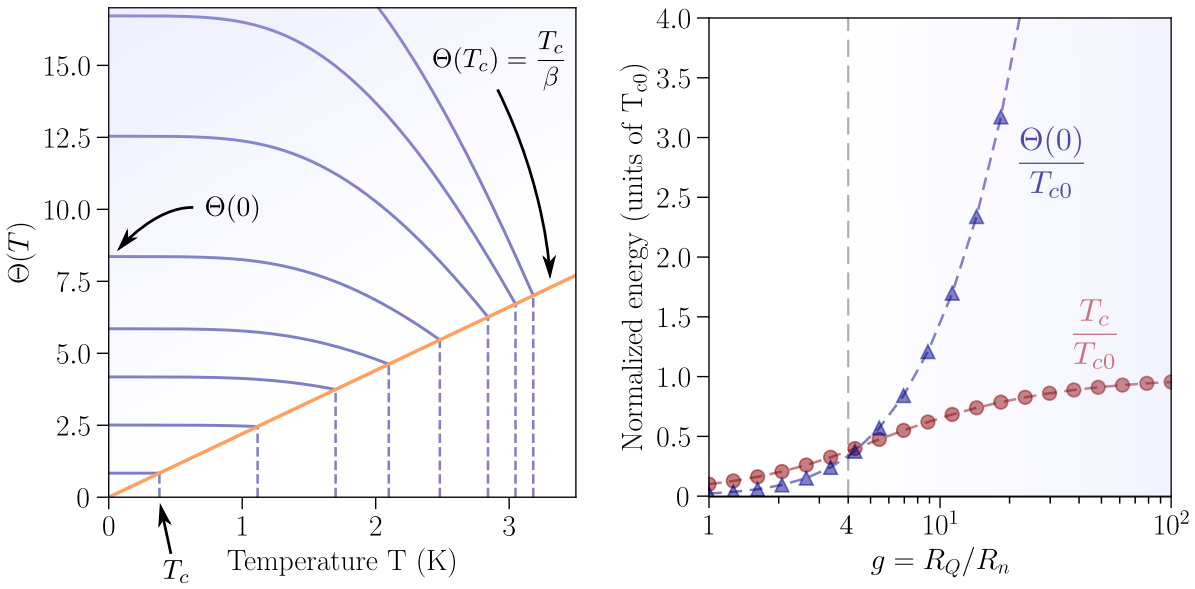

Fig. 5.6. Suppression of critical temperature with normal-state conductance via the BKT mechanism. Left: Result of the numerical solving of Eq. (5.6). Orange line is the BKT relation $\Theta(T_c) = T_c/\beta$. The superfluid stiffness decreases with temperature as the number of quasiparticles increases following the Mattis-Bardeen formula (this is the main difference with Fig. 1.2). At $T = T_c$ where the BKT jump of Θ occurs, superconductivity is suppressed abruptly. As disorder is increased (g decreased) the value of $\Theta(T_c)$ at the BKT transition gets closer to the zero-T value $\Theta(0)$. Eventually, for sufficiently strong disorder $T_c \sim \beta\Theta(0)$. **Right:** Resulting T_c and $\Theta(0)$ (in units of the mean-field critical temperature T_{c0}) versus normal-state conductance. Upon decrease of g both energy scales are reduced, and below $g = 4$ the critical temperature is ruled by phase fluctuations as can be seen from the proportionality $T_c \propto \Theta(0)$.

to zero at T_c because of the sudden proliferation of vortices breaking the quasi-long-range order. By increasing disorder, $\Theta(0)$ decreases and so does $\Theta(T_c) = (1/\beta)T_c$. Notice that low-$T$ and high-T values of Θ can be significantly different for small disorders ($g \gg 1$). It is only for strong disorders that $\Theta(0) \sim \Theta(T_c) \sim T_c$. The evolution of Θ and T_c with g is shown on the right panel and confirms this qualitative argument.
Upon increase of normal-state resistance the superfluid stiffness is reduced, in turn suppressing the critical temperature through the BKT mechanism.

It can be noted from Fig. 5.5**a** that the regime of phase-dominated superconducting transition takes place for normal-state resistances above the resistance quantum for Cooper pairs $h/(2e)^2$ (or $g = 4$).
Perhaps accidentally, this feature was already seen in the simple BKT model described above (see Fig. 5.6) where the critical conductance value $g = 4$ can be associated to the region where the spacing between mean-field and BKT transition temperatures becomes of the order of T_c itself. In this region only the BKT temperature describes superconductivity, irrespective of the *pairing* temperature (related to the gap).
One might also note that the resistance $R_c = h/(2e)^2$ is expected to delimitate the transition between superconducting and Bose glass insulator in the bosonic scenario of 2D superconductors discussed in section 1.4.

This simple and inaccurate [6] estimation has the merit of showing the transition between the mean-field, BCS region where phase fluctuations can be safely neglected ($T_c \sim T_{c0} \ll \Theta(0)$ for $g \gg 1$) and the highly disordered state where superconductivity is ruled by phase fluctuations.

Numerical simulations of a pseudogaped superconductor Interestingly the same qualitative results can be found by numerical simulations of an Anderson insulator with added attractive electron-electron interaction, as discussed in section 2.2.2. A compilation of the results of [Ghosal et al., 2001] is shown in Fig. 5.5**b**, displaying the decrease of critical temperature and superfluid stiffness and the uncorrelated increase of single particle gap. We have here used the (unproven) relation $\Delta_{\mathrm{OP}} = 2T_c$ to estimate the critical temperaature from the gap simulations of the author's work. One finds a striking resemblance with our experimental results.
Note that the work of [Ghosal et al., 2001] did not incorporate effects of quantum phase fluctuations to the simulation, but merely the (important) effect of disorder-induced gap spatial inhomogeneities. In this picture the microscopic origin of strong phase fluctuations seen by a disordered sample is the broad dispersion of gap amplitudes over the sample size. The latter effect is a direct consequence of Anderson localization of single electrons.

Universal bosonic scenario in low carrier density materials It was suggested that superconductors with low carrier density would be more likely to be ruled by phase fluctuations [Emery et al., 1995]. Interestingly, this observation is independent on the microscopic composition of such materials, and even on the very mechanism responsible for superconductivity. It follows that superconductors as diverse in composition as homogeneous, granular, heterostructures, layered cuprates or twisted bilayer graphene could behave similarly at low enough carrier density.

The phase-driven scenario has already been reported in a wide range of superconductors (see for example [Chand et al., 2012; Pracht, Bachar, et al., 2016; G. Singh et al., 2018]) but a careful look at the available data suggests that, in most cases, the onset of phase-dominated superconductivity coincides with the critical regime leading to the transition to an insulating (or metallic) state. By that is meant that, once $T_c \sim \Theta$ is reached, the superconducting state vanishes (see Fig. 5.7). In comparison our indium oxide data shows a (relatively) large disorder range where phase fluctuations dominate the superconducting state, in contrast to other experimental findings.

Fig. 5.7 shows a collection of superfluid stiffnesses and their related critical temperatures for structurally different superconductors found in the literature, as well as the critical line $\Theta = T_c$ (dashed black). a:InO samples (red markers) are the result of the present work.
It is found that these materials present a superconducting state governed by phase fluctuations when close enough to criticality, as demonstrated by the proximity to the line $\Theta = T_c$ (dashed black line of Fig. 5.7). This behavior holds for very diverse microscopic structures, ranging to intrinsically granular to homogeneous disorders, as well as 2D heterostructures and high-T_c superconductors. As the data reaches the $\Theta = T_c$ line the superconducting state breaks down. Indium oxide on the other hand presents data points lying on this critical line.

[6] Most equations that were used here are derived from perturbation theory, and therefore are not expected to be exact for strong fluctuations and nearly-critical disorder. We also abusively neglected amplitude fluctuations of the order parameter and possible effects of localization. This estimate must therefore be understood as a qualitative illustration of the physics at play.

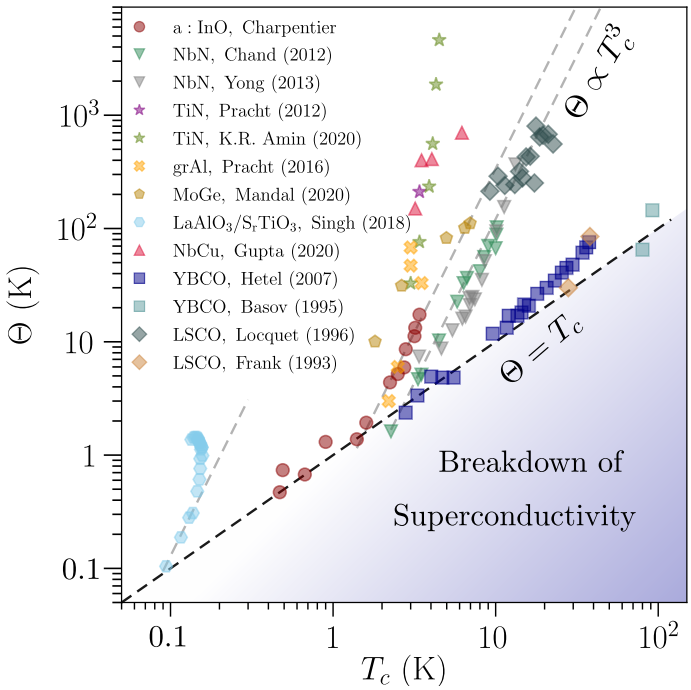

Fig. 5.7. Uemura plot Superfluid stiffness Θ versus critical temperature T_c for various superconductors of different microscopic compositions (amorphous, granular, heterostructures, high-T_c cuprates). Indium oxide samples studied in this work are represented by red circles. Black dashed line shows the phase boundary $\Theta = T_c$ indicating bosonic behavior. Dashed grey lines show the scaling $\Theta \propto T_c^3$.

The main point of this graph is the observation that in most cases, phase fluctuations are responsible for the quantum breakdown of the superconducting state irrespective of the material's chemical composition. As long as superconducting charge carrier density is low one should expect the suppression of long-range order to be the result of the jointed effects of both pair-breaking (fermionic scenario, dominant far from SIT), phase fluctuations (most effective near the SIT), and Coulomb repulsion, as suggested by the most recent theoretical advances [Benjamin Sacépé, Mikhail Feigel'man, et al., 2020].

One can also observe that some of the data presented here has the approximate scaling $\Theta \propto T_c^3$ when approaching criticality, displayed by dashed grey lines.
A possible interpretation of this fact implies the fractal nature of electronic wavefunctions in pseudo-gapped superconductors [M.V. Feigel'man et al., 2010]. In this framework it has been shown [M. V. Feigel'man and Ioffe, 2015] that the superfluid stiffness could follow a non-trivial dependence with the collective gap in the pseudo-gapped phase $\Theta \propto \Delta^a$.
Recent developments suggest that the exponent a could be of the order of 3 [M. Feigel'man, private communications]. Making the assumption $\Delta \propto T_c$, which is hard to justify close to the transition but should be correct at low enough disorder leads $\Theta \propto T_c^3$.

5.2 | Suppression of superconductivity at finite temperature driven by phase fluctuations

The measurements presented above concerned very low temperatures $T \approx 20$ mK. For standard superconductors an increase of temperature has the only effect of gradually closing the superconducting gap Δ above which single-particle excitations can exist and generate

dissipation. Superconductivity is exponentially suppressed as $\delta\Theta \propto \exp\left(-\Delta/k_B T\right)$.
In a pseudogapped superconductor like indium oxide however things are less clear: the pseudogap remains large even when leaving the superconducting state. Therefore single-particle excitations (related to pair-breaking effects) are most likely not the dominant factor of suppression in the superfluid.
We now discuss the unusual temperature dependence of superfluid density in indium oxide films.

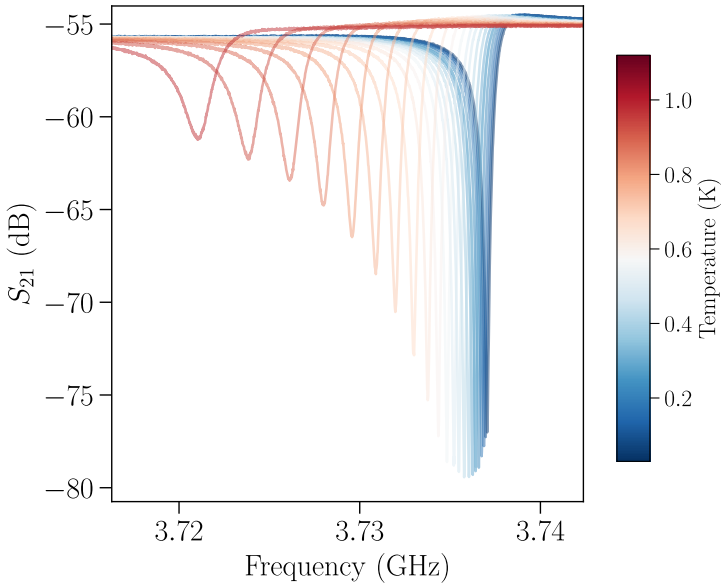

Fig. 5.8. Evolution of plasmon frequency with temperature. Single-tone spectroscopy of a weakly disordered indium oxide wire at various temperatures. Increase of sample temperature reduces the resonance frequency.

Fig. 5.8 displays the effect of an increase of temperature on a given resonator mode measured in transmission. The frequency (measured at the transmission minimum) decreases with temperature, evidencing the increase of kinetic inductance when heating the sample.

The superfluid density (or superfluid stiffness) at various temperatures can easily be accessed via the measurement of a mode frequency since $f(T) \propto \sqrt{\Theta(T)}$.
We then define the relative frequency shift as $\delta f(T)/f = \left(f(T) - f(T_{\min})\right)/f(T_{\min})$, where $T_{\min}$ is the cryostat base temperature (usually ~ 20 mK).
By proceeding to temperature sweeps for samples of distinct disorders one is able to compare the evolution of relative frequency shift with disorder, as displayed in Fig. 5.9**a**.

We show that the data can be fitted by the power-law formula

$$\frac{\delta f(T)}{f} \approx -\left(\frac{T}{T_1}\right)^{\alpha} \tag{5.7}$$

where T_1 and α are fitting parameters.

The power law exponent α is found to be comprised between 1.6 and 2.2 in this frequency range. The power law fit is valid at lowest temperatures only, as the pair-breaking mechanism

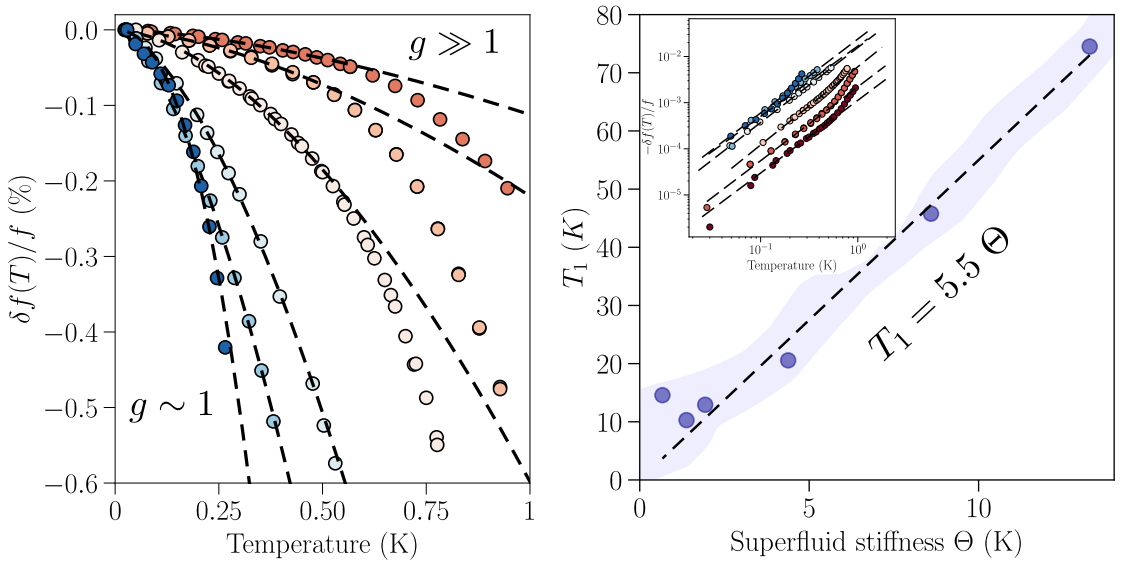

Fig. 5.9. Suppression of superfluid density with temperature a) Frequency shift versus temperature for several samples. Instead of the BCS activated reduction of the gap with thermal energy, one observes a power low at lowest temperatures. Black dashed line is a fit following $\delta f(T)/f = -(T/T_1)^{\alpha}$. **a)** Evolution of the fit parameter T_1 with superfluid density Θ. Inset shows the frequency shift in log-log scale, evidencing the power behavior at lowest T. Black dashed line shows $T_1 \sim 5.5\ \Theta$, another demonstration of the influence of phase fluctuations on superconductivity.

comes into play at higher temperatures, further reducing the mode frequency through the standard Mattis-Bardeen theory.
It can be shown (see Appendix) that substracting the pair-breaking model (with the appropriate superconducting gap Δ) to our data reveals a power law in the whole temperature range, confirming that both mechanisms (pair-breaking and phase fluctuations) contribute in parallel to the suppression of superfluidity.

The low-T power law displayed above cannot be explained by thermal breaking of Cooper pairs: at these low temperatures thermal energy $k_B T$ is much smaller than the gap Δ which should result in a mostly constant frequency. Here suppression of superconductivity finds its source in phase fluctuations.
This can be seen from Fig. 5.9**b**, where it is demonstrated that $T_1 \propto \Theta$, that is the frequency shift amplitude is related to the energy scale of phase fluctuations.
At finite temperatures phase fluctuations of the order parameter rule superfluidity.

5.2.1 Excitation of thermal plasmons

The mechanism leading to a phase-driven frequency shift taking the form of a power-law was sketched in section 3.4.4, where we showed that $T_1 \propto \Theta^{3/4}$ and the exponent $\alpha = 2$.
While this exponent is rather close to the one found experimentally (~ 1.6) the prefactor is off by orders of magnitude.

Indeed this simple model predicts T_1 of the form[7]

$$T_1 \sim \frac{1}{\xi}\sqrt{\hbar\omega_0\Theta(0)Lw} \tag{5.8}$$

where ξ, L and w are the dirty limit coherence length, resonator length and width respectively, and ω_0, $\Theta(0)$ are the zero temperature frequency and superfluid stiffness.
Taking reasonable values corresponding to our samples gives an estimation of $T_1 \sim 5000$ K, while experimentally T_1 is closer to $1 - 100$ K.

From this we conclude that the anomalous suppression of superconductivity at low temperatures is indeed related to classical phase fluctuations, in contrast to the usual BCS mechanism, but that a simple model accounting for one-dimensional plasmon excitations alone is not sufficient to reproduce the data.
It seems natural to consider other type of excitations below the gap, related to much shorter lengthscales.

5.2.2 Suppression by low-lying modes in pseudogap superconductors

Further study of the Hamiltonian Eq. (2.14) for pseudogapped superconductors leads to the observation that below a moderately large disorder short-scale bosonic collective modes appear under the gap [M. V. Feigel'man and Ioffe, 2018]. These low-energy and short-scale modes originate from the hopping of localized Cooper pairs.
New results from [A. Khvalyuk et al., 2023] suggest that these collective modes could also be responsible for the anomalous decrease of superconductivity upon increase of temperature.

This work discusses the consequences of strong spatial gap fluctuations in strongly disordered films on the superfluid density. When the superconducting gap distribution becomes broad, with regions where local pairing vanishes, it is shown that thermal agitation excites low-energy, short-scale modes, and produces a frequency shift resembling a power-law with exponent from 1.6 to 3 and $T_1 \sim T_c$, which matches our observations:

$$\frac{\delta\Theta}{\Theta}(T) \approx \left(\frac{T}{T_1}\right)^b \tag{5.9}$$

The related value of T_1 is estimated to be of the order of T_c, much closer to our data. Details on the actual value of T_1 remain to be clarified still.
In any case this work suggests that the frequency shift observed in the present thesis comes from low-energy collective excitation of the superconductor, and it turn implies the presence of a new channel of dissipation in inhomogeneous superconductors caused by sub-gap excitations that are not quasiparticles.

5.2.3 Suppression of low-temperature quality factor with disorder

From the arguments above we expect an increase of dissipation at microwave frequency in the pseudogap regime [M. V. Feigel'man and Ioffe, 2018], with a gradual suppression of internal quality factor as disorder is increased.
Fig. 5.10 shows the evolution of quality factor measured in the $2 - 5$ GHz range at low temperature ~ 20 mK for samples of varied disorder (the same samples from which we measured T_c and $\Theta(0)$). The input power is relatively low for each sample, but is definitely

[7] Note that by writing $\omega_0 \propto \sqrt{\Theta(0)}$ one retrieves $T_1 \propto \Theta(0)^{3/4}$ as stated above.

above the few photons limit and varies from one sample to the other. Also, as Q_i varies strongly with temperature, power, frequency and aging (this will be discussed in a later chapter) a strict comparison between the values shown in Fig. 5.10 must be made with caution.
Still, one can see a clear trend at large disorder ($g \leq 4$) corresponding to the pseudogap phase: Q_i is strongly reduced and seemingly weakly disorder-dependent. It vanishes abruptly at the transition with the insulator.

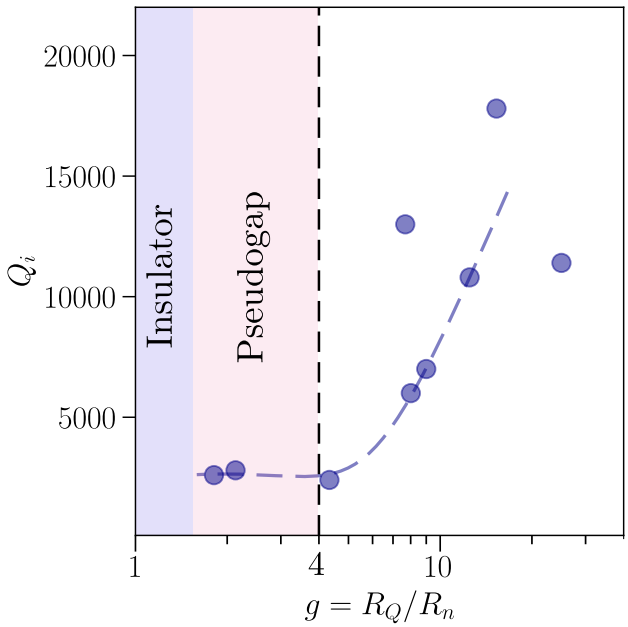

Fig. 5.10. Internal quality factor versus disorder. Quality factors are extracted from the transmission measurements at low temperature (~ 20 mK) and relatively low power. These measurements are obtained at different frequencies and powers (for technical reasons) and therefore only give a qualitative trend of the suppression of Q_i with disorder. Dashed line is only a guide for the eyes.

Conclusion

In this chapter we have shown how the tools of cQED could be used to study the superconducting side of the SIT in amorphous indium oxide.
We demonstrated that disorder induces a superconducting state ruled by phase fluctuations of the order parameter, consistent with the picture of a pseudogap of preformed Cooper pairs.

This important fact was strongly suggested by the numerous transport measurements available in the literature, which concluded that a gap in the single particle density of states remained in the non-superconducting phase. The resulting preformation of Cooper pairs was a clear indication of the survival of local pairing, while superconductivity was destroyed. This lead to believe that phase fluctuations were the main mechanism suppressing superconductivity, but clear experimental evidence was still required to conclude on the matter.

Table 5.1
Results on amorphous indium oxide resonators of increased disorder for transport and microwave measurements. (B) means measured in Bluefors at low frequency. (3D) corresponds to the a resonator measured in a 3D waveguide, as discussed in chapter 7.

Sample	w (μm)	L (mm)	T_c (K)	R_n (k$\Omega/\square$)	g	L_K (nH/$\square$)	Θ (K)
TC002 run 3	1	3.505	3.46	?	?	0.450	17.43
TC002 run 2	1	3.505	3.4	1.04	24.82	0.452	17.35
TC002 run 1	1	3.505	3.2	1.456	17.72	0.59	13.29
TC014	1	2.5	3.16	1.683	15.3	0.70	11.2
TC022	0.1	0.3	2.93	1.66	15.54	0.96	8.17
TC003	1	3.5?	2.8	2.06	12.49	0.91	8.6
TC040 (3D)	1	2	2.74	2.84	9.0	1.32	5.94
TC018	0.1	0.3	2.3	2.9	8.9	1	7.8
TC007 run 3 (B)	1	3.505	2.5	3.22	8.01	1.51	5.2
TC001	1	3.505	2.24	3.36	7.68	1.79	4.38
TC024 run 3	0.1	0.3	1.83	5.17	4.98	?	?
TC024 run 1	0.1	0.3	1.81	5.35	4.82	1.9	4.12
TC024 run 2	0.1	0.3	1.71	5.67	4.63	?	?
TC007 run 2	1	3.505	1.6	5.95	4.33	4.06	1.93
TC015	1	?	1.46	6.05	4.26	?	?
TC007 run 1	1	3.505	1.4	7.47	3.45	5.68	1.38
TC017 (B)	1	3.505	0.9	12	2.34	6.0	1.3
TC016 run 8	1	1.718	0.67	12.1	2.13	11.64	0.67
TC017	1	3.505	0.49	14.25	1.81	10.65	0.73
TC016 run 6	1	1.718	0.47	15.95	1.61	16.68	0.47

The experiment displayed in this chapter provides such a clear-cut conclusion, based on the combination of DC and microwave data. Our measurements were carried out both at nearly zero and at finite temperatures, using two different experimental techniques, and found consistent results.

On a more applicative side we demonstrated the large values of kinetic inductance achievable in this material, opening interesting opportunities for integration to superconducting quantum circuits, as will be discussed later.

CHAPTER 6

Nature of the QBS: First-order quantum phase transition

We have shown in the last two chapters that superconductivity was ruled by phase fluctuations of the order parameter in disordered indium oxide. This strongly suggests that, at zero temperature, the quantum phase transition between superconductor and insulator is also related to quantum phase fluctuations: boson-like electron pairs remain bound but loose their phase coherence in the insulating state.

One question remains, still; what is the nature of the SIT in amorphous indium oxide ? Does the order parameter go continuously to zero, as is commonly assumed ?

Based on the data presented in this thesis we argue that amorphous indium oxide could undergo a first-order transition, as evidenced by an abrupt suppression of both critical temperature and superfluid stiffness at a critical disorder.

6.1 | Abrupt suppression of superconductivity

6.1.1 Critical jump of transition temperature

Fig. 6.1 reminds the observation already discussed in chapter 4 regarding the SIT seen from transport measurements.
It is found that the suppression of critical temperature T_c is not continuous: at a critical conductance g_c the transition temperature drops from a finite value down to zero abruptly. At larger disorders the films become insulating (the resistance diverges at low temperature and T_c cannot be defined), with a peculiar re-entrant resistivity (see chapter 4 for a discussion).
The value of critical disorder g_c is seen to be size-dependent, as our two sample geometries display quite different phase transitions. The larger wires show a complete suppression of T_c at $g \sim 1.6$, while the narrow wires display an earlier SIT at $g \sim 4$.
In both case the suppression of T_c is sudden and seems discontinuous.

In addition, a previous experimental study of the SIT in a:InO [Shahar et al., 1992] seems to display such a non-vanishing T_c at the transition, where it is clear that the insulating behavior takes over at a finite value $T_c \sim 1.6$ K (see Fig. 4.6**c**).

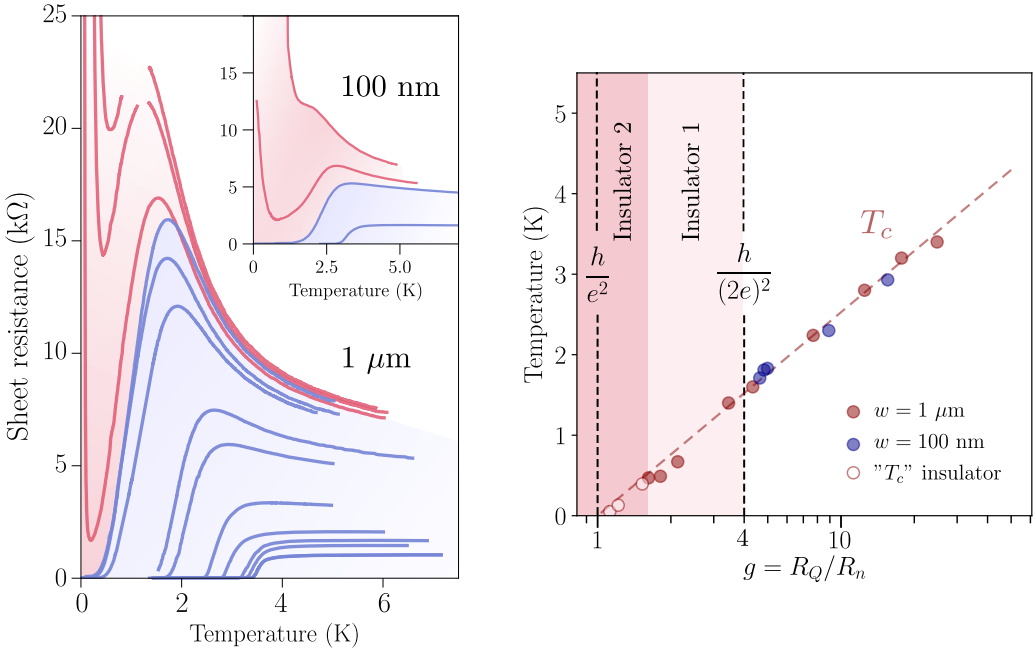

Fig. 6.1. Discontinuous suppression of critical temperature. Left: DC measurements on two indium oxide wire geometries demonstrate the abrupt change from a superconductor (finite T_c) to a re-entrant insulator (zero T_c). The maximum normal-state resistance and the minimum T_c achieved depend on system size. **Right:** Drop of critical temperature with normal-state conductance. At a critical conductance value T_c switches from a finite value to zero. This critical conductance is larger for the narrow wires.

6.1.2 Superfluid jump from the microwave measurements

Turning now to the SIT measured at microwave frequencies, we note that the superfluid stiffness Θ extracted from the kinetic inductance measurements vanishes at the same critical conductance g_c than the one observed in transport.

Fig. 6.2 displays a zoom on the phase diagram presented in previous chapters close to the SIT, where it is seen that the superfluid stiffness Θ and critical temperature T_c remain large ≈ 0.5 K at the transition.
At a critical conductance g_c these quantities drop to 0 abruptly, marking the direct transition to the insulating state where both critical temperature and superfluid stiffness are suppressed **concomitantly**.
Once again the SIT is seen to depend on the wire width w. Note that DC measurements were performed on wires 300 times shorter than the microwave resonator on the same chip, but the SIT of resonators and transport measurements coincide. Samples of smaller width w however display a different SIT.

Our indium oxide resonators and DC lines experience a sharp suppression of superconductivity at a given critical disorder strength.
We shall now examine this statement in light of available theoretical models.

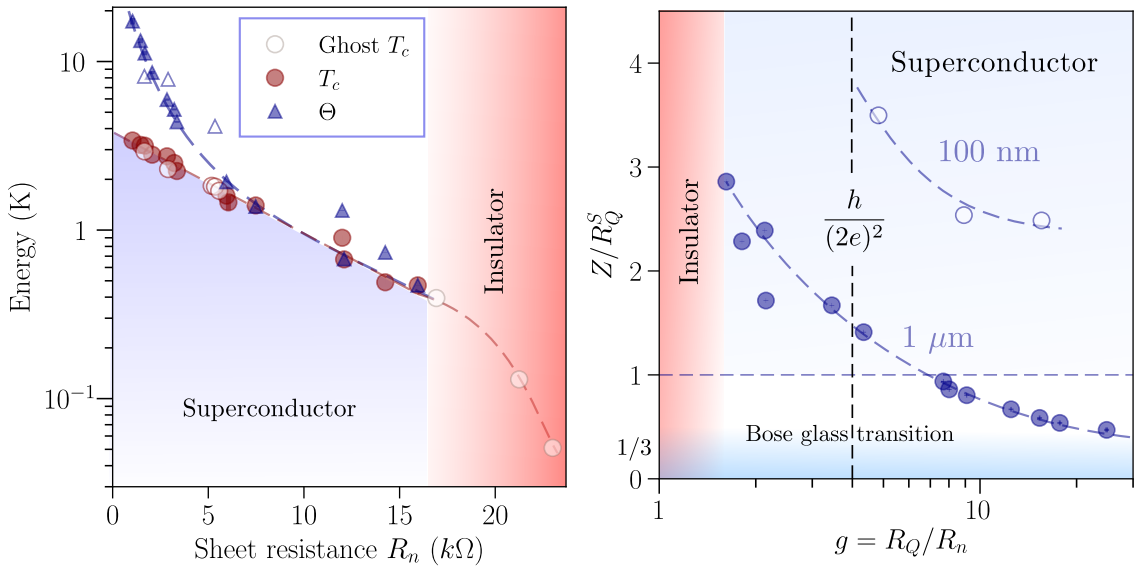

Fig. 6.2. Superfluid jump at the SIT a) Zoom of the phase diagram close to the SIT. Both microwave (superfluid stiffness) and DC (critical temperature) quantities remain finite and relatively large ≈ 0.5 K at the transition to insulation. Hollow grey circles in the insulator are ghost T_c extracted from the re-entrant insulators. **b)** Wave impedance $Z = \sqrt{L_K/(wC)}$ normalized by the superconducting resistance quantum $R_Q^S = h/(2e)^2$. 1 μm-wide resonators are represented by full blue circles, 100 nm-wide strips are empty circles. Phase coherence in narrow wires is suppressed at $R_Q^S = h/(2e)^2$. According to the (1+1)D BKT theory discussed in text, the blue region for $Z/R_Q^S < 1/3$ would be superconducting, while the region above $Z/R_Q^S > 1/3$ would be a Bose glass insulator. Resonators having a wave impedance larger than the quantum of resistance ($Z > R_Q^S$, shaded blue area on the graph) are referred to as *superinductors*.

6.2 | On sample dimensionality

Before turning to a discussion on the nature of the SIT in our indium oxide films it is relevant to remind the reader about the effective dimensionality of our samples. Indeed dimension depends rather strongly in the considered physical mechanism, as we see now.

Localization First, it is useful to determine the sample dimension with respect to disorder and localization. This is usually done by comparing the film thickness d to the coherence length ξ: a thick sample with $d > \xi$ is three-dimensional in that sense (superconducting correlations can vary within the film thickness).
In most of our samples the coherence length $\xi \sim 5$ nm $< d$ for a thickness $d = 40$ nm, making them 3D w.r.t disorder. [1]

[1] One can also define an effective dimension with respect to inelastic processes: a film of thickness d is three-dimensional if the phase-coherence length $L_\varphi = aT^{-p/2} < d$, and two-dimensional otherwise. Therefore upon cooling down this effective dimension might cross over from 3D to 2D as L_φ diverges.
Additional factors such as interactions between electrons may have a different effective dimension: for instance a sample is three-dimensional with respect to Coulomb interactions if the thermal length is smaller than the film thickness: $L_T = \sqrt{\hbar D/k_B T} \leq d$ [P. A. Lee et al., 1985].

Phase fluctuations Turning now to fluctuations of the superconducting phase, one must distinguish between quantum fluctuations, which originate from charge localization at the microscopic scale, and thermal ones.

Thermal phase fluctuations are related to vortices and the BKT transition in the 2D XY model. The relevant energy scale in this case is the vortex core energy $\mu \propto \Theta(0)$. The latter can be seen as the loss in condensation energy within a *normal* vortex core: for superconductors with small superfluid density vortices require less energy [Mondal, Kumar, et al., 2011].
We have shown that in our films the 2D superfluid stiffness can attain values of the order of a few Kelvin, comparable to T_c, making the BKT mechanism relevant for our films despite the fact that the thickness exceeds the coherence length.

In addition, a typical lengthscale of a thin superconducting film is a two-dimensional penetration depth, the *Pearl length* defined as $\Lambda = \dfrac{\lambda^2}{d}$ where λ is the London penetration depth and d the film thickness [Pearl, 1964]. The interaction between vortices in a thin film involves stray fields outside the superconductor, and are related to the lengthscale Λ.
If Λ exceeds the typical size of the sample L_0 a standard BKT transition rules superconductivity in the entire sample.

Now, the Pearl length can be related to the kinetic inductance as $L_K^{\square} = \mu_0 \frac{\lambda^2}{d} = \mu_0 \Lambda$.
In terms of the superfluid stiffness one can write $\Lambda = \left(\dfrac{\hbar}{2e}\right)^2 \dfrac{1}{\mu_0 \Theta}$. For our samples of width $w = 1\ \mu\mathrm{m}$ and length $L_0 = 3505\ \mu\mathrm{m}$, one sees that the condition $\Lambda > L_0$ corresponds to $\Theta < 1.78\ \mathrm{K}$, or in terms of dimensionless conductance $g \leq 5$.
From the experimental phase diagram of Fig. 5.5 one sees that these last two conditions are met when T_c and Θ become equal.

Plasmons Plasmons are collective excitations of Cooper pairs mediated by Coulomb interactions. In the geometry studied here (long and narrow superconducting wires) these excitations are mostly one-dimensional.
This can be seen by comparing the Pearl length to the wire width: having $\Lambda \gg w$ means that current is uniform over the wire cross-section. It is easy to see that sufficiently disordered films display $\Lambda \gg w$. In fact even low-disorder indium oxide films fulfill this condition: for $L_K^{\square} = 0.01\ \mathrm{nH}/\square$ the penetration depth is $\Lambda \approx 8\ \mu\mathrm{m} > w$.

In this regard long-wavelength plasmons studied in this thesis can be considered as one-dimensional, putting our system into the range of validity of the 1D Luttinger liquid model. We now discuss theoretically how such one-dimensional system can break down with disorder.

6.3 | Quantum phase transition by pinning of plasmons

There are not many available theories predicting a jump of superfluid density. One well known mechanism however comes to mind; a BKT transition (as discussed previously at temperatures close to T_c) could also apply at zero temperature and lead to a superfluid jump. This quantum BKT transition will be discussed now.

In section 3.1 we introduced plasmon excitations of a superconductor as the collective motion of Cooper pairs interacting through Coulomb repulsion in a one-dimensional system.[2] Low-energy density fluctuations in a 1D boson gas with short-range interactions[3] can be described by the Luttinger model [Haldane, 1981]

$$\mathcal{H} = \int dx \left(\frac{\pi v K}{2\hbar} \Pi^2 + \frac{\hbar v}{2\pi K} \left(\partial_x \theta\right)^2 \right) \tag{6.1}$$

where v is the velocity of sound-like plasma modes with dispersion $\omega(k) \approx v|k|$, as detailed in section 3.2.2 (neglecting long-range interactions here). From the superconducting phase φ one can define the operator $\Pi = -(\hbar/\pi)\partial_x \varphi$ and a canonically conjugate field θ with commutation relation $\left[\theta(x), \Pi(x')\right] = -i\hbar\delta\left(x - x'\right)$. The Cooper pair charge density is $\rho(x) = -(1/\pi)\partial_x \theta$.

Hamiltonian Eq. (6.1) describes a harmonic string, where the first term stands for the condensate kinetic energy (related to the superfluid stiffness Θ) and the second term the Coulomb interaction between charges (given by the charging energy $E_c = 4e^2/(2C_g)$ where C_g is the capacitance to ground).

The Luttinger parameter K is related to kinetic and charging energies as

$$K = \pi \sqrt{\frac{\Theta}{2E_c}} = \frac{R_Q^S}{2Z} \tag{6.2}$$

where last equality follows from the definition of the *wave impedance* $Z = \sqrt{L_K/C_g}$ where L_K and C_g are the inductance and capacitance per square respectively. The resistance quantum for Cooper pairs is noted $R_Q^S = h/(2e)^2$.
K is linked to the zero-point fluctuations of the charge density, and describes a quantum system of bosonic particles with Coulomb interactions *i.e.* the plasmons.
Note that Eq. (6.1) is quite general and the set (v, K) characterizes the low-energy properties of *any* (massless) one-dimensional system.

6.3.1 Localized-delocalized phase transition in presence of disorder

Adding disorder to the above system breaks translational invariance: the localizing effects of disorder perturb the charge distribution along the wire and one might expect some qualitative change in the plasmon behavior.

Disorder is taken into account by adding a second term to the Hamiltonian of Eq. (6.1), with a random potential V produced by impurities:

$$H_r = \int dx\, V(x)\rho(x) \propto \int dx\, \cos\left(2\theta(x)\right) \tag{6.3}$$

Disorder acts on the interacting electron system by pinning the charge density $\rho(x)$ on defects *i.e.* localize charges (see Fig. 6.3). By Heisenberg uncertainty this implies large local fluctuations of the phase that fight pinning and prevent phase and charge to have too well-defined values near the defects. Quantum phase fluctuations (described by the Π^2 term in Eq. (6.1))

[2] This chapter is partly inspired by the book on one-dimensional quantum systems [Thierry Giamarchi, 2003].

[3] By considering short-range interactions the velocity k remains frequency independent. Long-range Coulomb interactions must sometimes be taken into account as was already discussed in section 3.2.2, and the Luttinger liquid model is slightly modified (see [Thierry Giamarchi, 2003] page 100).

are controlled by the value of the Luttinger parameter K: the magnitude of quantum phase fluctuations increases with K.

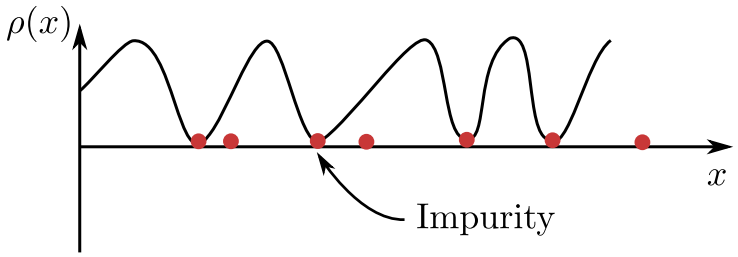

Fig. 6.3. Pinning of Cooper pair charge density by disorder in 1D. The cosine charge density is deformed by the presence of impurities that pin Cooper pairs at random sites.

The one-dimensional system of interacting bosons in a random potential described here is therefore characterized by the competition of disorder-induced pinning of charges, and quantum phase fluctuations that tend to oppose localization.
The superconducting phase along the wire must deform under the random potential induced by disorder, which has an energy cost. The kinetic energy the system has to pay is an *elastic* energy described by phase fluctuations (see section 1.1 where we discussed phase stiffness).

It is then natural to define the length scale below which such deformations of the phase can be neglected: for systems of size $L < \xi_{\rm loc}$ the superconducting phase remains unaffected by disorder.[4] It can be shown that this length, that shares strong similarities with the localization length in the Anderson problem, scales differently with disorder depending on the value of the parameter K[5]: at a critical value K_c one observes a quantum phase transition from a localized, insulating phase (called *Bose glass*), to a delocalized, superfluid of bosons.

[T. Giamarchi et al., 1988] used the renormalization group approach to show that such a transition occurs at the universal critical value $K_c = 3/2$. For $K > 3/2$ disorder does not significantly affect the collective modes (phase fluctuations efficiently fight off localization and $\xi_{\rm loc}$ remains large), while for $K < 3/2$ pinning takes over and leads to a localized, insulating phase at zero frequency (the *static* phase varies strongly over the vanishingly small scale $\xi_{\rm loc}$).

The existence of a characteristic lengthscale given by the Larkin length can be related to a characteristic frequency $\omega_{\rm loc} = v/\xi_{\rm loc}$ where v is the plasmon velocity [Houzet et al., 2019]. Modes with frequency ω exceeding this new characteristic frequency are delocalized (they are related to lengthscales $< \xi_{\rm loc}$), while low frequency modes with $\omega \ll \omega_{\rm loc}$ are pinned by disorder.

[4] $\xi_{\rm loc}$ is sometimes called the *Larkin length*, as first introduced as a quantity related to pinning of vortices by Larkin.

[5] For $K < 3/2$ (the localized phase) one has $\xi_{\rm loc} \propto \left(\frac{1}{D}\right)^{\frac{1}{3-2K}}$ where D is the disorder strength. It diverges as $K \to 3/2$.

6.3.2 (1 + 1)D Berezinskii-Kosterlitz-Thouless transition and quantum phase slips

The pinning of a Luttinger liquid by disorder (discussed above) can be seen as the proliferation of quantum phase slips, as we see now.

It is well known that the one-dimensional Luttinger liquid can be mapped to a classical system of $1+1$ dimension. To operate this mapping between a quantum system in dimension d to a classical system in dimension $d+1$ one considers the extra dimension as an imaginary time direction.[6]
Doing so allows to apply the results of 2D classical statistical physics to a 1D quantum system. For instance topological defects of the classical 2D XY model are vortices (see section 1.3), characterized by a winding of the phase field by 2π around their core in space. Vortices bind in pairs with logarithmic in distance interactions, and unbind at the transition temperature T_c where BKT transition occurs.

In a quantum 1D system the equivalent object is a Quantum Phase Slip, with simultaneous suppression of the order parameter during a short time τ_0 and winding of the phase $\varphi \to \varphi + 2\pi$. QPSs can then be seen as vortices in a $(1+1)$-dimensional space-time, bound in pairs in the ordered (delocalized) phase with interaction $\propto \ln d(x,\tau)$ in space-time [Zaikin et al., 1997]. Pushing the analogy further, this system experiences a $(1+1)$D BKT transition when QPS pairs unbind at the critical K_c. Just like the classical BKT mechanism the transition between ordered and disordered phases is sharp at $T=0$, albeit continuous.

Frequency dependence of the SIT Within this framework a 1D system can behave like an insulator at zero frequency ($\omega \ll \omega_{\mathrm{loc}}$) but still present collective excitations characteristic of superconductivity at larger frequencies.

The theoretical properties of this SIT have been further studied in the special case of a 1D Josephson junction chain by [Bard, Protopopov, Gornyi, et al., 2017] for DC measurements ($\omega = 0$), and in [Bard, Protopopov, and A. D. Mirlin, 2018; Houzet et al., 2019] regarding the microwave frequency response of a superinductor.
Notably the latter works predict a clear frequency dependence of the microwave properties for nearly critical samples: the density of plasmon modes decreases at lower frequencies, eventually vanishing as $\omega \to 0$. This translates into an increase of quality factor with frequency as $Q_i \propto \omega^2$ near the SIT.

Effect and existence of quantum phase slips The concept of quantum phase transitions induced by quantum phase slips is not new. In addition to the pinned Luttinger liquid approach described above [T. Giamarchi et al., 1988] superconductivity in nanowires was thought to be destroyed by the dissipative effects of quantum phase slips: the suppression of order parameter during a short phase slip event induces significant dissipation when the phase-slip probability is high [Zaikin et al., 1997; Bezryadin et al., 2000].
Recently the heat release induced by a phase slip event in a Josephson junction was evidenced through time-resolved thermometry [Gümüş et al., 2023], further demonstrating the dissipative

[6] For instance, a two-dimensional classical system with space coordinates (x,z) can be mapped to a system with x-coordinate in space and $z = v\tau$ time dimension (v is some velocity).

consequences of phase fluctuations on quantum circuits.

In some circumstances QPSs can be a coherent process, dual to Josephson tunneling [Mooij and Nazarov, 2006]. Experimental demonstrations of such effect using nanowires [Astafiev et al., 2012; Shaikhaidarov et al., 2022] or Josephson junctions [I. M. Pop et al., 2010; Crescini et al., 2023] are major milestones in understanding phase-charge duality and provide new methods in quantum metrology.

Experimental study of the phase-slip driven SIT in Josephson junction chains Recent experimental works have been carried out in 1D Josephson junction chains in order to investigate systems where the theory of pinned Luttinger liquids could apply.

Transport measurements in Josephson junction chains evidenced the scaling of critical voltage V_c (obtained from $I-V$ curves) with sample size (number of junctions N), consistently with the proposed theoretical model [Cedergren et al., 2017]. The authors interpret these data as a demonstration of the Bose glass insulator.

Shortly after a microwave frequency study of long JJ chains was presented in [Kuzmin et al., 2019]. The chains were designed to withstand a high density of plasmons (with a small frequency spacing) and were probed using standard cQED techniques allowing to extract the modes' dispersion relations and quality factors.
By varying the JJ size (therefore tuning the ratio E_J/E_c) the authors demonstrate an increase in the wave impedance to resistance quantum ratio $Z/R_Q^S = 1/(2K)$ (K is the dimensionless Luttinger parameter) up to values as high as ~ 3 (with impedance $Z \approx 23\ \mathrm{k}\Omega$), an order of magnitude larger than the theoretical prediction $= 1/3$ (see above).

Based on this observation the authors suggest that these samples are in the Bose glass regime, that is they should be insulating at zero frequency. Unfortunately in-situ transport measurement of these samples is not available, casting some doubt on the insulator hypothesis.
The authors however provide additional evidence by studying the frequency dependence of quality factor $Q_i(\omega)$. As discussed above the $(1+1)$ BKT transition should be accompanied by an increase of Q_i with ω for critically insulating samples. While such an observation can not be completely ruled out from the data displayed in [Kuzmin et al., 2019] one could argue that a clear increase of Q_i is not found.

We now compare our results on disordered indium oxide films to the phase-slip driven SIT.

6.3.3 Measurable quantities

The relevant quantity of interest is the wave impedance Z defined as

$$Z = \sqrt{\frac{L_K}{wC}} \tag{6.4}$$

where w is the wire width, C is the capacitance to ground per unit length and L_K is the kinetic inductance per square.
Z is proportional to the inverse of the Luttinger liquid constant $K = \pi\sqrt{\Theta/2E_c} = R_Q^S/(2Z)$. The (1+1)D BKT transition in presence of disorder predicts a critical impedance value Z_c at which superconductivity breaks down given by $Z_c \sim R_Q^S/3$ [T. Giamarchi et al., 1988] (*i.e.* a

Luttinger constant $K = 3/2$) as discussed in section 6.3.

We use the accurate determination of capacitance per unit length C in our geometry given by the capacitance model of Eq. (3.13) in the limit $k \to 0$ and w is controlled by design.
We shall see below that the (1+1)D BKT scenario of phase transition does not hold in amorphous indium oxide data.

Fig. 6.2**b** shows how indium oxide resonators compare with the phase-slip theory. The wave impedance Z normalized by the resistance quantum is represented versus disorder for two wire geometries: the plain blue markers are $1\ \mu$m-wide wires, while empty markers correspond to 100 nm-wide filaments. The *Bose glass* insulating state predicted in the model above should happen for normalized critical impedances larger than $1/3$. For $Z/R_Q^S < 1/3$ the system would be superconducting.
The data shown in Fig. 6.2**b** displays a different result: our films are superconducting (with plasma modes in microwave and zero resistance in DC) well above the Bose glass transition line.

Fig. 6.2**b** states that, **according to this theory all the indium oxide samples would be insulating, a statement clearly contradicted by DC and microwave measurements.**

6.3.4 Effect of wire width: universality of the transition ?

It is clear from the considerations above that wire dimensions play an essential part in the phase-slip driven transition. Indeed the wave impedance $Z = \sqrt{L_K/wC}$ should increase upon lowering the wire width w.
However the quantum phase transition driven by quantum phase slips occurs for a **universal** value of the wave impedance: if quantum phase slips were the only responsible for this phase transition, Z_c should not depend on the strip width.

In order to assess the universality of Z_c two different sets of samples were prepared (with width 1 and $0.1\ \mu$m). It appears from Fig. 6.2**b** that narrow wires have overall larger impedance than wider resonators, even at criticality.
This fact is once again in contradiction with the idea that the (1+1)D BKT transition is the only mechanism at play.

Note also that both geometries differ in the value of the critical disorder. While large strips remain superconducting down to $g = 1.6$, narrower films become insulating closer to $g = 4$ (*i.e.* $R_n = h/(2e)^2$). This is consistent with the observation that the SIT in DC measurements occured for a smaller critical resistance.

On phase-slip amplitude To further study the importance of phase slips in this transition it is useful to estimate the amplitude (or rate) of phase slips in a given system, characterized by its dimensions and disorder level.

Following BCS theory the phase-slip amplitude for moderately disordered films is (see Supp. Mat. of Astafiev et al., 2012):

$$E_{\mathrm{PS,BCS}} \approx \Delta \frac{R_Q^S}{R_\xi} \frac{L}{2\pi\xi} \exp\left(-A\frac{R_Q^S}{R_\xi}\right) \tag{6.5}$$

where Δ is the superconducting gap, $R_Q^S = h/4e^2$ is the resistance quantum for Cooper pairs, L and ξ are the wire length and superconducting coherence length respectively, and $R_\xi = R_\square \frac{\xi}{w}$ is the resistance of a wire of length ξ. The coefficient A is of order one.
This formula is expected to hold for low to moderate disorders only.

For strongly disordered superconductors with preformed pairs the phase-slip amplitude can be estimated as (see Supp. Mat. of Astafiev et al., 2012):

$$E_{\mathrm{PS,PG}} \approx \Theta \sqrt{\frac{L}{w}} \exp\left(-\eta w \sqrt{\Theta \nu d}\right) \tag{6.6}$$

where $\eta \sim 1$, and L, w, d are the wire length, width and thickness respectively. Θ is the 2D superfluid stiffness and ν the single particle density of states.
In both cases the phase-slip amplitude is exponentially suppressed with respect to the wire width $E_s \propto e^{-\alpha w}$. The width is therefore the dominant geometric parameter driving phase-slip processes.[7]

As an example let us cite the Coherent Quantum Phase Slip qubit demonstrated by [Astafiev et al., 2012], where a loop formed by disordered indium oxide is closed by a nanowire constriction. The small dimensions of this constriction (width $w = 40$ nm and length $L = 400$ nm) make it favorable for phase slippage. With a kinetic inductance of $L_K = 2.2$ nH/$\square$ the predictions for BCS and strongly disordered superconductors both give an estimation of $E_{\mathrm{PS}} \approx 5\,\mathrm{GHz} = 0.2\,\mathrm{K}$, in agreement with the spectroscopy measurements of [Astafiev et al., 2012].

Table 6.1
Estimation of phase slip amplitude for two geometries of wires close to the SIT.

Sample	w (μm)	L (mm)	R_n (k$\Omega/\square$)	L_K (nH/$\square$)	$E_{\mathrm{PS,BCS}}$ (GHz)	$E_{\mathrm{PS,PG}}$ (GHz)
TC018	0.1	0.3	2.9	1	2×10^{-12}	4×10^{-3}
TC024 run 1	0.1	0.3	5.3	1.9	5×10^{-4}	0.10
TC017	1	3.505	14.2	10.6	0	2×10^{-17}
TC016 run 6	1	1.71	15.9	16.6	0	10^{-13}

Table 6.1 shows the estimated amplitudes using the BCS and pseudoggaped formulae for our samples closest to SIT . We took a density of states $\nu = 0.5 \times 10^{46}$ J^{-1}m^{-3}, thickness $d = 40$ nm.
It can be seen that the wider strips ($w = 1$ μm) have a negligibly small phase-slip probability. The narrower strips on the other hand display a finite phase-slip amplitude, which could be underestimated by the crudeness of the model and the error bars on parameters.
Therefore based on this estimation one would expect a non-negligible (but still small) contribution from QPS in our narrow wires, and no influence at all of QPS in wider wires.

6.3.5 Effect of wire length

The localized-delocalized transition discussed above involves another essential parameter: the sample length. When the localization length ξ_{loc} is shorter than the sample length the latter

[7] The exponential dependence of phase slip amplitude with wire width was demonstrated in [Peltonen et al., 2013] using ultrathin NbN nanowire constrictions, in a configuration similar to that of [Astafiev et al., 2012].

behaves as a Cooper pair insulator (Bose glass). In the eventuality that the wire dimension is smaller than the localization length however superconducting behavior is still possible.

The DC measurements in this work were performed on 10 square-long wires, while the resonators were much longer (thousands of squares). Therefore if ξ_{loc} lies between 10 and $3500\ \mu\mathrm{m}$ a scenario in which the DC measurement device is superconducting (length $< \xi_{\mathrm{loc}}$) but the resonator is insulating (length $> \xi_{\mathrm{loc}}$) would be relevant.

To solve this issue we performed resistance measurements on a set of wires (width $w = 1\ \mu\mathrm{m}$) of different lengths L, with $L = 1\ \mu\mathrm{m}$ up to $L = 3500\ \mu\mathrm{m}$. The strips were prepared on the same chip with the same a:InO evaporation, allowing to ensure that disorder of the wires is uniform.

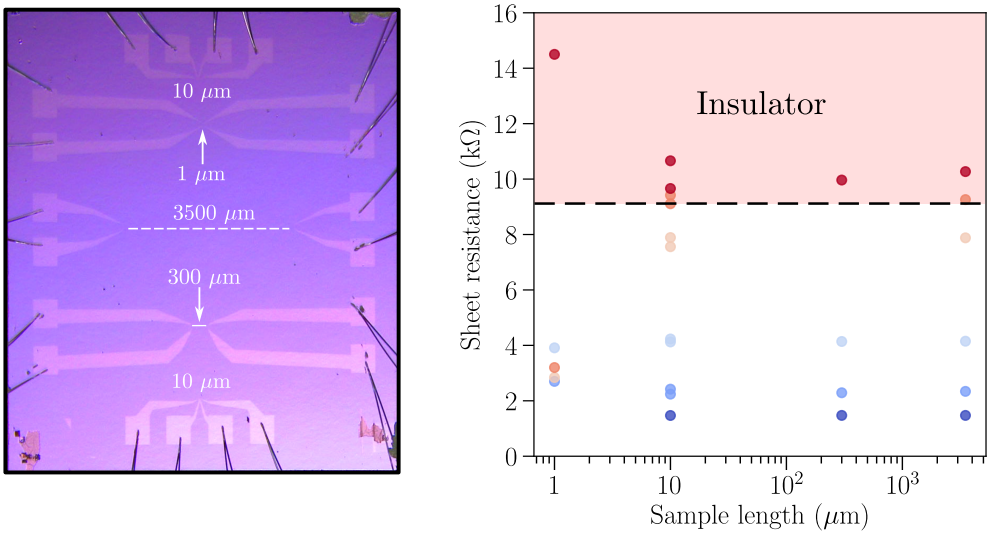

Fig. 6.4. Evaluation of the length-dependence of resistance at 4K. Left: A typical sample used to probe the resistance of indium oxide wires of the same width $w = 1\ \mu\mathrm{m}$, same disorder (all wires sit on the same chip over which the material was evaporated) but various lengths, ranging from $1\ \mu\mathrm{m}$ to $3500\ \mu\mathrm{m}$. We performed standard four-probe measurement at the lockin frequency ~ 10 Hz. **Right:** Resistance per square measured at 4 Kelvin versus wire length for six disorder strengths (one color per sample). The dashed horizontal line shows where the wires become insulating at low temperature (according to our resistance measurements described previously).

It appears that for lengths between 10 and $3500\ \mu\mathrm{m}$ the resistance per square measured at 4 K does not vary significantly, even for highly disordered samples which should become insulating at low temperature according to Fig. 4.1 (red shaded region in Fig. 6.4).
For the $1\ \mu\mathrm{m}$-long wires one observes some scattering, which could be understood as an increased error in the determination of the dimensions, resulting in some error in the calculation of the sheet resistance.

We find that the resistance is nearly constant when increasing the wire length by three orders of magnitude.

6.4 | Transition driven by long-range Coulomb interactions between localized Cooper pairs

While our indium oxide resonators withstand 1D modes and therefore could behave as Luttinger liquids, disorder is intrinsically three-dimensional in our films having thickness $d = 40$ nm several times larger than the superconducting coherence length $\xi \sim 5$ nm [B. Sacépé, Seidemann, et al., 2015].
Therefore an alternative theoretical description of such system should focus on the microscopic properties of fractal superconductors.

We have described the theory of fractal superconductivity in chapter 2: pairs of electrons are created by phonon-induced electron-electron attraction enhanced by electronic wavefunction fractality, the latter being a consequence of the proximity to the Anderson insulator-metal transition.
These electron pairs remain Anderson localized, and superconducting correlations happen by coherent tunneling between localized states. In this model superconductivity is strongly inhomogenous spatially and is characterized by large phase fluctuations.
Short-scale, low frequency bosonic modes emerge at the vicinity of the transition to the insulator and induce dissipation as should be seen in the quality factor Q_i of microwave resonators, as well as in the temperature dependence of the superfluid density (see section 5.2.2).

One more interaction must be taken into account in a fractal superconductor: localized Cooper pairs interact at long-range via Coulomb repulsion. This process involves a Coulomb gap of Cooper pairs Δ_C of the order of a few Kelvin, as discussed in section 4.4.
The transition between insulating and superconducting states is then governed by the competition between two energy scales: the condensation energy Δ leading to long-range order and the Coulomb repulsion Δ_C enhanced by localization. The hopping probability between localized states decreases with disorder strength, and eventually vanishes: the system enters an insulating state made of localized Cooper pairs repulsing each other by Coulomb interaction, forming a Coulomb glass of electron pairs [M. Müller and Ioffe, 2004; M. Müller and Pankov, 2007].

Nature of the transition Following an argument by [M. Feigel'man, Private communications] one can compare the ground-state energy density of an insulator with a Coulomb gap Δ_C

$$E_{\text{ins}} = -A_{\text{ins}} \nu_0 \, \Delta_C^2 \tag{6.7}$$

with the energy gain due to superconducting pairing

$$E_{\text{sc}} = -A_{\text{sc}} \nu_0 \, \Delta^2 \tag{6.8}$$

where Δ is the typical value of the superconducting order parameter.

It follows that the relevant quantity to determine the quantum critical point is the ratio between these two energy densities

$$\frac{E_{\text{sc}}}{E_{\text{ins}}} \propto \left(\frac{\Delta}{\Delta_C} \right)^2 \tag{6.9}$$

In the superconducting state long-range Coulomb interaction is screened and Δ_C is much smaller than pairing $\Delta_C \ll \Delta$. It can be shown that when the superconducting gap is of the order of the Coulomb gap $\Delta \sim \Delta_C$ the BCS collective gap Δ ceases abruptly to exist.
The theoretical model of SIT induced by Coulomb repulsion of preformed pairs developed by M. Feigel'man and coworkers [M. Feigel'man, I. Poboiko et al, In preparation] is built on the fact that superconducting state and Coulomb glass are two stable phases, both described by an order parameter. **It follows that this transition must be of the first order**: superconductivity is destroyed at a critical disorder where superconducting energy scales drop abruptly to zero.

It is important to specify why such effect is absent in most theories and experiment.
In fact, most superconductors are based on a metallic normal-state; in this case screening of Coulomb interactions is strongly efficient[8] and repulsion between charges can be safely neglected.
On the other hand, superconductivity in indium oxide films discussed in this thesis is built upon an Anderson insulator: here Coulomb interactions are very weak but non-negligible[9] ($\varepsilon \sim 1000$), and therefore compete with superconductivity. One expects to see a first-order transition of this kind for *fractal superconductors* only.

Estimation of the transition point We can now estimate the critical value of superfluid stiffness at the quantum critical point: superfluid stiffness and superconducting gap are related by $\Theta = \frac{1}{8} g \Delta$ where $g = h/(e^2 R_\square)$ is the dimensionless conductance.
The first-order transition occurs for $\Delta \sim \Delta_C$, the latter quantity being expressed in Eq. (4.4). This leads the minimum value of superfluid stiffness at the transition:

$$\Theta_c = \frac{1}{8} g_c \sqrt{\nu} \left(\frac{4e^2}{\kappa} \right)^{3/2} \tag{6.10}$$

where $\kappa \approx 1000\, 4\pi\varepsilon_0$, as discussed in relation to Eq. (4.3), and g_c is the critical value of dimensionless conductance at the transition. The density of states for pairs ν is half the DoS for electrons, which can be estimated for strongly disordered indium oxide as $\nu = \nu_0/2 \approx 1.5\, 10^{45}$ [B. Sacépé, J. Seidemann, Private communications].

We now recall that our larger films had a critical conductance $g_c = 1.6$. From Eq. (6.10) this leads a critical superfluid stiffness before the transition $\Theta_c = 0.49$ K. This is surprisingly close to the value measured experimentally $\Theta_c = 0.5$ K, see Fig. 6.2 for instance.

For the narrower films, we found a critical conductance $g_c = 5$. Eq. (6.10) gives $\Theta_c = 1.55$ K, very close to the critical values $T_c \sim 1.6$ K.

[8] In a metal Debye screening length is of atomic scale, $l_D \sim 0.3$ nm or less, which is much smaller than the coherence length ξ.

[9] In an Anderson insulator the screening length is $\sim \xi_{\mathrm{loc}} \sim \xi$. Preformed Cooper pairs are localized, thus reducing the effect of dynamical screening.

Conclusion

In this chapter we have commented on the nature of the superconductor-insulator transition in long amorphous indium oxide wires. It is found that the characteristic energy scales of superconductivity, the superfluid stiffness and critical temperature, remain finite on the superconducting side of the SIT, and drop to zero abruptly on the insulating side.
A first theoretical candidate for a discontinuous quantum phase transition is given by the localization of plasmons into a Bose gass insulator. We rule out this scenario by comparison with DC measurements performed alongside microwave spectroscopy.
Another possible theoretical mechanism involves long-range Coulomb repulsion of localized Cooper pairs in a fractal superconductor. Recent works suggest that this transition is of first-order, in agreement with our experimental data. Such observation is a major change of paradigm in the understanding of quantum phase transitions in disordered superconductors.

Part III

Properties of Strongly Disordered Indium Oxide Resonators and Applications

CHAPTER 7

Loss Mechanisms in a:InO Microwave Resonators

Superconducting resonators and qubits present higher loss than expected from BCS theory, for which all dissipative single-particle excitations should vanish at $T = 0$. Extensive works on superconducting circuits have singled out several mechanisms leading to this dissipation excess, among which dielectric loss and non-thermal quasiparticles (see McRae, H. Wang, et al., 2020 for a review).
Dielectric loss, often related to Two-Level Systems, is particularly detrimental to qubit coherence and is currently seen as a the main limiting factor in most superconducting circuits [Müller et al., 2019]. In addition to this, a large density of non-equilibrium quasiparticles is known to survive in superconductors beyond the BCS model, leading to dissipation and noise [Catelani and Pekola, 2022].

In this chapter we try to understand the loss mechanisms at play in strongly disordered indium oxide resonators.

7.1 | Decrease of dissipation with power and temperature

The evolution of quality factor with cavity photon number[1] and temperature is shown in Fig. 7.1. One sees an initial increase of Q_i at low photon number or low temperature. Such a behavior is seen for all our samples (Fig. 7.1 shows only a very limited selection of samples).[2] This effect is often attributed to Two-Level Systems (TLSs). While the latter are usually considered in amorphous solids around the resonator (oxides, resist residues ...) we shall see later that other mechanisms can lead to TLSs with the same experimental manifestations.

Two-Level Systems A thorough review on TLSs can be found in [Müller et al., 2019], where both theoretical models and experimental observations of TLSs are detailed. In the following paragraph we sketch crudely the main ideas of the Standard Tunneling Model.

[1] The average photon number circulating in the resonator at resonance (in our geometry) can be estimated by $n \approx 4P_{\mathrm{in}}Q_{\mathrm{tot}}^2/(\hbar\omega_r^2 Q_c)$ where P_{in} is the on-chip microwave power (counting attenuation along the line) and ω_r, Q_c, Q_{tot} are the fitted resonance frequency, coupling quality factor and total quality factor respectively.

[2] Regarding the values of internal quality factors extracted from transmission measurements, one should be aware of potentially deceptive effects originating from the microwave line; as pointed out in [Rieger, Günzler, M. Spiecker, Nambisan, et al., 2023] Fano interferences can induce significant uncertainties in the extraction of Q_i, especially in the overcoupled regime ($Q_i > Q_c$). We note however that most of the measurements shown here are in the undercoupled regime where such uncertainties are minimized.

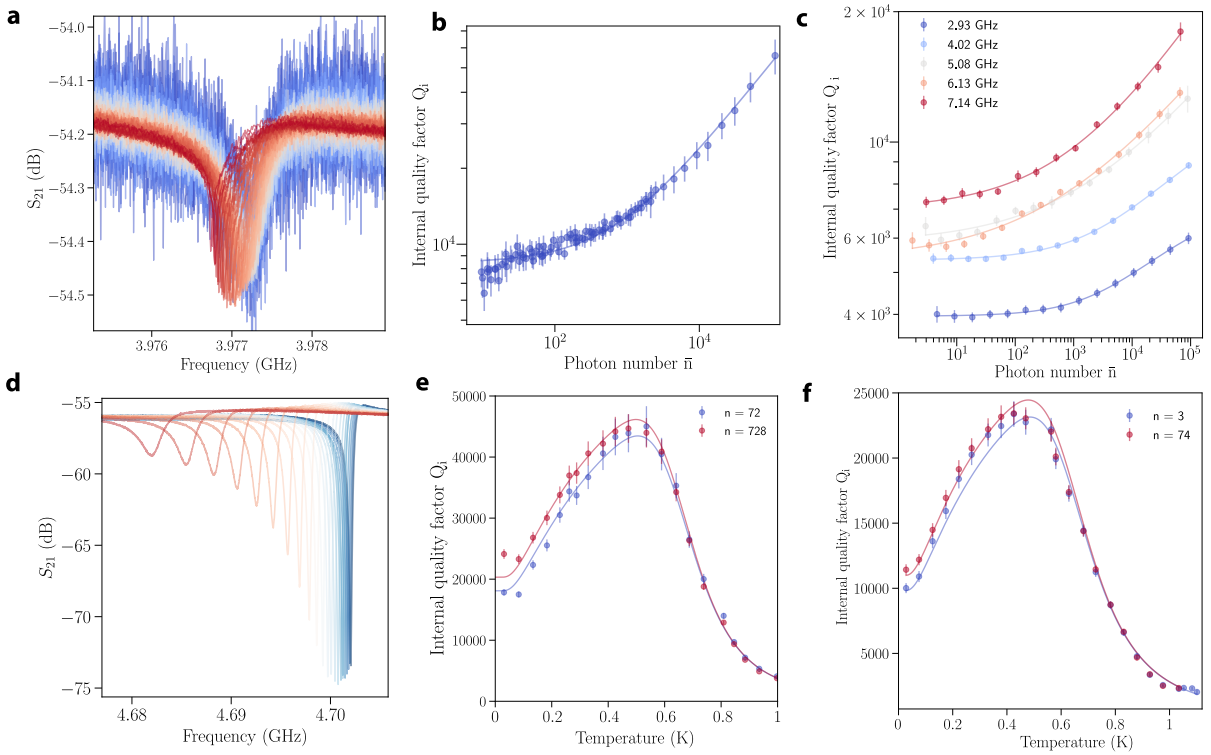

Fig. 7.1. Power (a-c) and temperature (d-f) dependence of internal quality factors. Upon increase of temperature or microwave power the plasmon frequencies decrease, as seen from the transmission traces (**a, d**). Fitting these curves allows the determination of the resonator internal quality factor. Power in panel **a** ranges from -20 dBm (blue) to 10 dBm (red). Temperature in panel **d** ranges from 20 mK (blue) to 1 K (red). Fig. **b, c, e, f** display the increase of Q_i with photon number and temperature for several samples (moderate disorder). Solid lines are fits following the TLS model Eq. (7.2). The measurements shown in panel **b** are related to a resonance with $f = 3.85$ GHz and $Q_c \sim 10^4$, and the ones from panel **e** have $f = 4.7$ GHz and $Q_c \sim 6\,10^3$.

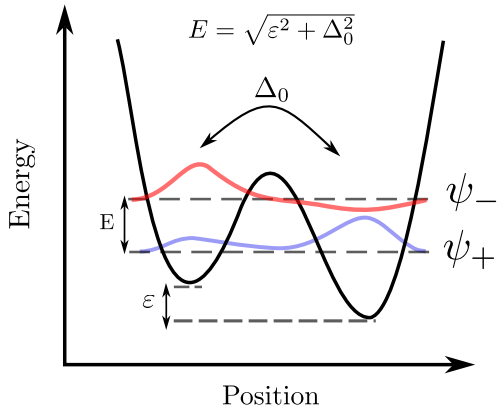

Fig. 7.2. Double-well potential modelling of a TLS. The energy difference E between the two eigenstates $|\psi_-\rangle$ and $|\psi_+\rangle$ is determined by the asymmetry energy ε and inter-well tunneling rate Δ_0. Adapted from [Müller et al., 2019].

A Two-Level System is a quite general concept describing a system that can exist in two energetic configurations. With some probability one of the two states will be occupied. A

common representation of a TLS is shown in Fig. 7.2, where the two available states are pictured as two potential wells separated by an energy barrier. At low temperatures and low excitations the TLS tunnels from one state to the other.
If these two states are related to charge displacement, their tunneling creates an effective electric dipole that can couple to its environment (for instance, our resonator, a superconducting qubit or a phonon bath), leading to dissipation and/or dephasing. The strength of such coupling is $g = \mathbf{p} \cdot \mathbf{E}$ where $\mathbf{p}$ is the TLS dipole moment and $\mathbf{E}$ is the electric field.

Further, because of their random microscopic origin (detailed later) the TLSs present in an amorphous material have a broad distribution of their characteristic energies (tunneling rate Δ_0 or asymmetry energy for instance), ensuring the presence of TLS at virtually all experimental measurement frequencies.
These TLSs also interact with each other, opening some interesting situations where a high-energy TLS can be coupled to a second TLS of lower energy $E < k_B T$. Thermal agitation randomly changes the state of the second TLS, which in turn affects the first TLS's frequency. If a resonator or a qubit has a resonant frequency in close vicinity to the first TLS it will couple to it, as evidenced by the increased environmental noise and degraded qubit coherence times observed experimentally.

Saturation of TLSs When excited by a large electric field $\mathbf{E}$ (corresponding to a large number of photons circulating in the resonator) the TLS switches between states faster than it loses energy. The resulting state becomes almost stationary with excitation probability $\sim 1/2$ and dissipation is reduced compared to the low power situation.
This *saturation* of two-level systems with power (or similarly with temperature) explains qualitatively the behavior of quality factor shown in Fig. 7.1: by increasing power or temperature above a threshold value TLSs saturate and do not contribute to the overall resonator dissipation.

Within the Standard Tunneling Model (that is, neglecting for now the TLS-TLS interactions), the saturation of TLS with photon number n is modelled by [Phillips, 1987; J. Gao, 2008]

$$\frac{1}{Q_i} = \sum_i p_i \tan\delta_i \frac{\tanh\left(\frac{\hbar\omega}{k_B T}\right)}{\sqrt{1+\left(\frac{n}{n_c}\right)^\beta}} + \tan\delta_0 \tag{7.1}$$

$$= F \frac{\tanh\left(\frac{\hbar\omega}{k_B T}\right)}{\sqrt{1+\left(\frac{n}{n_c}\right)^\beta}} + \frac{1}{Q_{\mathrm{Other}}} \tag{7.2}$$

where n_c is the saturation photon number, β takes into account the non-uniform distribution of electric field and the sum runs over all the volumes i that host TLS with dieletric loss rate $\tan\delta_i$. The weight p_i accounts for the participation in the different volumes and is mostly dictated by geometry (see below). For simplicity one can define $F = \sum_i p_i \tan\delta_i$ the prefactor accounting for TLS loss at lowest power. In the literature one might find the notation $F = 1/Q_{\mathrm{TLS}_0}$.

Using Eq. (7.2) allows to reproduce the evolution of Q_i with photon number n, as seen in Fig. 7.1.

To describe the temperature dependence one must account for the breaking of Cooper pairs when the temperature approaches T_c, as given by Mattis Bardeen formulae [Mattis et al., 1958], which enter the new temperature-dependent term $1/Q_{\mathrm{QP}}(T)$ in the full expression

$$\frac{1}{Q_i(n,T)} = \frac{1}{Q_{\mathrm{TLS}}(n,T)} + \frac{1}{Q_{\mathrm{QP}}(T)} + \frac{1}{Q_{\mathrm{Other}}} \tag{7.3}$$

The additional term models the decrease of quality factor as the thermal quasiparticle number increases, as can be seen clearly in Eq. (7.2) above 0.5 K. The sum of these two loss channels (TLS at low T and quasiparticles at higher T) in parallel fits the experimental data.

7.2 | Resonators in 3D Waveguides: reducing the participation of native oxides

So far we did not comment on the possible microscopic origins of TLSs: any system possessing two energetically equivalent states could be seen as a TLS.
A large variety of microscopic mechanisms reponsible for the formation of TLS have been suggested, amongst which the tunneling of an atom, group of atoms or dangling bond from one preferential position in space to another, electron tunneling or magnetic impurities.

Regarding the location of these defects, one obvious candidate is the amorphous oxide lying at the surfaces and interfaces of the circuit, potentially hosting a great deal of TLS. This is precisely the effects of TLSs present at these interfaces that a large body of works tried to mitigate in the last two decades in the hope for a significant enhancement of quality factors and qubit lifetimes.
An illustration of the main interfaces of interest in a superconducting circuit are depicted in Fig. 7.3. Oxide layers are usually a few nanometer thin, between the superconducting material and the substrate, or exposed to the open environment (air or vacuum).
It becomes evident that the circuit geometry influences quite a lot the electric field strength at a given interface i (volume V_i), which in turn dictates how strongly coupled to the circuit a TLS can be (with coupling $g = \mathbf{p} \cdot \mathbf{E_i}$).
To account for the electric field distribution in a given volume V_i one often defines a *participation ratio* p_i as

$$p_i = \int_{V_i} \frac{\varepsilon_i}{2} |\mathbf{E_i}(\mathbf{r})|^2 / E_{\mathrm{tot}} \, d\mathbf{r} \tag{7.4}$$

where ε_i and $\mathbf{E_i}(\mathbf{r})$ are the dielectric constant and electric field in the lossy volume V_i respectively, and E_{tot} is the total electric field energy in the entire space.

The product of participation ratio p_i and dielectric loss tangent $\tan\delta_i$ describes to which extent dielectric losses contribute to the overall dissipation in the volume V_i (see Eq. (7.2)) for a given geometry.
In typical coplanar waveguide geometries the Metal-Substrate participation ratio p_{MS} is found to be of the order $\sim 3\,10^{-3}$ and be the dominant interface for dielectric loss. The Substrate-Vacuum interface also participates strongly $p_{\mathrm{SV}} \sim 10^{-3}$, but can be reduced by diluting the electric field in this region (by increasing the gap between conductors for instance).

A more drastic way to reduce the participation ratios consists in moving the resonator into a 3D waveguide (as shown in Fig. 7.4). That way the electric field is diluted in a large volume and weakly couples to the resonator, reducing the dielectric loss. Using the electromagnetic

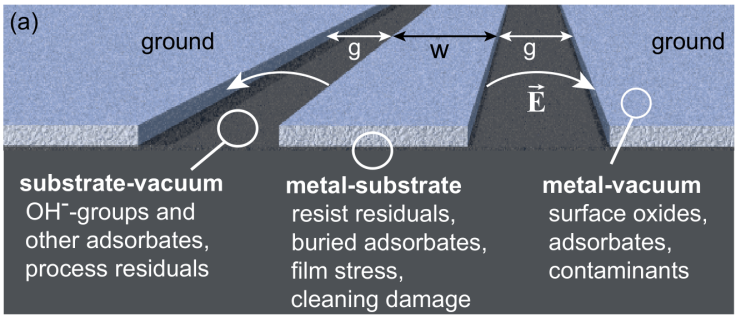

Fig. 7.3. Illustration of the surfaces hosting TLSs in a typical superconducting circuit. Thin layers of amorphous materials can be found between the superconductor and substrate (Metal-Substrate, MS interface) or in direct contact to the external environment (Metal-Vaccum, MV, or Substrate-Vaccum, SV). Each interface displays various kinds of glassy materials that can host TLS. From [Müller et al., 2019].

simulation software HFSS we simulated a resonator (2 mm-long, 1 μm-wide for a kinetic inductance of $L_K = 1.32$ nH/$\square$ representing a typical sample studied in this thesis) embedded in a 3D waveguide (perfect-$\mathbf{E}$ boundary conditions) and filled with air ($\varepsilon = 1$), as shown in the drawing of Fig. 7.4. Underneath the resonator we added a 3 nm-thin dielectric layer with dielectric constant $\varepsilon_{SiO_2} = 10$ modelling the amorphous silicon oxide growing a the surface of the silicon substrate, as is usually done in the literature.

By simulating the electromagnetic response of the whole device one can extract the electric field intensity in the Metal-Substrate region and compute the participation ratio, leading $p_{MS} \sim 3.17\,10^{-4}$, an order of magnitude smaller than the typical planar geometry, as expected.

Therefore, one expects a significant enhancement of quality factor in this geometry, provided dielectric losses are mainly located in MS and SV interfaces. To check this hypothesis we fabricated indium oxide resonators with parameters identical to the simulated design. The absence of metallic ground plane at the back of the sample should further reduce conduction and dielectric loss, and the waveguide, made of bulk aluminum, should not induce large dissipation.
Additional shielding of the sample holder and careful filtering on both inputs and outputs ensures a low-loss environment[3].

Fig. 7.5 (**Right**) shows the power evolution of quality factor for one of our resonators in 3D waveguide. Strikingly, the quality factor at low photon number ($n \sim 1$) is comparable to the values obtained previously in the microstrip geometry ($Q_i \sim 10^4$).
The quality factor still increases with power, consistently with a TLS model (see solid lines).

Interacting TLSs The temperature evolution of quality factor remains consistent with our previous observations, with an increase of $Q_i(T)$ for temperatures up to 0.5 K (see Fig. 7.5). Note one difference however: at the lowest temperatures $T < 0.2$ K the quality factor initially

[3]The waveguide is shielded inside a copper and a μ-metal shield at 20 mK, covered on the inside by black-paint epoxy and granules in order to absorb radiations. A gold plated copper shield at 700 mK and polished aluminum screens at 4 K, 20 K and 100 K further isolate the sample to radiations. Eccosorb and K&L low-pass filters are added at the sample's input and output. More details can be found in Appendix C

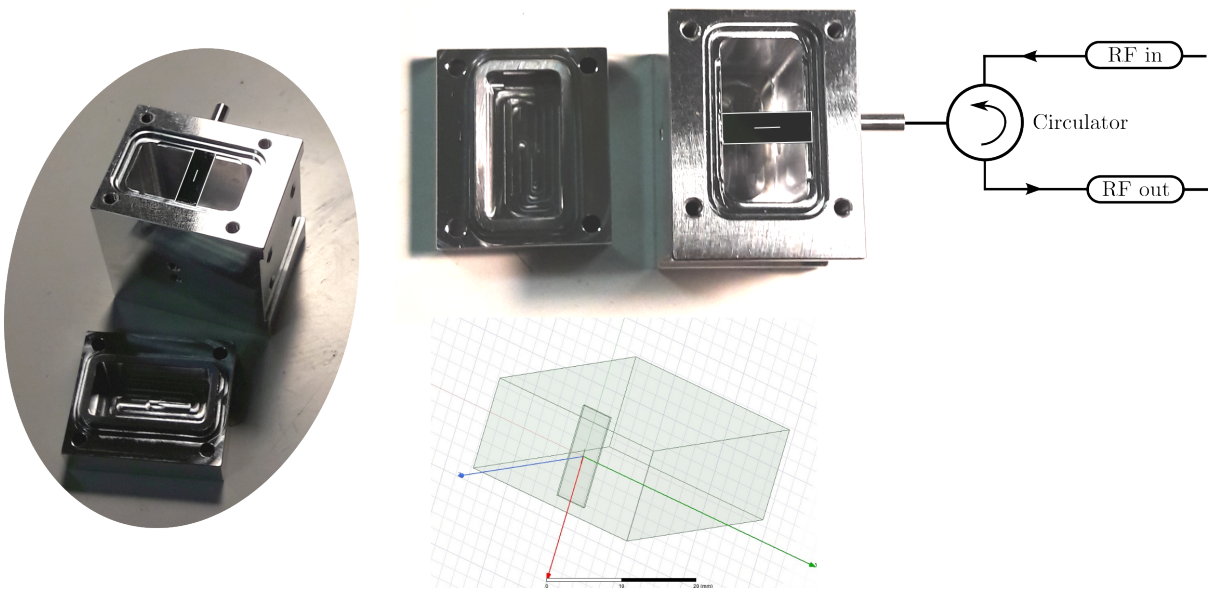

Fig. 7.4. 3D waveguide and resonator. The sample (a 2 mm long a:InO line deposited on silicon, outlined in white on the pictures) is embedded in a 3D aluminum waveguide. The lid is sealed by an indium wire which also sticks to the sample and holds it in place. RF excitation enters and exits the waveguide through a coaxial cable, and input and output (reflected) signals are separated by a circulator allowing to measure the reflection via the S_{21} scattering parameter of a VNA. Bottom drawing shows how the device can be simulated using HFSS electromagnetic software.

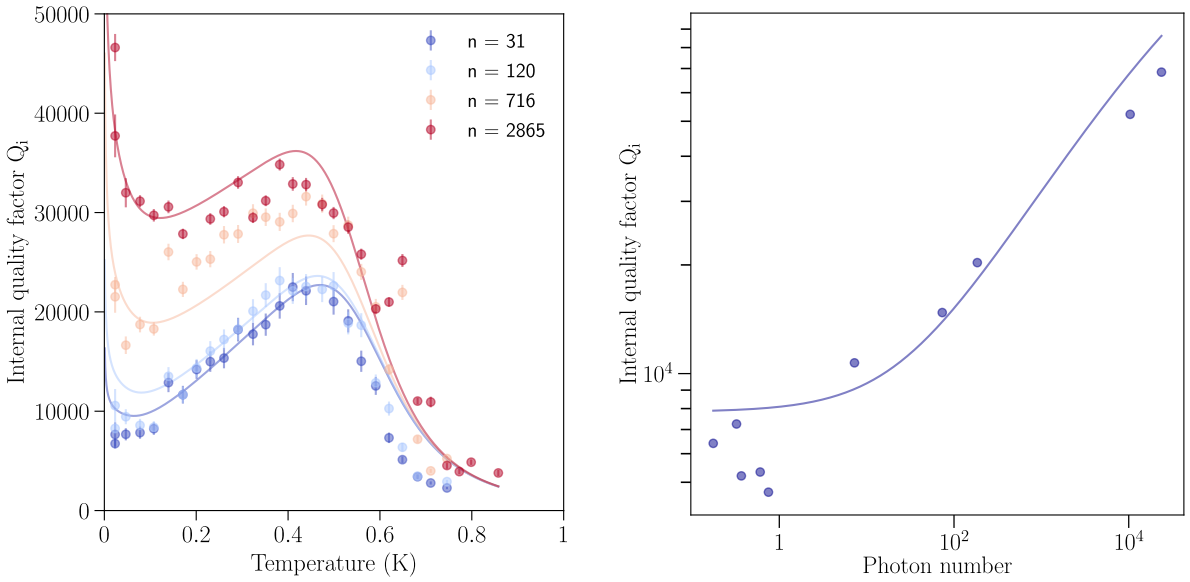

Fig. 7.5. Temperature and power dependence of an a:InO resonator in 3D geometry. Left: Evolution of quality factor with temperature for a 3D resonator (TC040). The quality factor shows three temperature regimes: Q_i first decreases, then increases and finally is reduced again. Solid lines are a fit to the TLS model including TLS-TLS interactions. **Right:** Quality factor versus photon number for the same resonator. Solid line is the prediction of the TLS model **using the same parameters as for the temperature dependence data**.

decreases with T.

This could be explained by the TLS-TLS interactions: as temperature increases thermally-driven switching of a given TLS causes dephasing in the nearby coupled TLSs [J. Burnett et al., 2014]. A modification of Eq. (7.2) taking into account the effect of interactions can be found in [Crowley et al., 2023]. Unfortunately such phenomenological model involves 7 fitting parameters, rendering it somehow useless for the precise extraction of relaxation and dephasing due to TLSs.
In an attempt to reduce the degrees of freedom of this fit we fitted together $Q_i(T)$ curves at different power, as shown in Fig. 7.5 **Left**, and plotted the resulting prediction for the power dependence with the exact same parameters, showing a good agreement with the data (Fig. 7.5 **Right**).

7.3 | Partial conclusion: InOx dissipation is not dominated by surface dielectric loss

In order to get a more quantitative estimation of the role of TLSs in our films, let us show some statistics. Fig. 7.6 shows a systematic fitting of a large variety of indium oxide resonators (different disorders and resonance frequencies), both in 2D microstrip and 3D waveguide geometries. The parameters extracted from a fit to the standard TLS model Eq. (7.2) are also displayed, demonstrating a TLS loss factor remaining of the order $F \sim 10^{-4}$ and an exponent β of order unity as expected from the theory.
The main difference between the microstrip and 3D waveguide samples seems to be the value of saturation photon number n_c: this critical power above which TLS start to saturate seems to decrease by one to two orders of magnitude in the 3D geometry.

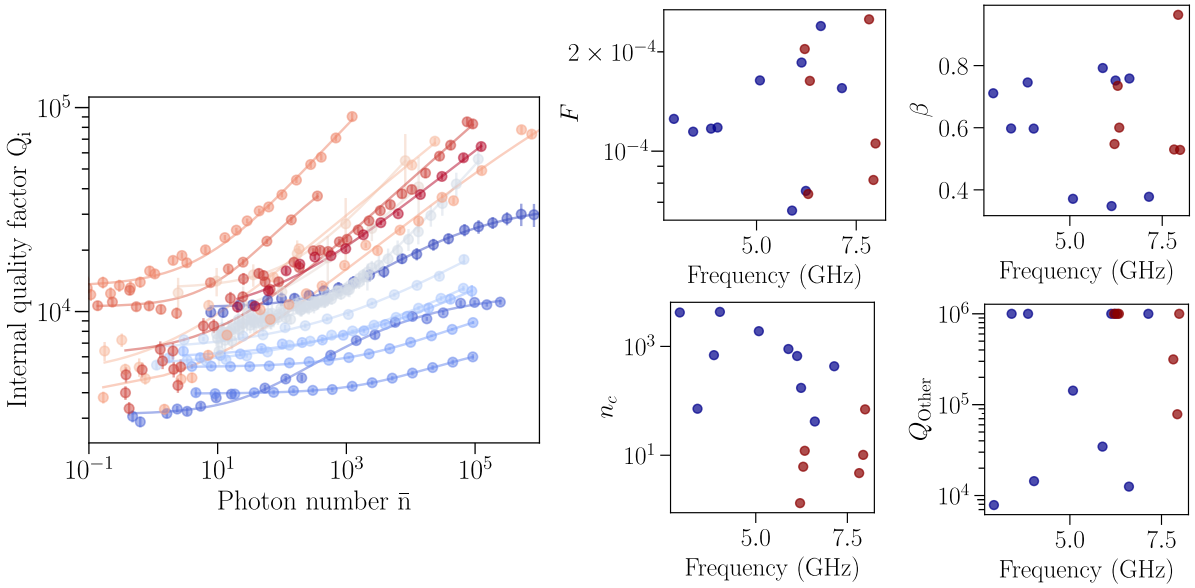

Fig. 7.6. Power dependence of quality factors for a large number of samples. Left: $Q_i(n)$ for samples of different disorders, resonance frequencies and geometries (both 2D microstrip and 3D waveguide) are shown and fitted by the TLS model of Eq. (7.2). **Right:** Extracted parameters from the TLS fit. Results for the 2D samples are shown in blue while 3D waveguide resonators are represented in red.

7.3.1 Metal-Substrate interface is not limiting the resonator quality factors

It is clear that changing the MS participation ratio by an order of magnitude did not improve the quality factor of our a:InO resonators. We want to stress that extra care was taken for the reduction of external sources of loss, and that quality factors as high as one million were measured in very similar conditions for pure aluminum resonators. Therefore the strong dissipation observed in a:InO is most likely related to the material itself.

To demonstrate that our films are not limited by dielectric loss at the MS interface, we display on Fig. 7.7 the quality factor as a function of the participation ratio for different materials. First, Transmon qubits in planar geometry and some coplanar waveguide resonators (CPW) are added to this graph. They align nicely to the expected TLS-limited quality factor $Q_i \sim [p_{\mathrm{MS}} \tan\delta]^{-1}$ where the loss tangent $\tan\delta$ is consistent with typical values found in the literature for high-quality silicon or sapphire substrates, commonly used in the cQED community. Dissipation in these materials seems to be limited by dielectric loss at the Metal-Substrate interface (or Substrate-Vacuum which is often found to be comparable).

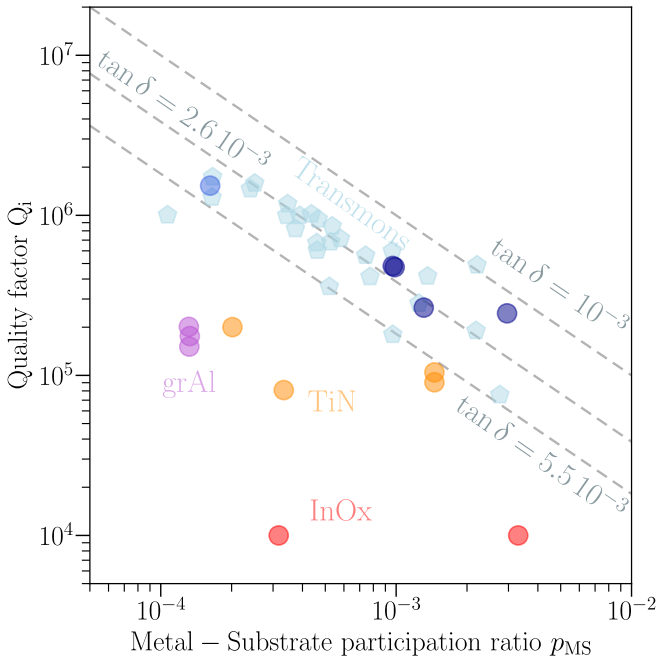

Fig. 7.7. Quality factor versus Metal-Substrate participation ratio for several materials and geometries. Light blue pentagons represent planar transmon qubits limited by dielectric loss (from [C. Wang et al., 2015]), blue circles show low kinetic inductance aluminum and granular aluminum CPW resonators (from [Grünhaupt, Nataliya Maleeva, et al., 2018]). All of these materials display a scaling of quality factor with participation ratio following $Q_i \sim [p_{\mathrm{MS}} \tan\delta]^{-1}$ shown by the dashed lines (for three loss tangent values representative of bulk silicon and sapphire). Several materials however do not obey the scaling limited by dielectric loss: high-L_K grAl in 3D waveguide, represented by purple dots [Grünhaupt, Nataliya Maleeva, et al., 2018] or ultrathin TiN (orange dots) [Amin et al., 2022]. Finally our indium oxide shown in red is the furthest from the TLS-limited regime, with a quality factor independent on the MS interface participation.

More surprisingly, Fig. 7.7 also displays data points that do not align to any plausible loss tangent value, and have a quality factor significantly lower than the upper bound set by dielectric loss at the interface (purple, orange and red dots). Such a feature was first demonstrated in high-kinetic inductance granular aluminum [Grünhaupt, Nataliya Maleeva, et al., 2018] and shortly after in ultrathin titanium nitride films [Amin et al., 2022]. In both case the deviation from the TLS-dominated loss was interpreted as the signature of non-equilibrium quasiparticles, the effects of which are increasingly perceptible as the film's kinetic inductance increases. Adding finally our indium oxide data demonstrates clearly that dissipation cannot be attributed to dielectric loss at the circuit interfaces, as the quality factors are orders of magnitude below their TLS-upper bound, and do not seem to vary with p_{MS}.

7.4 | Coplanar Waveguide Hybrid Device: reducing the Indium oxide volume

Naively one could think that, if dissipation mainly originates from the indium oxide film, then reducing its footprint by drastically shrinking its dimensions and diluting the electric field around it should enhance the quality factor. In order to test this hypothesis we designed a hydrid resonator consisting almost entirely in a lower kinetic inductance superconductor with good quality factors, and a small indium oxide wire at the center, as shown in Fig. 7.8.

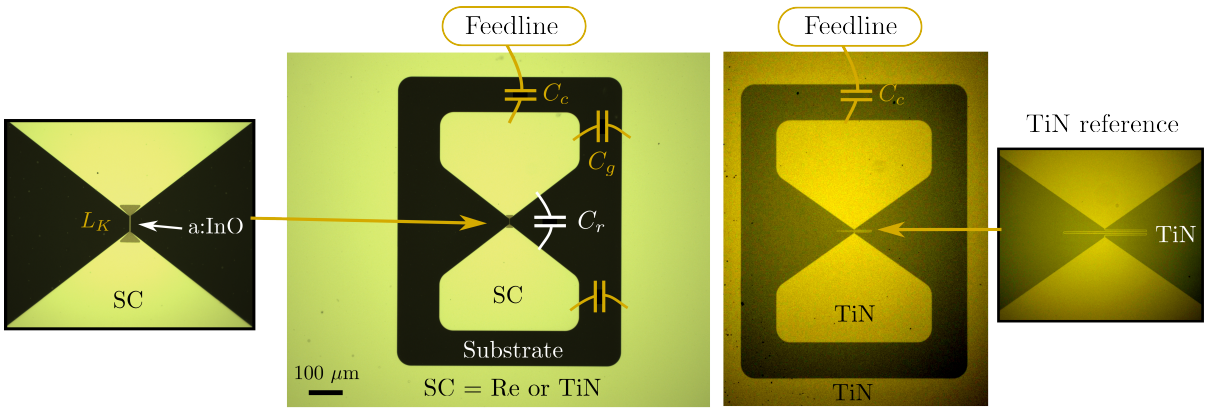

Fig. 7.8. Presentation of the hybrid Superconductor-Indium oxide resonator. Left: Dark field microscope image of the device, composed of a high quality superconductor (Titanium nitride or Rhenium, image shows a Rhenium sample) in a coplanar waveguide geometry, with two superconducting pads connected by a small indium oxide volume (see inset on the left). Full dark area is the underlying substrate (intrinsic Silicon or Sapphire depending on the sample). The device's resonance frequency is set by the capacitances to ground C_g and between the pads C_r, as well as the kinetic inductance of the a:InO wire. **Right:** For one sample (AC-TiN-15), a reference resonator fully composed of TiN is coupled to the same feedline. Its kinetic inductance is given by the longer high-disorder TiN wire wound in a meander (see right inset). The reference resonator allows to disentangle losses coming from the environment and indium oxide itself.

The geometry somehow resembles transmon qubit and resonator designs that showed long coherence times recently [Shearrow et al., 2018; Place et al., 2021; Deng et al., 2023; Crowley et al., 2023]: the coplanar ground plane is pushed far away from the resonator in order to

decrease the electric field intensity in the gap region, therefore reducing the losses induced by TLS at the substrate/vacuum interface.
The device capacitance comes mainly from the coupling between the two large pads and the ground plane (capacitance C_g in Fig. 7.8) and from the coupling between the two pads (C_r). The device inductance is mainly provided by a small volume of high kinetic inductance indium oxide ($L_K \sim 1-2$ nH/$\square$) connecting the pads (dimensions $10\ \mu\mathrm{m} \times 1\ \mu\mathrm{m} \times 40$ nm). As can be seen the a:InO wire is hundreds of microns away from the ground plane, ensuring a minimal contribution to the wire capacitance, hopefully reducing the excitation of TLS in the film.
In this geometry the resonance frequency is approximately given by $f_r \sim 1/\sqrt{(C_g/2 + C_r)L_K}$, and can be controlled by varying the a:InO wire length in order to obtain three resonators per chip, coupled to the same feedline.

For high quality superconductors we used 10 nm-thin titanium nitride films on high resistivity silicon, and rhenium on sapphire. The TiN was given to us by Julien Renard (Néel institute) and comes from the exact same film deposition as the works presented in [Amin et al., 2022]. The films have relatively large kinetic inductance $L_K \approx 33$ pH/$\square$ and high quality factor $Q_i \sim 10^5$ at single photon power.
The rhenium films were grown at SIMaP Grenoble by Bruno Gilles.
We used TiN and Re instead of a more accessible superconductor such as aluminum for one main reason: the contact between superconductor and indium oxide had to be of the best quality possible. To minimize surface inhomogeneities and granularity that could lead to a bad interface we used superconductors known for their smooth surface.

The fabrication work for this project was entirely done by Alexis Coissard[4], while I provided the electromagnetic simulations and designs, and measured the samples. We had the theoretical support of Lev Ioffe (Google Quantum AI) throughout this study.

On one sample (AC-TiN-15) a resonator entirely made of TiN was patterned alongside two hydrid a:InO/TiN resonators, in the idea of disentangling once and for all dissipation in indium oxide and the influence of the environment, design and packaging. This reference TiN resonator was designed by replacing the high-L_K wire by a longer TiN wire with a meander shape, thus providing the required inductance to obtain the wanted resonance frequency (see Fig. 7.8 **Right**).

Improved packaging In order to further reduce external sources of loss we designed a sample holder, fabricated in **pure** aluminum. A 3 mm hole is dug below the sample to minimize the fraction of electric field passing through the substrate, as shown in Fig. 7.9.
The sample holder is covered by an aluminum lid, sealed with an indium wire and pressed against the box with screws.

Results In a nutshell, this new design did not improve the quality factor of a:InO-based resonators. In most samples the low photon number Q_i of hybrid devices was 10^4 at most, sometimes even lower. Keeping in mind that the TiN and Re films used here have at least one

[4]The technical fabrication details are not the topic of this chapter, but to honor Alexis' hard work here are the main steps: the TiN film was etched by a SF_6 plasma after e-beam patterning. The sample was thoroughly cleaned in buffer HF acid to remove residual oxides at the exposed surfaces (notably between the pads where a:InO will be deposited). After a second step of lithography the indium oxide wire is deposited between the pads (at most 10 minutes were spent between the last chemical sample cleaning and its loading into the evaporator where it was quickly put under vacuum).

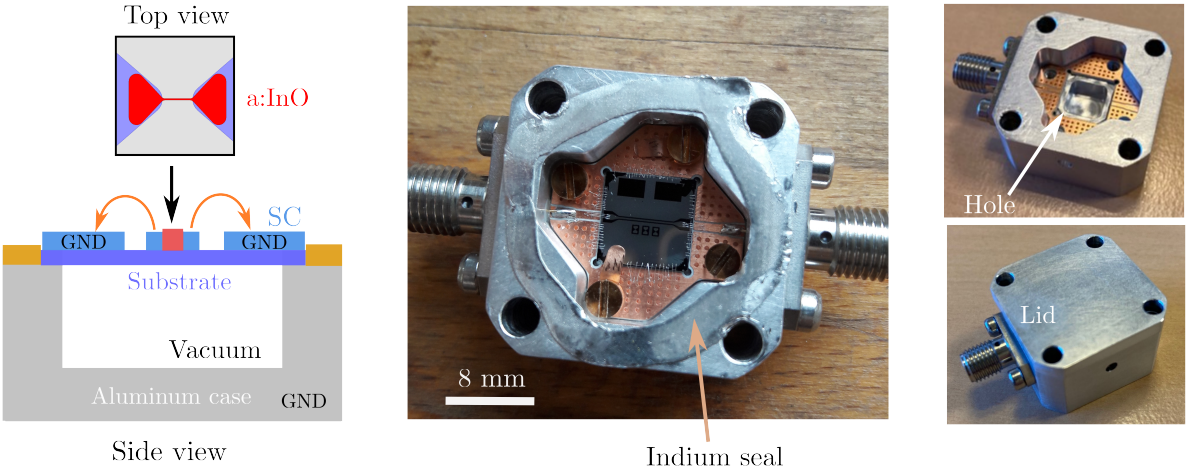

Fig. 7.9. Hybrid resonator packaging. Left: Side-view illustration of the sample environment. The sample lies atop a 3 mm-deep hole dug in the aluminum sample holder, so that the electric field (orange arrows) is mainly located in the sample plane. The ground plane is superconducting (Rhenium or TiN), and the same material composes the resonator pads, linked by a small volume of amorphous indium oxide (red). **Center:** Image of a sample mounted in the sample holder. The CPW feedline is micro-bonded to the RF lines, and is capacitively coupled to the three resonators (dark zones below the line). **Right:** Details of the hole in the sample holder, and the lid allowing a air-tight sealing. Some indium wire is also squeezed under the lid to act as a joint.

order of magnitude higher perfomances, this observation suggests that the limiting dissipation indeed comes from indium oxide itself.
One could argue however that a lossy interface between a:InO and TiN or Re could strongly reduce the resonator quality factor. This is true, but unfortunately quite difficult to prove.

We note that some hybrid devices display similar temperature dependence as the other indium oxide resonators studied in this thesis, namely a power-law frequency shift $\delta f(T)$ and a bell-shaped quality factor $Q_i(T)$. This once again suggests that the properties of Indium oxide are inherited by the hybrid device, along with their enhanced dissipation.

Finally, a most interesting result is the comparison to the reference TiN-only device. Fig. 7.10 shows a typical transmission trace for sample AC-TiN-15, where two of the resonators contain indium oxide and the last one is made of TiN entirely. It appears that the TiN resonator's performance is comparable to the study of [Amin et al., 2022] on the same film, with $Q_i \sim 10^5$ (even attaining one million at high power), while the resonators containing indium oxide have at least one order of magnitude lower quality factor.
With this last measurement we demonstrate without doubt that the environment, packaging and design do not cap quality factors at 10 000. Both the TiN and a:InO based resonators seemed to have a dissipation limited by their intrinsic properties.

Surprisingly enough, resonators made from pure indium have a quality factor of $Q_i \sim 10^4$, as shown in [McRae, Béjanin, et al., 2018]. The authors interpret this observation by noting that a thin layer of indium oxide could form atop their indium resonator.[5]

[5]This can be seen in two ways: either it confirms the dissipation measured in this thesis from bulk indium oxide, or it suggests that dissipation originates from surface oxides, growing after water exposure for instance

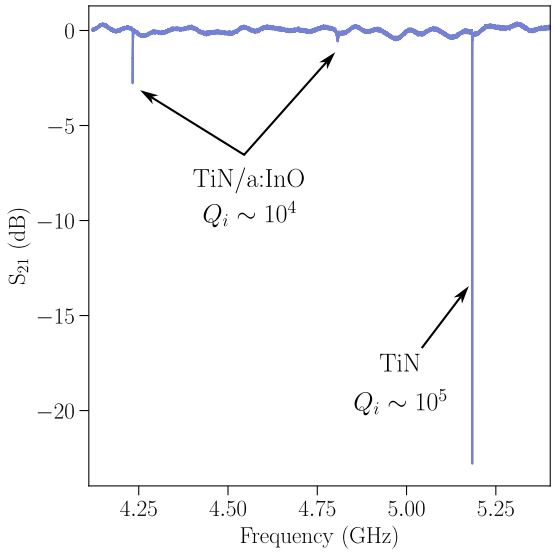

Fig. 7.10. Comparison of hybrid a:InO/TiN and all-TiN resonators. The first two resonators are hybrid a:InO/TiN resonators in the geometry shown in Fig. 7.8 (**Left**). The third resonator consists in TiN only, the inductive part of the device comes from the longer central length in a meander shape as displayed in Fig. 7.8 (**Right**) and the relatively high kinetic inductance $L_K \approx 33\ \mathrm{pH}/\square$ [Amin et al., 2022]. While the low power quality factor of the third resonator remains close to the one measured in [Amin et al., 2022] (a few 10^5), the two resonators incorporating a small volume of indium oxide have degraded quality factors below 10^4.

7.5 | Non-equilibrium quasiparticles as a source of dissipation

Another potential source of dissipation in superconductors is the presence of unbound electrons, known as Bogoliubov quasiparticles. While within BCS theory the number of such quasiparticle excitations should be exponentially small at low temperatures $k_B T \ll \Delta$, experimental works show that a relatively large residual quasiparticle (QP) population remains at the lowest temperatures (see Visser et al., 2011 for an example in aluminum).
The origins of such excess unpaired electrons are numerous and still not entirely understood. On very general grounds one can assume that non-thermal processes (such as radioactivity, cosmic rays ...) contribute to break Cooper pairs in the ground state, releasing quasiparticles [Cardani, Colantoni, et al., 2023].

The detrimental effects of excess QPs on superconducting circuits and qubits was foreseen not long after the birth of cQED [Martinis et al., 2009; Catelani, J. Koch, et al., 2011; Catelani, Schoelkopf, et al., 2011; Ioan M. Pop et al., 2014] and later works performed on large scale multiqubit processors demonstrated the existence of punctual release of quasiparticles (*quasiparticle bursts*) leading to correlated noise largely detrimental to quantum error correction schemes [McEwen et al., 2021; Wilen et al., 2021; Thorbeck et al., 2022].
These events were previously observed in the field of Kinetic Inductance Detectors (KIDs) as well as in disordered superconductors. Notably high kinetic inductance granular aluminum res-

([Detweiler et al., 2016] show that $-\mathrm{OH}$ hydroxyl groups form in presence of water.) The last interpretation could also apply to our resonators if the same oxide forms at the surface.

onators experience sudden drops of their resonance frequency approximately every 20 seconds, followed by a much slower relaxation back to their initial state [Grünhaupt, Nataliya Maleeva, et al., 2018; Henriques et al., 2019; Cardani, F. Valenti, et al., 2021]. These perturbations were interpreted as the signature of a punctual deposition of high energy particles on the circuit and substrate, starting a cascade of quasiparticle generation and recombination, potentially mediated by substrate phonons.
Further, anomalously low resonator quality factors measured in high-L_K grAl and TiN (beyond standard TLS limitations, see Fig. 7.7) were seen as the consequence of a larger-than-normal quasiparticle density in disordered superconductors [Grünhaupt, Nataliya Maleeva, et al., 2018; Amin et al., 2022].

On the origin of non-equilibrium quasiparticles A first source of quasiparticle generation is through absorption of infrared light. This effect can be strongly reduced by properly shielding the sample from external radiations, notably by using multiple light-tight shields at the different cryostat temperature stages [Barends et al., 2011; Córcoles et al., 2011].
The pair-breaking effect of weak residual magnetic fields can also lead to QP creation, and is routinely mitigated by the use of a μ-metal shield at base temperature (see [Gordon et al., 2022] and references therein).

More recently the effects of ambiant radioactivity on quasiparticle generation was demonstrated using qubits and resonators [Vepsäläinen et al., 2020; Cardani, F. Valenti, et al., 2021]. The method used in these works consists in modifying the sample environment by either heavily shielding it from radioactivity and cosmic rays (shielding the cryostat with lead bricks, or several kilometers under a mountain for instance) or on the contrary introducing a radioactive source in the cryostat's vicinity.
In both studies the qubits/resonator performances degraded when put in presence of the radioactive source, while they were enhanced under shielding. Also, QP burst rate observed in granular aluminum films was reduced by a factor 30 in the deep-underground lead-shielded environment, suggesting a correlation between these events and radioactivity.

By monitoring the quasiparticle population in real time in an aluminum island [Mannila et al., 2021] claim that mesoscopicaly large superconducting grains can remain free of quasiparticles for long times, up to seconds, between two QP burst events. Surprisingly, the QP burst rate in their experiment decreased continuously with time at base temperature in the cryostat (the decay rate was nearly inversely proportional to time after cool down). After 130 days in the cryostat the quasiparticle density had decreased by more than a factor ten. This observation seems incompatible with QP generation induced by radioactivity or cosmic rays.

Mitigation of quasiparticle density by engineering Strategies used to reduce the number of dissipative non-equilibrium quasiparticles are numerous, see [Catelani and Pekola, 2022] for a review.

A first idea consists in trapping QPS away from the sensitive parts of the circuit, in a vortex core, a normal metal electrode or a lower gap superconductor for instance.
A second approach aims at preventing pair breaking from happening in the first place: instead of trapping quasiparticles, one tries to trap phonons with energy larger than the gap, a potential pair-breaking agent. Phonons in the substrate are generated by the various sources discussed

above (such as ionizing radiations) and diffuse along the sample.[6] Each pair-breaking event is accompanied with the absorption of a phonon, and the recombination of two QPs re-emits a phonon with energy $\sim 2\Delta$.
A phonon trap is then simply a superconductor with lower gap than the main circuit, which role is to down-convert high energy phonons into lower energy excitations unable to break pairs in the circuit's larger-gap superconductor.
This approach has been used with success in MKID detectors [Karatsu et al., 2019] and resonators [Francesco Valenti et al., 2019; Henriques et al., 2019].
A similar scheme using a normal metal trap [Martinis, 2021] also turned out to be efficient [Patel et al., 2017; Iaia et al., 2022]. By turning the aluminum phonon-trapping ground plane to a normal metal using a magnetic field, [Bargerbos et al., 2023] obtained comparable quasiparticle density reduction, suggesting that phonon-traps made out of normal metals and superconductors have similar performances.

Coming back to our indium oxide samples, it is interesting to note that most of the geometries studied in this thesis include a combination of superconductors and normal metals which could act as phonon traps.
In the microstrip geometry the sample backside is gold-plated to act as a ground plane. The situation is similar to that of [Iaia et al., 2022], where a $10\ \mu\mathrm{m}$-thick copper backside ground plane provides a reduction in qubit errors by a factor 20, and [Bargerbos et al., 2023] where the $200\ \mathrm{nm}$-thick aluminum coplanar ground plane (turned into a metal in B field) allows a factor 2-5 improvement in qubit lifetime.
One important difference in phonon-trapping efficiency is of course the metal thickness: our gold ground plane is at most $200\ \mathrm{nm}$-thick, leading to a significantly reduced trapping rate. The presence of such an unintentional trap however must be kept in mind when discussing dissipation in indium oxide resonators in the microstrip geometry. Further efforts in reducing loss in our devices might involve a thicker metallic ground plane.
In the hybrid TiN/a:InO resonator discussed in last section, the TiN coplanar ground plane ($T_c = 3.9\ \mathrm{K}$) covers almost the entire chip. Unfortunately the gap of TiN is not much smaller than the one of indium oxide ($E_g \sim 450\ \mu\mathrm{eV}$), potentially reducing the effect of phonon trapping.
Finally, resonators in a 3D waveguide do not have metallization in contact with the substrate, and some samples in this configuration present enchanced frequency jitter, consistently with a larger density of non-equilibrium quasiparticles.

Influence of disorder on Two-Level Systems and quasiparticles We have seen so far that quality factors in indium oxide resonators are not limited by the usual TLS at the interfaces, but present features qualitatively consistent with TLS models. The other main loss mechanism, excess quasiparticle, could play a major role in the poor resonator performances reported here. We now discuss how disorder can influence the quasiparticle and TLS populations, and even bridge these two concepts.

Disorder in superconducting films generates spatial fluctuations of the gap amplitude $\Delta(\mathbf{r}) = \Delta_0 + \delta\Delta(\mathbf{r})$ where Δ_0 is the typical average gap value. Fluctuations $\delta\Delta(\mathbf{r})$ increase with disorder, as demonstrated by tunneling experiments [B. Sacépé, C. Chapelier, et al., 2008; Carbillet et al., 2020].

[6] According to [Martinis, 2021] more than 90% of the radiation energy on sample is converted into phonons, and about 57% of this phonon energy contributes in Cooper pair breaking.

Recent works put forward the idea that non-equilibrium quasiparticles could be trapped in these regions of lower gap (illustrated in Fig. 7.11). Such localized quasiparticles have a lower probability to recombine into a Cooper pair, resulting in an extra-long relaxation time [Bespalov et al., 2016; de Graaf et al., 2020].
Upon increase of disorder the traps become deeper, and the typical distance over which QPs can annihilate decreases: even a weak non-equilibrium agent can lead to a significant non-equilibrium quasiparticle concentration at $T = 0$ [Bespalov et al., 2016].

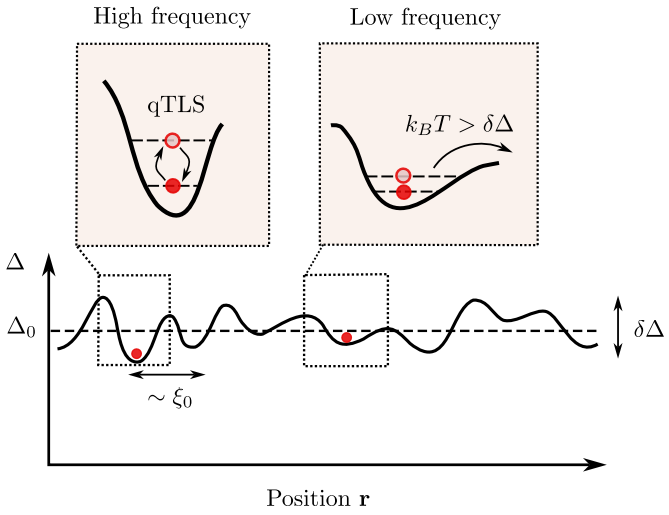

Fig. 7.11. Illustration of quasiparticles trapped by gap fluctuations. A quasiparticle (red dot) can localize in a superconducting region where local fluctuations of the gap $\delta\Delta$ are large. A well can contain multiple bound states, therefore forming an effective Two-Level System noted qTLS. The depth of the trap determines the qTLS frequency and its escape rate as illustrated in the insets. With modifications from [de Graaf et al., 2020].

Interestingly these traps can host multiple bound states. Keeping only the first two excited states then allows to introduce an effective Two-Level System arising from trapped quasiparticles, noted qTLS [de Graaf et al., 2020] (see Fig. 7.11).
The typical energy splitting of such a qTLS is proportional to the trap amplitude: as a consequence the qTLS density of states is not constant and depends rather strongly on frequency. QPs trapped in shallow wells recombine with higher probabilities than the ones localized in deep traps (but the latter are also less probable).
These qTLS[7], similarly to their glassy counterparts, should present the expected features predicted by the Standard Tunneling model, among which the power and temperature increase of quality factor observed in indium oxide.
The increase of Q_i with power was also interpreted as an enhanced de-trapping mechanism upon increase of circulating photon density, consistent with the experimental observation that relaxation times were reduced at stronger powers in granular aluminum [Grünhaupt, Nataliya Maleeva, et al., 2018].

More generally, the picture of trapped quasiparticles entails that even very rare non-equilibrium events (high energy impacts or any other source) lead to a relatively large quasiparticle density

[7] Potentially, another mechanism could create TLSs out of disorder. The hopping of localized Cooper pairs in a pseudogapped superconductor (see Chap. 2) could be seen as a local Two-Level System: the coherent tunneling of charge-$2e$ bosonic excitations generates a TLS-like electric dipole. [M. Feigel'man, Private communications.]

with exponentially slow relaxation time, detrimental to qubit coherence and resonator quality factors. This analysis seems to be applicable even in clean superconductors such as aluminum, where film thickness variations and Aronov-Altshuler effect can create shallow traps [de Graaf et al., 2020].

Finally, a recent work [Thorbeck et al., 2022] on a large scale multiqubits processor considers the interaction between ionizing radiations and TLS excitations: they observe that, while quasiparticle bursts do not significantly alter the qubit lifetimes, some TLSs experienced a long-lived frequency shift, suggesting a new interplay between radiations and defects.
The presence of strongly coupled TLSs of unknown origin was recently evidenced in granular aluminum [Kristen et al., 2023; Martin Spiecker et al., 2023]. The 'giant' TLSs found by [Kristen et al., 2023] have a an anomalously large dipole moment, orders of magnitude larger than the usual surface TLSs. Interestingly the number of such TLS increases with sample resistance, showcasing the effect of disorder.

We conclude by saying that all loss mechanisms mentioned so far (TLSs in glassy surfaces and in the bulk, non-thermal quasiparticles due to infrared radiations, cosmics rays and radioactivity...) must be considered when analyzing dissipation and decoherence in quantum circuits. More interestingly, these mechanisms are interdependent: high-energy radiations create quasiparticles than can get trapped and produce qTLSs or directly interact with surface TLSs. Inevitable gap fluctuations (even in clean superconductors) prevent excess quasiparticles from annihilating, resulting in a persisting quasiparticle background at $T = 0$.

7.5.1 Towards a universal upper bound on quality factor in superconductors ?

From the considerations above one could wonder if the quality factor of a superconducting resonator has an upper bound at a given disorder level.
To try to answer this important question we compile a set of data on superconducting resonators and plot the relation between quality factor Q_i and microwave response of the superconductor (represented here by the imaginary part of conductivity σ_2), as displayed in Fig. 7.12. All data points are taken at low power, near the single photon regime and at lowest temperature (few tens of mK).

In a two-fluid model of superconductivity one can write a complex, frequency-dependent conductivity $\sigma(\omega) = \sigma_1 + i\sigma_2$. The real part describes conduction via quasiparticles, and the imaginary part conduction from Cooper pairs.

Following [Tinkham, 1975] we write (for $\hbar\omega \ll \Delta$)

$$\sigma_1 = \frac{n_n e^2 \tau_n}{m_e} \tag{7.5}$$

$$\sigma_2 = \frac{n_s e^2}{m_e \omega} = \frac{1}{\mu_0 \lambda^2 \omega} \tag{7.6}$$

where n_n and n_s are the densities of quasiparticles (resp. paired electrons) and m_e is the electron mass. We expect the conservation of electrons: $n = n_s + n_n$ where n is the electronic density in the normal state. τ_n is the relaxation time for quasiparticles. In the normal state the Drude conductivity reads $\sigma_n = \frac{ne^2\tau_e}{m_e}$ where τ_e is the relaxation time for electrons.

To obtain the plot shown in Fig. 7.12 one then only needs to know the London penetration depth λ, or equivalently the sheet kinetic inductance (via $L_K^{\square} = \mu_0 \lambda^2 / d$ for a thin film of thickness d, or $L_K^{\square} = \mu_0 \lambda$ for the bulk), and the frequency at which the quality factor has been measured.

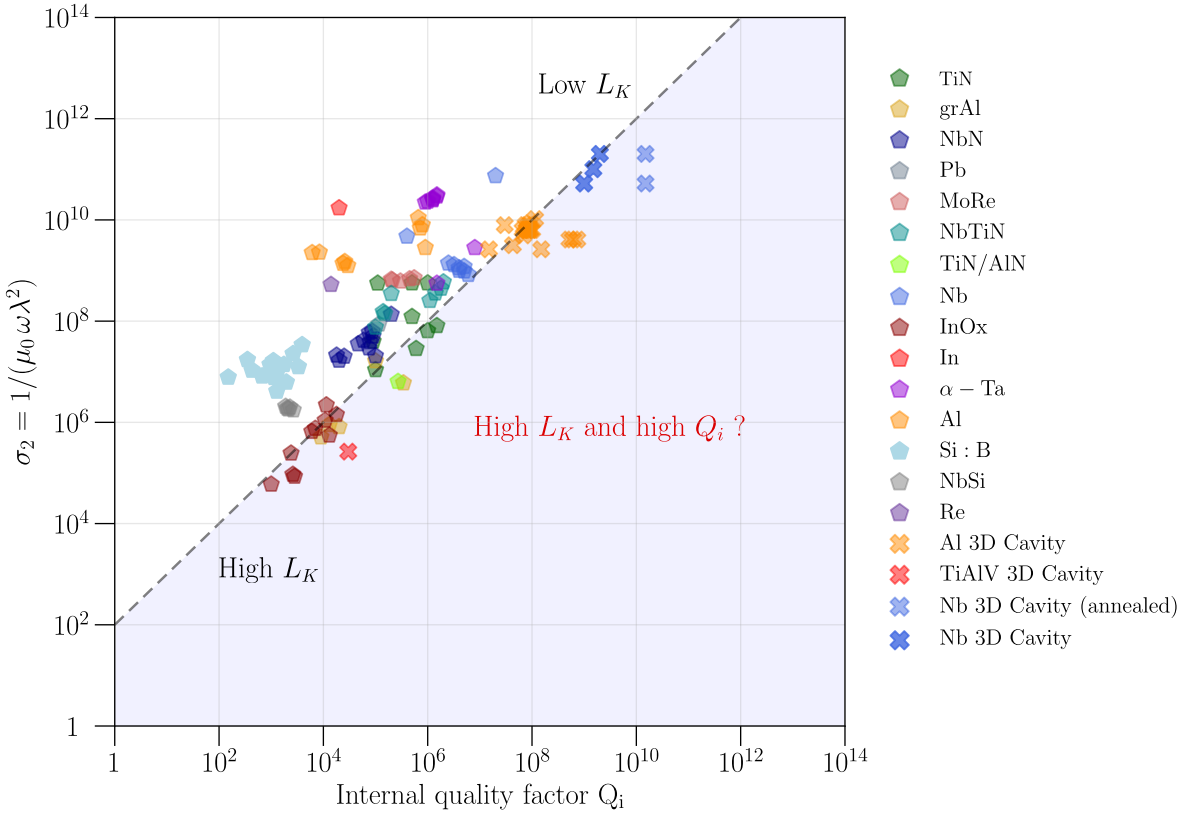

Fig. 7.12. Relation between internal quality factor and σ_2 in various materials. The quality factor is taken at low photon number $n \sim 1$ and lowest temperatures. Represented materials for planar resonators are: Ta [Lozano et al., 2022; Crowley et al., 2023; Jia et al., 2023], TiN [Amin et al., 2022; Richardson et al., 2020; R. Gao, W. Yu, et al., 2022; Sandberg et al., 2012; Shearrow et al., 2018], NbN [Niepce et al., 2019; Wei et al., 2020; C. X. Yu et al., 2021; Xu, Han, et al., 2019; Mahashabde et al., 2020; Foshat et al., 2023; Frasca et al., 2023], NbTiN [Müller et al., 2022; Bruno et al., 2015; Samkharadze et al., 2016], Nb [Verjauw et al., 2021; Noguchi et al., 2019; Altoé et al., 2022; Zhu et al., 2022], Al [Megrant et al., 2012; Jonathan Burnett et al., 2018; Earnest et al., 2018; Chien et al., 2023], NbSi [Le Sueur et al., 2018], TiN/Al [R. Gao, Ku, et al., 2022], grAl [He et al., 2021; Zhang et al., 2019; Rotzinger et al., 2016], Pb [Ebensperger et al., 2016], MoRe [V. Singh et al., 2014], Re [E. Dumur et al., 2016], In [McRae, Béjanin, et al., 2018], Si:B [Bonnet et al., 2022]. 3D cavities are also shown, in Nb [Romanenko et al., 2020], Al [Reagor et al., 2013; Kudra et al., 2020], TiAlV [Holland et al., 2017]. Dashed line shows the relation $\sigma_2 = 100\, Q_i$.

The materials displayed on this graph are very different intrinsically. Some are relatively clean, pure metals such as aluminum, niobium, lead, tantalum, rhenium or indium, some are strongly disordered nitrides or oxides, such as NbN, TiN, NbTiN, grAl, InOx. Some materials are more exotic alloys (boron-doped silicon Si:B, TiAlV, MoRe).
While most of these data concern planar superconducting resonators (mostly in CPW geometry), we also added 3D cavities that are known to provide high quality factors. The best Q_i in this study comes from SRF cavities used in accelerator physics by the Fermilab [Romanenko

et al., 2020].

As noted by [Dutta et al., 2022] most thin film superconductors belong to the *dirty limit*, that is their superfluid density is limited by electronic scattering. In our data survey only the purest niobium samples can be considered as clean; to estimate the superfluid density in these samples we use the method described in [Dutta et al., 2022], which give consistent results with the known literature.

Regarding the extraction of quality factors, we chose to take values in the single-photon regime, and at lowest temperature possible in order to get a fair comparison between these data obtained in different materials and experimental conditions. One important thing must be noted however: most of these quality factors are very likely to be limited by external loss mechanisms such as TLSs. This can be seen by the increase of quality factor with power or temperature in a large majority of these works.

It can be seen from Fig. 7.12 that quality factors generally increase with σ_2. A linear relation between these two quantities holds for seven orders of magnitude ($\sigma_2 \approx 100\, Q_i$, as displayed by the dashed line).
Note that we chose to use σ_2 to describe the microwave response, in part because it allows the normalization by the measurement frequency: it is well known that dissipation should be frequency-dependent.
Since $\sigma_2 \propto L_K^{-1} \propto n_s$ the results of Fig. 7.12 indicate that the quality factor grows with the density of Cooper pairs $Q_i \propto n_s$.
This seems compatible with the idea developed in [Bespalov et al., 2016; de Graaf et al., 2020]: quasiparticles trapped by gap fluctuations (which are enhanced by disorder) have a longer recombination time and induce dissipation.

As of now a superconductor having both large kinetic inductance and large quality factor (that would belong to the bottom right region of Fig. 7.12) has not been discovered. An important question is whether or not such a superconductor should exist.

Estimation of quasiparticle relaxation time To analyze this observation further I now try to relate quality factor and complex conductivity:[8]

$$Q_i = \frac{1}{\alpha}\frac{\sigma_2}{\sigma_1} \tag{7.7}$$

where the kinetic inductance fraction is $\alpha = L_K/(L_K + L_g)$. For strongly disordered superconductors one has $\alpha \sim 1$ while cleaner superconductors can have $\alpha \sim L_K/L_g \ll 1$.
Equation Eq. (7.7) is used frequently to describe the effect of quasiparticles on dissipation (at higher temperatures usually), see [Coumou et al., 2013] for instance.

[8] At microwave frequencies the surface resistance of a superconductor is the real part of the complex resistivity: $R_s = \mathrm{Re}\left[\frac{1}{\lambda(\sigma_1 + i\sigma_2)}\right] = \frac{1}{\lambda}\frac{\sigma_1}{\sigma_1^2 + \sigma_2^2}$. Since $\sigma_1^2 \ll \sigma_2^2$ one has $R_s = \frac{1}{\lambda}\frac{\sigma_1}{\sigma_2^2}$.

From the usual mapping of a superconductor at RF frequencies to a microwave transmission line: $Q_i = \omega\frac{L}{R_s}$ where $L = L_K + L_g$ is the total inductance [Pozar, 2011].
Injecting into the expression for R_s leads the result.

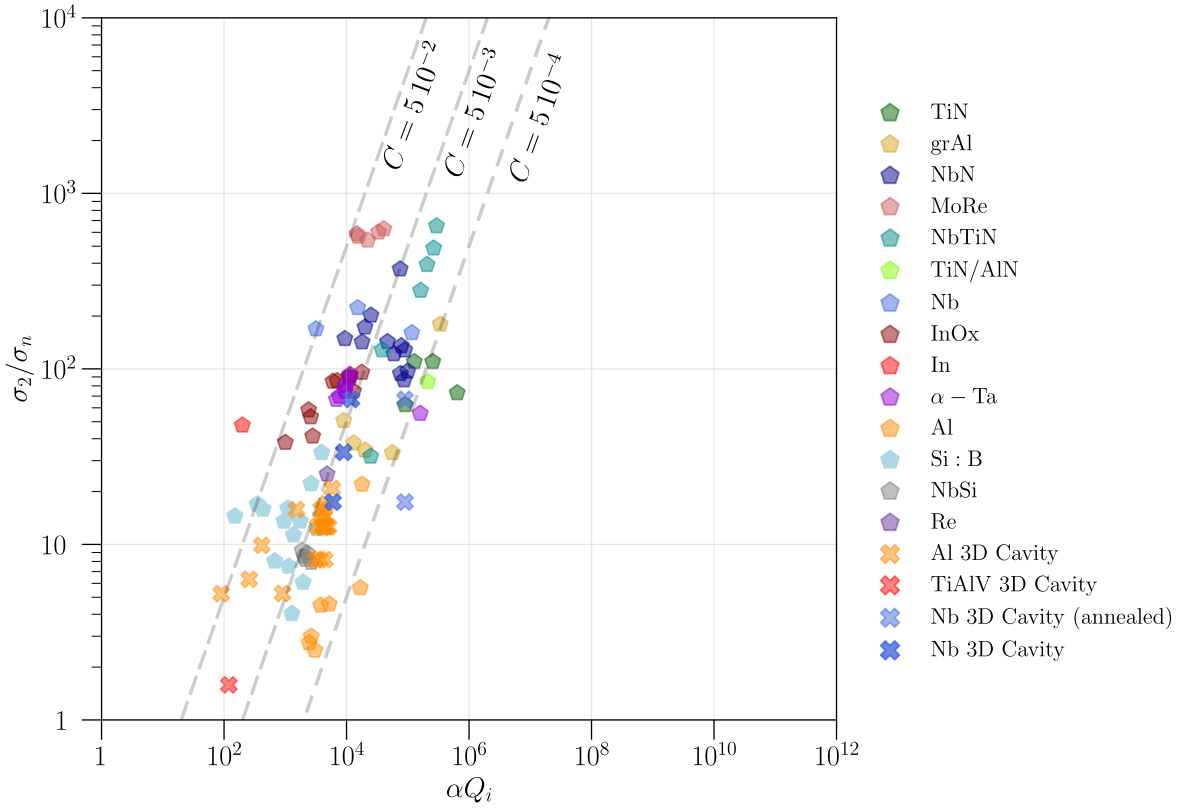

Fig. 7.13. Universal relation of superconductivity and dissipation. The quality factor is taken at low photon number $n \sim 1$ and lowest temperatures. Represented materials for planar resonators are: Ta [Lozano et al., 2022; Jia et al., 2023], TiN [Amin et al., 2022; Richardson et al., 2020; R. Gao, W. Yu, et al., 2022; Sandberg et al., 2012], NbN [Niepce et al., 2019; Wei et al., 2020; C. X. Yu et al., 2021; Xu, Han, et al., 2019; Foshat et al., 2023; Frasca et al., 2023], NbTiN [Müller et al., 2022; Bruno et al., 2015], Nb [Noguchi et al., 2019; Altoé et al., 2022; Zhu et al., 2022], Al [Megrant et al., 2012; Earnest et al., 2018; Chien et al., 2023], NbSi [Le Sueur et al., 2018], TiN/Al [R. Gao, Ku, et al., 2022], grAl [He et al., 2021; Zhang et al., 2019; Rotzinger et al., 2016], MoRe [V. Singh et al., 2014], Re [E. Dumur et al., 2016], In [McRae, Béjanin, et al., 2018], Si:B [Bonnet et al., 2022]. 3D cavities are also shown, in Nb [Romanenko et al., 2020], Al [Reagor et al., 2013; Kudra et al., 2020], TiAlV [Holland et al., 2017]. Dashed lines correspond to three values of the constant C.

Rewriting Eq. (7.7) by noting that $\sigma_1 = \sigma_n n_n(0)\tau_n/(n\tau_e)$ where $n_n(0)$ is the residual non-equilibrium quasiparticle density at $T = 0$:

$$\frac{\sigma_2}{\sigma_n} = C\,\alpha Q_i \tag{7.8}$$

where the prefactor C is related to quasiparticle density as $C = \left(\frac{n_n(0)}{n}\right)\left(\frac{\tau_n}{\tau_e}\right)$.
From this very simplistic two-fluid model one could potentially extract some relation between characteristics of a superconductor. This is what we investigate in Fig. 7.13, where we observe proportionality between σ_2/σ_n and αQ_i.

The normal state conductivity at low temperature σ_n is obtained from the references when available, and from [Hall, 1968] for pure metals when unspecified.

The kinetic inductance fraction α can be estimated from the geometry. For CPW resonators for instance, the geometric inductance L_g can be obtained by analytic formulas if the central conductor width and spacing to the ground are known. For cavities one must use electromagnetic simulations; for the aluminum cavities of [Reagor et al., 2013] for instance, the kinetic inductance fraction can be as small as $\alpha = 6\,10^{-6}$.

As can be seen on Fig. 7.13 the normalization by α and σ_n reduces considerably the scatter present in last graph. We plotted $\sigma_2/\sigma_n = C\,\alpha Q_i$ for three values of $C = 5\,10^{-2}$, $5\,10^{-3}\,5\,10^{-4}$. All data points are contained within this interval, with a best fit for $C \sim 5\,10^{-3}$.

Let us now try to analyze further this relation. What comes next is purely speculative and should not be taken too seriously at the moment.
Because of electron number conservation we can write $\frac{n_n}{n} = 1 - \frac{n_s}{n}$, and in the dirty limit $\frac{n_s}{n} \approx \frac{\pi\Delta\tau_e}{\hbar} \approx \left(\frac{l}{\xi}\right)^2$ [Dutta et al., 2022].
Since from Fig. 7.13 C is a constant, one gets

$$\tau_n = \frac{C\,\tau_e}{1 - n_s/n} = \frac{C\,\tau_e}{1 - \left(l/\xi\right)^2} \tag{7.9}$$

Eq. (7.9) gives the relation between relaxation time for quasiparticles τ_n and the characteristics of a superconductor in the dirty limit.
In the clean limit, for which all electrons are paired and $n_s \sim n$ one sees that $\tau_n \to \infty$, leading to a dissipationless flow of supercurrent $\rho_1 = 1/\sigma_1 \to 0$.
In practice however, the pure theoretical clean limit is rarely reached. One sees that $\tau_n = \tau_e$ for $n_s/n = 1 - C \sim 0.995$, which corresponds to the ultra clean Nb SRF cavity of [Romanenko et al., 2020], the purest material of this data set.

In the dirty limit the number of paired electrons decreases with disorder, and τ_n decreases. In the extreme dirty limit $l \ll \xi$ and Eq. (7.9) simplifies to $\tau_n \sim C\tau_e \sim 5\,10^{-3}\,\tau_e$.[9]

Finally since from Mattis-Bardeen theory $\frac{\sigma_2}{\sigma_n} \approx \frac{\pi\Delta}{\hbar\omega}$ one can write the quality factor for any superconductor

$$\alpha Q_i \sim \frac{1}{C}\frac{\pi\Delta}{\hbar\omega} \tag{7.10}$$

Taking for instance a NbN sample with data tabulated in [Dutta et al., 2022][10], $\alpha \approx 1$ and $\omega = 2\pi \times 4$ GHz one gets the estimate $Q_i \sim 10^5$, which is the order of magnitude measured in NbN microwave resonators.
For an aluminum 3D cavity such as the one of [Reagor et al., 2013] with $\alpha = 6\,10^{-6}$ and $T_c = 1.2$ K the quality factor becomes $Q_i \sim 10^9$.

[9] Using the Drude formula for τ_e one also gets $n_n\tau_n = \frac{Cm}{e^2}\sigma_n$, that is the relaxation rate scales with normal-state resistivity as $\frac{1}{\tau_n} \sim 5\,10^{-6} n_n\rho_n$. One would wonder if this decrease of quasiparticle relaxation time with disorder is related to an enhanced recombination time due to trapping of quasiparticles, as discussed in [Bespalov et al., 2016; de Graaf et al., 2020].

[10] $\Delta = 2.5$ meV, $n = 16.85\,10^{28}$ m^{-3}, $\rho_n = 1.14$ $\mu\Omega$m and $\tau_e = 855\,10^{-17}$ s.

Conclusion

This chapter aimed at investigating the main loss mechanisms in indium oxide resonators. It is found that some features are compatible with the presence of two-level systems (notably through the increase of quality factor with power and temperature), but these TLS are not present at the circuit interfaces. There is growing evidence that dissipation in our a:InO films is intrinsic, and related to the disorder strength.
Finally by compiling quality factors for superconductors in a broad range of disorders available from the literature we find that dissipation at microwave frequencies and superfluid density (seen as a measure of disorder) are simply related. This suggests a somewhat universal relation between material disorder and dissipation, the understanding of which could be of great importance for the fabrication of dissipationless superconducting circuits.

CHAPTER 8

a:InO in perpendicular magnetic field : an interplay of disorder and vortices

Applying a magnetic field to amorphous indium oxide films has been very fruitful in the past decades. Measurements of the sample resistance $R(B)$ under large fields have evidenced a Superconductor-Insulator Transition (this time driven by the magnetic field) and a giant magnetoresistance peak [Paalanen et al., 1992; Gantmakher et al., 2000; Maoz Ovadia et al., 2013]. It is believed that the B-driven insulating state is made of incoherent preformed Cooper pairs, with a pseudogap [Sambandamurthy et al., 2004; R. Crane et al., 2007; Shammass et al., 2012; Liu, Pan, et al., 2013; B. Sacépé, Seidemann, et al., 2015][1]

Surely, a microwave study of a:InO in magnetic field would provide interesting results [R. Crane et al., 2007]. More generally microwave resonators made of disordered superconductors have significant interest, both fundamental and technological.
Unlike clean materials, wires fabricated from superconductors like NbN [C. X. Yu et al., 2021], NbTiN [Xu, Han, et al., 2019; Samkharadze et al., 2016] or granular aluminum [Borisov et al., 2020] survive relatively large applied magnetic fields without dissipation.

In this chapter we study for the first time a:InO microwave resonators under perpendicular magnetic fields and obtain preliminary data.[2] We show an unusual suppression of superfluid density, and comment on the possible effects of vortex pinning.

8.1 | Suppression of superfluid density due to pair-breaking

For magnetic fields low enough so that no vortex has yet entered the superconducting strip, the effect of applied field is only to break Cooper pairs, therefore reducing the superconducting gap following $\delta\Delta/\Delta = (\pi/4)\Gamma/(k_B T_c)$ with the pair-breaking energy $\Gamma = D(ewB)^2/(6\hbar)$, where D is the diffusion constant, w the width of the stripline and e the electron charge [Tinkham, 1975].
The suppression of superconductivity by pair-breaking translates into an increase of kinetic inductance and therefore the reduction of resonator frequency as:

$$\frac{\delta f(B)}{f} = -\left(\frac{B}{B_0}\right)^2 \tag{8.1}$$

[1] Further, [M. Ovadia, Kalok, et al., 2015] evidenced a SIT driven by magnetic field occuring at finite (non-zero) temperature, suggesting by that occasion that indium oxide could be an interesting platform to look for signatures of Many-Body Localization (MBL) introduced by [D. Basko et al., 2006; D. M. Basko et al., 2007].

[2] A systematic study of a:InO resonators in B field is under way.

with $B_0 = (1/we)\sqrt{48\hbar k_B T_c/(\pi D)}$.

Using the BCS relation $\Delta = 1.76\, k_B T_c$ and the coherence length $\xi_0 = \sqrt{\hbar D/\Delta}$ one sees that B_0 scales as $B_0 \propto \hbar/(ew\xi_0)$. Therefore the main influence on the frequency shift amplitude at a fixed disorder is given by the strip width: the narrower the strip, the smaller the shift (and the less the superconducting resonator is affected by magnetic field). To further enhance B_0 the coherence length ξ_0 must be minimized, and therefore the superconducting film needs to be sufficiently disordered.

8.1.1 In the literature

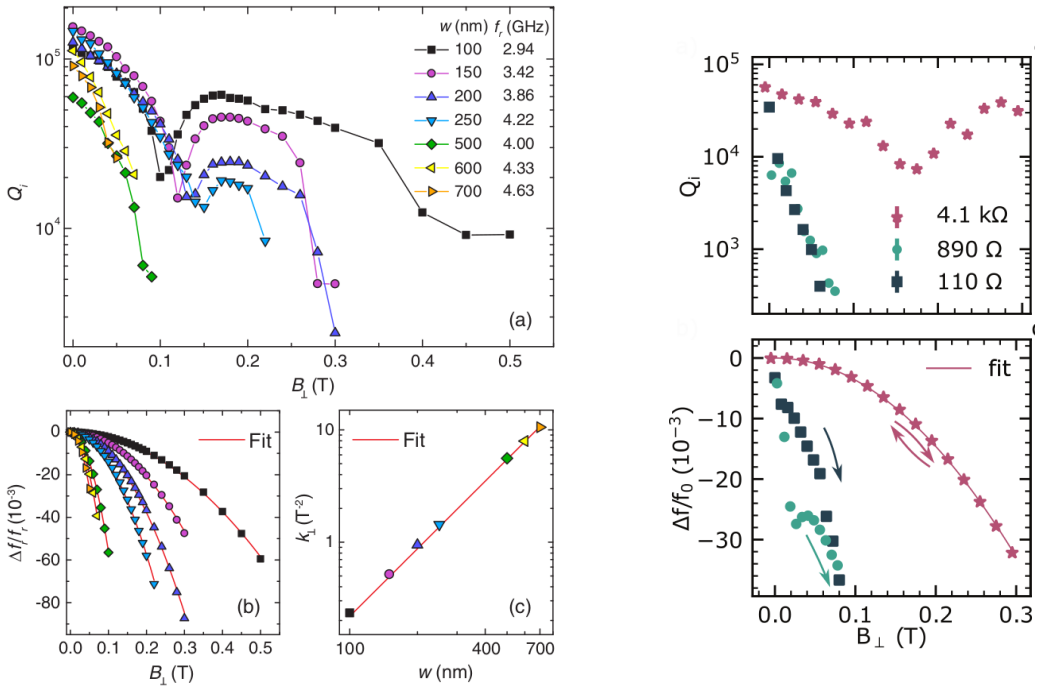

Fig. 8.1. NbTiN and NbN CPW resonators in perpendicular magnetic field. Left: Evolution of frequency shift and quality factors for NbTiN resonators of various central conductor widths w in perpendicular field. The frequency shift is nicely fitted by Eq. (8.1), with a prefactor $k = B_0^{-2}$ scaling with strip width as $\propto w^2$, as expected from the pair-breaking mechanism. From [Samkharadze et al., 2016]. **Right:** Same measurements for NbN resonators of three different widths (dark green corresponds to $w = 50\ \mu$m, light green $w = 2\ \mu$m and pink $w = 0.2\ \mu$m). Once again the frequency shift follows Eq. (8.1). From [C. X. Yu et al., 2021].

It turns out that Eq. (8.1) is fulfilled in a large variety of disordered superconducting wires, as displayed in Fig. 8.1 where we show the evolution of frequency shift and quality factors with applied perpendicular field in NbN and NbTiN films.
The results of [Samkharadze et al., 2016] in NbTiN films clearly demonstrate the scaling $B_0 \propto w^{-1}$ as expected from the pair-breaking scenario. Both [Samkharadze et al., 2016] and [C. X. Yu et al., 2021] (see also [Kroll et al., 2019; Borisov et al., 2020]) observed a reduction of quality factor with perpendicular field and, in the narrowest strips, a subsequent increase of $Q_i(B)$. This apparent dip in quality factor at $B \sim 0.1 - 0.2$ T is observed to shift with resonator frequency and was interpreted as the result of the coupling to a magnetic impurity.

This process follows the resonance condition $hf_r = g\mu_B B$, with an extracted Landé factor of the order of $g \sim 2$.
We note that, probably for technical reasons, most studies of resonators in perpendicular field do not show results for fields larger than ~ 0.5 T.[3]

8.1.2 In indium oxide resonators

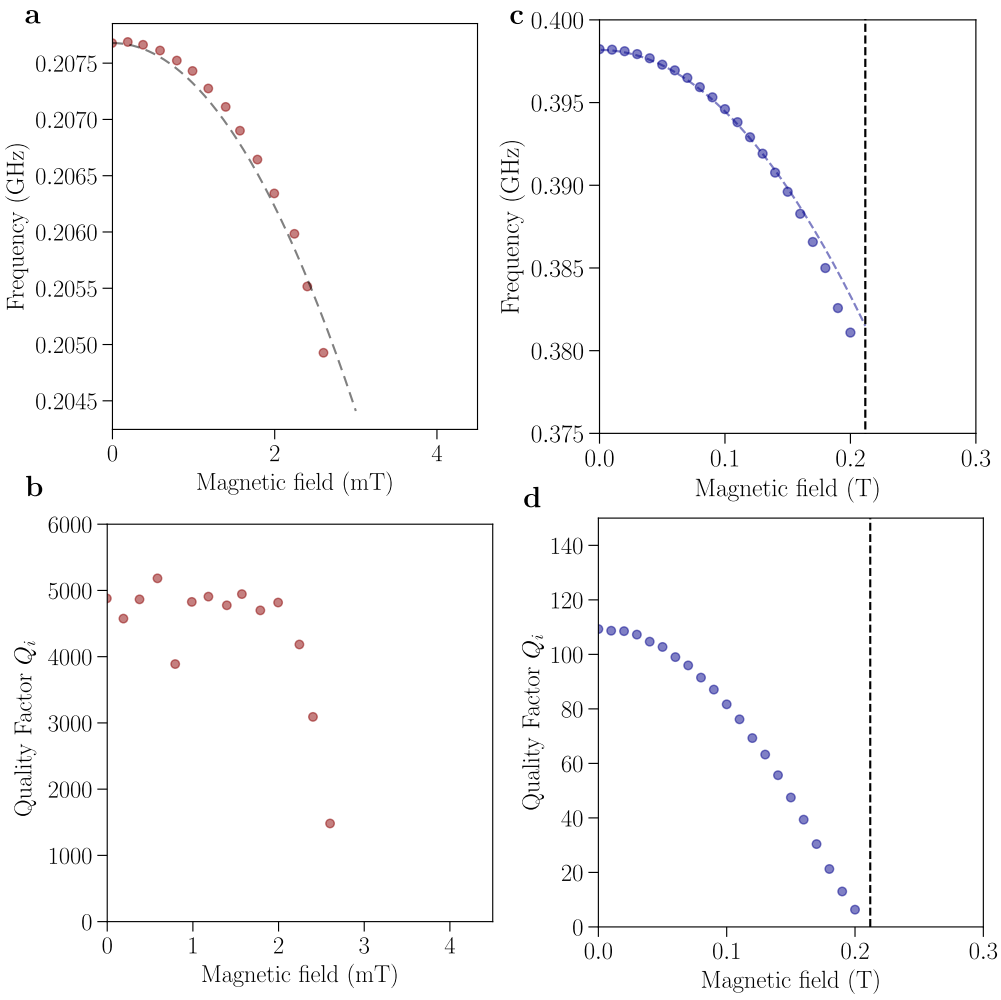

Fig. 8.2. Frequency and quality factor in perpendicular magnetic field for two disordered a:InO samples. a-b Sample TC017 (width $w = 1$ μm) has $L_K = 6$ nH/□ and $T_c \sim 1.1$ K. Resistance measurements $R(B)$ show a $B_{c2} \sim 40$ mT (see later). Black dashed line shows a fit to Eq. (8.1) with a $B_0 = 24$ mT, while the theoretical BCS prediction is $B_0 \sim 178$ mT. Above 2.6 mT the quality factor drops abruptly and the mode vanishes. **c-d** DC measurements on Sample TC047 (width $w = 100$ nm) could not be performed. Blue dashed line is a fit to Eq. (8.1) with $B_0 = 1$ T. Vertical dashed line shows the critical field $B_1 = 0.21$ T above which a first vortex enters the strip (Eq. (8.2)). Both mode frequency and quality factor disappear above B_1.

We now turn to disordered indium oxide resonators in perpendicular field only, allowing us to reach fields as high as 13 T in the transverse plane. Microwave measurements are performed

[3]Most works focus on the parallel field response, and it is often very costly and challenging to operate a multi-axis coil able to reach large fields on all directions.

at low frequencies ($f \sim 1$ MHz up to ~ 4 GHz), in the **setup B** presented in Appendix C.3.

Fig. 8.2 displays the decrease of frequency and quality factor for two indium oxide resonators of different geometries and disorders. Both samples show a quadratic suppression of superfluid density according to Eq. (8.1). As expected, the narrower strip (width 100 nm) withstands magnetic field better than its wider counterpart (width $w = 1$ μm), as the former displays measurable resonances up to $B \sim 0.2$ T while the latter is suppressed at much lower fields $B \sim 2.5$ mT.

For strongly disordered indium oxide one should expect that the above model would fail to describe quantitatively the data, as Ginzburg Landau and BCS formalisms are not supposed to capture the physics of pseudogapped superconductors. At moderate disorders one should however expect a qualitative agreement with the pair-breaking formula presented here.

8.2 | New observations in indium oxide

In this section we discuss new results which were not commented previously, and go beyond the usual pair-breaking mechanism.

Fig. 8.3 displays the result of the application of a perpendicular magnetic field to the indium oxide sample TC007 which was studied previously at zero-field. The wire is 1 μm-wide and 3.5 mm-long, with a measured critical temperature $T_c = 2.5$ K (normal state resistance $R_n = 3.2$ k$\Omega/\square$), and the zero-B kinetic inductance measured via two-tones spectroscopy is $L_K = 1.5$ nH$/\square$. From the measurement of the resistance upon increase of field $R(B)$ we extract a critical field $B_{c2} \sim 11$ T where resistance starts to increase.

First, the quality factor $Q_i(B)$ drops at low field ($B \sim$ a few mT) and saturates upon increase of field at a value $Q_i \sim 100$.
Secondly, the frequency shift has a completely different behavior: instead of being curved downwards (as expected for a quadratic suppression $\propto B^2$) we observe an *upward* curvature (see Fig. 8.3 panels **b-d**). As B increases the frequency shift slows down, almost in a logarithmic fashion, up to the relatively large perpendicular field $B = 1.8$ T.
The frequency shift amplitude is also much larger: while the latter was smaller than a few tens of MHz in previous data, here the frequency decreases by more than 200 MHz, about 50% of the initial frequency.

To further confirm this unusual behavior, we performed two-tones spectroscopy at several fields to extract the field-dependent kinetic inductance $L_K(B)$.[4] The resulting evolution of kinetic inductance is displayed in panel **c**.
Knowing the inductance at zero-field $L_K(0)$ one can finally convert this quantity into a superfluid stiffness $\Theta(B)$, as shown in panel **d** (red triangles). The superfluid stiffness can also be obtained from the frequency shift (and knowing $L_K(0)$), leading to the blue data points on panel **d**.
As can be seen both data sets coincide, demonstrating that the measurement of the frequency shift is a robust (and much faster) measurement of the superfluid density suppression. This demonstrates that it is acceptable to work with the more convenient $f(B)$.

[4] As discussed in the rest of this thesis the kinetic inductance is extracted from the dispersion relation $\omega(k)$ of plasmons.

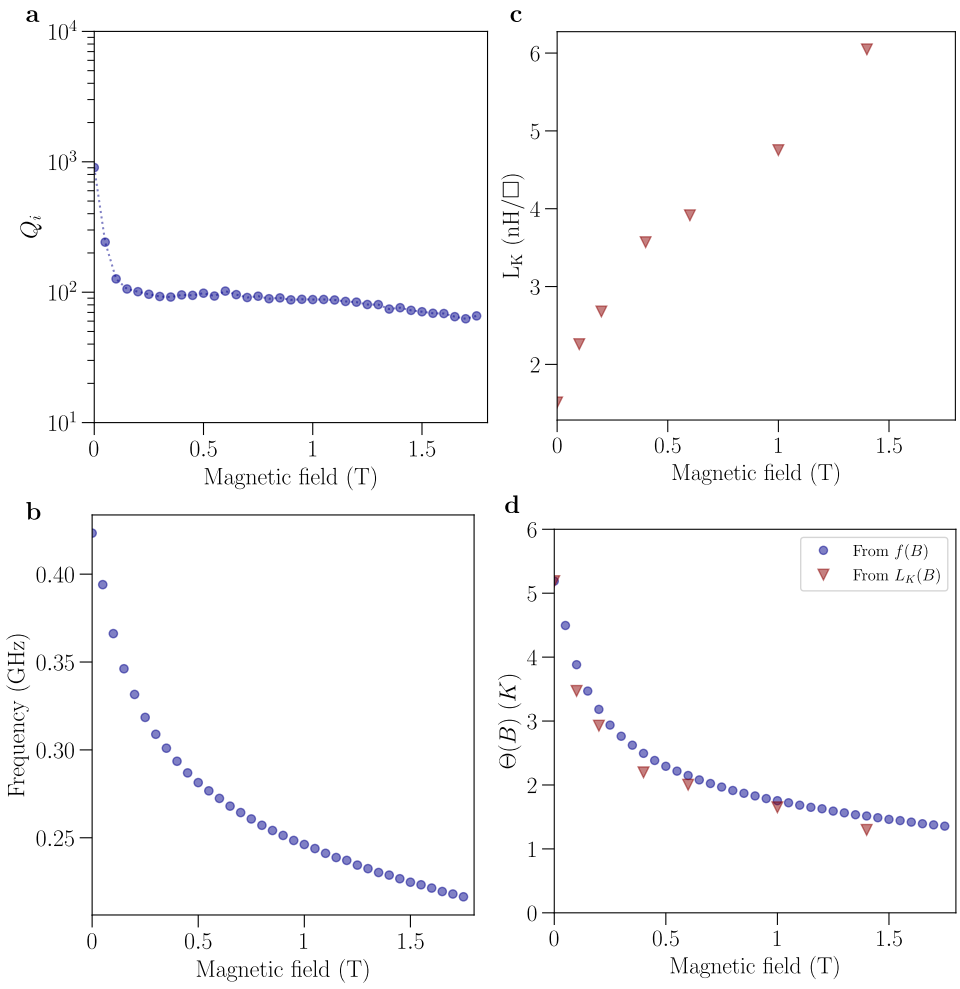

Fig. 8.3. Microwave response of a disordered indium oxide wire in perpendicular magnetic field. Sample TC007 (width $w = 1\ \mu\mathrm{m}$) was previously measured in a cryostat without field. In this new measurement run it displayed a normal state resistance $R_n = 3.2\ \mathrm{k}\Omega/\square$ and critical temperature $T_c = 2.5\ \mathrm{K}$. From the $R(B)$ measurement we extract a critical field $B_{c2} \sim 11\ \mathrm{T}$. **a-b** At larger fields (up to 1.8 T) the quality factor initially drops and seemingly saturates at $Q_i \sim 100$ while the frequency continuously decreases. **c** Using two-tones spectroscopy at various fields we extract the B-dependent kinetic inductance $L_K(B)$. **d** From the measurements of $f(B)$ and $L_K(B)$ we obtain the evolution of superfluid stiffness with B, $\Theta(B)$. Both curves obtained from very different methods coincide nicely.

One notes that the peculiar suppression of superfluid stiffness $\Theta(B)$ can be extrapolated to higher fields. Doing so would result in a final suppression of Θ to zero for very high magnetic fields of a few tens of Tesla, close to B_{c2}. On the contrary it is found that both Q_i and f disappear above $1.8\ \mathrm{T}$.

Additionally, previous measurements of the superfluid stiffness in disordered indium oxide present a similar trend versus perpendicular magnetic field: Fig. 8.4 shows $\Theta(B)$ for three measurement frequencies, as measured in [R. Crane et al., 2007]. The strongly disordered sample (see legend) is patterned into a disk and inserted in a resonant microwave cavity, allowing the measurement of the complex conductivity $\sigma(\omega, T, B)$. From the imaginary part $\sigma(\omega, B)$ the authors extract the superfluid stiffness versus B at a fixed temperature $T = 0.5\ \mathrm{K}$. It is found that $\Theta(B)$ has an upward curvature, similarly to what was seen in Fig. 8.3 panels

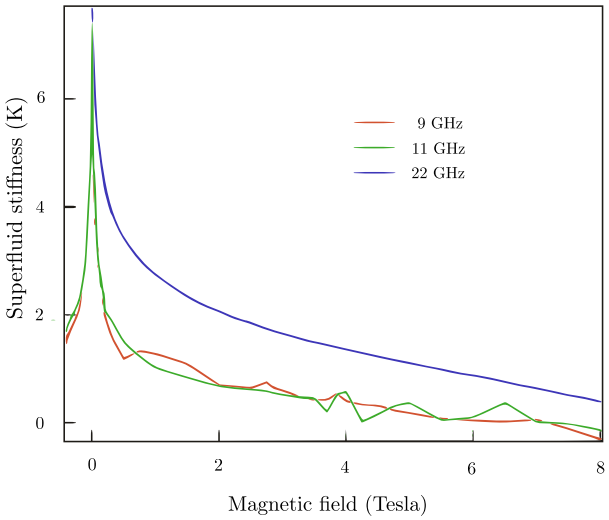

Fig. 8.4. AC measurement of superfluid stiffness versus perpendicular field in an indium oxide film at $T = 0.5$ K. A 20 nm-thick disordered aInO sample shaped as a 3 mm-diameter disk is placed in a microwave resonant cavity, allowing the measurement of the complex conductivity. Sample has $T_c \approx 2$ K, $R_n \approx 7$ kΩ/□ and $B_{c2} \approx 9.5$ T, as measured in DC on a companion co-evaporated sample. From [R. Crane et al., 2007]

b-d. This observation from a different group and in different experimental conditions confirms the unusual behavior of superfluid density at higher field in disordered indium oxide.

8.2.1 Critical field for the penetration of vortices in a thin film

So far we considered theoretically the effects of a weak magnetic field, at which no vortex has yet penetrated the strip. Obviously at larger fields the effect of vortices becomes important and must be taken into account. This is what we expose in this section.

The expulsion of magnetic field from a narrow superconducting strip made of thin film of type-II superconductor is quite different from the bulk case. For a thin film of thickness d and bulk penetration depth λ one can define a 2D penetration length Λ (the Pearl length already discussed in this thesis) as $\Lambda = \lambda^2/d = L_K^{\square}/\mu_0$. For strongly disordered films the London length is large, and for a narrow strip of width w one easily has $\Lambda \gg w$. Therefore screening of magnetic field is very weak, and vortices interact via stray fields outside the film over the long distance $\sim \Lambda$.
For these reasons the critical field above which a first vortex can appear in the strip is not related to the usual bulk H_{c1}.

Critical field B_1 It can be shown that two competing forces act on a vortex in this geometry [Likharev, 1971; Stan et al., 2004]. A first force tries to *expel* the vortex by pushing it towards the edges of the wire, because of image antivortices building up outside the strip. A second force tends to *attract* the vortex towards the center of the strip, from interactions with Meissner currents. This second force is proportional to B: at large enough fields the second force overcomes the first one, and a vortex penetrates the strip.

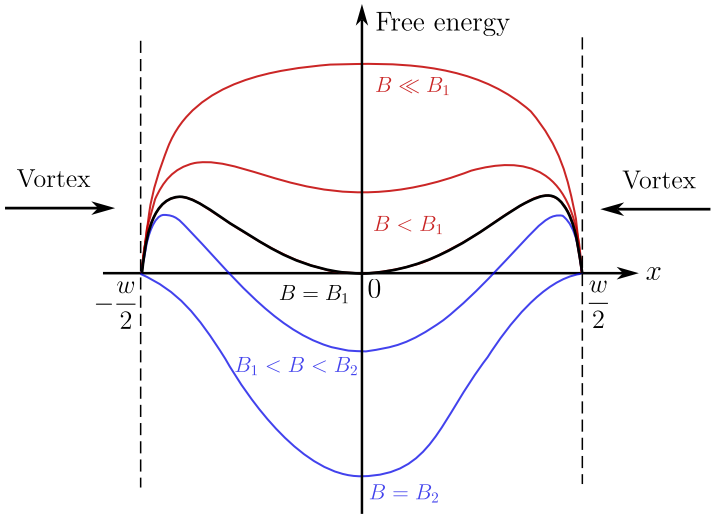

Fig. 8.5. Vortex free energy for different applied magnetic fields. Dependence of Gibbs free energy for a single vortex on its position with respect to the center of the strip x (width w) for several applied fields, and under condition $\xi \ll w \ll \Lambda$. At very low fields the energy cost to enter the strip is large and the vortex is expelled (red curves). Above the critical field B_1 the free energy becomes negative and it is energetically favorable for a vortex to penetrate the strip (black curve). At higher fields $B_1 < B < B_2$ the minimum of free energy is absolutely stable and vortex configurations lower the system energy. However the presence of a surface barrier at the edges prevents vortices from entering the film (first blue curve). Finally at $B > B_2$ the surface barrier vanishes and vortices freely enter the strip to lower the total energy. From [Likharev, 1971; Stan et al., 2004].

This situation leads to a critical field B_1 at which the free energy is minimum and has a stable equilibrium: vortices can exist in the wire only above B_1 defined as [Likharev, 1971; Stan et al., 2004]

$$B_1 = \frac{2}{\pi}\frac{\Phi_0}{w^2}\ln\frac{w}{4\xi} \tag{8.2}$$

where $\Phi_0 = h/(2e)$ and ξ is the dirty limit coherence length.

Eq. (8.2) is quite remarkable, as it states that this critical field is independent of disorder and superconducting characteristics of the material (apart from the weak dependence on ξ in the logarithm).

An illustration of the behavior of free energy across the wire width is displayed in Fig. 8.5, representing the different regimes of magnetic fields. At low magnetic fields the energy cost for a vortex to enter the strip is large and the vortex is expelled out of the wire. At $B > B_1$ vortex configurations tend to lower the system energy.

Critical field B_2 Looking at the $B > B_1$ region of Fig. 8.5 one sees that regions where the free energy remains large exist close to the strip edges. The existence of such surface barriers preventing a vortex from entering the strip was discussed by [Likharev, 1971] in the case $\xi \ll w \ll \Lambda$.

The critical field above which surface barriers vanish, allowing a first vortex to penetrate is [Likharev, 1971; Maksimova, 1998]

$$B_2 = \frac{\Phi_0}{2\pi\xi w} \tag{8.3}$$

Fig. 8.5 illustrates the suppression of surface barriers above B_2: vortices can enter the wire freely to lower the total free energy.

Relation with indium oxide samples For sample TC017 (panels **a-b** of Fig. 8.2), this critical field is $B_1 \sim 5$ mT, not far above the field at which the resonance is lost.
For sample TC047 (panels **c-d** of Fig. 8.2) the critical field $B_1 \sim 0.21$ T is represented by the dashed vertical line. It turns out that both quality factor and resonance cease to exist close to B_1, as shown by the vertical black dashed line. At the second critical field $B_2 = 0.65$ T resonances have already disappeared.

Discussing now sample TC007 which presented an unsual suppression of superfluid density (Fig. 8.3), we estimate $B_1 \sim 5$ mT and $B_2 \sim 0.21$ T. Therefore vortices clearly entered the wire, potentially suppressing both frequency and quality factor.

8.2.2 Observing both pair-breaking and vortex-related effects

Can we observe the cross-over between pair-breaking and vortex related physics ?

By studying a narrower wire $w = 300$ nm (sample TC050) as displayed in Fig. 8.6 we answer positively to this question. On all plots the black dashed vertical line represents the first critical field B_1, and the red vertical line the second critical field B_2. Panel **a** clearly shows a change in the frequency behavior exactly at B_1: at lower fields the shift is small, and above B_1 it becomes much larger, with an upward curvature similarly to sample TC007 (note here the log scale on x axis). Converting the frequency into superfluid stiffness $\Theta(B)$ leads to the data presented in panel **d**.
We show in panel **c** that the low-B part of the frequency shift actually follows the quadratic law $\propto B^2$ of Eq. (8.1), with parameter $B_0 = 0.25$ T. Taking $T_c = 2.5$ K, $w = 300$ nm and $D = 0.3$ cm^2/s gives the theoretical value $B_0 = 0.89$ T. Once again the estimation from BCS theory predicts a weaker effect of pair breaking than what is found experimentally.
At lowest fields the resonator is indeed free of vortices, and the superfluid density suppression is driven by pair-breaking.

Penetration of vortices induces dissipation. This can be seen from panel **b**, where it appears that the resonator quality factor drops abruptly by more than an order of magnitude very close to the first critical field B_1 (vertical black line). The drop actually occurs at slightly lower field (around 30 mT). By using Eq. (8.2) and setting $w = 350$ nm (to account for an eventual broadening of the strip during the lithography process for instance) we get a new estimation for B_1 exactly at the jump, as displayed by the blue vertical line. Further comments on dissipation will be done later.

How do vortices enter the strip below B_2 ? As evidenced by Fig. 8.6 the two critical fields for vortex entry B_1 and B_2 are not identical. Both quantities mostly depend on the strip width, so the ratio B_2/B_1 is expected to decrease upon reduction of w.
This is indeed what is seen, with $B_2/B_1 \sim 42$ for sample TC007, $B_2/B_1 \sim 13$ for sample TC017 and $B_2/B_1 \sim 5$ for sample TC050.

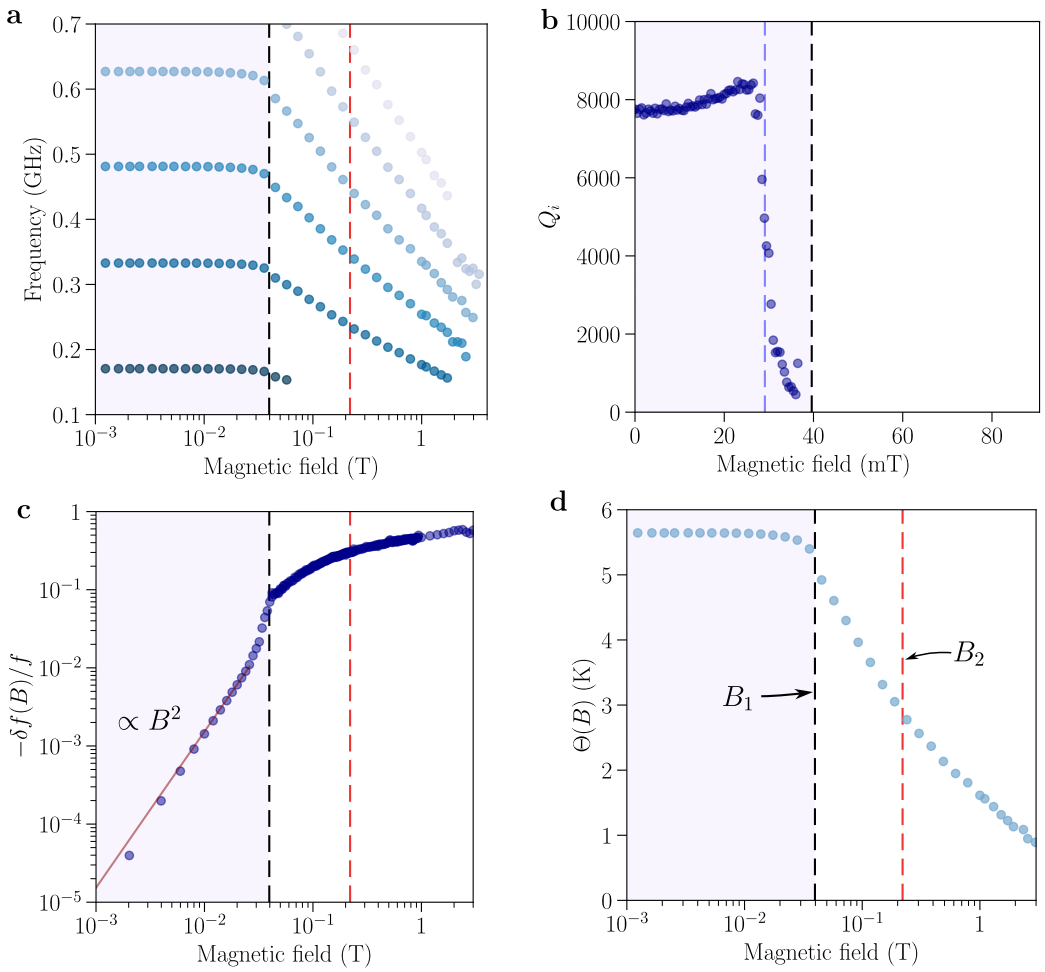

Fig. 8.6. Observing both pair-breaking and penetration of vortices. Sample TC050 has width $w = 300$ nm, and has a kinetic inductance at zero-B $L_K \sim 1.4$ nH/□. On all panels the black vertical dashed line shows the first penetration field $B_1 \approx 39.6$ mT calculated from Eq. (8.2) and $\xi = 5$ nm, as measured in indium oxide. Red dashed line shows the critical field for the surface barrier $B_2 \sim 0.22$ T according to Eq. (8.3). **a** Frequency versus magnetic field for the first modes of the resonator. At $B = B_1$ the frequency behavior changes clearly, with a much faster reduction of frequency. Above B_2 one observes a slight change of slope. **b** Quality factor versus field. At fields approaching B_1, Q_i drops abruptly, down to a few hundreds. Dashed blue line shows an estimation of B_1 by taking a larger width $w = 350$ nm. **c** Normalized frequency shift $-\delta f(B)/f$ in log-log scale. At low fields below B_1 the frequency shift is $\propto B^2$, as predicted from Eq. (8.1). Red line is the square law $\propto B^2$ with $B_0 = 0.25$ T. Above B_1 the shift has much larger amplitude and is not a simple power law. **d** Extracted evolution of superfluid stiffness $\Theta(B)$.

Looking carefully at panels of **a-d** of Fig. 8.6 one can notice a small 'break' in the frequency suppression happening at B_2. Above B_2 the superfluid stiffness suppression seems to slow down slightly. This is quite unexpected as one would expect a larger number of vortices penetrating in the strip in this range of magnetic fields.

This also raises the following question: since vortices start to enter the strip at $B_1 < B_2$ (as evidenced by the plots above and previous studies [Stan et al., 2004]) then they must go through the surface barrier, even at low temperatures where thermal energy is weak.
Then, how do they enter the film ? One possibility for this would be the quantum tunneling of

vortices through this energy barrier. Although quite exotic, this mechanism could be in part favored by the presence of a pseudogap that reduces single particle excitations. [M. Feigel'man, Private communications]

To our knowledge this question was never raised before. In fact experimental works of [Stan et al., 2004] focused on field-cooled resonators, hence avoiding the issue of edge barriers.

8.3 | Effect of weak pinning on superfluid density

We now need to account for the disordered nature of our indium oxide films. In this section we follow some preliminary calculations made by Mikhail Feigel'man to describe the suppression of superfluid density in disordered superconductors under applied magnetic field.

In absence of pinning the Lorentz force would tend to guide vortices towards the center of the strip, consistently with Fig. 8.5. At moderate fields, the middle region of the wire only is filled with vortices, while the outer regions are free of vortex.
The effect of disorder is to *pin* vortices before they reach the center, with an effect that opposes the Lorentz force. As a result vortices occupy only two substripes of the wire: both center region and outer parts of the wire contain no vortex.
In the region filled with vortices a constant current J_c flows: this quantity depends on the pinning strength and therefore on sample disorder. It follows that penetration of vortices is hindered by pinning.

This consideration modifies the equation for the first penetration field B_1 as

$$B_* = B_1 \left(\frac{1}{2} + \sqrt{\frac{1}{4} + j_c^2} \right) \tag{8.4}$$

where the dimensionless parameter j_c is defined as $j_c = (2L_K J_c)/(wB_1) \propto w$.
For a narrow wire (or low disorder $L_K \ll 1$) one has $j_c \ll 1$ and the penetration field is given by Eq. (8.2): $B_* \approx B_1$. For larger films $B_* > B_1$.

One now has to take into account two contributions to the superfluid stiffness. First, the center vortex-free region is almost unaffected by magnetic field (only the small pair-breaking effect must be considered). Second, the rest of the wire has a much lower superfluid stiffness due to the presence of pinned vortices, as can be seen by the increase of kinetic inductance with B: $L_K(B) = L_K(0) \left[1 + \frac{B}{B_1} \frac{\xi}{2wj_c} \right]$.

Vortex-free and vortex-full contributions to the total superfluid stiffness act in parallel, allowing to obtain the full expression for the supression of superfluid density valid above B_*:

$$\frac{f(B)}{f(0)} \approx \left[\sqrt{\left(j_c \frac{B_1}{B} \right)^2 + \frac{B_1}{B}} + \frac{1 - \sqrt{\left(j_c \frac{B_1}{B} \right)^2 + \frac{B_1}{B}}}{1 + \frac{B}{B_1} \frac{\xi}{2wj_c}} \right]^{1/2} \times \left(1 - \frac{\pi^2}{6} \frac{\xi^2}{w^2} \right) \tag{8.5}$$

where the only unknown parameter is the dimensionless j_c.

Fig. 8.7 shows the result of a fit for the frequency shift of samples TC007 and TC050 with the vortex-pinning model Eq. (8.5), keeping j_c as a free parameter.

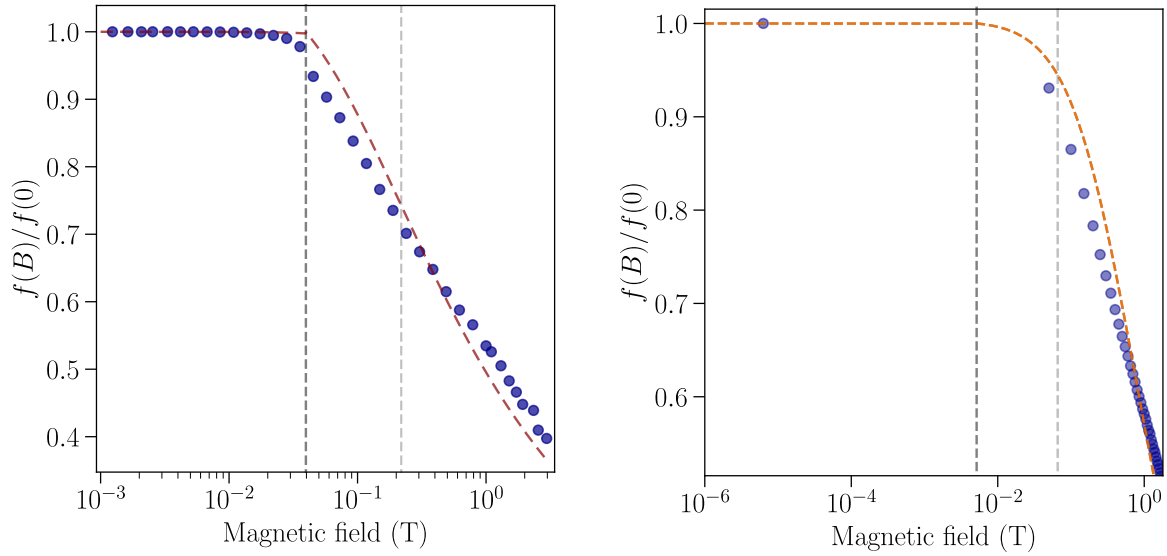

Fig. 8.7. Comparison of a:InO data and the vortex-pinning model for two samples. For both samples black vertical line shows the critical field B_1, the grey vertical line represents B_2, and red dashed line is a fit to Eq. (8.5), j_c being the only fitting parameter. **Left:** Sample TC050 ($w = 300$ nm). From the fit one finds $j_c = 0.013$. **Right:** Sample TC007 ($w = 1$ μm). One gets $j_c = 0.18$. Note that for this sample (and from the available data) it is not easy to say whether the effect of vortex pinning becomes visible at B_1 or at B_2.

By fitting the $f(B)$ curves to the model one can extract the parameter j_c, which is found to be small, as expected. For the narrowest wire we obtain $j_c = 0.013$, and for the larger strip $j_c = 0.18$. Recalling that one should have the scaling $j_c \propto w$, these observations are reasonable.

To further confirm this unsual suppression of superfluid stiffness with magnetic field and its interpretation as the manifestation of pinned vortices, we need to perform a systematic measurement of a:InO of various widths and disorders. Such study is currently work in progress.

8.3.1 Hysteretic behavior and vortex-induced dissipation

We now briefly comment on dissipation induced by magnetic field.

Most a:InO samples presented in this preliminary study display an abrupt drop of quality factor at a perpendicular field close to the first penetration field B_1. See for instance Fig. 8.2 panels **b-d**, Fig. 8.3 panel **a**, or Fig. 8.6 panel **b**.

A similar observation was detailed in granular aluminum resonators [Borisov et al., 2020], and was interpreted as the effect of fluxons (vortices) nucleating in the film.
The authors show that when applying a field up to 0.6 mT the frequency shift (following the pair-breaking $\propto B^2$ model) is reversible: measurements made when ramping the field up or down give the exact same result. When applying a field $B > 0.6$ mT for the first time however, Q_i drops sharply, and the frequency shift becomes non-reversible.
The authors define a critical field B_{th} below which the effect of B on superconductivity is reversible (the system is in the so-called *elastic* regime), and above which up and down sweeps

no longer coincide (defining the *plastic* regime).

I argue that B_{th} could in fact be related to the field for first vortex penetration in presence of pinning B_*. The wires studied in [Borisov et al., 2020] have width $w = 10\ \mu\mathrm{m}$, and using the estimation for grAl $\xi \sim 5\ \mathrm{nm}$, leads $B_1 \sim 0.08\ \mathrm{mT}$ while the second critical field is $B_2 = 6.5\ \mathrm{mT}$. This clearly shows that $B_1 < B_{\mathrm{th}} < B_2$, which is inconsistent with the apparent absence of vortices observed from the frequency shift and quality factors below B_{th}. From the model of pinned vortices presented above one can get the correct order of magnitude for B_{th}.[5]

Vortices trapped in the wire could also be at the origin of the hysteretic behavior seen at low fields in a:InO, displayed in Fig. 8.8. Ramping the field up or down does not result in the same quality factor and frequency. This effect is usually understood as an effect of trapped vortices on the RF response of a superconductor [Bothner et al., 2012].
Vortices in the superconducting coil providing the applied field are also likely trapped, leading to a shift of the 'real' zero-field by a few mT.

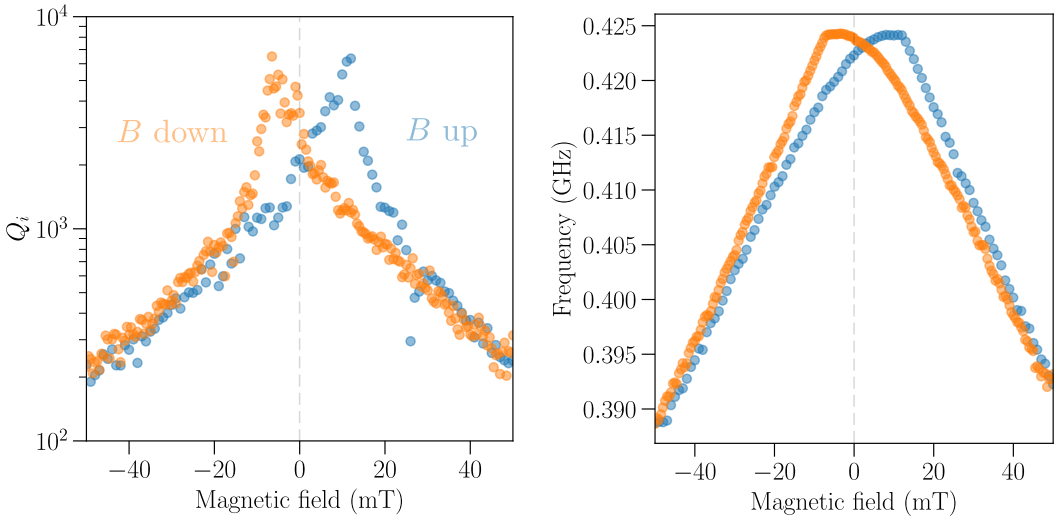

Fig. 8.8. Hysteretic behavior at low field. By ramping up (blue data) and down (orange) a weak magnetic field on sample TC007 we observe a hysteresis. Before this measurement the field had been ramped above $B_1 = 5\ \mathrm{mT}$, therefore entering the plastic regime.

Also similar to our data is the behavior of quality factor just above the drop. It can be seen from Fig. 8.6 **b** that Q_i increases slightly before B_1. A strikingly similar observation was made in grAl below B_{th} (Fig. 3 of [Borisov et al., 2020]), where the quality factor increased by up to 15% before dropping.
This effect was thought of as the result of quasiparticle trapping inside a vortex core located at a current node of the resonator, as discussed in [Nsanzineza et al., 2014].

[5] The wires of [Borisov et al., 2020] have comparable inductance L_K with our $1\ \mu$m-wide films, which suggests that the disorder-dependent J_c is also of the same order of magnitude. Our $1\ \mu$m-wide InOx wire had $j_c \sim 0.18$. To estimate this parameter for a ten times wider films of same disorder we multiply by 10 and obtain $j_c \sim 1.8$. Plugging this into Eq. (8.4) gives the estimation $B_* \approx 0.2\ \mathrm{mT}$, which is the order of magnitude of $B_{\mathrm{th}} = 0.6\ \mathrm{mT}$ discussed in [Borisov et al., 2020].

Conclusion

In this chapter we show some preliminary results on disordered indium oxide resonators in perpendicular magnetic fields. It is found that microwave resonances can survive up to 3 Tesla, but at the cost of a low quality factor.
Interestingly the suppression of superfluid density with B follows an unusual behavior, signaling that a mechanism other than simple pair-breaking is at play. We find a relatively good agreement with a simple model of weakly pinned vortices in a disordered superconductor. The critical field for the penetration of vortices is strongly width-dependent, and a systematic study of various resonator geometries would allow a better understanding of these unusual features of indium oxide films.

Conclusion and Perspectives

8.4 | Conclusion

This thesis aimed at exploring experimentally the complex interplay of electronic disorder and superconductivity. For this we used a prototypical disordered material, amorphous indium oxide, which was studied in great lengths for the past three decades and has puzzled generations of experimentalists and theoreticians alike. While an Anderson insulator at large disorders, this material can turn superconducting by making it cleaner. A large body of works suggests, both experimentally and theoretically, that this quantum phase transition between two seemingly opposite states (an insulator characterized by the localization of charge carriers and a superconducting state with long-range order) is highly non-trivial: preformed electron pairs subsist in the insulating state, leading to a gapped insulator. This questions both the meaning of an insulator made of Cooper pairs, and of the very origin of superconductivity in materials with a tendency towards insulation.

In this thesis we performed a systematic study of disordered indium oxide films across the Superconductor-Insulator Transition tuned by disorder, combining for the first time transport measurements and microwave measurements of the superfluid density using modern spectroscopy techniques. From the microwave response of indium oxide resonators we were able to accurately extract the material's kinetic inductance (and consequently the superfluid stiffness) for various disorders, and relate it to important intrinsic transport properties such as the critical temperature or the normal-state resistance.
These measurements demonstrate without ambiguity the role of superconducting phase fluctuations on superconductivity in presence of strong disorder: the critical temperature becomes equal to the superfluid stiffness, signaling that the superconductor is limited by its resilience against phase fluctuations. By increasing disorder both T_c and superfluid density decrease together, while the single particle gap for single electrons remains unaffected by disorder, as was shown in previous work. These observations further confirm the picture of preformed Cooper pairs: the mechanism leading to paired electrons becomes unrelated to superconductivity, the latter being destroyed by phase fluctuations of the order parameter.

The second main finding of this thesis concerns the nature of the Superconductor-Insulator Transition. While it was widely believed that this transition should be a continuous, second order transition characterized by a smooth suppression of superconducting energy scales, our measurements in strongly disordered indium oxide tell otherwise. We observed a sharp, discontinuous jump of both critical temperature and superfluid stiffness to zero when entering the insulator. These findings, which can not be explained by available theories, open important questions about the nature of this phase transition which could be an unexpected first-order transition. This paves the way for more complete theories that would incorporate more 'ingredients', such as the effect of long-range Coulomb repulsion between electrons (or electron pairs) for instance, which has been overlooked so far.
I hope that our measurements brought some new insight on this topic, which is rather old (its study started more than 30 years ago) but never fails to bring new excitement and unexpected discoveries.

The rest of the thesis contains additional studies of indium oxide microwave resonators, some of which would need to be continued.
We studied the dissipation of indium oxide microwave resonators and found that losses where significantly larger than the one routinely measured in cleaner materials. By engineering the sample geometry and its environment, we concluded that the larger contribution to loss was

not originating from the direct environment of the device (such as surface dielectric dissipation) but was rather intrinsic: strongly disordered indium oxide itself limits the resonator quality factors.
A similar claim was recently made in relation to granular aluminum and titanium nitride films, suggesting that materials with the largest kinetic inductances also have poor performances. This observation could be somewhat detrimental to the field of superconducting quantum devices, as active efforts are currently made to find a material having both large kinetic inductance and low loss.
To our view this problem might actually have larger consequences than expected: by compiling data obtained from resonators made out of superconductors of very different disorder levels, from really dirty material to state-of-the-art ultra-clean cavities used in accelerator physics, we report a simple and somehow universal relation of dissipation and material cleanliness: the less disordered the better.
Together with recent developments in the study of non-equilibrium quasiparticles evidenced in resonators and qubits, our findings suggest the presence of an intrinsic loss mechanism that concerns not only disordered materials, but any type of superconductors. A better understanding of this limitation would become mandatory in the design of next-generation superconducting quantum circuits.

8.5 | Perspectives

Making these indium oxide resonators opened more questions than we could answer: it triggered some new ideas which I briefly summarize here.

Magnetic field and Superconductor-Insulator Transition For instance, we were curious about the effect of a perpendicular magnetic field on narrow indium oxide wires. As discussed in chapter 8 we found an interesting behavior of superfluid density with applied field, which could be related to the pinning of vortices by disorder. According to a simple model and our preliminary results, this feature depends rather strongly on the wire geometry, especially its width. Ongoing works are carried out in order to study the effect of wire width on the suppression of superconductivity, and on the quality factor reduction. We have demonstrated that resonances could survive up to 3 Tesla (and maybe more) in perpendicular field, at the cost of strong dissipation (low quality factor). Microwave resonators resilient to large *parallel* magnetic fields were demonstrated in the literature (up to a few Tesla), but not in *perpendicular* field.
Better understanding of the loss mechanisms in this configuration would be of great use in hybrid devices operated in perpendicular fields. One exciting perspective would be to couple superconducting resonators to the fractional quantum Hall effect for instance. Field resilient resonators are long awaited in various situations, from spin qubits to parametric amplifiers.

Similarly to what was done in this thesis, one could study the nature of the Superconductor-Insulator Transition driven by magnetic field. It is well established that, at a critical magnetic field, phase coherence between localized electron pairs breaks down, leading to an insulating state of incoherent localized Cooper pairs. A measurement of the superfluid density at large fields would provide valuable information about the mechanisms leading to the B-driven SIT (by looking for scaling laws or, on contrary, observe a superfluid jump). One fundamental question is whether this transition driven by magnetic field is of first or second order.

Measurement of insulating indium oxide dielectric constant We already started using indium oxide resonators in hybrid devices, to probe... indium oxide !
During my PhD I worked on setting up an experiment that would allow the measurement of the dielectric constant in insulating InOx. According to recent theories the dielectric constant in an Anderson insulator could have a fundamental impact on pseudogapped superconductors, and knowledge of this quantity is essential to estimate Coulomb interactions. Such measurement was already done in a different setting, and in the disorder-tuned SIT [Ebensperger, 2021]. Additionaly some measurements suggest the divergence of sample resistance at finite temperature under magnetic field [M. Ovadia, Kalok, et al., 2015]. A finite-T insulator could be the signature of Many-Body Localization in indium oxide [D. Basko et al., 2006; D. M. Basko et al., 2007], and might be accompanied with a non-trivial behavior of dielectric constant.
That is why I designed a device composed of two superconducting indium oxide wires separated by a small, strongly disordered indium oxide slab (with a DC four-probe measurement included), as displayed on Fig. 8.9.

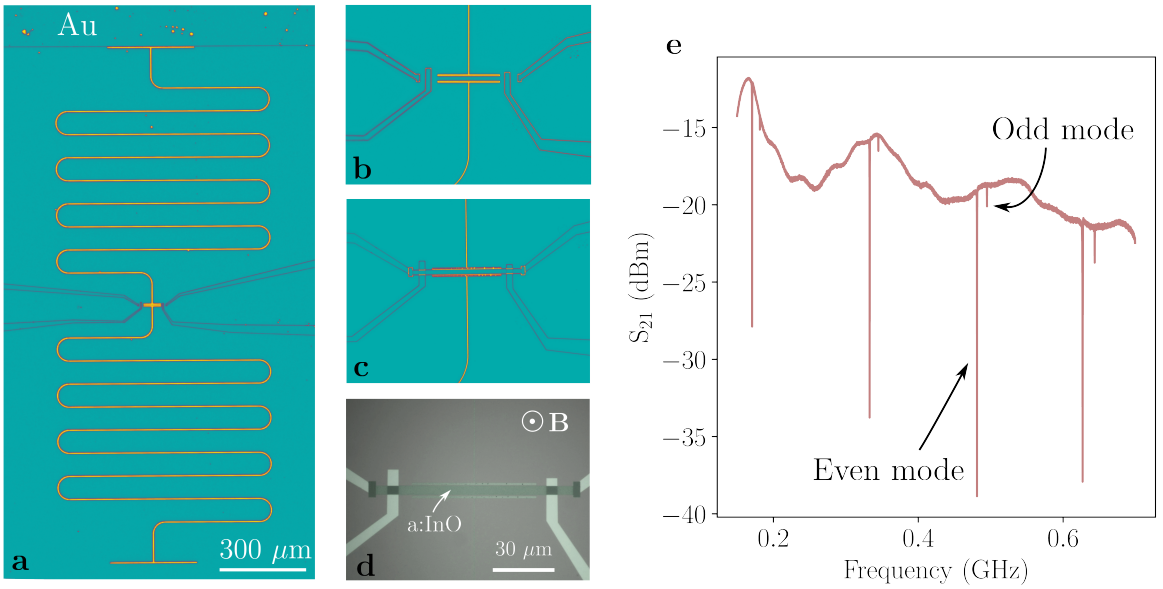

Fig. 8.9. Dielectric constant measurement scheme. Microscope images of a first test device. Two long ($L > 4$ mm) and narrow ($w = 300$ nm) moderately disordered indium oxide resonators (meanders) are separated by a small gap, allowing the coupling of the two wires, and forming a capacitance (panels **a-b**). This geometry shifts slightly the dispersion relation of the two resonators, leading to groups of even/odd modes (see panel **e**). In a second fabrication step a strongly disordered indium oxide strip is deposited in the gap between the two resonators, without contact with the wires. A four probe DC measurement setup allows the measurement of resistance (see panels **c-d**). By applying a perpendicular magnetic field the central indium oxide wire turns insulating, and its dielectric constant $\varepsilon(B,T)$ modifies the capacitance, which translates into a change in the spacing between even and odd modes (see panel **e**).

The idea would be to apply a perpendicular magnetic field that would turn the disordered indium oxide into an insulator, while the resonators, resilient to field, allow to measure the frequency shift due to the variation of $\varepsilon(B,T)$. This study was put on hold for some time but should be continued soon.

Non-linearities, losses and applications to cQED A second important direction for future works concerns resonators made of indium oxide. As mentioned in chapter 7 the loss mechanism responsible for low quality factors in our films remains unknown, although probably intrinsically related to the material itself. While some features are consistent with a model of Two-Level Systems, it appears that these TLS, if there are any, should be present in the indium oxide bulk.
Several recent works put forward the idea that the presence of a coupled TLS bath could be detected by applying a second, detuned microwave tone [Capelle et al., 2020; Kirsh et al., 2017; Zhang et al., 2019]. By saturating TLSs asymmetrically around the resonance frequency with the pump tone, the authors observe a frequency shift with microwave power and a significant enhancement of quality factor. We started investigating the effect of this pump-probe technique on aInO resonators, in the hope of extracting some valuable knowledge about these mysterious TLSs.

Another point of interest is the magnitude of non-linearities in aInO resonators. By considering the non-linearity of current-phase relations in a superconductor, one can estimate the Kerr coefficient K that describes the frequency shift at low power induced by non-linear effects, as $\omega(n) = \omega(0) - Kn$ were n is the average photon number in the resonator. In Appendix D.2 we derived a simple expression for the Kerr coefficient based on mean-field theories (therefore neglecting the pseudogap).
Fig. 8.10 shows the frequency shift at low photon number for sample TC007, which had dimensions $3.5\ \mathrm{mm}$ by $1\ \mu\mathrm{m}$. The result Eq. (D.24) is written in terms of the coherence length ($\xi \sim 5\ \mathrm{nm}$ in indium oxide), the angular frequency ω and the superfluid stiffness Θ ($= 1.93\ \mathrm{K}$ for this sample), giving the estimation $K/(2\pi) = 8$ Hz/photon. We extracted $K/(2\pi) = 100$ Hz/photon from the linear fit of frequency, as shown in Fig. 8.10. The apparent discrepancy between experimental data and the simple theory for a conventional superconductor in the dirty limit is not so surprising: for these strongly disordered films one should turn instead to a theory including the effect of strong disorder and pseudogap. This has not been done so far.

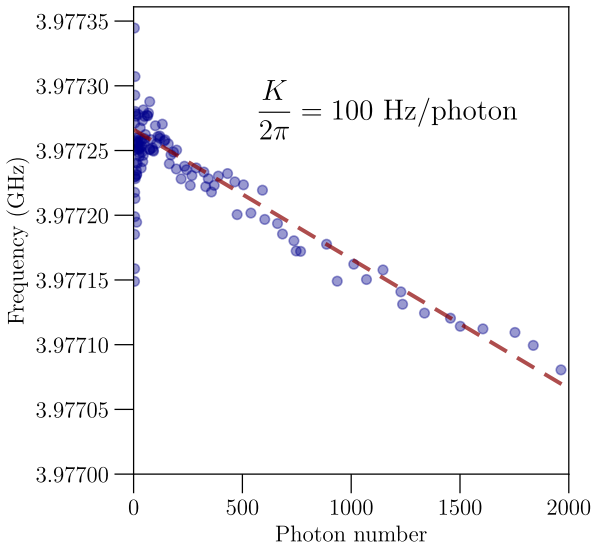

Fig. 8.10. Measurement of the self-Kerr coefficient from the frequency shift. Extraction of the Kerr coefficient from the linear decrease of frequency with photon number for sample TC007 run 2. The fit $f(n) = f(0) - K/(2\pi)n$ gives the estimation $K/(2\pi) = 100$ Hz/photon.

It turns out that most of our samples do not show a clear linear decrease of frequency with photon number, even near $n \sim 1$. In some samples the frequency even seems to increase slightly with power, suggesting that non-linear processes other than Kerr effect are at play. One candidate would be the previously mentioned TLSs in a:InO, the effect of which could be detected by a pump-probe experiment, as we are currently investigating.

Understanding the non-linearities of a:InO resonators is a prerequisite towards the integration of this material in cQED technological applications. One could for instance exploit such non-linearities to provide the anharmonicity of a transmon qubit (as was done for instance in [Winkel et al., 2020; Joshi et al., 2022]) or parametric amplifiers [M. R. Vissers et al., 2016; Chaudhuri et al., 2017; Ranzani et al., 2018; Malnou, M. Vissers, et al., 2021; Malnou, Aumentado, et al., 2022; Xu, Cheng, et al., 2023].

There are other applications for which strong anharmonicity is not wanted, but large impedance (and strong zero-point fluctuations) are highly beneficial.
As we showed in this work indium oxide provides high kinetic inductances, which can be used to generate compact and easy-to-fabricate large impedance environments. Making a *superinductance* only requires to increase the oxygen content in the evaporation chamber. Large inductances made from strongly disordered materials have already been used for the fabrication of fluxonium qubits [Hazard et al., 2019; Grünhaupt, Martin Spiecker, et al., 2019; Rieger, Günzler, M. Spiecker, Paluch, et al., 2022], metrology [Shaikhaidarov et al., 2022], and more generally could be used in replacement for Josephson junctions and Josephson junction arrays.

Appendix

APPENDIX A

Insulators and Localization

In this chapter we aim at giving a more precise description of the effects of disorder on a metal. We first show that quantum corrections to the conductivity become necessary at low temperatures. By increasing the disorder level we show that electrons become *localized* by disorder, and discuss the important consequences on electronic transport. We finally argue that strongly disordered systems can develop interesting short-scale features (namely electronic wavefunction *fractality*).

A.1 | Disorder and Weak localization

Conduction electrons of a disordered metal suffer elastic scattering when encountering an impurity or any other defect.[1] Electron motion remains ballistic on distances below the *elastic mean free path* l_e, and becomes diffusive at larger lengthscales. The value of l_e varies greatly depending on the metal and its disorder level: it ranges from ~ 100 nm for rather clean samples, down to a few nanometers for strongly disordered metals. In most cases the Fermi wavelength $\lambda_F = 2\pi/k_F$ remains shorter than the mean free path, leading to the condition

$$k_F l_e \gg 1 \tag{A.1}$$

When this condition is met, one can model the electron motion quasiclassically.
The conductivity in a disordered metal can be expressed by the Einstein relation $\sigma = e^2 \nu_0 D$ where $D = v_F l_e/d$ is the diffusion constant in dimension d and ν_0 is the electron density of states at the Fermi level. Electrons can diffuse over the length $l_e = v_F \tau_e$ within the time interval τ_e. This allows to write the well known Drude conductivity as[2]

$$\sigma_{\mathrm{D}} = e^2 \nu_0 D = \frac{n e^2 \tau_e}{m} \tag{A.2}$$

where n is the electron density. Eq. (A.2) is the classical contribution to conductivity in a *dirty* metal.

Still, at low enough temperature electrons must be seen as waves governed by quantum mechanics. In absence of interactions between electrons in disordered low-dimensional conductors it is known that quantum interferences of electronic wavefunctions lead to their *localization* over a short lengthscale called the localization length ξ_{loc}. The resulting ground state is insulating (transport at $T = 0$ is completely suppressed). This process is the Anderson localization which will be introduced in section A.3.

[1] See [B. Altshuler et al., 1985] for a detailed review on disorder and weak localization.
[2] In three dimensions for a free-electron model one has $\nu_0 = m k_F/(\pi^2 \hbar^2)$ and $n = k_F^3/(3\pi^2)$.

In many practical situations however Anderson localization cannot fully develop, as it requires complete phase coherence of the electron wave functions. While phase coherence is maintained during elastic collisions with impurities, inelastic processes (such as electron-electron or electron-phonon scattering or other mechanisms) destroy phase coherence. Consequently quantum coherence of electrons in such disordered metals can only survive during the finite time τ_φ, allowing the electrons to propagate coherently over distances of the order $L_\varphi = \sqrt{D\tau_\varphi}$ called the dephasing length.
When inelastic scattering (enhanced by a finite temperature for instance) becomes non-negligible the dephasing length can be shorter than the localization length: $L_\varphi < \xi_{\rm loc}$. In this situation an electron can propagate coherently within a localization volume: Anderson localization (also called *strong* localization) cannot occur. This limiting case is called *weak localization* and can be seen as a precursor of the strong, fully quantum coherent process.

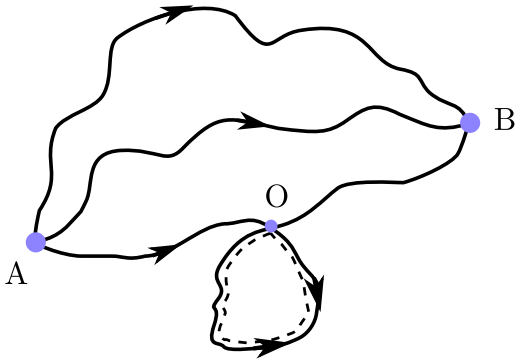

Fig. A.1. Three different paths for an electron propagating from point A to B. While most possible paths have different lengths and therefore generate different dephasings, some form loops (here O is the intersection of such trajectory). Within this loop clockwise and counter-clockwise moving waves interact coherently.

An electron propagating from point A to point B (see Fig. A.1) has infinitely many possible paths. It performs a random walk by colliding defects elastically, following one of the available paths with a given probability P_{AB} which can be obtained by summing the probability intensities of all possible trajectories:

$$P_{AB} = |\sum_i A_i|^2 = \sum_i |A_i|^2 + \sum_{i\neq j} A_i A_j^* \tag{A.3}$$

The second term of Eq. (A.3) describes quantum interferences between distinct paths. Most of them have quite different lengths (and therefore different dephasings from A to B[3]) and as such these interference terms will vanish upon averaging.
One particular type of interfering paths contributes to the total probability: these are the loops formed by self-intersecting paths (see point O of Fig. A.1). Such loop can be traveled in both directions (clockwise and counter-clockwise) by the electron wave function, defining two coherent amplitudes A_1 and A_2. These two waves interfere, which enhances the probability to find the electron at point O:

$$P_O = |A_1 + A_2|^2 = |A_1|^2 + |A_2|^2 + 2\,\mathrm{Re}\{A_1 A_2^*\} = 4|A_1|^2 \tag{A.4}$$

[3]The phase difference can be written $\Delta\varphi = \frac{1}{\hbar}\int_A^B \mathbf{p}\cdot\mathbf{dl}$ where $\mathbf{p}$ is the electron momentum.

which is twice the value one would obtain by neglecting the interference terms.
Thus for every self-intersecting path followed by an electron the probability to find the latter in B decreases because of quantum interferences. This translates into a reduction of the sample conductivity.
One can now write the total conductivity as the sum of a classical term given by the Drude formula (for which interferences are neglected) and a weak localization correction including quantum interferences:

$$\sigma = \sigma_{\mathrm{D}} + \sigma_{\mathrm{WL}} \tag{A.5}$$

The correction $\sigma_{\mathrm{WL}} < 0$ can be calculated according to the sample dimensionality (see B. Altshuler et al., 1985).

This effect is enhanced by disorder: by adding more impurities one increases the probability of forming loops, further reducing the conductivity. By suppressing inelastic scattering processes (*e.g* decrease the temperature) the dephasing length L_φ is enhanced strongly, restoring phase coherence over large lengthscales. Quantum interferences becomes increasingly important, up to a point where all electrons are constrained to move within extremely short distances: they become *localized*.

We now describe the process of *strong* localization, that is, we consider $L_\varphi > \xi_{\mathrm{loc}}$. We shall see that many features of this Anderson localization can be studied by scaling arguments, *i.e.* by considering the effects of scaling (increasing or decreasing the sample size) on certain quantities such as the conductance. It turns out that the concept of scaling is indissociable from the notion of fractals, which we briefly define now.

A.2 | Self-similarity and fractal dimension

Introduced by Benoit Mandelbrot the concept of fractal can be summarized as follows [Mandelbrot, 1982]:

Definition A.2.1 (Fractal) *A fractal is a rough or fragmented geometric shape that can be split into parts, each of which is (at least approximately) a reduced-size copy of the whole.*

Although this definition is not the only one adopted to describe fractals it conveys the general concept and will be enough for the purpose of this discussion.

The Minkowski-Bouligand (or box-counting) dimension is one the many different (and not necessarily equivalent) ways of defining the fractal dimension. It consists in approximating a fractal set S by covering it with boxes of arbitrary size ε. For $\varepsilon \to 0$ the number of such boxes needed to fully cover the set is related to the fractal dimension.

Definition A.2.2 (Box-counting dimension) *Suppose that $N(\varepsilon)$ is the number of boxes of size ε required to cover the set. Then the box-counting dimension is defined as*

$$D = \lim_{\varepsilon \to 0} \frac{\log N(\varepsilon)}{\log\big(1/\varepsilon\big)} \tag{A.6}$$

Therefore for a given ε

$$N(\varepsilon) \propto \varepsilon^{-D} \tag{A.7}$$

which states the usual fact that the measure (area, volume ...) of an object in dimension D is multiplied by n^D when its size is multiplied by n. For instance when the lateral size l of a

square is doubled, the resulting augmented square has an area $2^2 = 4$ times larger. The same treatment for a cube in 3D would result in a $2^3 = 8$ times larger volume.

For usual (non-fractal) objects the fractal dimension D is equal to the euclidian dimension d the object lives in. For fractal objects however the fractal dimension can be larger than the object topological dimension and smaller than the dimension of the euclidian space that contains it, as we shall see through a simple example.

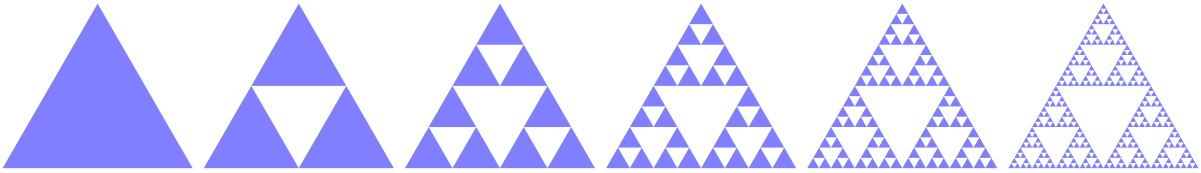

Fig. A.2. An example of self-similar geometric shape. Six first iterations of the Sierpiński triangle. To obtain iteration $n+1$ we take three copies of iteration n and scale them by $\varepsilon = 1/2$.

One example of fractal: the Sierpiński triangle By construction doubling the object lateral size creates three copies of itself, therefore the Sierpiński triangle has a fractal dimension $D = \dfrac{\log(3)}{\log(2)} \approx 1.585$ which is larger than its topological dimension ($= 1$ which can be demonstrated) but still smaller than the dimension of a plane $d = 2$. The fractal is then not a line and neither a surface, but rather somewhere in between with a non-integer fractal dimension.[4]
The construction of an object by self-similarity is at the heart of the scaling theories often used in physics. We will describe later how such a process allows to define the dimensionless conductance of a disordered sample.

Multifractality In some complex systems different regions of an object have different fractal properties. Therefore the system must be described by locally defined fractal dimensions. These so-called *multi-fractal phenomena* are ubiquitous in physics and chemistry [Stanley et al., 1988]. One well known example of this is the theory of percolation (at a critical concentration p_c a cluster with multifractal features forms over the whole sample).

Short scale fractals In many physical situations the system that we are willing to describe is not fractal at all length scales, but rather up to some length ζ (called the *correlation length*). It presents self-similarity only for lengths shorter than ζ:

- at scales $L > \zeta$ the system looks uniform
- at scales $L < \zeta$ the system looks fractal

[4] Fun note: the Sierpiński triangle has the property of having an infinite perimeter and a strictly zero area for an infinite iteration order.

A.3 | Anderson Localization

We have seen that quantum interferences of waves induced by disorder modify the transport properties of a metal. While the phase coherence of wavepackets is altered by the presence of impurities, it must be noted that wavefunctions are still extended in the whole sample.
Anderson [P. W. Anderson, 1958a] showed that this is not anymore true when disorder is strong. In this limit the envelop of an electronic wave function centered in $\mathbf{r_0}$ decays exponentially as

$$|\Psi(\mathbf{r})|^2 \propto \frac{1}{\xi_{\mathrm{loc}}^d} \exp\left(-|\mathbf{r}-\mathbf{r_0}|/\xi_{\mathrm{loc}}\right) \tag{A.8}$$

where the localization length ξ_{loc} is the typical size of the wavepacket, as shown in Fig. A.3 and d is the dimension.

Electrons are *localized* in space, and the ground state of the system is a collection of such localized states with exponentially small overlap. Coherent tunneling of electrons between two localized sites must occur between levels of same energy, but the latter are far apart in space and tunneling is ineffective: the system becomes an insulator.
The important consequences of strong localization on electronic transport will be discussed now.

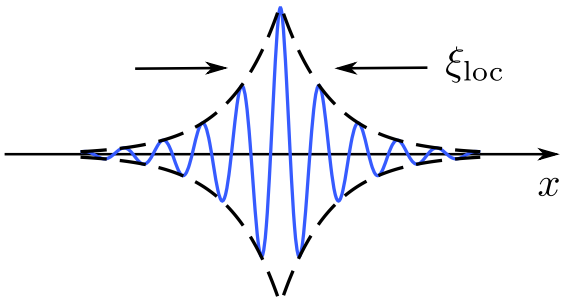

Fig. A.3. Typical wavefunction for a localized state with localization length ξ_{loc}. The envelop follows Eq. (A.8).

It should be noted that, while we are here mostly interested in the Anderson localization of electrons in metals, such localization effect is in fact a property of waves in a broader sense, and therefore applies to different areas of physics. Indeed strong localization has been experimentally demonstrated using classical waves (such as light or sound).[5]

A.3.1 Mobility edge

Mott argued that a critical energy scale E_c called the *mobility edge* separates in energy extended and localized states [S. N. Mott, 1978; N. Mott, 1987].

Fig. A.4 shows the density of state as a function of energy. States with $E_F > E_c$ are extended and conduction is metallic, while for $E < E_c$ states are localized and conductivity tends to zero with temperature.
The figure also shows a schematic representation of electronic wavefunctions just above and below the mobility edge. For $E > E_c$ electronic wavefunctions form a linear combination of plane waves which spatial extent goes over the whole sample size, albeit strong fluctuations of

[5] See [Lagendijk et al., 2009] for a review.

the wave envelop amplitude. Eigenstates just below E_c are separated spatially, each of which has a typical size $\xi_{\rm loc}$ and vanishingly small overlap. The sample is then an insulator.

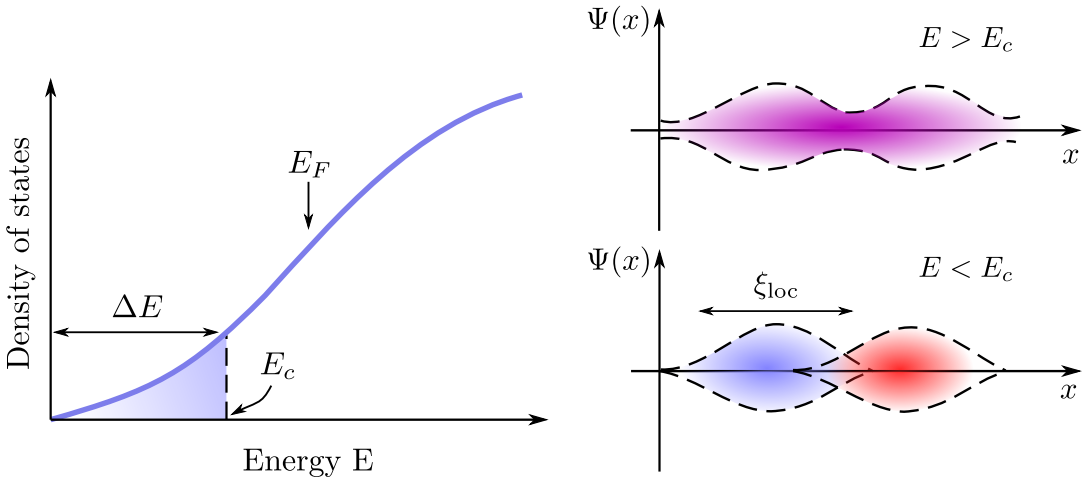

Fig. A.4. Mobility edge. Left: When Fermi energy E_F lies above the mobility edge E_c conduction is metallic. When $E < E_c$ states become localized (shaded area). **Right:** Suggested form of the wavefunction envelops just above (top) and below (bottom) the mobility edge. In the metallic state wavefunctions are extended, while in the localized state wavefunctions have negligible overlap in space.

A.3.2 Dimensionless conductance

One of the main consequences of the localization of waves is the prediction that intensive quantities (such as the conductivity or the diffusion constant) might acquire a dependence with system size L close to the mobility edge.

Edwards et al., 1972 demonstrated that the relevant quantity for this matter is a dimensionless conductance defined as

$$g(L) = \frac{\hbar}{e^2} G(L) \tag{A.9}$$

where g depends explicitely on L and $G(L)$ is the sample conductance.

One can define the *classical* dimensionless conductance $g_{\rm D}$ for an Ohmic conductor of linear size L by writing Ohm's law:

$$g_{\rm D}(L) = \frac{\hbar}{e^2} \sigma_{\rm D} L^{d-2} \tag{A.10}$$

We will see that, when localization becomes relevant, the scaling of dimensionless conductance $g(L)$ with sample size L might strongly deviate from the Ohmic (classical) conductance $g_{\rm D}$ which scales linearly with L.

Interpretation of $g(L)$ and Thouless criterion Starting from Ohm's law mentioned above and using Einstein's relation $\sigma = e^2 \nu D$ where ν is the density of states per unit volume one can rewrite the dimensionless conductance as a ratio of energies

$$g(L) = \left(\nu L^d\right) \frac{\hbar D}{L^2} = \frac{E_T}{\delta} \tag{A.11}$$

where $E_T = \hbar D/L^2$ is the Thouless energy and $\delta = 1/\nu L^d$ is the mean level spacing between energy levels.

The Thouless energy is related to a time scale for diffusion (*Thouless time*) $\tau_L = L^2/D$. On the other hand since δ is the smallest energy scale of the system it must be related to the longest time scale, called the *Heisenberg time* $\tau_H = \hbar/\delta$. One can then see the dimensionless conductance $g(L)$ as the ratio of these two characteristic times:

$$g(L) = \frac{\tau_H}{\tau_L} \tag{A.12}$$

The Thouless time is the time it takes for a conducting electron to travel across the entirety of the sample (with a diffusive motion induced by disorder). The Heisenberg time is the longest time that an electron wavepacket can propagate inside a sample of size L without visiting the same region twice (*i.e* after the time τ_H the electron has explored the whole volume L^d). Depending on the relative values of τ_H and τ_L conduction at the scale L might change.

When disorder is small the electron motion is only weakly impeded by scattering on impurities and the Thouless time is rather short, at least much shorter than the time it takes to explore the whole sample. Therefore one has $g > 1$ (and $g \gg 1$ in the case of almost clean conductor). When the Thouless time exceeds the Heisenberg time however, a wavepacket is unable to travel from one end of the sample to the other and is localized inside the sample. Therefore $g < 1$ corresponds to the localized state.
This simple qualitative argument suggests that the transition between extended and localized states occurs for [D. J. Thouless, 1977]

$$g \sim 1 \tag{A.13}$$

One can estimate the dimensionless conductance at the scale of the mean free path. Indeed at $L \sim l_e$ we expect scattering (and therefore interference) effects to be unimportant, meaning that classical models for transport should hold. Using the classical dimensionless conductance of Eq. (A.10) in three dimension ($d = 3$) one gets $g(l_e) \approx \frac{2}{3}(k_F l_e)^2$. The critical point is such that $g_c \sim 1$ and therefore one obtains the Ioffe-Regel criterion for localization:

$$k_F l_e \sim 1 \tag{A.14}$$

Another important interpretation of the meaning of the dimensionless conductance $g(L)$ was given by [D. Thouless, 1974], setting the foundations for the celebrated scaling theory of localization which will be discussed further below. Thouless considered the changes experienced by a sample when its size is increased, starting from a sample of size L^d in d dimension and making a larger one of size $(2L)^d$, as pictured in Fig. A.5.
The sample of size L^d has eigenstates with a typical spacing between energy levels $\delta \sim (\nu L^d)^{-1}$. When increasing the sample size one must consider overlaps between the subsystems of size L^d, overlaps which can be estimated by the variation of energy ΔE generated by a change in the sample boundary conditions.[6]
Consider now a localized wavefunction in the sample of size L^d. Its spatial extent decays exponentially, so that its mean value is negligibly small at the boundary. Therefore a change in the boundary conditions will leave the eigenstate mostly unaffected, and $\Delta E/\delta$ is exponentially small. On the contrary an extended state will largely overlap over all the subsystems, up to

[6] As an example, one could consider the periodic conditions $\Psi(x + L, y, z) = e^{i\eta}\Psi(x, y, z)$.

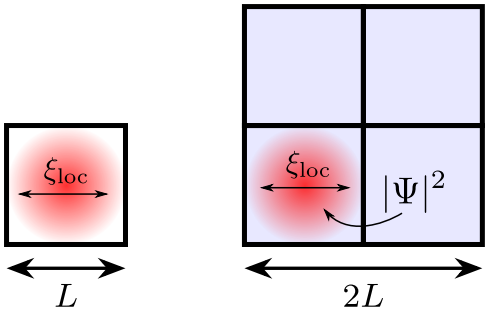

Fig. A.5. Constructing large systems by self-similarity. Red halo represents a state localized in the volume L^d, while blue color stands for an extended state over the whole volume $(2L)^d$. The localized state remains unaffected by scaling up.

the boundaries of the largest sample, and is strongly affected by a change in the boundary conditions: $\Delta E/\delta$ is large. Thouless argued that the conductance is in fact related to this ratio, as $g(L) \propto \Delta E/\delta$ [P. A. Lee et al., 1985].

From the previous argument it becomes clear that the system size plays a crucial role in the transport properties, and must be compared to some characteristic length scales. Fig. A.6 displays three lengths relevant for quantum transport in disordered media.
By comparing these lengths to the system size L different regimes can be defined, such as the *ballistic* transport for $L < l_e$, *diffusive* transport for $l_e < L < \xi_{\mathrm{loc}}$ (with weak-localization corrections) and finally *strong localization* for samples with $\xi_{\mathrm{loc}} < L$.

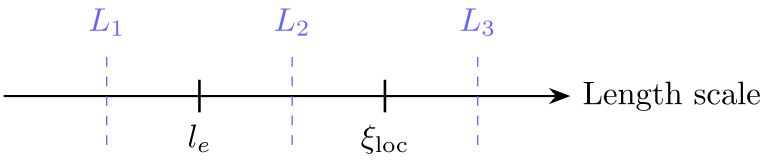

Fig. A.6. Characteristic lengths involved in electronic transport. Depending on the system size L transport at $T = 0$ is either ballistic (L_1), diffusive (L_2) or absent due to localization (L_3).

A.3.3 Scaling theory

The scaling hypothesis is the assumption that the conductance $g(2L)$ of the system of size $2L$ can be computed using only the conductance of the system of size $L > l_e$, that is

$$g(2L) = f[g(L)] \tag{A.15}$$

where f is some function.
This scaling process has a cutoff at short scales given by the mean free path. For instance the dimensionless conductance $g(l_e)$ defined at this length scale is a microscopic measure of disorder: it is large for small disorders and small for large disorders.

If instead of doubling the system size one increases the length by the infinitesimal quantity dL, one obtains

$$\beta(g) = \frac{L}{g}\frac{dg}{dL} = \frac{d\log(g)}{d\log(L)} \tag{A.16}$$

where β is again an unknown function. Note the formal similarity with the definition of the fractal dimension. We shall see later that this likeliness is not incidental and has important consequences.

The β function (or *scaling function*) is a measure of the evolution of conductance with system size. For instance, if $\beta(g) = \text{constant}$ one has: $g(L) \propto L^{\beta(g)}$. If $\beta(g)$ varies with g, or changes sign, then the dependence of conductivity with size might become non-trivial.

We can infer asymptotic expressions for the β function based on physical arguments:

- For large $g \gg 1$ the sample is a good conductor and therefore should obey Ohm's law $G(L) = \sigma_{\mathrm{D}} L^{d-2}$ where σ_{D} is the Drude conductance. The electron wave function is extended and is almost plane-wave like. This leads to the value of β for $g \to \infty$: $\beta = d - 2$. Note that in two dimensions ($d = 2$) $\beta \to 0$ and therefore conductance does not depend on the system size.
- When g is small, we have a poor conductor (a highly disordered sample). Therefore the system is most likely in the localized regime described above in which all states decay exponentially when the size is larger than the localization length ($L > \xi_{\mathrm{loc}}$). Thus $g \sim g_0 \exp\left(-L/\xi_{\mathrm{loc}}\right)$, leading to $\beta(g) \sim -L/\xi_{\mathrm{loc}} = \log\left(g/g_0\right)$ as $g \to 0$. Note that $\beta(g)$ is negative, meaning that the conductance g decreases when L increases.

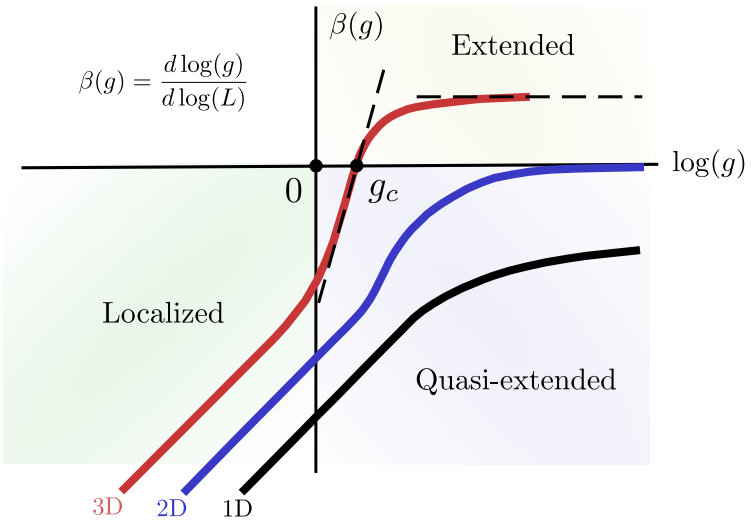

Fig. A.7. Scaling theory of localization. Evolution of the scaling function $\beta(g)$ with conductance g for different dimensions. $\beta(g)$ describes with what exponent the conductance $g(L)$ grows with the system size. For extended states, this scaling is linear with L: $g(L) \propto L^{\beta(g)} = L^{d-2}$ which is nothing but Ohm's law. When localization kicks in the scaling function becomes negative. As a result conductivity decreases with system size in the localized region. In 3D a transition between extended and localized states occurs for a critical conductance g_c. Adapted from [Abrahams et al., 1979].

Starting from the limits detailed above and writing asymptotic expansions for large and small g then interpolating, [Abrahams et al., 1979] obtained an estimation of the value of $\beta(g)$ for

any g in different dimensions as displayed in Fig. A.7. It appears that the results of this scaling procedure are qualitatively different depending on the sample dimension, as we shall see now.

- $d = 1$. In one dimension $\beta(g)$ is always negative. Therefore if we enlarge the system the conductance will decrease, irrespective of the level of disorder. For sufficiently large systems all states will be localized.
- $d = 2$. Abrahams et al., 1979 showed that $\beta(g)$ is also always negative, even at its limit $g \to \infty$ for which $\beta(g) = 0^-$. As a result states are localized for large L, and in the limit of infinite length a true 2D conductor cannot exist.
- $d = 3$. The case of three dimensional systems is more complex. Indeed $\beta(g)$ changes sign at some conductance g_c, for which $\beta(g_c) = 0$. Therefore if $g > g_c$ conductivity increases with L and converges to the value given by Ohm's laws for sufficiently large g. In contrast if $g < g_c$ conductivity decreases when L increases and eventually vanishes when electronic states are exponentially localized and do not overlap.

As a result a transition from a metallic to an insulating phase should occur at the critical conductance g_c (which, as predicted by the Thouless criterion should be $g_c \sim 1$).

Consequences on the localization length In the case of electronic transport in 3D one can use the scaling theory of localization described previously to study the scaling of the localization length with disorder. Assuming that disorder can be described by a parameter W, Abrahams et al., 1979 used the properties of the β-function near the critical point to show that the localization length diverges upon approching criticality for $W > W_c$ as

$$\xi_{\text{loc}} \sim |W - W_c|^{-\nu} \tag{A.17}$$

where $\nu \approx 1.6$. Thus the localization length diverges at the mobility edge (from the insulating side).

Consequences on the correlation length and diffusion constant On the metallic side of the transition (*i.e* $\beta > 0$ and $W < W_c$) one has the scaling of the diffusion constant with disorder as

$$D \propto |W_c - W|^{\nu} \tag{A.18}$$

Eq. (A.18) shows that within the scaling theory of localization, diffusion constant (and conductivity $\sigma \propto D$) decrease continuously to zero, vanishing at $W = W_c$ similarly to a second-order transition.
A length scale naturally emerges from the scaling theory, the *correlation length* ζ which diverges at the mobility edge (from the metallic side):

$$\zeta \propto |W_c - W|^{-\nu} \tag{A.19}$$

For lengths larger than ζ the system looks uniform and the conduction is Ohmic while for $L < \zeta$ conduction is non-Ohmic.
Therefore correlation length (on the metallic side) and localization length (on the insulating side) diverge at the transition with the same exponent ν as displayed in Fig. A.8.

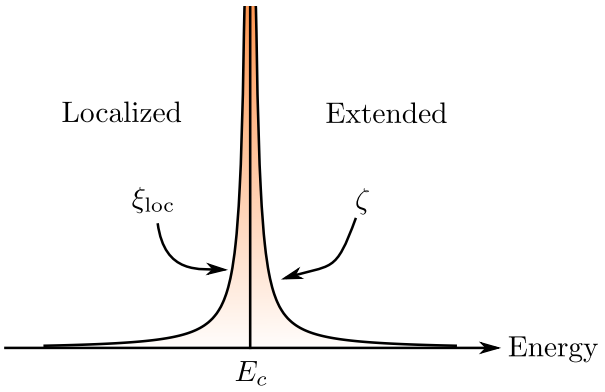

Fig. A.8. Divergence of the localization and correlation lengths as ξ (or ζ) $\sim |E - E_c|^{-\nu}$ where E_c is the mobility edge.

A.3.4 Eigenfunction fractality: a hand-waving approach

While the scaling theory is extremely fruitful to describe localization, the existence of a short scale cutoff (of the order of the mean free path) implies that scaling theory ignores the structure of wavefunctions inside the localization volume. It turns out that wavefunctions have a very interesting fractal structure near the mobility edge.

Let us first remark that, at $L \gg \zeta$ one expects electronic states to be uniform (insensitive to disorder and thus extended). Hence the β-function should be close to unity in three dimensions (this is again Ohm's law). At $L \ll \zeta$ on the contrary all states are localized and the β-function vanishes to 0.
One may note that the first case ($\beta(g) = 1$) corresponds to a uniform state in **3D**, while in the second case $\beta(g_c) = 0$ is close to the expected value for a uniform state **in 2D**. Based on this observation [Cohen et al., 1983] defined an *effective dimension* D as

$$D = \beta(g) + 2 \tag{A.20}$$

Starting from a large length $L > \zeta$ and decreasing it, eventually passing below ζ then corresponds to a continuous variation of the dimension D from 3 to 2. This is equivalent to passing from extended to localized states.
Noting $N(\varepsilon)$ the number of boxes of size ε needed to cover the space occupied by a wavefunction within the system of size L, one sees that $N(\varepsilon)$ scales as $N(\varepsilon) \propto \varepsilon^D$, which is a definition of the fractal dimension D.
In the extended case $D = 3$ and the wavefunction occupies all available space. Multiplying L by two leads to $2^D = 8$ boxes of size L fully occupied by the wavefunction. In the strongly localized case $D = 2$ and the wavefunctions occupy a much smaller volume, around their localization centers. Increasing the system size does not significantly affect the space occupied by a wavefunction. For any intermediate state $2 \leq D \leq 3$ the wavefunctions are non-uniform and have a strongly inhomogeneous spatial distribution. They occupy a small fraction $\sim L^D$ of the available volume L^3

A.3.5 Multifractality and Anderson localization

Further study of the wavefunction distribution at the mobility edge revealed a *multifractal* behavior [Castellani et al., 1986], defined by the existence of an infinite set of critical exponents describing the scaling of the Inverse Participation Ratio (IPR) of the eigenfunctions intensities

$|\Psi^2(\mathbf{r})|$. The IPR is defined as [7]

$$P_q = \int |\Psi^{2q}(\mathbf{r})| d^d\mathbf{r} \tag{A.21}$$

where q is the order of the moment considered. Multifractality is then evidenced by the scaling of P_q with system size L:

$$P_q \propto L^{-D_q(q-1)} \tag{A.22}$$

which states that, not only P_q has a fractal structure for a given q with fractal dimension $D_q < d$, but also the critical exponent varies with q (and therefore is multifractal) [A. Mirlin, 2000].

Note that for an extended state the eigenfunction distribution is uniform $|\Psi^2(\mathbf{r})| = 1/L^d$ in d dimension, which leads $P_2 = L^{-d}$. Therefore all available states *participate* equally, and extended states provide the lowest value of the IPR. In the opposite limit of exponentially localized states with negligible overlaps $P_2 \sim \xi_{\text{loc}}^{-d}$. This suggests an interpretation of the participation ratio: P^{-1} is a measure of the volume in space occupied by a wavefunction Ψ. An illustration of the wavefunction intensities in an Anderson insulator is shown in Fig. A.9.
For the Anderson problem in 3D the fractal dimension at criticality can be estimated by $D_2 \approx 1.3$ [Mildenberger et al., 2002]. Therefore at the mobility edge localized states occupy a volume L^{D_2} much smaller than the available volume L^3.

An important result of [Cuevas et al., 2007] is the fact that multifractality appears at some distance from the mobility edge: setting L_0 the microscopic short-scale cutoff for fractal behaviors (the size of smallest fractal structure) and the related upper energy scale $E_0 = (\nu_0 L_0^3)^{-1}$, it is observed that the localization length ξ_{loc} and correlation length ζ are much larger than L_0. As a result in the insulating state (and for $E_F - E_c \leq 0$ not too large) multifractal behavior is still present, forming a *multifractal insulator*. This is also true in the metallic state ($E_F - E_c \geq 0$ not too large) which is a *multifractal metal* in which extended states can be seen as a collection of fractal structures within "shells" of size ζ (the correlation length) paving the available space. Upon approaching the mobility edge ζ diverges until covering the whole space at E_c: critical wavefunctions become pure fractals. A schematic representation of this is shown in Fig. A.10.
Then the multifractal metal survives upon decrease of disorder (with decreasing ζ) as long as $\zeta > L_0$[8] .

The minimal disorder for which fractality is still present can be quite far from the mobility edge, which will become essential for understanding the emergent superconductivity in strongly disordered materials, the subject of next chapter.

A.4 | Thermally activated transport

So far localization was considered in a sample at $T = 0$ for which quantum interferences were not smeared out by temperature. Obviously real experiments are carried out at finite

[7] We implicitely consider normalized eigenfunctions here. The IPR is in fact defined in the most general case (for $q = 2$) as a ratio of moments of order 2 to the square of moments of order 1: $P = \int |\Psi(\mathbf{r})|^4 d\mathbf{r} / \left[\int |\Psi(\mathbf{r})|^2 d\mathbf{r}\right]^2$ (see D. Thouless, 1974 page 118).

[8] The multifractal insulator survives symmetrically when going deeper in the insulator, with fractal shells of decreasing size ξ_{loc}.

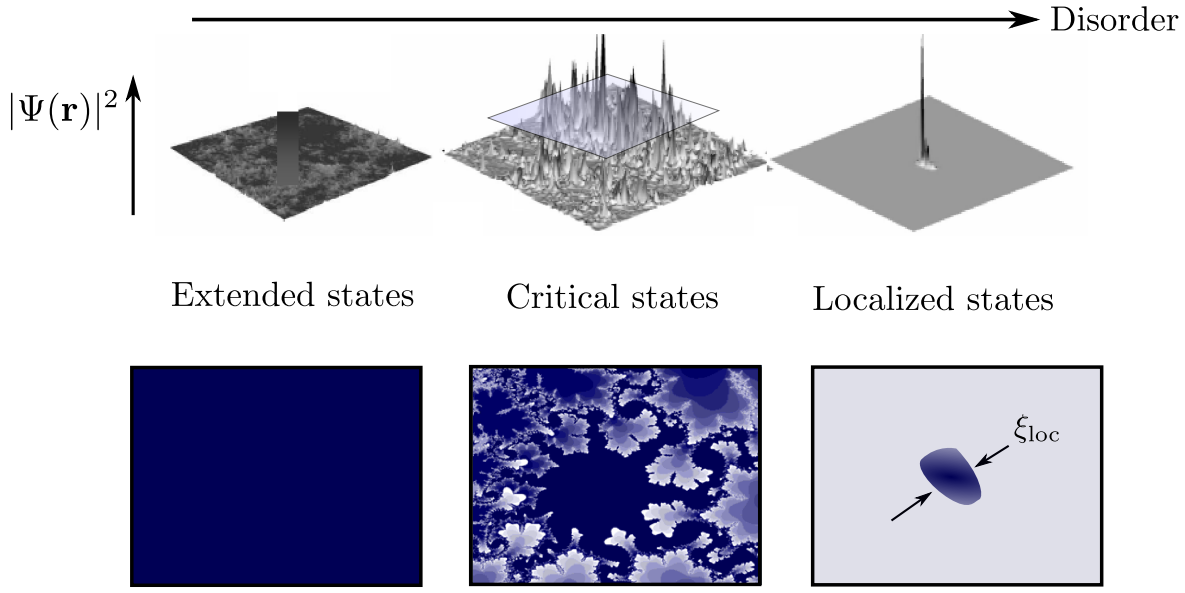

Fig. A.9. Fractal wavefunctions across the metal-insulator transition. The wavefunction intensity $|\Psi(\mathbf{r})|^2$ is shown in 3D space (top) and along a horizontal cut (bottom). Darker blue corresponds to larger intensity. **Left:** At low disorder wavefunctions are extended and their intensity is uniform (they occupy all available space). **Center:** At critical disorder $E_F = E_c$ wavefunctions present a multifractal structure (one sees the self-similarity, with several distinct self-similar structures signaling multifractality). They occupy a small volume L^{D_2}. **Right:** For localized states ($E_F \ll E_c$) wavefunctions are exponentially suppressed far from the localization center $\mathbf{r_0}$ and occupy the small volume $\xi_{\rm loc}^d$. Adapted from [Cuevas et al., 2007].

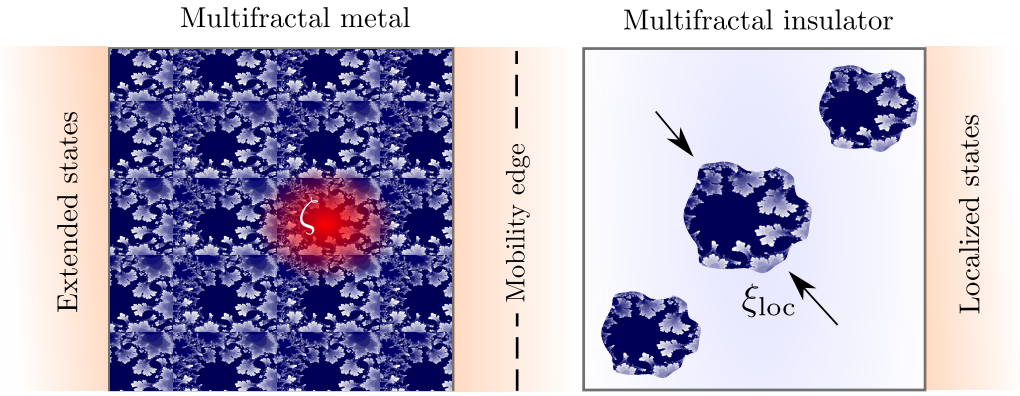

Fig. A.10. Multifractal insulator and metal close to the mobility edge. Not far from the metal-insulator transition both extended and localized states present a local multifractal behavior at the scale of the correlation (or localization) length. These fractal puddles merge at the mobility edge. Adapted from [Cuevas et al., 2007].

temperatures (and finite sample lengths) and one should expect that these conditions modify the results of the theory of localization.

Scaling at finite temperatures

Thouless [D. J. Thouless, 1977] suggested that inelastic scattering of electrons would destroy phase coherence and therefore reduce the probablity of quantum interferences leading to

Anderson localization. This argument sets a cutoff lengthscale for quantum interferences defined as

$$L_\varphi(T) = \sqrt{D\tau_\varphi} \tag{A.23}$$

where D is the diffusion constant for *elastic* scattering and τ_φ is the *inelastic* scattering time, or *dephasing* time (the average time between two inelastic collisions). Quantum interferences and the related localization effects are cut off for characteristic lengths larger than L_φ.[9] This mechanism was already introduced in relation to weak-localization.

$L_\varphi(T)$ explicitely depends on temperature since inelastic processes are temperature-dependent. The estimation $L_\varphi = aT^{-p/2}$ (where p is an integer depending on the considered inelastic process) is often used to describe the temperature dependence of this length scale [P. A. Lee et al., 1985]. $L_\varphi(T)$ diverges as T tends to zero, and one retrieves the usual model of strong localization discussed above. For finite temperature however $L_\varphi(T)$ defines the largest length for which localization is effective.
A direct consequence is the fact that decreasing the sample temperature increases the length scale L_φ over which quantum interferences are effective, leading to an increasingly measurable effect of localization. **The increase of resistance upon decrease of temperature is a demonstration of localization effects**.[10]

Dimension crossover One finds that the temperature-dependence of conductivity varies strongly with the sample dimension.
More precisely one must define the dimensions as effective dimensions with respect to inelastic processes: a film of thickness d is three-dimensional if $L_\varphi < d$, and two-dimensional otherwise. Therefore upon cooling down this effective dimension might cross over from 3D to 2D as L_φ diverges.
Additional factors such as interactions between electrons may have a different effective dimension: for instance a sample is three-dimensional with respect to Coulomb interactions if the thermal length is smaller than the film thickness: $L_T = \sqrt{\hbar D/k_B T} \leq d$ [P. A. Lee et al., 1985].

Activated hopping between localized states We now turn to transport at small (but finite) temperatures $T > 0$ in the localized phase ($E_F < E_c$). There L_φ is arbitrarily large and strong localization effects are very much present.
[Miller et al., 1960] demonstrated that the probability for a localized electron to *hop* to a near neighbour is non-zero for electrons with energy $\sim k_B T$ below the Fermi level, which translates into the formula

$$\sigma \propto \exp\left(-\frac{T_0}{T}\right) \tag{A.24}$$

[9] Thouless derived Eq. A.23 by considering the effects of a change in boundary conditions $\Delta E \sim E_{\mathrm{Th}}$ (as in section A.3.2) and comparing it to the uncertainty in the energy level spacing in a block of size L^d induced by inelastic processes $\Delta E_{\mathrm{in}} \sim \hbar/\tau_\varphi$. If the incertainty ΔE_{in} is larger than the change due to boundary conditions ΔE a localized electronic wavefunction becomes sensitive to boundary condition changes, which corresponds to an extended state. Using $E_{\mathrm{Th}} \sim \hbar D/L^2$ immediately leads that a sample of size $L > L_\varphi$ has only extended states. The electron is then localized only if $L < L_\varphi$ (which usually corresponds to $\tau_\varphi \gg 1$, that is inelastic scattering is weak).

[10] In the regime of weak-localization the size-dependence $\sigma(L)$ of the conductivity is known. Since L_φ defines the upper cutoff for localization effects, the temperature-dependence of a disordered sample can be obtained by $\sigma(T) = \sigma(L_\varphi(T))$.

where T_0 is an *activation energy*.
T_0 can be be estimated as the average level spacing between localized states $T_0 \sim \delta_{\text{loc}}$, *i.e.* for conduction to occur thermal energy must overcome the typical energy separation between localized electrons.

Mott variable range hopping Based on this model [N. F. Mott, 1969] made the observation that the hopping probability should depend on the distance between localized sites, and on their energy difference.[11] The resulting conductance becomes:

$$\sigma \propto \exp\left[-\left(\frac{T_{\text{Mott}}}{T}\right)^{\frac{1}{d+1}}\right] \tag{A.25}$$

this equation describes the *Mott variable range hopping* which is expected to be the dominant mechanism for conduction in an Anderson insulator without interactions.

Coulomb gap and Efros-Shklovskii law The derivation of Mott's law implicitely assumed that the density of states ν_0 is a constant close to E_F, and neglected interactions between localized electrons.
Shortly later [Pollak, 1970] and [Efros et al., 1975] demonstrated that the density of states near the Fermi level was suppressed by long-range Coulomb interactions, forming a *Coulomb gap* that shapes the DoS as $\nu(E) \propto |E - E_F|^{d-1}$ in d dimensions.

The argument for the existence of a gap is as follows: considering the hopping of a localized electron from site i (with energy $E_i < E_F$) to an unoccupied site j (energy $E_j > E_F$) implies the creation of an electron-hole pair, with (attractive) Coulomb interaction $-e^2/(\kappa r_{ij})$ where κ is the dielectric constant (in units of $4\pi\varepsilon_0$) and r_{ij} the distance in space between them. Thus the hopping from i to j has the energy cost

$$\Delta E = E_i - E_j - \frac{e^2}{\kappa r_{ij}} > 0 \tag{A.26}$$

This energy cost is always positive, since it corresponds to a perturbation of the ground state. In order to prove that the density of states is suppressed near the Fermi level, we assume that

[11] For two localized electrons separated by the distance R the overlap of their wavefunctions is $\propto \exp(-2R/\xi_{\text{loc}})$. The available states the electron can jump to in the energy range dE and at distance R is $\frac{4}{3}\pi R^3 \nu_0 dE = W^{-1} dE$ in 3D. Therefore the typical energy spacing between these states is W: this is the energy barrier that must be overcome by thermal excitations for conduction to happen.
Mott then used the previous activated hopping argument, but now taking into account the overlaps between wavefunctions, leading to the probability for hopping of the form

$$P \sim \exp\left[-2\frac{R}{\xi_{\text{loc}}} - \frac{W}{k_B T}\right]$$

The important step of his reasoning is the observation that an optimal value of R describes the most probable hopping. Indeed for a large distance R between sites the cost in energy $\propto R^{-3}$ is small, but the overlap between these states is exponentially small and therefore hopping is less probable. On the contrary if R is small the overlap will be large but the energy cost is also large. Therefore an optimal distance R_0 gives the largest hopping probability and can be obtained by looking for the minimum of the term in brackets in last equation.

This leads to $R_0 = (C/T)^{1/4}$. Injecting into the activation formula (and generalizing the argument to dimension d) leads to Eq. (A.25).

it is not the case, with a constant DoS $\nu_0 = \nu(E_F)$ and look for a contradiction.

Let us consider an electron-hole pair close to the Fermi level with energy $\in [E_F - \varepsilon, E_F + \varepsilon]$ and satisfying the inequality $\varepsilon < \Delta_C = e^3 \nu_0^{1/2} / \kappa^{3/2}$.

The typical distance R between two such states is given by $(4/3)\pi R^3 \nu_0 \varepsilon \approx 1$ that is $R \sim (\nu_0 \varepsilon)^{-1/3}$ (we drop here constants ~ 1).
The Coulomb interaction between these states is obtained by replacing r_{ij} by R in Eq. (A.26), which leads to the inequality

$$\Delta E = E_i - E_j - \frac{e^2}{\kappa}(\nu_0 \varepsilon)^{1/3} > 0 \tag{A.27}$$

Noting that both states are within a distance in energy ε from the Fermi level, $|E_j - E_i| \leq 2\varepsilon$, and inequality (A.27) is not fulfilled for $\varepsilon < \Delta_C$, which contradicts the hypothesis. Therefore the DoS has a gap near E_F induced by Coulomb interactions, with a typical size Δ_C.

By taking into account this gap and using an analogy with Mott's derivation [Efros et al., 1975] were able to show that conductivity at low enough temperature should have the form:

$$\sigma \propto \exp\left[-\left(\frac{T_{\mathrm{ES}}}{T}\right)^{1/2}\right] \tag{A.28}$$

which is independent of the dimension d.
This mechanism leads to a much larger resistance than the one predicted by Mott.

Coulomb interactions are indeed of great importance in Anderson localized insulators, for which interactions are very poorly screened by localized electrons. At low temperatures this leads to an *electron glass* (or *Coulomb glass*), a highly correlated state of matter which presents glassy features such as aging, ultra-slow relaxation and memory effects, as evidenced by a large body of experimental works.

Note that the derivation of the Coulomb gap above can also be carried out for *electron pairs*, in an exactly similar fashion (one simply has to make the substitution $e \to 2e$). This allows to define a Coulomb gap for pairs of electrons.

APPENDIX B

Fabrication

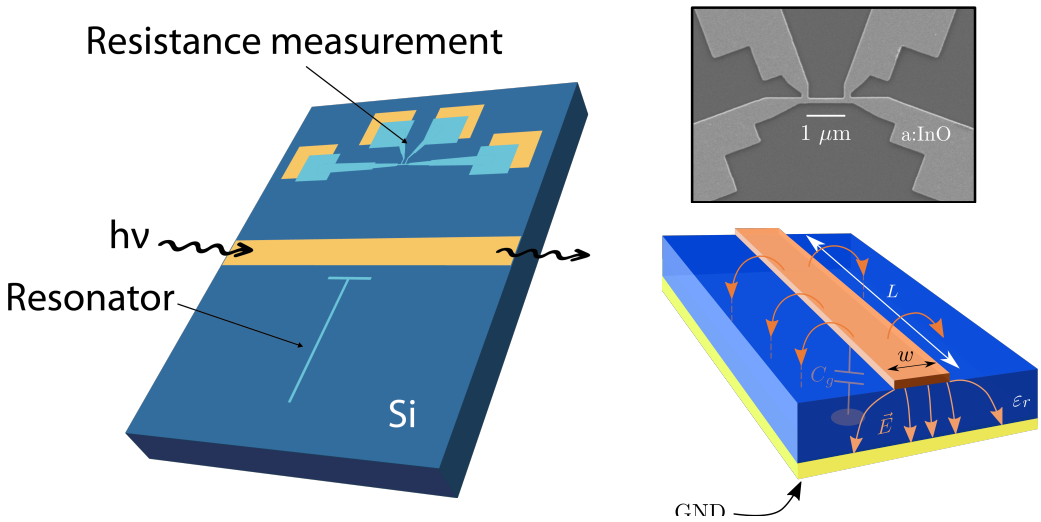

Fig. B.1. Illustration of a typical sample. Yellow metal is gold (with a thin Titanium layer underneath for adherence). In most cases gold features are buried into the substrate and filled to the same thickness to provide a perfectly flat device. Light blue represents amorphous indium oxide deposited as a second step. Sample backside is also coated with a thicker gold layer.

Preparation of the chips The sample preparation starts by patterning alignment marks, DC pads and the center microwave feedline on a 2 inch silicon wafer (resistivity $\rho > 10\ \mathrm{k\Omega \cdot cm}$). One wafer allows for the preparation of 16 8.1 mm by 8.1 mm chips.
After resist deposition (PMMA 3% for 30 seconds at rotation speed 4000 rpm) the lines are patterned by e-beam lithography and the exposed part is cleaned of its resist by a standard MIBK:IPA developer for 60s, then 30s in IPA.

To facilitate the DC contact between metallic pads and the deposited indium oxide (further step) and not form a step we decided to bury the DC pads by etching the silicon substrate through the PMMA mask. In order to reduce the fabrication steps all other gold features (alignment marks and MW feedline) are processed in the same step and are therefore also etched.
We used a $\mathrm{SF_6}$ plasma to dig a $100\ \mathrm{nm}$-deep trench in the substrate at the position of the ebeam-patterned lines.

The wafer is then loaded into a Plassys evaporator where 5 nm of Ti and 95 nm of gold are deposited on the patterned side (forming the MW feedline, the DC pads and alignment

marks at once). The etched trenched are completely filled with gold, allowing a perfectly flat substrate surface, ready for next step. The wafer is then flipped upside down, and 10nm of Ti + 200 nm of gold is deposited on the whole wafer backside.
After lift off of gold and cleaning, the wafer is diced into 8.1 mm by 8.1 mm chips.

Making a resonator sample A properly cleaned sample is coated in resist (PMMA 3% for 30 seconds at 4000 rpm) and the resonator line as well as the DC four-probe Hall bar is patterned by ebeam lithography. Alignment is made by locating the previously deposited gold markers at the four corners of the chip.
We then proceed to development of the resist: exposed regions are intended to be filled with indium oxide in next step.
Here are a few comments on resist removal for sensitive and small structures.

Cold development technique During my PhD we developed a slight improvement to the standard removal of resist in ebeam-exposed regions. While the latter is done in a mix of MIBK solvant and IPA at room temperature after an exposure at relatively low electron density, it was suggested in the literature that an alternative, called *cold development*, could improve pattern quality, allow sub-$10\ \mathrm{nm}$ resolution and remove efficiently PMMA residues [Hu et al., 2004; Ocola et al., 2006; Cord et al., 2007].

By decreasing the temperature of the development bath, partially exposed polymer chains lying at the edges of the pattern (that should not be removed in an ideal case) get 'frozen out', and become less sensitive to the developer. As a result structures processed at cold temperatures are sharper than the ones obtained with the usual room-temperature method.
[Cord et al., 2007] studied the effect of development temperature and exposure dose on lithographic resolution. They found that, by lowering the temperature, exposure doses had to be increased as well to compensate the reduced PMMA sensitivity. They showed that there exists a sweet spot at T=-15°C where exposure dose remains low enough to avoid cross-linking and at which e-beam resolution is maximum, allowing the patterning of sub-$10\ \mathrm{nm}$ structures. In any case development in a bath kept at temperatures between -20°C and 5°C always show better results than the standard recipe.

For the fabrication of sensitive structures (such as the $100\ \mathrm{nm}$-wide resonators) we used higher doses than usual (approximately twice the standard recipe) and a (3:1) IPA/DI water mix as a developer kept cold at 3°C in a chiller bath for 90s. The chemical reaction is stopped by immersion in a DI water beaker kept at the same cold temperature 3°C.
After working on this process I passed on the recipe to some of my collegues who now use it routinely. Cold development already helped increasing the quality of small Josephson junctions used in our group, see [Milchakov, 2022] for an example.

B.1 | Indium oxide deposition and characterization

After patterning, samples are cleaned by a $\mathrm{O_2}$ plasma for a few seconds to further remove resist residues lying at the bottom of the trench. They are now ready for indium oxide evaporation.

Indium oxide deposition is made in a dedicated egun evaporator. The sample is fixed upside down above an InOx target (a 99.999% purity $\mathrm{In_2O_3}$ pellet from Neyco, shown in inset of Fig. B.2), protected by a mobile screen. The evaporation chamber pressure is reduced by a

turbo pump for an entire night. Then cold water circulation around the chamber is turned on for about an hour. A tank placed alongside the chamber is filled with liquid nitrogen, further reducing the pressure down to $\sim 6\,10^{-7}$ mbar, and cooling down the sample substrate (sample temperature cannot be measured however).

Once the pressure is low and stable, an oxygen bottle connected to the evaporator is open. The oxygen partial pressure is controlled via a valve, leaking a low pressure of $1 - 6\,10^{-5}$ mbar into the chamber. Fig. B.2 shows the effect of oxygen pressure on the measured InOx resistance at 4K, and on the RRR, defined as the ratio between resistance at 300 K and at 4K. Once the pressure stabilized egun power is turned on and an evaporation rate of 2 Angström per second is reached. Note that the transition takes place between a solid InOx target and its vapor phase, making it a *sublimation* rather than an evaporation.
We aim at a thickness of 47 nm to obtain a 40 nm-thick film, as measured by AFM (see Fig. B.3).
Lift off is made in acetone. It is important to stress that indium oxide is very sensitive to annealing: indium oxide deposition must always be the last fabrication step of our process.

From a disordered sample it is possible to decrease the resistance by annealing. We do it in a lamp oven kept under vaccum to have a better control on the chemical composition. Anneling temperature must always be lower than 60°C to avoid crystallization, and the higher the temperature the higher the resistance reduction. After several annealing cycles resistance is less and less affected by aging and temperature.

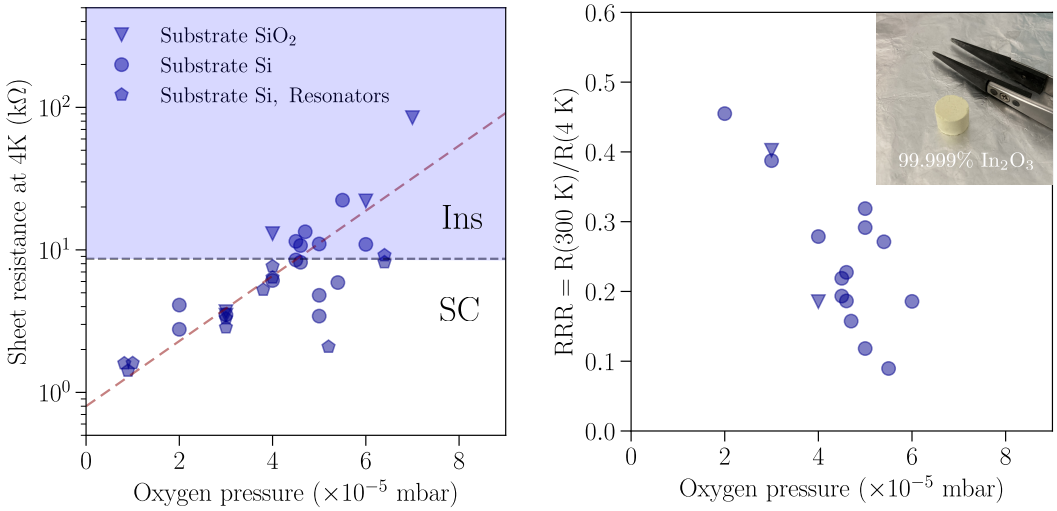

Fig. B.2. Indium oxide resistance at 4K and RRR versus partial oxygen pressure during evaporation. Resistances are obtained by four-probe measurements in different settings. Some of the samples were measured along with microwave resonators (pentagons), the others are measured from a Hall bar in a helium dipstick on silicon substrates (circles) and silicon with silicon oxide (triangles). The filled blue region shows where the samples measured at lower temperatures become insulating (the horizontal line therefore shows the SIT). Inset picture shows a typical amorphous indium oxide target used in this work.

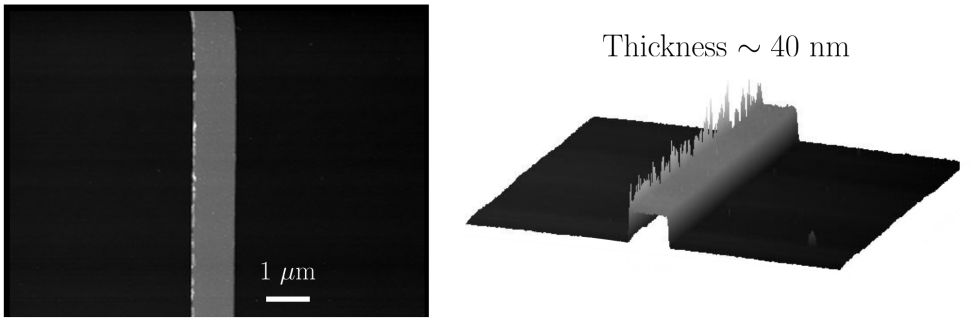

Fig. B.3. AFM image of an indium oxide resonator. The thickness obtained from AFM spectroscopy is ~ 40 nm.

APPENDIX C

Experimental Setup

In this thesis we used mainly two cryostats (called A and B here), each in several different configurations. Sample A allows for the microwave measurement in the usual frequency range used in cQED (2-12 GHz) and was previously used for the measurement of qubits and quantum limited parametric amplifiers and devices. Cryostat B on the contrary is brand new and we performed the first measurements in this fridge that includes a powerful 13 Tesla magnet. In cryostat B two different setups are installed: the first one operates in the usual 4-8 GHz range and without applied field, while the second is low frequency ($f < 4$ GHz) and can be immersed in perpendicular magnetic fields up to 13 T.

C.1 | A few general concepts

C.1.1 Thermalization of microwave radiation and noise mitigation

In most of this work we focused on properties of indium oxide resonators in their ground state. To achieve such a demanding condition we need to combine very low sample temperatures, small excitation signals, and proper isolation from envionmental noise.

To enter the *quantum regime*, where quantum fluctuations are predominent over thermal (classical) fluctuations one must have $\hbar\omega \gg k_B T$, where $\omega/(2\pi)$ is the microwave excitation frequency. In turns out that this condition is met when the average number of microwave photons injected into the sample is close to unity.
Therefore a proper experimental setup must provide a strongly reduced input signal (number of photons ~ 1, achieved by strongly attenuating the signal) and extremely low temperatures (provided by a dilution cryostat). For a measurement bandwidth in the range $0.5 - 20$ GHz the condition $\hbar\omega > k_B T$ is met for a maximum temperature of $T = 20$ mK, which is the typical base temperature of a dilution fridge.
Additionaly the measurement apparatus, at room temperature, radiates Johnson-Nyquist noise which must be filtered out. Finally environmental excitations such as ambient electromagnetic fields, radioactivity and mechanical vibrations must be mitigated as they might perturb the device from its ground state.

Attenuators

An attenuator is a dissipative, two-port component (usually matched to $50\ \Omega$) that can be used for attenuating an incoming signal, but also thermalize it.
Following [Planat, 2020; Leger, 2021] an attenuator can be modelled by a 'mirror' with power transparency $|t| \leq 1$, coupled to a phonon bath thermalized at the temperature T_{att} (which is typically the temperature of the cryostat stage to which the attenuator is solidly attached).

Now, an input signal A_{in} at temperature T_{in} entering the attenuator will be partly transmitted and partly mixed with the noise generated by the attenuator B_{att} at temperature T_{att} as [Leger, 2021]

$$A_{\text{out}}(\omega, T_{\text{in}}, T_{\text{att}}) = |t|^2 A_{\text{in}}(\omega, T_{\text{in}}) + \left(1 - |t|^2\right) B_{\text{att}}(\omega, T_{\text{att}}) \tag{C.1}$$

Eq. (C.1) not only states that the amplitude of the signal exiting the attenuator is reduced, but also that its average temperature is a mix of the input temperature T_{in} and the phonon bath temperature T_{att}. Therefore to properly thermalize a microwave signal generated by a source at room temperature, it is mandatory to attenuate it at different stages of the cryostat, at increasingly low phonon temperatures, and with sufficiently low transparency (large attenuation) to couple strongly to the cryogenic environment.

Attenuators can be discrete (based on lumped element resistors) or distributed, for which the resistance of a coaxial cable provides the needed attenuation. We use both types of attenuators.

C.1.2 Measuring resistances at very low bias

DC measurements are made at very low frequencies ($f \sim 13$ Hz) using a standard lock-in technique. A typical four-probe setup is shown in Fig. C.1.

Superconducting samples When measuring superconducting samples we use a current polarization, where the digital Lock-in amplifier (SR830 or SR810 by Stanford Research Systems) generates a voltage (typically 0.1 V) through a polarization resistor, typically 100 MΩ for an input current on sample $I = 1$ nA.

To check the reliability of measurements we collect the current exiting the sample, using a homemade current/voltage converter (and amplifier with gain $\sim 10^8 - 10^9$) to obtain a voltage that can be measured by the lockin. We found that at room temperature only 80% or less was going through the indium oxide wire. By cooling down the sample below 100 K 100% of the input is retrieved at the output, allowing a reliable measurement of the wire resistance. We suggest that this discrepancy could originate from leakage of the input current through the substrate: for strongly disordered indium oxide the room temperature resistance is of the order of $2 - 3$ kΩ/□ which is comparable to the resistance to the substrate resistance (our substrates do no have insulating oxide coating that would prevent this effect). At lower temperatures the high resistivity silicon substrate becomes more resititive that the indium oxide sample.

To measure the resistance a second lockin is used to collect the differential voltage from the two voltage probes on sample. Before entering the lock-in the differential voltage is amplified (gain 10^4 typically) using a Femto low-noise amplifier.

Measuring insulating samples Measuring samples with a tendency towards insulation can be tricky. Upon divergence of the resistance happens a moment where the polarization resistor becomes of the order of the sample's resistance, causing the measured resistance to saturate. To avoid this issue we voltage-polarize the sample by sending a small voltage excitation to the sample (typically of the order of 100 μV) using a voltage divider and collect the output current. The voltage bias can also be separately measured via a second lockin as a sanity check.

Such a method allows for the measurement of very large resistances, limited by the current-voltage amplifier maximum gain (typically $1\ \mathrm{G}\Omega$).

C.2 | Cryostat A

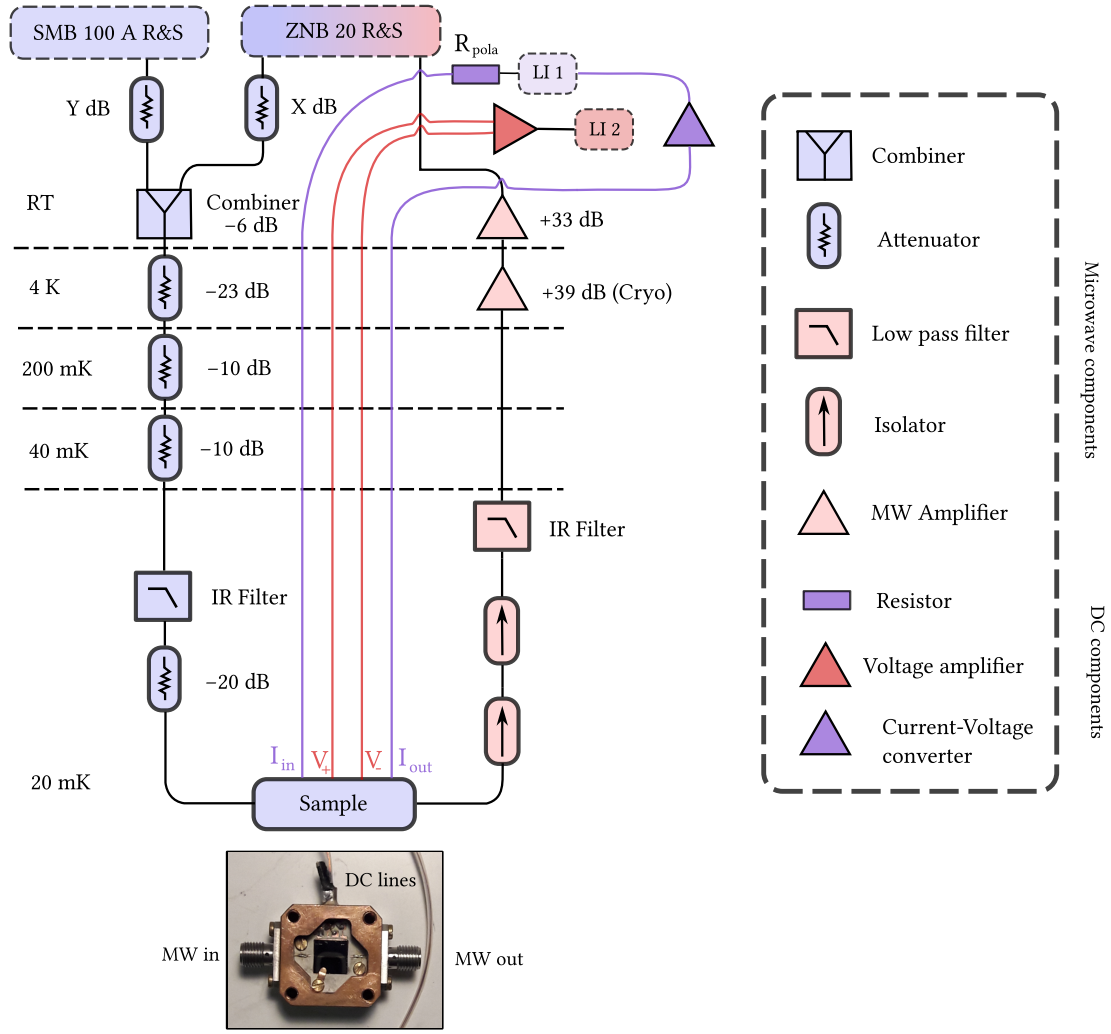

Fig. C.1. Schematic of Setup A. SMB 100 A is a microwave source, and ZNB 20 is a Vector Network Analyzer (VNA). LI stands for Lock-in amplifier. See main text for details of the different microwave and DC components. Incoming microwave signal goes down the input line where it is attenuated (blue), goes through the sample and goes back to the VNA after proper amplification and filtering (red). Bottom picture shows the sample holder, composed of a through MW transmission line on a PCB, and four DC pads connected to the four DC wires.

The first cryostat used in this thesis is a table-top, inverted dilution wet refrigerator called a *Sionludi*. It is built at Néel institute by the cryogenics team (and initially designed by Eric Eyraud and Wolfgang Wernsdorfer). A detailed presentation of this exact same cryostat can be found in previous PhD thesis defended in the Quantum Coherence team [Puertas, 2018; Planat, 2020; Leger, 2021].
The setup is almost identical to the one used in [Leger, 2021]. We added four DC lines from room-temperature down to the sample holder at 20 mK, allowing DC measurements. We also modified the typical microwave sample holder and added four connection pads to which the

device's DC structures could be bonded.

C.2.1 Input line

After being generated by the VNA, the incoming microwave signal is sent down the input line (blue line on Fig. C.1), towards the device.
As mentioned previously the signal must be strongly attenuated to reach the low photon regime, and thermalize properly the input signal. This is done by anchoring discrete attenuators to several stages of the cryostat (at $4\ \mathrm{K}$, $200\ \mathrm{mK}$, $40\ \mathrm{mK}$ and $20\ \mathrm{mK}$), with an additional attenuation at room temperature X if necessary.

A home-made distributed attenuator is added at low temperature to act as a IR filter (see Fig. C.1). Details on their fabrication and characteristics can be found in [Leger, 2021]. These $5\ \mathrm{cm}$-long SC040/50-CN-CN coaxial cables from Coax Co. have a very soft attenuation of a few dB at operating frequencies, but efficiently cut off infrared radiations.

For two-tones measurements an additional microwave source can be used at room temperature to deliver a microwave tone that can be combined to the VNA signal, via a microwave combiner (attenuation -6 dB).

C.2.2 Output line

The signal leaving the sample is very weak: it must be strongly amplified before reaching the measurement apparatus. This is done by adding a cryogenic High Electron Mobility Transistor (HEMT) amplifier (we use the LNF-LNC1-12A from Low Noise Factory, operating in the $2-12$-GHz range) at 4K, and a room-temperature amplifier.

To decouple the outgoing wave from the noise radiated by the components on the output line (such as the HEMT, RT amplifier and VNA) we use non-reciprocal elements, called *isolators*, which attenuate in the RT $\rightarrow$ sample direction only, and add IR filters.

C.2.3 Sample shielding

Necessary for the operation of the dilution fridge, polished aluminum shields are anchored at each stage of the cryostat [Puertas, 2018]. This reduces strongly the infrared radiation coming on the sample.

To further reduce the effect of external radiations potentially at the origin of the large non-equilibrium quasiparticle distribution found experimentally, we shield the sample in a copper cylinder surrounded by a high magnetic permeability metal (1.5 mm-thick CryoShield cylinder from Magnetic Shield Ltd). The inside of the cylinder is coated with a mix of Stycast black epoxy, silicon balls and carbon powder, aiming at absorbing IR radiations in the sample's vicinity.

C.2.4 Cryogenic trick to measure resistances reliably up to 7 K

The $R(T)$ curves presented in this thesis are particularly smooth compared to what is usually found by measuring the resistance when cooling down the cryostat from room temperature. The reason is that we operated the cryostat in a special regime at which the temperature could be controlled and stabilized above 1 Kelvin.

In a typical dilution refrigerator the maximum temperature that can be achieved when the helium mixture is condensed is of the order of 900 mK. Above this temperature pressures of the circulating gas become too large and dilution fails to operate.
To be able to control the temperature above 1 K we collect a large part of the helium mixture in the storage tank and induce the circulation of the remaining helium gas by turning on primary pump and compressor. The helium gas forced through the loop experiences a Joule-Thomson effect, which cools it down. By turning on a heater we can control the temperature and make it stable. Gradually increasing the heater temperature allows for the slow and steady measurement of $R(T)$ up to 7 K.

C.2.5 Setup for 3D waveguide measurements

For the measurements involving a 3D waveguide the sample holder is replaced by the 3D aluminum cavity. The latter has only one port, used both for incoming and outgoing (reflected) signals. To decouple these two excitations we use a circulator, a three-port component which role is to allow the progagation of waves in a given order (say, clock-wise for instance) and attenuate in the other directions. This allows to separate input and output signals and allow the final measurement of the reflected signal as a *transmission* measurement.

Since the main goal of these waveguide measurements was to study dissipation, we also added K&L low-pass filters before and after the sample.

C.3 | Cryostat B

Cryostat B is a brand new Bluefors dry dilution refrigerator equipped with a 13 Tesla magnet, 4 microwave lines and 24 heavily filtered DC lines. For the indium oxide measurements discussed in this thesis we used two different setups in this cryostat. The first one is a standard high-frequency setup without magnetic field, similar to usual cQED setups, and the second one is a low frequency setup $f < 4$ GHz compatible with the application of a perpendicular magnetic field up to 13 T.
Most of the operation, as well as wiring work and instrument maintenance was made by Frédéric Gay and Florent Blondelle from the Automatisation et Caractérisation team at Néel Institute.

C.3.1 High-frequency, no magnetic field

The first, high frequency setup in Cryostat B is very similar to Cryostat A. The sample holder is solidly anchored to the coldest plate of the fridge, and the cryostat is closed and cooled down without magnet.
The HEMT amplifier is a 4-8 GHz cryogenic amplifier from Low Noise Factory (LNF-LNC4_8C). The sample is decoupled from the HEMT noise by a double 4-8 GHz isolator on the output line (LNF-ISISC4_8A).
The sample holder, made of pure aluminum and light-tight, was designed to maximize quality factor (see chapter 7) and therefore did not allow the integration of DC measurements.

C.3.2 Low-frequency, 13 Tesla magnet

The sample is mounted on a homemade bulk silver (and gold plated) cold finger inserted at the center of a large magnet. Setup is illustrated in Fig. C.2.

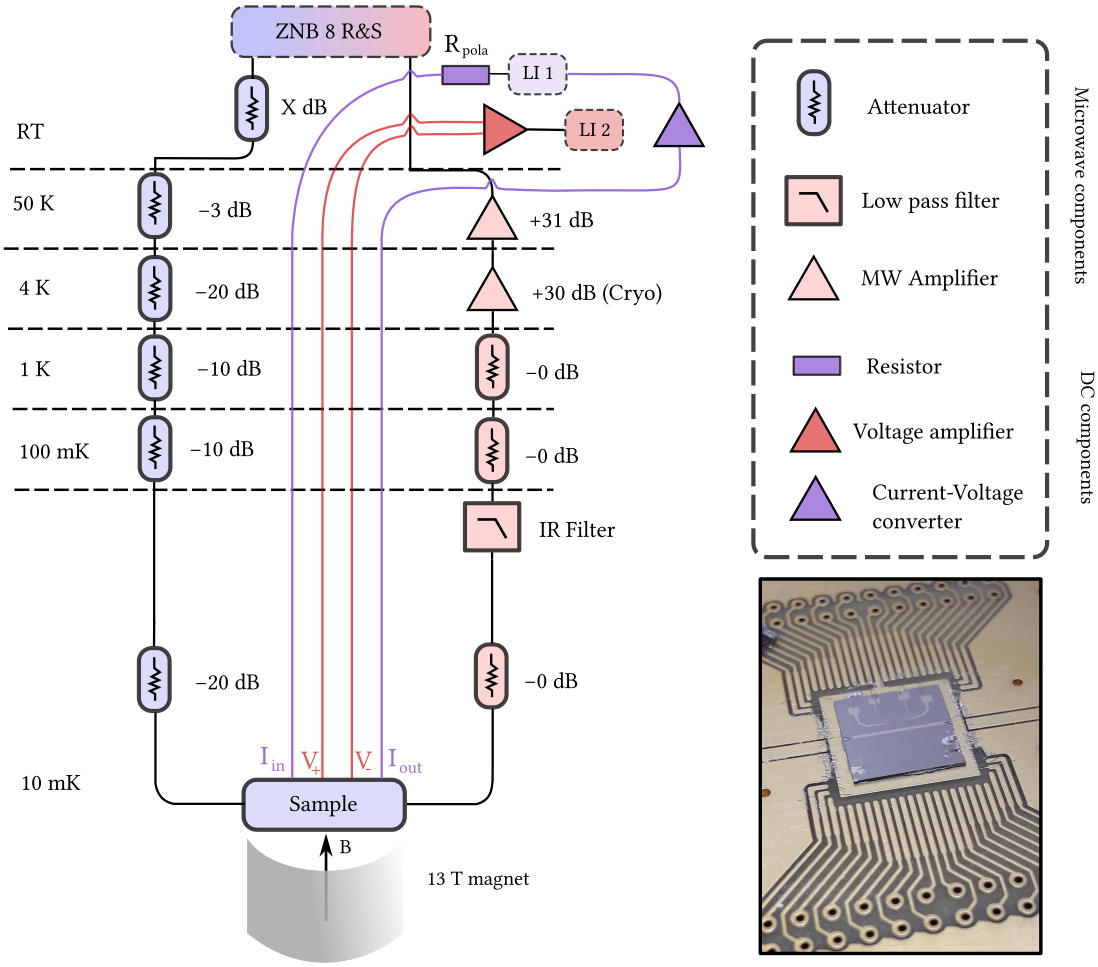

Fig. C.2. Schematic of Setup B for high magnetic fields. ZNB 8 is a Vector Network Analyzer (VNA). LI stands for Lock-in amplifier. See main text for details of the different microwave and DC components. Incoming microwave signal goes down the input line where it is attenuated (blue), goes through the sample and goes back to the VNA after proper amplification and filtering (red). The sample is stuck on a silver cold finger at the center of a large magnetic coil. Bottom picture show a sample glued to the sample holder, with 24 DC lines.

Because of the large magnetic fields one cannot use isolators to protect the output signal from the 4K noise generated by the HEMT. In order to replace it we fabricated a long dissipative coaxial cable that acts as a low-pass filter with relatively small attenuation at low frequencies and large attenuation above 4 K. We used a 0.034 inch diameter cupro-nickel coaxial cable (CN-CN034 from CryoCoax) with PTFE inner insulation. We chose a very long one meter cable to increase the overall attenuation and wound it into a compact shape as shown in Fig. C.3.
The cryogenic amplifier operates in the 10 MHz - 2 GHz range (from Arizona state university), followed by a room temperature amplifier ZKL-2+ from Minicircuits. The sample is not shielded by μ-metal, as it is designed to be immersed in a magnetic field.

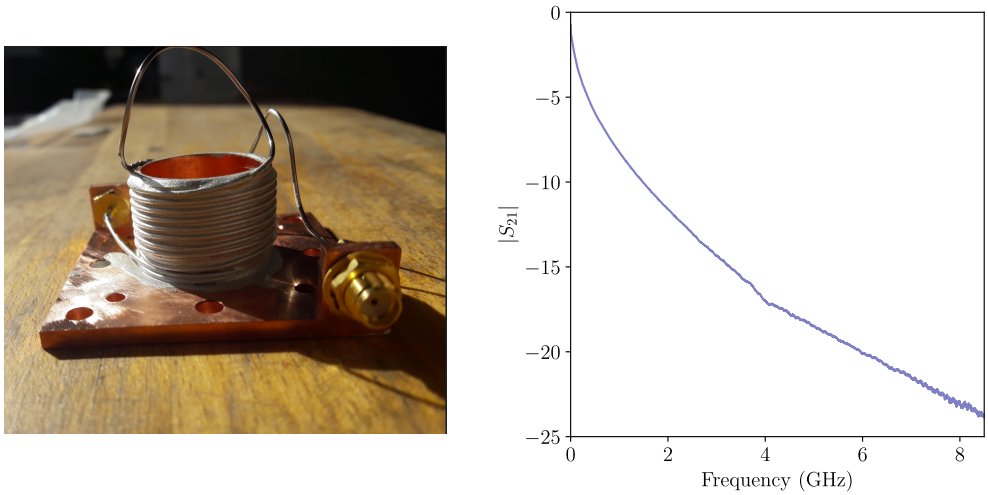

Fig. C.3. Dissipative coaxial cable as a low-pass filter. One meter of coaxial cable is wound around a copper cylinder and glued into place with silver epoxy. Right: room-temperature measurement of the coaxial cable attenuation versus frequency.

Capacitance and Kerr non-linearity model

D.1 | Distributed Capacitance of an Infinite Thin Film Superconducting Stripline

In this section we detail the analytical model derived by Denis Basko [Private communications] to account for the long-range Coulomb interactions in the capacitance of a stripline, that we used to provide a precise determination of the frequency of plasmon resonances.

Consider an infinitely long and infintely thin stripline of width $w \ll h$, where h is the distance to the ground plane (in a microstrip geometry, *i.e.* h is the thickness of the substrate of permittivity ε.)
By defining the inductance per unit length L' and capacitance per unit length C' in units of $4\pi\varepsilon_0$, one can express the plasmon frequency at wavevector $|k|$ as

$$\omega_k = \frac{|k|}{\sqrt{4\pi\varepsilon_0 C'_k L'}} \tag{D.1}$$

The inverse capacitance calculated by D. Basko reads

$$\frac{1}{C'_k} = \frac{4}{1+\varepsilon}\left[\min_{\rho(y)} \int_{-w/2}^{w/2} dy dy' \rho(y)\rho(y') K_0\left(|y-y'||k|\right) - \sum_{j=1}^{\infty} \zeta_j K_0\left(2jh|k|\right)\right] \tag{D.2}$$

where the coefficients ζ_j are given in section 3.2.2, and the minimum is taken over all the functions $\rho(y)$ such that $\int_{-w/2}^{w/2} \rho(y)dy = 1$ and accounts for charge distribution across the strip. Let us note $\mathcal{K}$ this minimum.

Then the capacitance becomes

$$\frac{1}{C'_k} = \frac{4}{1+\varepsilon}\left[\mathcal{K} - \sum_{j=1}^{\infty} \zeta_j K_0\left(2jh|k|\right)\right] \tag{D.3}$$

$\mathcal{K}$ can be estimated numerically as $\mathcal{K} = -\ln|kw| + 1.50 + 0.1|kw|^2 + \delta$ with $|\delta| < 0.01$ for $|k|w < 1$.
$\mathcal{K}$ can be evaluated by the Python code:

```
import numpy as np
from scipy.special import kn as BesselK
from scipy.linalg import solve

def coeffK(kw, npt=1000, tw= t * w):
```

```
    y = np.linspace(-0.5, 0.5, npt+1)
    yy = y[:, np.newaxis] - y[np.newaxis, :]
    yy = np.sqrt(yy**2 + max(tw, 1./npt)**2)
    mtx = besselK(0, yy * kw)
    x = solve(mtx, np.ones(npt+1))
    return 1/np.sum(x)
```

D.2 | Model for the Kerr Non-linearity and thermal phase fluctuations

D.2.1 Non-linear Ohm's law

K. Maki provides two equations that describe the effect of an applied electromagnetic field on a dirty superconductor at $T = 0$ using Gor'kov equations [Maki, 1964]:

$$\Delta = \Delta_0 e^{-\pi\zeta/4} \text{ for } \zeta \leq 1 \tag{D.4}$$

$$\mathbf{j_q} = -\frac{2e^2N}{\hbar m}\tau\Delta\left(\frac{\pi}{2} - \frac{2}{3}\zeta\right)\mathbf{A_q} \text{ for } \zeta \leq 1 \tag{D.5}$$

$$\zeta = \frac{\tau}{3\hbar\Delta}\left(p_F v_s\right)^2 \tag{D.6}$$

where Δ_0 is the gap at $T = 0$ and $\zeta = 0$, i.e without electromagnetic drive.
Eq. (D.5) is a non-linear Ohm's law.

D.2.2 Non-linear current-phase relation

Using $v_s = \frac{\hbar}{m}\partial_x\varphi$ where $\varphi(x)$ is the superconducting phase, $D = \frac{1}{3}\tau v_F^2$ where D is a diffusion constant and v_F the Fermi velocity, one rewrites ζ as

$$\zeta = \frac{\hbar D}{2\Delta}\left(\frac{\partial\varphi}{\partial x}\right)^2 \approx \xi^2\left(\frac{\partial\varphi}{\partial x}\right)^2 \tag{D.7}$$

in which we have used the dirty limit coherence length $\xi = \sqrt{\hbar D/2\Delta_0}$.

One can now reexpress the prefactor of Eq. (D.5) using the optical weight conservation $L_K^{\square} = \hbar R_n^{\square}/\pi\Delta_0$ and the Drude conductivity $\sigma_0 = e^2N\tau/m$, and using the kinetic inductance per unit length $l = L_K^{\square}/w$ where w is the wire width, t is the film thickness.
Expanding Eq. (D.4) to first order in ζ, Eq. (D.5) becomes:

$$\mathbf{j_q} = -\frac{1}{ltw}\left(1 - \frac{\pi}{4}\zeta + O(\zeta)\right)\left(1 - \frac{3}{4\pi}\zeta\right)\mathbf{A_q} \tag{D.8}$$

$$= -\frac{1}{ltw}\left(1 - \alpha\zeta + O(\zeta)\right)\mathbf{A_q} \tag{D.9}$$

with $\alpha = \frac{\pi}{4} + \frac{3}{4\pi}$.

Integrating the current density of Eq (D.9) gives the current flowing in the wire of section wt. This leads the current-flux relation

$$I(\Phi) = -\frac{1}{l}\frac{\partial\Phi}{\partial x}\left(1 - \alpha\xi^2\left(\frac{2e}{\hbar}\right)^2\left(\frac{\partial\Phi}{\partial x}\right)^2\right) \tag{D.10}$$

in which we have introduced the flux $\Phi(x) = \left(\hbar/2e\right)\varphi(x)$.
One retrieves the well known linear relation $I(\Phi) = -\frac{1}{l}\partial_x\Phi$ but with an additional higher order term.

D.2.3 Hamiltonian

The hamiltonian of a transmission line resonator writes

$$\hat{H} = \int_0^L \left(\frac{\hat{q}^2}{2c} + \frac{1}{2}lI(\Phi)^2\right) dx \tag{D.11}$$

where l and c are the kinetic inductance and capacitance per unit length respectively.
Using Equ. D.10 the hamiltonian is rewritten

$$\hat{H} = \int_0^L \left[\frac{\hat{q}^2}{2c} + \frac{1}{2l}\left(\frac{\partial\Phi}{\partial x}\right)^2\left(1 - \alpha\xi^2\left(\frac{2e}{\hbar}\right)^2\left(\frac{\partial\Phi}{\partial x}\right)^2\right)^2\right] dx \tag{D.12}$$

$$\approx \int_0^L \left[\frac{\hat{q}^2}{2c} + \frac{1}{2l}\left(\frac{\partial\Phi}{\partial x}\right)^2\right] dx - 2\int_0^L \left[\frac{1}{2l}\alpha\xi^2\left(\frac{2e}{\hbar}\right)^2\left(\frac{\partial\Phi}{\partial x}\right)^4\right] dx \tag{D.13}$$

$$= \hat{H}_0 + \hat{H}_{\mathsf{NL}} \tag{D.14}$$

$\hat{H}_0$ is the linear part of the hamiltonian while $\hat{H}_{\mathsf{NL}}$ is a non-linear perturbation.

Writing the observables using canonical quantization for the linear part of the hamiltonian :

$$\hat{\Phi}(x) = \sum_n \phi_n(x)\hat{\chi}_n \tag{D.15}$$

$$\hat{q}(x) = \sum_n \frac{1}{L}\phi_n(x)\hat{q}_n \tag{D.16}$$

where

$$\hat{\chi}_n = \sqrt{\frac{\hbar}{2\omega_n Lc}}\left(a_n + a_n^\dagger\right) \tag{D.17}$$

$$\hat{q}_n = -i\sqrt{\frac{\hbar\omega_n Lc}{2}}\left(a_n - a_n^\dagger\right) \tag{D.18}$$

in which L is the resonator length, and $\omega_n = \frac{k_n}{\sqrt{lc}}$ is the resonance frequency of mode n.
From the boundary conditions, one writes the flux as $\phi_n(x) = \sqrt{2}\cos(k_n x)$ with $k_n = \frac{n\pi}{L}$.
The normalization has been chosen so that

$$\int_0^L \phi_n(x)\phi_m(x)\,dx = L\delta_{nm} \tag{D.19}$$

$$\int_0^L \left(\partial_x\phi_n\right)\left(\partial_x\phi_m\right)\,dx = Lk_n^2\delta_{nm} \tag{D.20}$$

The linear part $\hat{H}_0$ can be written in the usual quantum harmonic oscillator form

$$\hat{H}_0 = \sum_n \hbar\omega_n a_n^\dagger a_n \tag{D.21}$$

where the constant term has been dropped.
The perturbation term is

$$\hat{H}_{\mathsf{NL}} = -\frac{l}{L^2}\alpha\xi^2\left(\frac{2e}{\hbar}\right)^2\int_0^L\left(\sum_n\sqrt{\hbar\omega_n}\sin\left(k_n x\right)\left(a_n+a_n^\dagger\right)\right)^4 dx \tag{D.22}$$

Following the method described in [Weißl et al., 2015] one can rewrite the Hamiltonian as

$$H = H_0 + H_{\mathsf{NL}} = \sum_n \hbar\omega_n' a_n^\dagger a_n - \frac{\hbar}{2}\sum_{n,m} K_{nm} a_n^\dagger a_n\, a_m^\dagger a_m \tag{D.23}$$

with $\omega_n' = \omega_n - \left(K_{nn} + \sum_m K_{nm}\right)/4$ and where the Kerr coefficients are:

$$K_{nm} = 3\alpha\left(1-\frac{1}{4}\delta_{nm}\right)\frac{\xi^2}{Lw}\frac{\hbar\omega_n\omega_m}{\Theta} \tag{D.24}$$

where we have introduced the 2D superfluid stiffness $\Theta = (\hbar/2e)^2 L_K^{-1}$.

This leads to a shift of the mode frequencies with applied microwave drive (Kerr effect) as

$$\omega_n \to \omega_n' - \frac{1}{2}\sum_m K_{nm}N_m \tag{D.25}$$

where $N_m = \langle a_m^\dagger a_m\rangle$ is the bosonic occupation number of mode m.

Eq. (D.25) states that mode n is shifted to lower frequencies when another mode m is populated. The amplitude of this effect is the Kerr coefficient K_{nm}. Note that for $n = m$, the mode n interacts with itself and its frequency is reduced as $\omega_n \to \omega_n \frac{1}{2}K_{nn}$. This last relation should be observed experimentally as the slope of a linear decrease of frequency with photon number N_n for N_n small enough.
The main parameters involved in this final result are ξ and Θ, related to disorder, and L and w given by the sample geometry. The mode frequency ω_n is actually related to both disorder and geometry, and it is sometimes instructive to recast this result with some charging energy.

Relation with charging energy and Transmon anharmonicity Writing the frequency $\omega_n = \frac{n\pi w}{L}\frac{1}{\sqrt{L_K^\square C^\square}}$ and using the definitions of superfluid stiffness and charging energy $\Theta = (\hbar/2e)^2 1/L_K^\square$ and $E_c = (2e)^2/2C^\square$, one can easily express the plasmon frequency of mode n as

$$\hbar\omega_n = n\pi\frac{w}{L}\sqrt{2E_c\Theta} \tag{D.26}$$

Injecting into Eq. (D.24) gives

$$\hbar K_n \sim 6\pi^2\frac{(n\xi)^2 w}{L^3}E_c \tag{D.27}$$

as the superfluid stiffnesses cancel out. Therefore the Kerr coefficient is merely governed by geometric parameters of the wire (dimensions L and w, coherence length ξ and charging energy E_c given by the capacitance to ground).

While the apparent absence of kinetic inductance in this result seems surprising at first glance, it is not inconsistent: to have a large non-linearity one can rely on geometry only, but for it to operate at low-enough frequency suitable for standard microwave measurements one must

provide a large L_K. In that sense Kerr non-linearity and kinetic inductance are strongly related.

Such device therefore resembles a transmon qubit with anharmonicity $\sim E_c$ [Jens Koch et al., 2007].
Experimental studies of linearities and realizations of transmons using the non-linearity of a small volume of disordered superconductor confirm this model [N. Maleeva et al., 2018; Winkel et al., 2020; Joshi et al., 2022].

D.2.4 Frequency shift induced by thermal excitation of 1D plasmons

We now show how the thermal population of one-dimensional plasmons induces a low-T suppression of superfluid density (seen experimentally as a frequency shift) using Eq. (D.25) to describe the interaction between plasmonic modes in the superconducting wire.
We now consider the thermal population of plasmons, which are bosonic collective excitations and should therefore follow the Bose-Einstein statistics $N_m = \langle a_m^\dagger a_m \rangle = \dfrac{1}{e^{\hbar\beta\omega_m} - 1}$ where $\beta = 1/k_B T$.
Combining these last two equations allows to estimate the shift of resonance frequency of mode n due to the thermal population of long-wavelength plasmons as

$$\frac{\Delta f_n(T)}{f_n(0)} \approx -\frac{3}{2}\frac{\xi^2}{Lw\Theta}\sum_m \frac{\hbar\omega_m}{e^{\hbar\beta\omega_m} - 1} \tag{D.28}$$

Assuming a linear dispersion relation (*i.e.* neglecting the weak effect of long-range Coulomb interaction on $\omega(k)$) we write $\omega_m \approx m\omega_0$, allowing to rewrite last equation in the simple form

$$\frac{\Delta f_n(T)}{f_n(0)} = -\gamma \sum_m \frac{m}{e^{mz} - 1} \tag{D.29}$$

where we have introduced the dimensionless parameters $z = \hbar\beta\omega_0$ and $\gamma = 3\hbar\omega_0\xi^2/(2Lw\Theta)$.

The sum can be calculated, leading to the frequency shift in the form of a power law

$$\frac{\Delta f_n(T)}{f_n(0)} = -\left(\frac{T}{T_K}\right)^2 \tag{D.30}$$

with

$$k_B T_K \approx \frac{2}{3\sqrt{\alpha}}\frac{\sqrt{Lw}}{\xi}\sqrt{\Theta\hbar\omega_0} \tag{D.31}$$

APPENDIX E

Some calculations and models

E.1 | Optical sum rule and superfluid stiffness

We re-derive crudely the relation between the $T = 0$ superfluid stiffness and the superconducting gap $\Theta = g\Delta/8$ for dirty superconductors (where $g = h/(e^2 R_\square)$ and Δ are the dimensionless conductance and superconducting gap respectively) that is often referred to as a prediction of BCS superconductors in the dirty limit [Mattis et al., 1958; Abrikosov et al., 1968]. While the result is usually obtained within the framework of BCS theory it is in fact more general and is related to the concept of spectral weight conservation.

In dirty superconductors (the inverse scattering time is larger than the gap $\tau^{-1} \gg \Delta/\hbar$) the density of superconducting carriers at $T = 0$ is much smaller than the total density of electrons: $n_s(0) \ll n$. This quantity decreases when τ is reduced by disorder.

Let us consider the Drude conductivity of a normal metal $\sigma(\omega)$ given by

$$\sigma(\omega) = \sigma'(\omega) - i\sigma''(\omega) \tag{E.1}$$

$$\sigma'(\omega) = \frac{\sigma_0}{1 + (\omega\tau)^2} \tag{E.2}$$

$$\sigma''(\omega) = \frac{\sigma_0\, \omega\tau}{1 + (\omega\tau)^2} \tag{E.3}$$

where the DC Drude conductivity is $\sigma_0 = ne^2\tau/m$ (m is the electron mass).

The total spectral weight under $\sigma'(\omega)$ is

$$\int_0^\infty \sigma'(\omega)\, d\omega = \frac{\pi}{2}\frac{ne^2}{m} \tag{E.4}$$

The optical sum rule [Tinkham, 1975] states that the quantity in the LHS of Eq. (E.4) must remain constant, even in the presence of a superconducting transition. The total spectral weight cannot deviate from Eq. (E.4), but can vary in magnitude in some energy ranges as long as spectral weight conservation is respected.
This is what happens when Cooper pairs condense into the superconducting state: at frequencies below $2\Delta/\hbar$ dissipation vanishes and a whole part of the spectral weight comes missing (grey region). To fulfill the conservation rule a Dirac peak at zero frequency grows, giving the contribution of superconducting carriers to the real part of conductivity:

$$\sigma'_s(\omega) = \frac{\pi n_s e^2}{2m}\delta(\omega) \tag{E.5}$$

This relation comes by taking the limit $\tau \to \infty$ in Eq. (E.2) and fulfills Eq. (E.4).

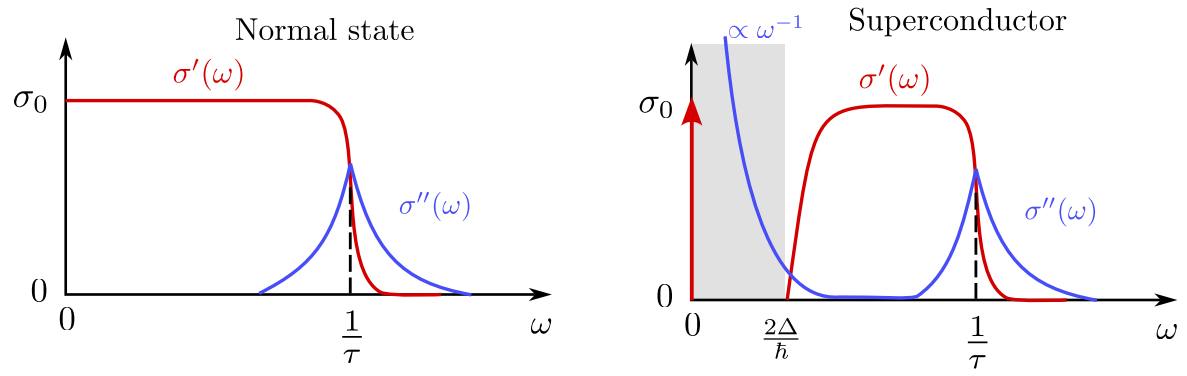

Fig. E.1. Complex conductivity in the normal and superconducting states. The real part of conductivity (in red) must obey the sum rule, therefore the dissipationless state related to superconductivity must involve a redistribution of the missing spectral weight (grey region) through the $\omega = 0$ Dirac peak.

Above $2\Delta/\hbar$ Cooper pairs break and conductivity gradually retrieves its normal-state value. This boundary between these two regions is of course not abrupt, and a rigorous calculation would provide a more precise estimation of the frequency cutoff. For the sake of simplicity we assume here that the transition is sharp, so that the missing spectral weight ends at $2\Delta/\hbar$ exactly.

We now estimate the spectral weight below the cutoff in two ways. First a direct calculation from Eq. (E.2) gives, in the dirty limit ($\tau^{-1} \gg \Delta/\hbar$):

$$\int_0^{2\Delta/\hbar} \sigma'(\omega)\, d\omega \approx \frac{ne^2\tau}{m}\left(\frac{2\Delta}{\hbar}\right) \tag{E.6}$$

Second, using the superconducting state conductivity $\sigma'_s(\omega)$:

$$\int_0^{2\Delta/\hbar} \sigma'_s(\omega)\, d\omega \approx \frac{\pi}{2}\frac{n_s e^2\tau}{m} \tag{E.7}$$

These two integrals both describe the area of the missing region, and should be equal. This leads to

$$\frac{n_s}{n} = \frac{4\Delta\tau}{\pi\hbar} \tag{E.8}$$

As expected, the smaller τ, the smaller the superconducting carrier fraction n_s/n. The density of paired electrons $n_s(0)$ decreases with disorder.

Rewriting last equation in terms of the 2D superfluid stiffness $\Theta = \hbar^2 n_s/(2m)$ and using the definition of dimensionless conductance $g = h/e^2\sigma_0$ one easily gets

$$\Theta = \frac{1}{\pi^2}\Delta g \tag{E.9}$$

which is almost identical to the BCS relation $\Theta = \Delta g/8$.

Looking now at the imaginary part of conductivity $\sigma''(\omega)$ one has in the superconducting state (taking $\tau \to \infty$):

$$\sigma''_s(\omega) = \frac{n_s e^2}{m\omega}$$

Unlike normal metals for which this quantity is negligible, $\sigma''(\omega)$ dominates the conductivity of a superconductor at frequencies well below the gap.
This relates to the kinetic inductance discussed in this thesis as $L_K^{\square} = 1/(\omega\sigma_s''(\omega))$.

Bibliography

Abrahams, E., P. W. Anderson, D. C. Licciardello, and T. V. Ramakrishnan (Mar. 1979). "Scaling Theory of Localization: Absence of Quantum Diffusion in Two Dimensions". In: *Physical Review Letters* 42.10, pp. 673–676. DOI: 10.1103/physrevlett.42.673 (Cited on pages 157, 158).

Abrikosov, A. A., L. P. Gor'kov, I. Ye Dzyaloshinskii, and Noel Corngold (Mar. 1968). "Quantum Field Theoretical Methods in Statistical Physics". In: *American Journal of Physics* 36.3, pp. 280–280. DOI: 10.1119/1.1974503 (Cited on page 181).

Adler, Joan, Christian Holm, and Wolfhard Janke (Dec. 1993). "High-temperature series analyses of the classical Heisenberg and XY models". In: *Physica A: Statistical Mechanics and its Applications* 201.4, pp. 581–592. DOI: 10.1016/0378-4371(93)90130-v (Cited on page 82).

Altoé, M. Virginia P., Archan Banerjee, Cassidy Berk, Ahmed Hajr, Adam Schwartzberg, Chengyu Song, Mohammed Alghadeer, Shaul Aloni, Michael J. Elowson, John Mark Kreikebaum, Ed K. Wong, Sinéad M. Griffin, Saleem Rao, Alexander Weber-Bargioni, Andrew M. Minor, David I. Santiago, Stefano Cabrini, Irfan Siddiqi, and D. Frank Ogletree (Apr. 2022). "Localization and Mitigation of Loss in Niobium Superconducting Circuits". In: *PRX Quantum* 3.2. DOI: 10.1103/prxquantum.3.020312 (Cited on pages 124, 126).

Altshuler, B.L. and A.G. Aronov (1985). "Electron–Electron Interaction In Disordered Conductors". In: *Electron–Electron Interactions in Disordered Systems*. Elsevier, pp. 1–153. DOI: 10.1016/b978-0-444-86916-6.50007-7 (Cited on pages 15, 149, 151).

Altshuler, Boris L., Vladimir E. Kravtsov, Igor V. Lerner, and Igor L. Aleiner (Apr. 2009). "Jumps in Current-Voltage Characteristics in Disordered Films". In: *Physical Review Letters* 102.17. DOI: 10.1103/physrevlett.102.176803 (Cited on page 75).

Amin, Kazi Rafsanjani, Carine Ladner, Guillaume Jourdan, Sébastien Hentz, Nicolas Roch, and Julien Renard (Apr. 2022). "Loss mechanisms in TiN high impedance superconducting microwave circuits". In: *Applied Physics Letters* 120.16, p. 164001. DOI: 10.1063/5.0086019 (Cited on pages 68, 115–120, 124, 126).

Anderson, P. W. (Mar. 1958a). "Absence of Diffusion in Certain Random Lattices". In: *Physical Review* 109.5, pp. 1492–1505. DOI: 10.1103/physrev.109.1492 (Cited on pages 15, 153).

– (Dec. 1958b). "Random-Phase Approximation in the Theory of Superconductivity". In: *Physical Review* 112.6, pp. 1900–1916. DOI: 10.1103/physrev.112.1900 (Cited on page 31).

Anderson, P. W., K. A. Muttalib, and T. V. Ramakrishnan (July 1983). "Theory of the "universal" degradation of T_c in high-temperature superconductors". In: *Physical Review B* 28.1, pp. 117–120. DOI: 10.1103/physrevb.28.117 (Cited on page 5).

Anderson, P.W. (1959). "Theory of dirty superconductors". In: *Journal of Physics and Chemistry of Solids* 11.1, pp. 26–30. DOI: https://doi.org/10.1016/0022-3697(59)90036-8 (Cited on page 21).

Aslamasov, L.G. and A.I. Larkin (1968). "The influence of fluctuation pairing of electrons on the conductivity of normal metal". In: *Physics Letters A* 26.6, pp. 238–239. DOI: https://doi.org/10.1016/0375-9601(68)90623-3 (Cited on pages 69, 70).

Astafiev, O. V., L. B. Ioffe, S. Kafanov, Yu. A. Pashkin, K. Yu. Arutyunov, D. Shahar, O. Cohen, and J. S. Tsai (Apr. 2012). "Coherent quantum phase slip". In: *Nature* 484.7394, pp. 355–358. DOI: 10.1038/nature10930 (Cited on pages 35, 77, 100–102).

Bard, M., I. V. Protopopov, I. V. Gornyi, A. Shnirman, and A. D. Mirlin (Aug. 2017). "Superconductor-insulator transition in disordered Josephson-junction chains". In: *Physical Review B* 96.6. DOI: 10.1103/physrevb.96.064514 (Cited on page 99).

Bard, M., I. V. Protopopov, and A. D. Mirlin (Dec. 2018). "Decay of plasmonic waves in Josephson junction chains". In: *Physical Review B* 98.22. DOI: 10.1103/physrevb.98.224513 (Cited on page 99).

Barends, R., J. Wenner, M. Lenander, Y. Chen, R. C. Bialczak, J. Kelly, E. Lucero, P. O'Malley, M. Mariantoni, D. Sank, H. Wang, T. C. White, Y. Yin, J. Zhao, A. N. Cleland, John M. Martinis, and J. J. A. Baselmans (Sept. 2011). "Minimizing quasiparticle generation from stray infrared light in superconducting quantum circuits". In: *Applied Physics Letters* 99.11, p. 113507. DOI: 10.1063/1.3638063 (Cited on page 120).

Bargerbos, Arno, Lukas Johannes Splitthoff, Marta Pita-Vidal, Jaap J. Wesdorp, Yu Liu, Peter Krogstrup, Leo P. Kouwenhoven, Christian Kraglund Andersen, and Lukas Grünhaupt (Feb. 2023). "Mitigation of Quasiparticle Loss in Superconducting Qubits by Phonon Scattering". In: *Physical Review Applied* 19.2. DOI: 10.1103/physrevapplied.19.024014 (Cited on page 121).

Basko, D. M., I. L. Aleiner, and B. L. Altshuler (Aug. 2007). "Possible experimental manifestations of the many-body localization". In: *Physical Review B* 76.5. DOI: 10.1103/physrevb.76.052203 (Cited on pages 129, 145).

– (May 2006). "Metal–insulator transition in a weakly interacting many-electron system with localized single-particle states". In: *Annals of Physics* 321.5, pp. 1126–1205. DOI: 10.1016/j.aop.2005.11.014 (Cited on pages 129, 145).

Baturina, T. I., A. Yu. Mironov, V. M. Vinokur, M. R. Baklanov, and C. Strunk (Dec. 2007). "Localized Superconductivity in the Quantum-Critical Region of the Disorder-Driven Superconductor-Insulator Transition in TiN Thin Films". In: *Physical Review Letters* 99.25. DOI: 10.1103/physrevlett.99.257003 (Cited on page 68).

Baturina, T. I., S. V. Postolova, A. Yu. Mironov, A. Glatz, M. R. Baklanov, and V. M. Vinokur (Jan. 2012). "Superconducting phase transitions in ultrathin TiN films". In: *EPL (Europhysics Letters)* 97.1, p. 17012. DOI: 10.1209/0295-5075/97/17012 (Cited on page 68).

Beasley, M. R., J. E. Mooij, and T. P. Orlando (Apr. 1979). "Possibility of Vortex-Antivortex Pair Dissociation in Two-Dimensional Superconductors". In: *Physical Review Letters* 42.17, pp. 1165–1168. DOI: 10.1103/physrevlett.42.1165 (Cited on pages 7, 9).

Benfatto, L., C. Castellani, and T. Giamarchi (Dec. 2009). "Broadening of the Berezinskii-Kosterlitz-Thouless superconducting transition by inhomogeneity and finite-size effects". In: *Physical Review B* 80.21. DOI: 10.1103/physrevb.80.214506 (Cited on page 69).

Berezinsky, V. L. (1971). "Destruction of long range order in one-dimensional and two-dimensional systems having a continuous symmetry group. I. Classical systems". In: *Sov. Phys. JETP* 32, pp. 493–500 (Cited on page 7).

Bespalov, Anton, Manuel Houzet, Julia S. Meyer, and Yuli V. Nazarov (Sept. 2016). "Theoretical Model to Explain Excess of Quasiparticles in Superconductors". In: *Physical Review Letters* 117.11. DOI: 10.1103/physrevlett.117.117002 (Cited on pages 122, 125, 127).

Bezryadin, A., C. N. Lau, and M. Tinkham (Apr. 2000). "Quantum suppression of superconductivity in ultrathin nanowires". In: *Nature* 404.6781, pp. 971–974. DOI: 10.1038/35010060 (Cited on pages 69, 99).

Bonnet, P., F. Chiodi, D. Flanigan, R. Delagrange, N. Brochu, D. Débarre, and H. le Sueur (Mar. 2022). "Strongly Nonlinear Superconducting Silicon Resonators". In: *Physical Review Applied* 17.3. DOI: 10.1103/physrevapplied.17.034057 (Cited on pages 124, 126).

Borisov, K., D. Rieger, P. Winkel, F. Henriques, F. Valenti, A. Ionita, M. Wessbecher, M. Spiecker, D. Gusenkova, I. M. Pop, and W. Wernsdorfer (Sept. 2020). "Superconducting granular aluminum resonators resilient to magnetic fields up to 1 Tesla". In: *Applied Physics Letters* 117.12, p. 120502. DOI: 10.1063/5.0018012 (Cited on pages 129, 130, 139, 140).

Bothner, D., T. Gaber, M. Kemmler, D. Koelle, R. Kleiner, S. Wünsch, and M. Siegel (July 2012). "Magnetic hysteresis effects in superconducting coplanar microwave resonators". In: *Physical Review B* 86.1. DOI: 10.1103/physrevb.86.014517 (Cited on page 140).

Bouadim, Karim, Yen Lee Loh, Mohit Randeria, and Nandini Trivedi (July 2011). "Single- and two-particle energy gaps across the disorder-driven superconductor–insulator transition". In: *Nature Physics* 7.11, pp. 884–889. DOI: 10.1038/nphys2037 (Cited on pages 22, 24–27).

Bruno, A., G. de Lange, S. Asaad, K. L. van der Enden, N. K. Langford, and L. DiCarlo (May 2015). "Reducing intrinsic loss in superconducting resonators by surface treatment and deep etching of silicon substrates". In: *Applied Physics Letters* 106.18. DOI: 10.1063/1.4919761 (Cited on pages 124, 126).

Buchholz, D. Bruce, Qing Ma, Diego Alducin, Arturo Ponce, Miguel Jose-Yacaman, Rabi Khanal, Julia E. Medvedeva, and Robert P. H. Chang (Sept. 2014). "The Structure and Properties of Amorphous Indium Oxide". In: *Chemistry of Materials* 26.18, pp. 5401–5411. DOI: 10.1021/cm502689x (Cited on page 14).

Burdastyh, M. V., S. V. Postolova, T. Proslier, S. S. Ustavshikov, A. V. Antonov, V. M. Vinokur, and A. Yu. Mironov (Jan. 2020). "Superconducting phase transitions in disordered NbTiN films". In: *Scientific Reports* 10.1. DOI: 10.1038/s41598-020-58192-3 (Cited on page 68).

Burnett, J., L. Faoro, I. Wisby, V. L. Gurtovoi, A. V. Chernykh, G. M. Mikhailov, V. A. Tulin, R. Shaikhaidarov, V. Antonov, P. J. Meeson, A. Ya. Tzalenchuk, and T. Lindström (June 2014). "Evidence for interacting two-level systems from the 1/f noise of a superconducting resonator". In: *Nature Communications* 5.1. DOI: 10.1038/ncomms5119 (Cited on page 114).

Burnett, Jonathan, Andreas Bengtsson, David Niepce, and Jonas Bylander (Mar. 2018). "Noise and loss of superconducting aluminium resonators at single photon energies". In: *Journal of Physics: Conference Series* 969, p. 012131. DOI: 10.1088/1742-6596/969/1/012131 (Cited on page 124).

Camarota, B., F. Parage, F. Balestro, P. Delsing, and O. Buisson (Jan. 2001). "Experimental Evidence of One-Dimensional Plasma Modes in Superconducting Thin Wires". In: *Physical Review Letters* 86.3, pp. 480–483. DOI: 10.1103/physrevlett.86.480 (Cited on pages 35, 39).

Capelle, Thibault, Emmanuel Flurin, Edouard Ivanov, Jose Palomo, Michael Rosticher, Sheon Chua, Tristan Briant, Pierre-François Cohadon, Antoine Heidmann, Thibaut Jacqmin, and Samuel Deléglise (Mar. 2020). "Probing a Two-Level System Bath via the Frequency Shift of an Off-Resonantly Driven Cavity". In: *Physical Review Applied* 13.3. DOI: 10.1103/physrevapplied.13.034022 (Cited on page 146).

Carbillet, C., V. Cherkez, M. A. Skvortsov, M. V. Feigel'man, F. Debontridder, L. B. Ioffe, V. S. Stolyarov, K. Ilin, M. Siegel, D. Roditchev, T. Cren, and C. Brun (July 2020). "Spectroscopic evidence for strong correlations between local superconducting gap and local Altshuler-Aronov density of states suppression in ultrathin NbN films". In: *Physical Review B* 102.2. DOI: 10.1103/physrevb.102.024504 (Cited on pages 19, 121).

Cardani, L., I. Colantoni, A. Cruciani, F. De Dominicis, G. D'Imperio, M. Laubenstein, A. Mariani, L. Pagnanini, S. Pirro, C. Tomei, N. Casali, F. Ferroni, D. Frolov, L. Gironi, A.

Grassellino, M. Junker, C. Kopas, E. Lachman, C. R. H. McRae, J. Mutus, M. Nastasi, D. P. Pappas, R. Pilipenko, M. Sisti, V. Pettinacci, A. Romanenko, D. Van Zanten, M. Vignati, J. D. Withrow, and N. Z. Zhelev (Jan. 2023). "Disentangling the sources of ionizing radiation in superconducting qubits". In: *The European Physical Journal C* 83.1. DOI: 10.1140/epjc/s10052-023-11199-2 (Cited on page 119).

Cardani, L., F. Valenti, N. Casali, G. Catelani, T. Charpentier, M. Clemenza, I. Colantoni, A. Cruciani, G. D'Imperio, L. Gironi, L. Grünhaupt, D. Gusenkova, F. Henriques, M. Lagoin, M. Martinez, G. Pettinari, C. Rusconi, O. Sander, C. Tomei, A. V. Ustinov, M. Weber, W. Wernsdorfer, M. Vignati, S. Pirro, and I. M. Pop (May 2021). "Reducing the impact of radioactivity on quantum circuits in a deep-underground facility". In: *Nature Communications* 12.1. DOI: 10.1038/s41467-021-23032-z (Cited on page 120).

Carlson, E. W., V. J. Emery, S. A. Kivelson, and D. Orgad (2002). *Concepts in High Temperature Superconductivity*. DOI: 10.48550/ARXIV.COND-MAT/0206217 (Cited on page 2).

Castellani, C and L Peliti (June 1986). In: *Journal of Physics A: Mathematical and General* 19.8, pp. L429–L432. DOI: 10.1088/0305-4470/19/8/004 (Cited on pages 16, 159).

Catelani, G., J. Koch, L. Frunzio, R. J. Schoelkopf, M. H. Devoret, and L. I. Glazman (Feb. 2011). "Quasiparticle Relaxation of Superconducting Qubits in the Presence of Flux". In: *Physical Review Letters* 106.7. DOI: 10.1103/physrevlett.106.077002 (Cited on page 119).

Catelani, G. and J. P. Pekola (Feb. 2022). "Using materials for quasiparticle engineering". In: *Materials for Quantum Technology* 2.1, p. 013001. DOI: 10.1088/2633-4356/ac4a75 (Cited on pages 108, 120).

Catelani, G., R. J. Schoelkopf, M. H. Devoret, and L. I. Glazman (Aug. 2011). "Relaxation and frequency shifts induced by quasiparticles in superconducting qubits". In: *Physical Review B* 84.6. DOI: 10.1103/physrevb.84.064517 (Cited on page 119).

Cea, T., D. Bucheli, G. Seibold, L. Benfatto, J. Lorenzana, and C. Castellani (May 2014). "Optical excitation of phase modes in strongly disordered superconductors". In: *Physical Review B* 89.17. DOI: 10.1103/physrevb.89.174506 (Cited on page 36).

Cedergren, Karin, Roger Ackroyd, Sergey Kafanov, Nicolas Vogt, Alexander Shnirman, and Timothy Duty (Oct. 2017). "Insulating Josephson Junction Chains as Pinned Luttinger Liquids". In: *Physical Review Letters* 119.16. DOI: 10.1103/physrevlett.119.167701 (Cited on page 100).

Cha, Min-Chul, Matthew P. A. Fisher, S. M. Girvin, Mats Wallin, and A. Peter Young (Oct. 1991). "Universal conductivity of two-dimensional films at the superconductor-insulator transition". In: *Physical Review B* 44.13, pp. 6883–6902. DOI: 10.1103/physrevb.44.6883 (Cited on page 12).

Chaikin, P. M. and T. C. Lubensky (1995). *Principles of Condensed Matter Physics*. Cambridge University Press. DOI: 10.1017/CBO9780511813467 (Cited on pages 3, 7).

Chand, Madhavi, Garima Saraswat, Anand Kamlapure, Mintu Mondal, Sanjeev Kumar, John Jesudasan, Vivas Bagwe, Lara Benfatto, Vikram Tripathi, and Pratap Raychaudhuri (Jan. 2012). "Phase diagram of the strongly disordered s-wave superconductor NbN close to the metal-insulator transition". In: *Physical Review B* 85.1. DOI: 10.1103/physrevb.85.014508 (Cited on pages 18, 33, 68, 85).

Chaudhuri, S., D. Li, K. D. Irwin, C. Bockstiegel, J. Hubmayr, J. N. Ullom, M. R. Vissers, and J. Gao (Apr. 2017). "Broadband parametric amplifiers based on nonlinear kinetic inductance artificial transmission lines". In: *Applied Physics Letters* 110.15. DOI: 10.1063/1.4980102 (Cited on page 147).

Chien, Wei-Chen, Yu-Han Chang, Cheng Xin Lu, Yen-Yu Ting, Cen-Shawn Wu, Sheng-Di Lin, and Watson Kuo (May 2023). "Large parametric amplification in kinetic inductance dominant resonators based on 3 nm-thick epitaxial superconductors". In: *Materials for Quantum Technology* 3.2, p. 025005. DOI: 10.1088/2633-4356/acd744 (Cited on pages 124, 126).

Chin, C. C., D. E. Oates, G. Dresselhaus, and M. S. Dresselhaus (Mar. 1992). "Nonlinear electrodynamics of superconducting NbN and Nb thin films at microwave frequencies". In: *Physical Review B* 45.9, pp. 4788–4798. DOI: 10.1103/physrevb.45.4788 (Cited on page 39).

Chockalingam, S. P., Madhavi Chand, John Jesudasan, Vikram Tripathi, and Pratap Raychaudhuri (June 2008). "Superconducting properties and Hall effect of epitaxial NbN thin films". In: *Physical Review B* 77.21. DOI: 10.1103/physrevb.77.214503 (Cited on page 68).

Cohen, Morrel H., E. N. Economou, and C. M. Soukoulis (Sept. 1983). "Polaron Formation near a Mobility Edge". In: *Physical Review Letters* 51.13, pp. 1202–1205. DOI: 10.1103/physrevlett.51.1202 (Cited on pages 16, 159).

Córcoles, Antonio D., Jerry M. Chow, Jay M. Gambetta, Chad Rigetti, J. R. Rozen, George A. Keefe, Mary Beth Rothwell, Mark B. Ketchen, and M. Steffen (Oct. 2011). "Protecting superconducting qubits from radiation". In: *Applied Physics Letters* 99.18, p. 181906. DOI: 10.1063/1.3658630 (Cited on page 120).

Cord, Bryan, Jodie Lutkenhaus, and Karl K. Berggren (2007). "Optimal temperature for development of poly(methylmethacrylate)". In: *Journal of Vacuum Science & Technology B: Microelectronics and Nanometer Structures* 25.6, p. 2013. DOI: 10.1116/1.2799978 (Cited on page 166).

Coumou, P. C. J. J., E. F. C. Driessen, J. Bueno, C. Chapelier, and T. M. Klapwijk (Nov. 2013). "Electrodynamic response and local tunneling spectroscopy of strongly disordered superconducting TiN films". In: *Physical Review B* 88.18. DOI: 10.1103/physrevb.88.180505 (Cited on page 125).

Crane, R., N. P. Armitage, A. Johansson, G. Sambandamurthy, D. Shahar, and G. Grüner (May 2007). "Survival of superconducting correlations across the two-dimensional superconductor-insulator transition: A finite-frequency study". In: *Physical Review B* 75.18. DOI: 10.1103/physrevb.75.184530 (Cited on pages 32, 33, 35, 129, 133, 134).

Crane, R. W., N. P. Armitage, A. Johansson, G. Sambandamurthy, D. Shahar, and G. Grüner (Mar. 2007). "Fluctuations, dissipation, and nonuniversal superfluid jumps in two-dimensional superconductors". In: *Physical Review B* 75.9. DOI: 10.1103/physrevb.75.094506 (Cited on pages 32, 33, 35).

Crescini, Nicolò, Samuel Cailleaux, Wiebke Guichard, Cécile Naud, Olivier Buisson, Kater W. Murch, and Nicolas Roch (Mar. 2023). "Evidence of dual Shapiro steps in a Josephson junction array". In: *Nature Physics*. DOI: 10.1038/s41567-023-01961-4 (Cited on page 100).

Crowley, Kevin D., Russell A. McLellan, Aveek Dutta, Nana Shumiya, Alexander P. M. Place, Xuan Hoang Le, Youqi Gang, Trisha Madhavan, Nishaad Khedkar, Yiming Cady Feng, Esha A. Umbarkar, Xin Gui, Lila V. H. Rodgers, Yichen Jia, Mayer M. Feldman, Stephen A. Lyon, Mingzhao Liu, Robert J. Cava, Andrew A. Houck, and Nathalie P. de Leon (2023). *Disentangling Losses in Tantalum Superconducting Circuits*. DOI: 10.48550/ARXIV.2301.07848 (Cited on pages 114, 116, 124).

Cuevas, E. and V. E. Kravtsov (Dec. 2007). "Two-eigenfunction correlation in a multifractal metal and insulator". In: *Physical Review B* 76.23. DOI: 10.1103/physrevb.76.235119 (Cited on pages 16, 160, 161).

de Graaf, S. E., L. Faoro, L. B. Ioffe, S. Mahashabde, J. J. Burnett, T. Lindström, S. E. Kubatkin, A. V. Danilov, and A. Ya. Tzalenchuk (Dec. 2020). "Two-level systems in superconducting quantum devices due to trapped quasiparticles". In: *Science Advances* 6.51. DOI: 10.1126/sciadv.abc5055 (Cited on pages 122, 123, 125, 127).

Deng, Hao, Zhijun Song, Ran Gao, Tian Xia, Feng Bao, Xun Jiang, Hsiang-Sheng Ku, Zhisheng Li, Xizheng Ma, Jin Qin, Hantao Sun, Chengchun Tang, Tenghui Wang, Feng Wu, Wenlong Yu, Gengyan Zhang, Xiaohang Zhang, Jingwei Zhou, Xing Zhu, Yaoyun Shi, Hui-Hai Zhao, and Chunqing Deng (Feb. 2023). "Titanium Nitride Film on Sapphire Substrate with Low Dielectric Loss for Superconducting Qubits". In: *Physical Review Applied* 19.2. DOI: 10.1103/physrevapplied.19.024013 (Cited on page 116).

Detweiler, Zachary M., Steven M. Wulfsberg, Matthew G. Frith, Andrew B. Bocarsly, and Steven L. Bernasek (June 2016). "The oxidation and surface speciation of indium and indium oxides exposed to atmospheric oxidants". In: *Surface Science* 648, pp. 188–195. DOI: 10.1016/j.susc.2015.10.026 (Cited on page 119).

Doron, A., I. Tamir, T. Levinson, M. Ovadia, B. Sacépé, and D. Shahar (Dec. 2017). "Instability of Insulators near Quantum Phase Transitions". In: *Physical Review Letters* 119.24. DOI: 10.1103/physrevlett.119.247001 (Cited on page 75).

Driessen, E. F. C., P. C. J. J. Coumou, R. R. Tromp, P. J. de Visser, and T. M. Klapwijk (Sept. 2012). "Strongly Disordered TiN and NbTiN s-Wave Superconductors Probed by Microwave Electrodynamics". In: *Physical Review Letters* 109.10. DOI: 10.1103/physrevlett.109.107003 (Cited on page 35).

Dubouchet, Thomas, Benjamin Sacépé, Johanna Seidemann, Dan Shahar, Marc Sanquer, and Claude Chapelier (Dec. 2018). "Collective energy gap of preformed Cooper pairs in disordered superconductors". In: *Nature Physics* 15.3, pp. 233–236. DOI: 10.1038/s41567-018-0365-8 (Cited on pages 20, 21, 62).

Dumur, E., B. Delsol, T. Weissl, B. Kung, W. Guichard, C. Hoarau, C. Naud, K. Hasselbach, O. Buisson, K. Ratter, and B. Gilles (Apr. 2016). "Epitaxial Rhenium Microwave Resonators". In: *IEEE Transactions on Applied Superconductivity* 26.3, pp. 1–4. DOI: 10.1109/tasc.2016.2547221 (Cited on pages 124, 126).

Dumur, Etienne (Feb. 2015). "A V-shape superconducting artificial atom for circuit quantum electrodynamics". Theses. Université Grenoble Alpes (Cited on page 49).

Dupré, O, A Benoit, M Calvo, A Catalano, J Goupy, C Hoarau, T Klein, K Le Calvez, B Sacépé, A Monfardini, and F Levy-Bertrand (Feb. 2017). "Tunable sub-gap radiation detection with superconducting resonators". In: *Superconductor Science and Technology* 30.4, p. 045007. DOI: 10.1088/1361-6668/aa5b14 (Cited on pages 35, 77).

Dutta, Surajit, Pratap Raychaudhuri, Sudhansu S Mandal, and T V Ramakrishnan (June 2022). "Superfluid density in conventional superconductors: from clean to strongly disordered". In: *Journal of Physics: Condensed Matter* 34.33, p. 335601. DOI: 10.1088/1361-648x/ac76fd (Cited on pages 125, 127).

Earnest, C T, J H Béjanin, T G McConkey, E A Peters, A Korinek, H Yuan, and M Mariantoni (Nov. 2018). "Substrate surface engineering for high-quality silicon/aluminum superconducting resonators". In: *Superconductor Science and Technology* 31.12, p. 125013. DOI: 10.1088/1361-6668/aae548 (Cited on pages 124, 126).

Ebensperger, Nikolaj (2021). *Dielectric properties on the insulating side of the superconductor-insulator transition*. en. DOI: 10.18419/OPUS-11782 (Cited on pages 72, 145).

Ebensperger, Nikolaj, Markus Thiemann, Martin Dressel, and Marc Scheffler (Oct. 2016). "Superconducting Pb stripline resonators in parallel magnetic field and their application for microwave spectroscopy". In: *Superconductor Science and Technology* 29.11, p. 115004. DOI: 10.1088/0953-2048/29/11/115004 (Cited on page 124).

Edwards, J T and D J Thouless (Apr. 1972). "Numerical studies of localization in disordered systems". In: *Journal of Physics C: Solid State Physics* 5.8, pp. 807–820. DOI: 10.1088/0022-3719/5/8/007 (Cited on page 154).

Efros, A L and B I Shklovskii (Feb. 1975). "Coulomb gap and low temperature conductivity of disordered systems". In: *Journal of Physics C: Solid State Physics* 8.4, pp. L49–L51. DOI: 10.1088/0022-3719/8/4/003 (Cited on pages 163, 164).

Emery, V. J. and S. A. Kivelson (Mar. 1995). "Importance of phase fluctuations in superconductors with small superfluid density". In: *Nature* 374.6521, pp. 434–437. DOI: 10.1038/374434a0 (Cited on pages 27, 82, 85).

Feigel'man, M V, D A Ivanov, and E Cuevas (May 2018). "Dielectric response of Anderson and pseudogapped insulators". In: *New Journal of Physics* 20.5, p. 053045. DOI: 10.1088/1367-2630/aac0d7 (Cited on pages 28, 72).

Feigel'man, M. V. and L. B. Ioffe (Sept. 2015). "Superfluid density of a pseudogapped superconductor near the superconductor-insulator transition". In: *Phys. Rev. B* 92 (10), p. 100509. DOI: 10.1103/PhysRevB.92.100509 (Cited on page 86).

– (Jan. 2018). "Microwave Properties of Superconductors Close to the Superconductor-Insulator Transition". In: *Phys. Rev. Lett.* 120 (3), p. 037004. DOI: 10.1103/PhysRevLett.120.037004 (Cited on pages 36, 78, 89).

Feigel'man, M. V., L. B. Ioffe, V. E. Kravtsov, and E. A. Yuzbashyan (Jan. 2007). "Eigenfunction Fractality and Pseudogap State near the Superconductor-Insulator Transition". In: *Physical Review Letters* 98.2. DOI: 10.1103/physrevlett.98.027001 (Cited on page 28).

Feigel'man, M. V., L. B. Ioffe, and M. Mézard (Nov. 2010). "Superconductor-insulator transition and energy localization". In: *Phys. Rev. B* 82 (18), p. 184534. DOI: 10.1103/PhysRevB.82.184534 (Cited on page 28).

Feigel'man, M. V., S. E. Korshunov, and A. B. Pugachev (Apr. 1997). "Parity effect and charge-binding transition in submicron Josephson junction arrays". In: *Journal of Experimental and Theoretical Physics Letters* 65.7, pp. 566–571. DOI: 10.1134/1.567397 (Cited on page 73).

Feigel'man, M.V., L.B. Ioffe, V.E. Kravtsov, and E. Cuevas (July 2010). "Fractal superconductivity near localization threshold". In: *Annals of Physics* 325.7, pp. 1390–1478. DOI: 10.1016/j.aop.2010.04.001 (Cited on pages 28–30, 32, 86).

Finkel'stein, A.M. (1986). "Superconducting transition temperature in amorphous films". In: *JETP Lett* 45.46 (Cited on page 6).

– (1994). "Suppression of superconductivity in homogeneously disordered systems". In: *Physica B: Condensed Matter* 197.1, pp. 636–648. DOI: https://doi.org/10.1016/0921-4526(94)90267-4 (Cited on page 65).

Fiory, A. T., A. F. Hebard, and W. I. Glaberson (Nov. 1983). "Superconducting phase transitions in indium/indium-oxide thin-film composites". In: *Physical Review B* 28.9, pp. 5075–5087. DOI: 10.1103/physrevb.28.5075 (Cited on page 32).

Fisher, Matthew P. A. (Aug. 1990). "Quantum phase transitions in disordered two-dimensional superconductors". In: *Physical Review Letters* 65.7, pp. 923–926. DOI: 10.1103/physrevlett.65.923 (Cited on page 9).

Fisher, Matthew P. A., G. Grinstein, and S. M. Girvin (Jan. 1990). "Presence of quantum diffusion in two dimensions: Universal resistance at the superconductor-insulator transition". In: *Physical Review Letters* 64.5, pp. 587–590. DOI: 10.1103/physrevlett.64.587 (Cited on page 12).

Fisher, Matthew P. A. and D. H. Lee (Feb. 1989). "Correspondence between two-dimensional bosons and a bulk superconductor in a magnetic field". In: *Physical Review B* 39.4, pp. 2756–2759. DOI: 10.1103/physrevb.39.2756 (Cited on page 11).

Fisher, Matthew P. A., Peter B. Weichman, G. Grinstein, and Daniel S. Fisher (July 1989). "Boson localization and the superfluid-insulator transition". In: *Physical Review B* 40.1, pp. 546–570. DOI: 10.1103/physrevb.40.546 (Cited on page 12).

Fisher, Michael E., Michael N. Barber, and David Jasnow (Aug. 1973). "Helicity Modulus, Superfluidity, and Scaling in Isotropic Systems". In: *Physical Review A* 8.2, pp. 1111–1124. DOI: 10.1103/physreva.8.1111 (Cited on page 3).

Foshat, Paniz, Paul Baity, Sergey Danilin, Valentino Seferai, Shima Poorgholam-Khanjari, Hua Feng, Oleg A. Mukhanov, Matthew Hutchings, Robert H. Hadfield, Muhammad Imran, Martin Weides, and Kaveh Delfanazari (2023). *Characterizing Niobium Nitride Superconducting Microwave Coplanar Waveguide Resonator Array for Circuit Quantum Electrodynamics in Extreme Conditions*. DOI: 10.48550/ARXIV.2306.02356 (Cited on pages 124, 126).

Frasca, Simone, Ivo Nikolaev Arabadzhiev, Sebastien Yves Bros de Puechredon, Fabian Oppliger, Vincent Jouanny, Roberto Musio, Marco Scigliuzzo, Fabrizio Minganti, Pasquale Scarlino, and Edoardo Charbon (2023). *High-kinetic inductance NbN films for high-quality compact superconducting resonators*. DOI: 10.48550/ARXIV.2302.13930 (Cited on pages 124, 126).

Gantmakher, V. F., M. V. Golubkov, V. T. Dolgopolov, A. Shashkin, and G. E. Tsydynzhapov (June 2000). "Observation of the parallel-magnetic-field-induced superconductor-insulator transition in thin amorphous InO films". In: *Journal of Experimental and Theoretical Physics Letters* 71.11, pp. 473–476. DOI: 10.1134/1.1307996 (Cited on page 129).

Gao, Jiansong (2008). "The Physics of Superconducting Microwave Resonators". en. PhD thesis. DOI: 10.7907/RAT0-VM75 (Cited on page 110).

Gao, Ran, Hsiang-Sheng Ku, Hao Deng, Wenlong Yu, Tian Xia, Feng Wu, Zhijun Song, Minghua Wang, Xiaohe Miao, Chao Zhang, Yue Lin, Yaoyun Shi, Hui-Hai Zhao, and Chunqing Deng (July 2022). "Ultrahigh Kinetic Inductance Superconducting Materials from Spinodal Decomposition". In: *Advanced Materials* 34.32, p. 2201268. DOI: 10.1002/adma.202201268 (Cited on pages 124, 126).

Gao, Ran, Wenlong Yu, Hao Deng, Hsiang-Sheng Ku, Zhisheng Li, Minghua Wang, Xiaohe Miao, Yue Lin, and Chunqing Deng (Mar. 2022). "Epitaxial titanium nitride microwave resonators: Structural, chemical, electrical, and microwave properties". In: *Physical Review Materials* 6.3. DOI: 10.1103/physrevmaterials.6.036202 (Cited on pages 124, 126).

Garg, Ramesh (Dec. 1979). "Design equations for coupled microstrip lines". In: *International Journal of Electronics* 47.6, pp. 587–591. DOI: 10.1080/00207217908938683 (Cited on page 48).

Ghosal, Amit, Mohit Randeria, and Nandini Trivedi (Nov. 2001). "Inhomogeneous pairing in highly disordered s-wave superconductors". In: *Phys. Rev. B* 65 (1), p. 014501. DOI: 10.1103/PhysRevB.65.014501 (Cited on pages 22–27, 81, 85).

Giamarchi, T. and H. J. Schulz (Jan. 1988). "Anderson localization and interactions in one-dimensional metals". In: *Physical Review B* 37.1, pp. 325–340. DOI: 10.1103/physrevb.37.325 (Cited on pages 98–100).

Giamarchi, Thierry (Dec. 2003). "Luttinger Liquids". In: *Quantum Physics in One Dimension*. Oxford University Press, pp. 70–99 (Cited on page 97).

Givan, U. and Z. Ovadyahu (Oct. 2012). "Compositional disorder and transport peculiarities in the amorphous indium oxides". In: *Phys. Rev. B* 86 (16), p. 165101. DOI: 10.1103/PhysRevB.86.165101 (Cited on page 17).

Goldman, Allen M. and Nina Marković (Nov. 1998). "Superconductor-Insulator Transitions in the Two-Dimensional Limit". In: *Physics Today* 51.11, pp. 39–44. DOI: 10.1063/1.882069 (Cited on page 5).

Goldman, Allen M. and Stuart A. Wolf, eds. (1984). *Percolation, Localization, and Superconductivity*. Springer US. DOI: 10.1007/978-1-4615-9394-2 (Cited on page 7).

Gordon, R. T., C. E. Murray, C. Kurter, M. Sandberg, S. A. Hall, K. Balakrishnan, R. Shelby, B. Wacaser, A. A. Stabile, J. W. Sleight, M. Brink, M. B. Rothwell, K. P. Rodbell, O. Dial, and M. Steffen (Feb. 2022). "Environmental radiation impact on lifetimes and quasiparticle tunneling rates of fixed-frequency transmon qubits". In: *Applied Physics Letters* 120.7, p. 074002. DOI: 10.1063/5.0078785 (Cited on page 120).

Graham, Mark R., C. J. Adkins, Haim Behar, and Ralph Rosenbaum (Feb. 1998). "Experimental study of the Ioffe-Regel criterion for amorphous indium oxide films". In: *Journal of Physics: Condensed Matter* 10.4, p. 809. DOI: 10.1088/0953-8984/10/4/010 (Cited on pages 62, 64).

Graybeal, J. M. and M. R. Beasley (Apr. 1984). "Localization and interaction effects in ultrathin amorphous superconducting films". In: *Physical Review B* 29.7, pp. 4167–4169. DOI: 10.1103/physrevb.29.4167 (Cited on page 6).

Grieg, D. and H. Engelmann (Dec. 1952). "Microstrip-A New Transmission Technique for the Kilomegacycle Range". In: *Proceedings of the IRE* 40.12, pp. 1644–1650. DOI: 10.1109/jrproc.1952.274144 (Cited on page 40).

Grünhaupt, Lukas, Nataliya Maleeva, Sebastian T. Skacel, Martino Calvo, Florence Levy-Bertrand, Alexey V. Ustinov, Hannes Rotzinger, Alessandro Monfardini, Gianluigi Catelani, and Ioan M. Pop (Sept. 2018). "Loss Mechanisms and Quasiparticle Dynamics in Superconducting Microwave Resonators Made of Thin-Film Granular Aluminum". In: *Physical Review Letters* 121.11. DOI: 10.1103/physrevlett.121.117001 (Cited on pages 115, 116, 120, 122).

Grünhaupt, Lukas, Martin Spiecker, Daria Gusenkova, Nataliya Maleeva, Sebastian T. Skacel, Ivan Takmakov, Francesco Valenti, Patrick Winkel, Hannes Rotzinger, Wolfgang Wernsdorfer, Alexey V. Ustinov, and Ioan M. Pop (Apr. 2019). "Granular aluminium as a superconducting material for high-impedance quantum circuits". In: *Nature Materials* 18.8, pp. 816–819. DOI: 10.1038/s41563-019-0350-3 (Cited on page 147).

Gümüş, E., D. Majidi, D. Nikolić, P. Raif, B. Karimi, J. T. Peltonen, E. Scheer, J. P. Pekola, H. Courtois, W. Belzig, and C. B. Winkelmann (Jan. 2023). "Calorimetry of a phase slip in a Josephson junction". In: *Nature Physics*. DOI: 10.1038/s41567-022-01844-0 (Cited on page 99).

Haldane, F. D. M. (Dec. 1981). "Effective Harmonic-Fluid Approach to Low-Energy Properties of One-Dimensional Quantum Fluids". In: *Physical Review Letters* 47.25, pp. 1840–1843. DOI: 10.1103/physrevlett.47.1840 (Cited on page 97).

Hall, L A (1968). *Survey of electrical resistivity measurements on 16 pure metals in the temperature range 0 to 273 K*. Tech. rep. DOI: 10.6028/nbs.tn.365 (Cited on page 126).

Halperin, B. I. and David R. Nelson (Sept. 1979). "Resistive transition in superconducting films". In: *Journal of Low Temperature Physics* 36.5-6, pp. 599–616. DOI: 10.1007/bf00116988 (Cited on page 11).

Haviland, D. B., Y. Liu, and A. M. Goldman (May 1989). "Onset of superconductivity in the two-dimensional limit". In: *Physical Review Letters* 62.18, pp. 2180–2183. DOI: 10.1103/physrevlett.62.2180 (Cited on page 68).

Hazard, T.M., A. Gyenis, A. Di Paolo, A.T. Asfaw, S.A. Lyon, A. Blais, and A.A. Houck (Jan. 2019). "Nanowire Superinductance Fluxonium Qubit". In: *Physical Review Letters* 122.1. DOI: 10.1103/physrevlett.122.010504 (Cited on page 147).

He, Q., P. OuYang, M. Dai, H. Guan, J. Hu, S. He, Y. Wang, and L. F. Wei (June 2021). "Lumped element granular aluminum resonators with high kinetic inductances". In: *AIP Advances* 11.6, p. 065204. DOI: 10.1063/5.0046910 (Cited on pages 124, 126).

Hebard, A. F. and A. T. Fiory (Jan. 1980). "Evidence for the Kosterlitz-Thouless Transition in Thin Superconducting Aluminum Films". In: *Physical Review Letters* 44.4, pp. 291–294. DOI: 10.1103/physrevlett.44.291 (Cited on page 34).

Henriques, Fabio, Francesco Valenti, Thibault Charpentier, Marc Lagoin, Clement Gouriou, Maria Martínez, Laura Cardani, Marco Vignati, Lukas Grünhaupt, Daria Gusenkova, Julian Ferrero, Sebastian T. Skacel, Wolfgang Wernsdorfer, Alexey V. Ustinov, Gianluigi Catelani, Oliver Sander, and Ioan M. Pop (Nov. 2019). "Phonon traps reduce the quasiparticle density in superconducting circuits". In: *Applied Physics Letters* 115.21, p. 212601. DOI: 10.1063/1.5124967 (Cited on pages 120, 121).

Holland, Eric T., Yaniv J. Rosen, Nicholas Materise, Nathan Woollett, Thomas Voisin, Y. Morris Wang, Sharon G. Torres, Jorge Mireles, Gianpaolo Carosi, and Jonathan L DuBois (Nov. 2017). "High-kinetic inductance additive manufactured superconducting microwave cavity". In: *Applied Physics Letters* 111.20. DOI: 10.1063/1.5000241 (Cited on pages 124, 126).

Houzet, Manuel and Leonid I. Glazman (June 2019). "Microwave Spectroscopy of a Weakly Pinned Charge Density Wave in a Superinductor". In: *Physical Review Letters* 122.23. DOI: 10.1103/physrevlett.122.237701 (Cited on pages 98, 99).

Hsieh, Yun-Da, Ying-Jer Kao, and Anders W Sandvik (Sept. 2013). "Finite-size scaling method for the Berezinskii–Kosterlitz–Thouless transition". In: *Journal of Statistical Mechanics: Theory and Experiment* 2013.09, P09001. DOI: 10.1088/1742-5468/2013/09/p09001 (Cited on page 82).

Hu, Wenchuang (Walter), Koshala Sarveswaran, Marya Lieberman, and Gary H. Bernstein (2004). "Sub-10 nm electron beam lithography using cold development of poly(methylmethacrylate)". In: *Journal of Vacuum Science & Technology B: Microelectronics and Nanometer Structures* 22.4, p. 1711. DOI: 10.1116/1.1763897 (Cited on page 166).

Iaia, V., J. Ku, A. Ballard, C. P. Larson, E. Yelton, C. H. Liu, S. Patel, R. McDermott, and B. L. T. Plourde (Oct. 2022). "Phonon downconversion to suppress correlated errors in superconducting qubits". In: *Nature Communications* 13.1. DOI: 10.1038/s41467-022-33997-0 (Cited on page 121).

Jia, Haolin, Boyi Zhou, Tao Wang, Yanfu Wu, Iina Yang, Zengqian Ding, Shuming Li, Kanglin Xiong, and Jiagui Feng (2023). *α-tantalum (110) films grown on a-plane sapphire substrate by molecular beam epitaxy for low-loss superconducting coplanar waveguide resonators*. DOI: 10.48550/ARXIV.2306.09566 (Cited on pages 124, 126).

Joshi, Chaitali, Wenyuan Chen, Henry G. LeDuc, Peter K. Day, and Mohammad Mirhosseini (Dec. 2022). "Strong Kinetic-Inductance Kerr Nonlinearity with Titanium Nitride Nanowires". In: *Physical Review Applied* 18.6. DOI: 10.1103/physrevapplied.18.064088 (Cited on pages 147, 180).

Kamlapure, Anand, Tanmay Das, Somesh Chandra Ganguli, Jayesh B. Parmar, Somnath Bhattacharyya, and Pratap Raychaudhuri (Oct. 2013). "Emergence of nanoscale inhomogeneity in the superconducting state of a homogeneously disordered conventional superconductor". In: *Scientific Reports* 3.1. DOI: 10.1038/srep02979 (Cited on pages 18, 34).

Kamlapure, Anand, Mintu Mondal, Madhavi Chand, Archana Mishra, John Jesudasan, Vivas Bagwe, L. Benfatto, Vikram Tripathi, and Pratap Raychaudhuri (Feb. 2010). "Measurement of magnetic penetration depth and superconducting energy gap in very thin epitaxial NbN films". In: *Applied Physics Letters* 96.7, p. 072509. DOI: 10.1063/1.3314308 (Cited on page 34).

Karatsu, K., A. Endo, J. Bueno, P. J. de Visser, R. Barends, D. J. Thoen, V. Murugesan, N. Tomita, and J. J. A. Baselmans (Jan. 2019). "Mitigation of cosmic ray effect on microwave kinetic inductance detector arrays". In: *Applied Physics Letters* 114.3. DOI: 10.1063/1.5052419 (Cited on page 121).

Khvalyuk, A. V. and M. V. Feigel'man (Dec. 2021). "Distribution of the order parameter in strongly disordered superconductors: An analytic theory". In: *Phys. Rev. B* 104 (22), p. 224505. DOI: 10.1103/PhysRevB.104.224505 (Cited on page 32).

Khvalyuk, Anton, Thibault Charpentier, Nicolas Roch, Benjamin Sacépé, and Mikhail Feigel'man (2023). "Near-power-law temperature dependence of the superfluid stiffness in strongly disordered superconductors". In: DOI: https://doi.org/10.48550/arXiv.2311.15126 (Cited on pages 53, 54, 56, 89).

Kirsh, Naftali, Elisha Svetitsky, Alexander L. Burin, Moshe Schechter, and Nadav Katz (June 2017). "Revealing the nonlinear response of a tunneling two-level system ensemble using coupled modes". In: *Physical Review Materials* 1.1. DOI: 10.1103/physrevmaterials.1.012601 (Cited on page 146).

Koch, Jens, Terri M. Yu, Jay Gambetta, A. A. Houck, D. I. Schuster, J. Majer, Alexandre Blais, M. H. Devoret, S. M. Girvin, and R. J. Schoelkopf (Oct. 2007). "Charge-insensitive qubit design derived from the Cooper pair box". In: *Physical Review A* 76.4. DOI: 10.1103/physreva.76.042319 (Cited on page 180).

König, E. J., A. Levchenko, I. V. Protopopov, I. V. Gornyi, I. S. Burmistrov, and A. D. Mirlin (Dec. 2015). "Berezinskii-Kosterlitz-Thouless transition in homogeneously disordered superconducting films". In: *Physical Review B* 92.21. DOI: 10.1103/physrevb.92.214503 (Cited on page 68).

Kosterlitz, J M and D J Thouless (Apr. 1973). "Ordering, metastability and phase transitions in two-dimensional systems". In: *Journal of Physics C: Solid State Physics* 6.7, pp. 1181–1203. DOI: 10.1088/0022-3719/6/7/010 (Cited on page 7).

Kowal, D. and Z. Ovadyahu (Feb. 2008). "Scale dependent superconductor–insulator transition". In: *Physica C: Superconductivity* 468.4, pp. 322–325. DOI: 10.1016/j.physc.2007.07.012 (Cited on pages 17, 69).

Kristen, Maximilian, Jan Nicolas Voss, Micha Wildermuth, Jürgen Lisenfeld, Hannes Rotzinger, and Alexey V. Ustinov (2023). *Observation of giant two-level systems in a granular superconductor*. DOI: 10.48550/ARXIV.2307.09078 (Cited on page 123).

Kroll, J.G., F. Borsoi, K.L. van der Enden, W. Uilhoorn, D. de Jong, M. Quintero-Pérez, D.J. van Woerkom, A. Bruno, S.R. Plissard, D. Car, E.P.A.M. Bakkers, M.C. Cassidy, and L.P. Kouwenhoven (June 2019). "Magnetic-Field-Resilient Superconducting Coplanar-Waveguide Resonators for Hybrid Circuit Quantum Electrodynamics Experiments". In: *Physical Review Applied* 11.6. DOI: 10.1103/physrevapplied.11.064053 (Cited on page 130).

Krupko, Yu., V. D. Nguyen, T. Weißl, É. Dumur, J. Puertas, R. Dassonneville, C. Naud, F. W. J. Hekking, D. M. Basko, O. Buisson, N. Roch, and W. Hasch-Guichard (Sept. 2018). "Kerr nonlinearity in a superconducting Josephson metamaterial". In: *Physical Review B* 98.9. DOI: 10.1103/physrevb.98.094516 (Cited on pages 42, 53).

Kudra, M., J. Biznárová, A. Fadavi Roudsari, J. J. Burnett, D. Niepce, S. Gasparinetti, B. Wickman, and P. Delsing (Aug. 2020). "High quality three-dimensional aluminum microwave cavities". In: *Applied Physics Letters* 117.7. DOI: 10.1063/5.0016463 (Cited on pages 124, 126).

Kulik, I. O. (1973). "Surface-charge oscillations in superconductors". In: *Zh. Ekps. Teor. Fiz* 65, pp. 2016–2022 (Cited on page 39).

Kuzmin, R., R. Mencia, N. Grabon, N. Mehta, Y.-H. Lin, and V. E. Manucharyan (June 2019). "Quantum electrodynamics of a superconductor–insulator phase transition". In: *Nature Physics* 15.9, pp. 930–934. DOI: 10.1038/s41567-019-0553-1 (Cited on pages 77, 100).

Lagendijk, Ad, Bart van Tiggelen, and Diederik S. Wiersma (Aug. 2009). "Fifty years of Anderson localization". In: *Physics Today* 62.8, pp. 24–29. DOI: 10.1063/1.3206091 (Cited on page 153).

Larkin, A. (Nov. 1999). "Superconductor-insulator transitions in films and bulk materials". In: *Annalen der Physik* 511.7-9, pp. 785–794. DOI: 10.1002/andp.199951107-932 (Cited on pages 9, 65, 68).

Le Sueur, Hélène, Artis Svilans, Nicolas Bourlet, Anil Murani, Laurent Bergé, Louis Dumoulin, and Philippe Joyez (2018). *Microscopic charged fluctuators as a limit to the coherence of disordered superconductor devices*. DOI: 10.48550/ARXIV.1810.12801 (Cited on pages 124, 126).

Lee, Patrick A. and T. V. Ramakrishnan (Apr. 1985). "Disordered electronic systems". In: *Reviews of Modern Physics* 57.2, pp. 287–337. DOI: 10.1103/revmodphys.57.287 (Cited on pages 95, 156, 162).

Leger, Sébastien (June 2021). "Electrodynamique quantique d'une jonction Josephson couplée à un environnement fortement dissipatif". Theses. Université Grenoble Alpes [2020-....] (Cited on pages 169–172).

Lemarié, G., A. Kamlapure, D. Bucheli, L. Benfatto, J. Lorenzana, G. Seibold, S. C. Ganguli, P. Raychaudhuri, and C. Castellani (May 2013). "Universal scaling of the order-parameter distribution in strongly disordered superconductors". In: *Physical Review B* 87.18. DOI: 10.1103/physrevb.87.184509 (Cited on pages 18, 34).

Levy-Bertrand, F., T. Klein, T. Grenet, O. Dupré, A. Benoit, A. Bideaud, O. Bourrion, M. Calvo, A. Catalano, A. Gomez, J. Goupy, L. Grünhaupt, U. v. Luepke, N. Maleeva, F. Valenti, I. M. Pop, and A. Monfardini (Mar. 2019). "Electrodynamics of granular aluminum from superconductor to insulator: Observation of collective superconducting modes". In: *Physical Review B* 99.9. DOI: 10.1103/physrevb.99.094506 (Cited on page 34).

Likharev, K. K. (June 1971). "The formation of a mixed state in planar semiconductor films". In: *Radiophysics and Quantum Electronics* 14.6, pp. 722–727. DOI: 10.1007/bf01033185 (Cited on pages 134, 135).

Liu, Wei, Minsoo Kim, G. Sambandamurthy, and N. P. Armitage (July 2011). "Dynamical study of phase fluctuations and their critical slowing down in amorphous superconducting films". In: *Physical Review B* 84.2. DOI: 10.1103/physrevb.84.024511 (Cited on pages 32–34).

Liu, Wei, LiDong Pan, Jiajia Wen, Minsoo Kim, G. Sambandamurthy, and N. P. Armitage (Aug. 2013). "Microwave Spectroscopy Evidence of Superconducting Pairing in the Magnetic-Field-Induced Metallic State of InOx Films at Zero Temperature". In: *Physical Review Letters* 111.6. DOI: 10.1103/physrevlett.111.067003 (Cited on pages 32–34, 129).

Lozano, D. P., M. Mongillo, X. Piao, S. Couet, D. Wan, Y. Canvel, A. M. Vadiraj, Ts. Ivanov, J. Verjauw, R. Acharya, J. Van Damme, F. A. Mohiyaddin, J. Jussot, P. P. Gowda, A. Pacco, B. Raes, J. Van de Vondel, I. P. Radu, B. Govoreanu, J. Swerts, A. Potočnik, and K. De Greve (2022). *Manufacturing high-Q superconducting α-tantalum resonators on silicon wafers*. DOI: 10.48550/ARXIV.2211.16437 (Cited on pages 124, 126).

Ma, Michael and Patrick A. Lee (Nov. 1985). "Localized superconductors". In: *Physical Review B* 32.9, pp. 5658–5667. DOI: 10.1103/physrevb.32.5658 (Cited on pages 22, 23).

Maekawa, Sadamishi and Hidetoshi Fukuyama (1982). "Localization Effects in Two-Dimensional Superconductors". In: *Journal of the Physical Society of Japan* 51.5, pp. 1380–1385. DOI: 10.1143/JPSJ.51.1380. eprint: https://doi.org/10.1143/JPSJ.51.1380 (Cited on page 5).

Mahashabde, Sumedh, Ernst Otto, Domenico Montemurro, Sebastian de Graaf, Sergey Kubatkin, and Andrey Danilov (Oct. 2020). "Fast Tunable High-Q Factor Superconducting Microwave Resonators". In: *Physical Review Applied* 14.4. DOI: 10.1103/physrevapplied.14.044040 (Cited on page 124).

Maki, Kazumi (May 1964). "The Behavior of Superconducting Thin Films in the Presence of Magnetic Fields and Currents". In: *Progress of Theoretical Physics* 31.5, pp. 731–741. DOI: 10.1143/ptp.31.731 (Cited on pages 56, 177).

Maki, Kazumi and R. S. Thompson (Feb. 1989). "Fluctuation conductivity of high-T_c superconductors". In: *Phys. Rev. B* 39 (4), pp. 2767–2770. DOI: 10.1103/PhysRevB.39.2767 (Cited on page 70).

Maksimova, G. M. (Oct. 1998). "Mixed state and critical current in narrow semiconducting films". In: *Physics of the Solid State* 40.10, pp. 1607–1610. DOI: 10.1134/1.1130618 (Cited on page 135).

Maleeva, N., L. Grünhaupt, T. Klein, F. Levy-Bertrand, O. Dupre, M. Calvo, F. Valenti, P. Winkel, F. Friedrich, W. Wernsdorfer, A. V. Ustinov, H. Rotzinger, A. Monfardini, M. V. Fistul, and I. M. Pop (Sept. 2018). "Circuit quantum electrodynamics of granular aluminum resonators". In: *Nature Communications* 9.1. DOI: 10.1038/s41467-018-06386-9 (Cited on pages 35, 77, 180).

Malnou, M., J. Aumentado, M.R. Vissers, J.D. Wheeler, J. Hubmayr, J.N. Ullom, and J. Gao (Apr. 2022). "Performance of a Kinetic Inductance Traveling-Wave Parametric Amplifier at 4 Kelvin: Toward an Alternative to Semiconductor Amplifiers". In: *Physical Review Applied* 17.4. DOI: 10.1103/physrevapplied.17.044009 (Cited on page 147).

Malnou, M., M.R. Vissers, J.D. Wheeler, J. Aumentado, J. Hubmayr, J.N. Ullom, and J. Gao (Jan. 2021). "Three-Wave Mixing Kinetic Inductance Traveling-Wave Amplifier with Near-Quantum-Limited Noise Performance". In: *PRX Quantum* 2.1. DOI: 10.1103/prxquantum.2.010302 (Cited on page 147).

Mandal, Soumyajit, Surajit Dutta, Somak Basistha, Indranil Roy, John Jesudasan, Vivas Bagwe, Lara Benfatto, Arumugam Thamizhavel, and Pratap Raychaudhuri (Aug. 2020). "Destruction of superconductivity through phase fluctuations in ultrathin MoGe films". In: *Physical Review B* 102.6. DOI: 10.1103/physrevb.102.060501 (Cited on page 34).

Mandelbrot, Benoit B (Nov. 1982). *The fractal geometry of nature*. de. New York, NY: W.H. Freeman (Cited on page 151).

Mannila, E. T., P. Samuelsson, S. Simbierowicz, J. T. Peltonen, V. Vesterinen, L. Grönberg, J. Hassel, V. F. Maisi, and J. P. Pekola (Dec. 2021). "A superconductor free of quasiparticles for seconds". In: *Nature Physics* 18.2, pp. 145–148. DOI: 10.1038/s41567-021-01433-7 (Cited on page 120).

Martinis, John M. (June 2021). "Saving superconducting quantum processors from decay and correlated errors generated by gamma and cosmic rays". In: *npj Quantum Information* 7.1. DOI: 10.1038/s41534-021-00431-0 (Cited on page 121).

Martinis, John M., M. Ansmann, and J. Aumentado (Aug. 2009). "Energy Decay in Superconducting Josephson-Junction Qubits from Nonequilibrium Quasiparticle Excitations". In: *Physical Review Letters* 103.9. DOI: 10.1103/physrevlett.103.097002 (Cited on page 119).

Mattis, D. C. and J. Bardeen (July 1958). "Theory of the Anomalous Skin Effect in Normal and Superconducting Metals". In: *Physical Review* 111.2, pp. 412–417. DOI: 10.1103/physrev.111.412 (Cited on pages 79, 83, 111, 181).

Matveev, K. A. and A. I. Larkin (May 1997). "Parity Effect in Ground State Energies of Ultrasmall Superconducting Grains". In: *Physical Review Letters* 78.19, pp. 3749–3752. DOI: 10.1103/physrevlett.78.3749 (Cited on page 29).

McEwen, Matt, Lara Faoro, Kunal Arya, Andrew Dunsworth, Trent Huang, Seon Kim, Brian Burkett, Austin Fowler, Frank Arute, Joseph C. Bardin, Andreas Bengtsson, Alexander Bilmes, Bob B. Buckley, Nicholas Bushnell, Zijun Chen, Roberto Collins, Sean Demura, Alan R. Derk, Catherine Erickson, Marissa Giustina, Sean D. Harrington, Sabrina Hong,

Evan Jeffrey, Julian Kelly, Paul V. Klimov, Fedor Kostritsa, Pavel Laptev, Aditya Locharla, Xiao Mi, Kevin C. Miao, Shirin Montazeri, Josh Mutus, Ofer Naaman, Matthew Neeley, Charles Neill, Alex Opremcak, Chris Quintana, Nicholas Redd, Pedram Roushan, Daniel Sank, Kevin J. Satzinger, Vladimir Shvarts, Theodore White, Z. Jamie Yao, Ping Yeh, Juhwan Yoo, Yu Chen, Vadim Smelyanskiy, John M. Martinis, Hartmut Neven, Anthony Megrant, Lev Ioffe, and Rami Barends (Dec. 2021). "Resolving catastrophic error bursts from cosmic rays in large arrays of superconducting qubits". In: *Nature Physics* 18.1, pp. 107–111. DOI: 10.1038/s41567-021-01432-8 (Cited on page 119).

McRae, C. R. H., J. H. Béjanin, C. T. Earnest, T. G. McConkey, J. R. Rinehart, C. Deimert, J. P. Thomas, Z. R. Wasilewski, and M. Mariantoni (May 2018). "Thin film metrology and microwave loss characterization of indium and aluminum/indium superconducting planar resonators". In: *Journal of Applied Physics* 123.20. DOI: 10.1063/1.5020514 (Cited on pages 118, 124, 126).

McRae, C. R. H., H. Wang, J. Gao, M. R. Vissers, T. Brecht, A. Dunsworth, D. P. Pappas, and J. Mutus (Sept. 2020). "Materials loss measurements using superconducting microwave resonators". In: *Review of Scientific Instruments* 91.9, p. 091101. DOI: 10.1063/5.0017378 (Cited on page 108).

Medvedeva, Julia E., D. Bruce Buchholz, and Robert P. H. Chang (Aug. 2017). "Recent Advances in Understanding the Structure and Properties of Amorphous Oxide Semiconductors". In: *Advanced Electronic Materials* 3.9, p. 1700082. DOI: 10.1002/aelm.201700082 (Cited on page 15).

Megrant, A., C. Neill, R. Barends, B. Chiaro, Yu Chen, L. Feigl, J. Kelly, Erik Lucero, Matteo Mariantoni, P. J. J. O'Malley, D. Sank, A. Vainsencher, J. Wenner, T. C. White, Y. Yin, J. Zhao, C. J. Palmstrøm, John M. Martinis, and A. N. Cleland (Mar. 2012). "Planar superconducting resonators with internal quality factors above one million". In: *Applied Physics Letters* 100.11, p. 113510. DOI: 10.1063/1.3693409 (Cited on pages 124, 126).

Milchakov, Vladimir (Mar. 2022). "Optimized transmon molecule for high fidelity quantum non demolition readout using cross-Kerr coupling". Theses. Université Grenoble Alpes [2020-....] (Cited on page 166).

Mildenberger, A., F. Evers, and A. D. Mirlin (July 2002). "Dimensionality dependence of the wave-function statistics at the Anderson transition". In: *Physical Review B* 66.3. DOI: 10.1103/physrevb.66.033109 (Cited on page 160).

Miller, Allen and Elihu Abrahams (Nov. 1960). "Impurity Conduction at Low Concentrations". In: *Physical Review* 120.3, pp. 745–755. DOI: 10.1103/physrev.120.745 (Cited on page 162).

Mirlin, A (Mar. 2000). "Statistics of energy levels and eigenfunctions in disordered systems". In: *Physics Reports* 326.5-6, pp. 259–382. DOI: 10.1016/s0370-1573(99)00091-5 (Cited on pages 16, 160).

Misra, S., L. Urban, M. Kim, G. Sambandamurthy, and A. Yazdani (Jan. 2013). "Measurements of the Magnetic-Field-Tuned Conductivity of Disordered Two-Dimensional MoGe and InOx Superconducting Films: Evidence for a Universal Minimum Superfluid Response". In: *Physical Review Letters* 110.3. DOI: 10.1103/physrevlett.110.037002 (Cited on pages 32–34).

Mitra, Sreemanta, Girish C. Tewari, Diana Mahalu, and Dan Shahar (Apr. 2016). "Finite-size effects in amorphous indium oxide". In: *Physical Review B* 93.15. DOI: 10.1103/physrevb.93.155408 (Cited on page 17).

Mondal, Mintu, Anand Kamlapure, Somesh Chandra Ganguli, John Jesudasan, Vivas Bagwe, Lara Benfatto, and Pratap Raychaudhuri (Feb. 2013). "Enhancement of the finite-frequency superfluid response in the pseudogap regime of strongly disordered superconducting films". In: *Scientific Reports* 3.1. DOI: 10.1038/srep01357 (Cited on pages 34, 35).

Mondal, Mintu, Sanjeev Kumar, Madhavi Chand, Anand Kamlapure, Garima Saraswat, G. Seibold, L. Benfatto, and Pratap Raychaudhuri (Nov. 2011). "Role of the Vortex-Core Energy on the Berezinskii-Kosterlitz-Thouless Transition in Thin Films of NbN". In: *Physical Review Letters* 107.21. DOI: 10.1103/physrevlett.107.217003 (Cited on page 96).

Mooij, J. E. and Yu. V. Nazarov (Feb. 2006). "Superconducting nanowires as quantum phase-slip junctions". In: *Nature Physics* 2.3, pp. 169–172. DOI: 10.1038/nphys234 (Cited on page 100).

Mooij, J. E. and Gerd Schön (July 1985). "Propagating plasma mode in thin superconducting filaments". In: *Physical Review Letters* 55.1, pp. 114–117. DOI: 10.1103/physrevlett.55.114 (Cited on pages 38, 39, 43).

Mott, N (July 1987). "The mobility edge since 1967". In: *Journal of Physics C: Solid State Physics* 20.21, pp. 3075–3102. DOI: 10.1088/0022-3719/20/21/008 (Cited on pages 15, 153).

Mott, N. F. (Apr. 1969). "Conduction in non-crystalline materials". In: *Philosophical Magazine* 19.160, pp. 835–852. DOI: 10.1080/14786436908216338 (Cited on page 163).

Mott, Sir Nevill (Nov. 1978). "Metal–insulator transitions". In: *Physics Today* 31.11, pp. 42–47. DOI: 10.1063/1.2994815 (Cited on pages 15, 153).

Müller, Clemens, Jared H Cole, and Jürgen Lisenfeld (Dec. 2019). "Towards understanding two-level-systems in amorphous solids: insights from quantum circuits". en. In: *Rep. Prog. Phys.* 82.12, p. 124501 (Cited on pages 108, 109, 112).

Müller, M, T Luschmann, A Faltermeier, S Weichselbaumer, L Koch, G B P Huber, H W Schumacher, N Ubbelohde, D Reifert, T Scheller, F Deppe, A Marx, S Filipp, M Althammer, R Gross, and H Huebl (Feb. 2022). "Magnetic field robust high quality factor NbTiN superconducting microwave resonators". In: *Materials for Quantum Technology* 2.1, p. 015002. DOI: 10.1088/2633-4356/ac50f8 (Cited on pages 124, 126).

Müller, M. and L. B. Ioffe (Dec. 2004). "Glass Transition and the Coulomb Gap in Electron Glasses". In: *Physical Review Letters* 93.25. DOI: 10.1103/physrevlett.93.256403 (Cited on pages 73, 104).

Müller, M. and S. Pankov (Apr. 2007). "Mean-field theory for the three-dimensional Coulomb glass". In: *Physical Review B* 75.14. DOI: 10.1103/physrevb.75.144201 (Cited on page 104).

Nagata, Takahiro (2019). "Indium oxide". In: *Single Crystals of Electronic Materials*. Elsevier, pp. 523–546. DOI: 10.1016/b978-0-08-102096-8.00015-x (Cited on page 14).

Nelson, David R. and J. M. Kosterlitz (Nov. 1977). "Universal Jump in the Superfluid Density of Two-Dimensional Superfluids". In: *Physical Review Letters* 39.19, pp. 1201–1205. DOI: 10.1103/physrevlett.39.1201 (Cited on page 8).

Niepce, David, Jonathan Burnett, and Jonas Bylander (Apr. 2019). "High Kinetic Inductance NbN Nanowire Superinductors". In: *Physical Review Applied* 11.4. DOI: 10.1103/physrevapplied.11.044014 (Cited on pages 124, 126).

Noat, Y., V. Cherkez, C. Brun, T. Cren, C. Carbillet, F. Debontridder, K. Ilin, M. Siegel, A. Semenov, H.-W. Hübers, and D. Roditchev (July 2013). "Unconventional superconductivity in ultrathin superconducting NbN films studied by scanning tunneling spectroscopy". In: *Physical Review B* 88.1. DOI: 10.1103/physrevb.88.014503 (Cited on pages 18, 34).

Noguchi, Takashi, Agnes Dominjon, Matthias Kroug, Satoru Mima, and Chiko Otani (Aug. 2019). "Characteristics of Very High Q Nb Superconducting Resonators for Microwave Kinetic Inductance Detectors". In: *IEEE Transactions on Applied Superconductivity* 29.5, pp. 1–5. DOI: 10.1109/tasc.2019.2904592 (Cited on pages 124, 126).

Nsanzineza, I. and B. L. T. Plourde (Sept. 2014). "Trapping a Single Vortex and Reducing Quasiparticles in a Superconducting Resonator". In: *Physical Review Letters* 113.11. DOI: 10.1103/physrevlett.113.117002 (Cited on page 140).

Ocola, L. E. and A. Stein (Nov. 2006). "Effect of cold development on improvement in electron-beam nanopatterning resolution and line roughness". In: *Journal of Vacuum Science & Technology B: Microelectronics and Nanometer Structures Processing, Measurement, and Phenomena* 24.6, pp. 3061–3065. DOI: 10.1116/1.2366698 (Cited on page 166).

Olsson, Peter and Petter Minnhagen (Feb. 1991). "On the helicity modulus, the critical temperature and Monte Carlo simulations for the two-dimensional XY-model". In: *Physica Scripta* 43.2, pp. 203–209. DOI: 10.1088/0031-8949/43/2/016 (Cited on page 82).

Ovadia, M., D. Kalok, I. Tamir, S. Mitra, B. Sacépé, and D. Shahar (Aug. 2015). "Evidence for a Finite-Temperature Insulator". In: *Scientific Reports* 5.1. DOI: 10.1038/srep13503 (Cited on pages 129, 145).

Ovadia, M., B. Sacépé, and D. Shahar (Apr. 2009). "Electron-Phonon Decoupling in Disordered Insulators". In: *Physical Review Letters* 102.17. DOI: 10.1103/physrevlett.102.176802 (Cited on page 75).

Ovadia, Maoz, David Kalok, Benjamin Sacépé, and Dan Shahar (June 2013). "Duality symmetry and its breakdown in the vicinity of the superconductor–insulator transition". In: *Nature Physics* 9.7, pp. 415–418. DOI: 10.1038/nphys2636 (Cited on page 129).

Ovadyahu, Z (Sept. 1986). "Some finite temperature aspects of the Anderson transition". In: *Journal of Physics C: Solid State Physics* 19.26, pp. 5187–5213. DOI: 10.1088/0022-3719/19/26/018 (Cited on pages 14, 17).

– (June 2022a). "Interaction-induced spatial correlations in a disordered glass". In: *Physical Review B* 105.23. DOI: 10.1103/physrevb.105.235101 (Cited on page 17).

– (Nov. 2022b). "Relation between disorder and homogeneity in an amorphous metal". In: *Physical Review B* 106.18. DOI: 10.1103/physrevb.106.184205 (Cited on page 15).

Ovadyahu, Z., B. Ovryn, and H. W. Kraner (Apr. 1983). "Microstructure and Electro-Optical Properties of Evaporated Indium-Oxide Films". In: *Journal of The Electrochemical Society* 130.4, pp. 917–921. DOI: 10.1149/1.2119858 (Cited on page 15).

Ovadyahu, Z. and M. Pollak (Nov. 2003). "History-dependent relaxation and the energy scale of correlation in the electron glass". In: *Physical Review B* 68.18. DOI: 10.1103/physrevb.68.184204 (Cited on page 17).

Ovadyahu, Zvi (Oct. 2019). "Structural Dynamics in Thermal Treatment of Amorphous Indium Oxide Films". In: *physica status solidi (b)* 257.1, p. 1900310. DOI: 10.1002/pssb.201900310 (Cited on page 14).

Ovadyahu, Zvi and Yoseph Imry (Dec. 1981). "Magnetoconductive effects in an effectively two-dimensional system. Weak Anderson localization". In: *Physical Review B* 24.12, pp. 7439–7442. DOI: 10.1103/physrevb.24.7439 (Cited on page 17).

Paalanen, M. A., A. F. Hebard, and R. R. Ruel (Sept. 1992). "Low-temperature insulating phases of uniformly disordered two-dimensional superconductors". In: *Physical Review Letters* 69.10, pp. 1604–1607. DOI: 10.1103/physrevlett.69.1604 (Cited on page 129).

Patel, U., Ivan V. Pechenezhskiy, B. L. T. Plourde, M. G. Vavilov, and R. McDermott (Dec. 2017). "Phonon-mediated quasiparticle poisoning of superconducting microwave resonators". In: *Physical Review B* 96.22. DOI: 10.1103/physrevb.96.220501 (Cited on page 121).

Pearl, J. (Aug. 1964). "CURRENT DISTRIBUTION IN SUPERCONDUCTING FILMS CARRYING QUANTIZED FLUXOIDS". In: *Applied Physics Letters* 5.4, pp. 65–66. DOI: 10.1063/1.1754056 (Cited on page 96).

Peltonen, J. T., O. V. Astafiev, Yu. P. Korneeva, B. M. Voronov, A. A. Korneev, I. M. Charaev, A. V. Semenov, G. N. Golt'sman, L. B. Ioffe, T. M. Klapwijk, and J. S. Tsai (Dec.

2013). "Coherent flux tunneling through NbN nanowires". In: *Physical Review B* 88.22. DOI: 10.1103/physrevb.88.220506 (Cited on page 102).
Phillips, W A (Dec. 1987). "Two-level states in glasses". In: *Reports on Progress in Physics* 50.12, pp. 1657–1708. DOI: 10.1088/0034-4885/50/12/003 (Cited on page 110).
Place, Alexander P. M., Lila V. H. Rodgers, Pranav Mundada, Basil M. Smitham, Mattias Fitzpatrick, Zhaoqi Leng, Anjali Premkumar, Jacob Bryon, Andrei Vrajitoarea, Sara Sussman, Guangming Cheng, Trisha Madhavan, Harshvardhan K. Babla, Xuan Hoang Le, Youqi Gang, Berthold Jäck, András Gyenis, Nan Yao, Robert J. Cava, Nathalie P. de Leon, and Andrew A. Houck (Mar. 2021). "New material platform for superconducting transmon qubits with coherence times exceeding 0.3 milliseconds". In: *Nature Communications* 12.1. DOI: 10.1038/s41467-021-22030-5 (Cited on page 116).
Planat, Luca (June 2020). "Resonant and traveling-wave parametric amplification near the quantum limit". Theses. Université Grenoble Alpes [2020-....] (Cited on pages 169, 171).
Pollak, M. (1970). "Effect of carrier-carrier interactions on some transport properties in disordered semiconductors". In: *Discussions of the Faraday Society* 50, p. 13. DOI: 10.1039/df9705000013 (Cited on page 163).
Poniatowski, Nicholas R. (June 2019). "Superconductivity, broken gauge symmetry, and the Higgs mechanism". In: *American Journal of Physics* 87.6, pp. 436–443. DOI: 10.1119/1.5093291 (Cited on page 3).
Pop, I. M., I. Protopopov, F. Lecocq, Z. Peng, B. Pannetier, O. Buisson, and W. Guichard (June 2010). "Measurement of the effect of quantum phase slips in a Josephson junction chain". In: *Nature Physics* 6.8, pp. 589–592. DOI: 10.1038/nphys1697 (Cited on page 100).
Pop, Ioan M., Kurtis Geerlings, Gianluigi Catelani, Robert J. Schoelkopf, Leonid I. Glazman, and Michel H. Devoret (Apr. 2014). "Coherent suppression of electromagnetic dissipation due to superconducting quasiparticles". In: *Nature* 508.7496, pp. 369–372. DOI: 10.1038/nature13017 (Cited on page 119).
Pourret, A., H. Aubin, J. Lesueur, C. A. Marrache-Kikuchi, L. Bergé, L. Dumoulin, and K. Behnia (Sept. 2006). "Observation of the Nernst signal generated by fluctuating Cooper pairs". In: *Nature Physics* 2.10, pp. 683–686. DOI: 10.1038/nphys413 (Cited on page 34).
Pozar, D.M. (2011). *Microwave Engineering, 4th Edition*. Wiley (Cited on pages 40, 47, 49, 125).
Pracht, Uwe S., Nimrod Bachar, Lara Benfatto, Guy Deutscher, Eli Farber, Martin Dressel, and Marc Scheffler (Mar. 2016). "Enhanced Cooper pairing versus suppressed phase coherence shaping the superconducting dome in coupled aluminum nanograins". In: *Physical Review B* 93.10. DOI: 10.1103/physrevb.93.100503 (Cited on page 85).
Pracht, Uwe S., Marc Scheffler, Martin Dressel, David F. Kalok, Christoph Strunk, and Tatyana I. Baturina (Nov. 2012). "Direct observation of the superconducting gap in a thin film of titanium nitride using terahertz spectroscopy". In: *Physical Review B* 86.18. DOI: 10.1103/physrevb.86.184503 (Cited on page 34).
Probst, S., F. B. Song, P. A. Bushev, A. V. Ustinov, and M. Weides (Feb. 2015). "Efficient and robust analysis of complex scattering data under noise in microwave resonators". In: *Review of Scientific Instruments* 86.2, p. 024706. DOI: 10.1063/1.4907935 (Cited on pages 49–51).
Probst, Sebastian (2015). "Resonator tools". In: *GitHub*. DOI: https://github.com/sebastianprobst/resonator_tools (Cited on page 51).
Puertas, Javier (June 2018). "Probing light-matter interaction in the many-body regime of superconducting quantum circuits". Theses. Université Grenoble Alpes (Cited on pages 171, 172).

Ranzani, L., M. Bal, Kin Chung Fong, G. Ribeill, X. Wu, J. Long, H.-S. Ku, R. P. Erickson, D. Pappas, and T. A. Ohki (Dec. 2018). "Kinetic inductance traveling-wave amplifiers for multiplexed qubit readout". In: *Applied Physics Letters* 113.24. DOI: 10.1063/1.5063252 (Cited on page 147).

Raychaudhuri, Pratap and Surajit Dutta (Dec. 2021). "Phase fluctuations in conventional superconductors". In: *Journal of Physics: Condensed Matter* 34.8, p. 083001. DOI: 10.1088/1361-648x/ac360b (Cited on page 82).

Reagor, Matthew, Hanhee Paik, Gianluigi Catelani, Luyan Sun, Christopher Axline, Eric Holland, Ioan M. Pop, Nicholas A. Masluk, Teresa Brecht, Luigi Frunzio, Michel H. Devoret, Leonid Glazman, and Robert J. Schoelkopf (May 2013). "Reaching 10 ms single photon lifetimes for superconducting aluminum cavities". In: *Applied Physics Letters* 102.19. DOI: 10.1063/1.4807015 (Cited on pages 124, 126, 127).

Richardson, C. J. K., A. Alexander, C. G. Weddle, B. Arey, and M. Olszta (June 2020). "Low-loss superconducting titanium nitride grown using plasma-assisted molecular beam epitaxy". In: *Journal of Applied Physics* 127.23, p. 235302. DOI: 10.1063/5.0008010 (Cited on pages 124, 126).

Rieger, D., S. Günzler, M. Spiecker, A. Nambisan, W. Wernsdorfer, and I.M. Pop (July 2023). "Fano Interference in Microwave Resonator Measurements". In: *Physical Review Applied* 20.1. DOI: 10.1103/physrevapplied.20.014059 (Cited on page 108).

Rieger, D., S. Günzler, M. Spiecker, P. Paluch, P. Winkel, L. Hahn, J. K. Hohmann, A. Bacher, W. Wernsdorfer, and I. M. Pop (Dec. 2022). "Granular aluminium nanojunction fluxonium qubit". In: *Nature Materials* 22.2, pp. 194–199. DOI: 10.1038/s41563-022-01417-9 (Cited on page 147).

Romanenko, A., R. Pilipenko, S. Zorzetti, D. Frolov, M. Awida, S. Belomestnykh, S. Posen, and A. Grassellino (Mar. 2020). "Three-Dimensional Superconducting Resonators at $T < 20$ mK with Photon Lifetimes up to $\tau = 2$ s". In: *Physical Review Applied* 13.3. DOI: 10.1103/physrevapplied.13.034032 (Cited on pages 124, 126, 127).

Rosenbaum, Ralph (Aug. 1991). "Crossover from Mott to Efros-Shklovskii variable-range-hopping conductivity in InO films". In: *Physical Review B* 44.8, pp. 3599–3603. DOI: 10.1103/physrevb.44.3599 (Cited on page 17).

Rotzinger, H, S T Skacel, M Pfirrmann, J N Voss, J Münzberg, S Probst, P Bushev, M P Weides, A V Ustinov, and J E Mooij (Nov. 2016). "Aluminium-oxide wires for superconducting high kinetic inductance circuits". In: *Superconductor Science and Technology* 30.2, p. 025002. DOI: 10.1088/0953-2048/30/2/025002 (Cited on pages 124, 126).

Sacépé, B., C. Chapelier, T. I. Baturina, V. M. Vinokur, M. R. Baklanov, and M. Sanquer (Oct. 2008). "Disorder-Induced Inhomogeneities of the Superconducting State Close to the Superconductor-Insulator Transition". In: *Physical Review Letters* 101.15. DOI: 10.1103/physrevlett.101.157006 (Cited on pages 18–20, 33, 68, 82, 121).

Sacépé, B., J. Seidemann, M. Ovadia, I. Tamir, D. Shahar, C. Chapelier, C. Strunk, and B. A. Piot (June 2015). "High-field termination of a Cooper-pair insulator". In: *Physical Review B* 91.22. DOI: 10.1103/physrevb.91.220508 (Cited on pages 67, 68, 104, 129).

Sacépé, Benjamin, Claude Chapelier, Tatyana I. Baturina, Valerii M. Vinokur, Mikhail R. Baklanov, and Marc Sanquer (Dec. 2010). "Pseudogap in a thin film of a conventional superconductor". In: *Nature Communications* 1.1. DOI: 10.1038/ncomms1140 (Cited on pages 18, 33, 68).

Sacépé, Benjamin, Thomas Dubouchet, Claude Chapelier, Marc Sanquer, Maoz Ovadia, Dan Shahar, Mikhail Feigel'man, and Lev Ioffe (Jan. 2011). "Localization of preformed Cooper pairs in disordered superconductors". In: *Nature Physics* 7.3, pp. 239–244. DOI: 10.1038/nphys1892 (Cited on pages 18, 19, 29, 62, 72, 79–81).

Sacépé, Benjamin, Mikhail Feigel'man, and Teunis M. Klapwijk (July 2020). "Quantum breakdown of superconductivity in low-dimensional materials". In: *Nature Physics* 16.7, pp. 734–746. DOI: 10.1038/s41567-020-0905-x (Cited on pages 5, 12, 78, 86).

Sambandamurthy, G., L. W. Engel, A. Johansson, and D. Shahar (Mar. 2004). "Superconductivity-Related Insulating Behavior". In: *Physical Review Letters* 92.10. DOI: 10.1103/physrevlett.92.107005 (Cited on page 129).

Samkharadze, N., A. Bruno, P. Scarlino, G. Zheng, D.P. DiVincenzo, L. DiCarlo, and L.M.K. Vandersypen (Apr. 2016). "High-Kinetic-Inductance Superconducting Nanowire Resonators for Circuit QED in a Magnetic Field". In: *Physical Review Applied* 5.4. DOI: 10.1103/physrevapplied.5.044004 (Cited on pages 124, 129, 130).

Sandberg, Martin, Michael R. Vissers, Jeffrey S. Kline, Martin Weides, Jiansong Gao, David S. Wisbey, and David P. Pappas (June 2012). "Etch induced microwave losses in titanium nitride superconducting resonators". In: *Applied Physics Letters* 100.26, p. 262605. DOI: 10.1063/1.4729623 (Cited on pages 124, 126).

Scalapino, Douglas J., Steven R. White, and Shoucheng Zhang (Apr. 1993). "Insulator, metal, or superconductor: The criteria". In: *Physical Review B* 47.13, pp. 7995–8007. DOI: 10.1103/physrevb.47.7995 (Cited on page 27).

Schrieffer, J Robert (1999). *Theory of superconductivity*. Advanced book classics (Cited on page 3).

Seibold, G., L. Benfatto, C. Castellani, and J. Lorenzana (May 2012). "Superfluid Density and Phase Relaxation in Superconductors with Strong Disorder". In: *Physical Review Letters* 108.20. DOI: 10.1103/physrevlett.108.207004 (Cited on page 27).

Shahar, D. and Z. Ovadyahu (Nov. 1992). "Superconductivity near the mobility edge". In: *Phys. Rev. B* 46 (17), pp. 10917–10922. DOI: 10.1103/PhysRevB.46.10917 (Cited on pages 17, 18, 62, 64, 70, 71, 93).

Shaikhaidarov, Rais S., Kyung Ho Kim, Jacob W. Dunstan, Ilya V. Antonov, Sven Linzen, Mario Ziegler, Dmitry S. Golubev, Vladimir N. Antonov, Evgeni V. Il'ichev, and Oleg V. Astafiev (July 2022). "Quantized current steps due to the a.c. coherent quantum phase-slip effect". In: *Nature* 608.7921, pp. 45–49. DOI: 10.1038/s41586-022-04947-z (Cited on pages 100, 147).

Shammass, I., O. Cohen, M. Ovadia, I. Gutman, and D. Shahar (Apr. 2012). "Superconducting correlations in thin films of amorphous indium oxide on the insulating side of the disorder-tuned superconductor-insulator transition". In: *Physical Review B* 85.14. DOI: 10.1103/physrevb.85.140507 (Cited on pages 17, 129).

Shearrow, Abigail, Gerwin Koolstra, Samuel J. Whiteley, Nathan Earnest, Peter S. Barry, F. Joseph Heremans, David D. Awschalom, Erik Shirokoff, and David I. Schuster (Nov. 2018). "Atomic layer deposition of titanium nitride for quantum circuits". In: *Applied Physics Letters* 113.21. DOI: 10.1063/1.5053461 (Cited on pages 116, 124).

Sherman, D., G. Kopnov, D. Shahar, and A. Frydman (Apr. 2012). "Measurement of a Superconducting Energy Gap in a Homogeneously Amorphous Insulator". In: *Physical Review Letters* 108.17. DOI: 10.1103/physrevlett.108.177006 (Cited on page 20).

Sherman, Daniel, Boris Gorshunov, Shachaf Poran, Nandini Trivedi, Eli Farber, Martin Dressel, and Aviad Frydman (Jan. 2014). "Effect of Coulomb interactions on the disorder-driven superconductor-insulator transition". In: *Physical Review B* 89.3. DOI: 10.1103/physrevb.89.035149 (Cited on pages 20, 21, 62, 81, 82).

Sherman, Daniel, Uwe S. Pracht, Boris Gorshunov, Shachaf Poran, John Jesudasan, Madhavi Chand, Pratap Raychaudhuri, Mason Swanson, Nandini Trivedi, Assa Auerbach, Marc Scheffler, Aviad Frydman, and Martin Dressel (Jan. 2015). "The Higgs mode in disordered

superconductors close to a quantum phase transition". In: *Nature Physics* 11.2, pp. 188–192. DOI: 10.1038/nphys3227 (Cited on page 34).
Singh, G., A. Jouan, L. Benfatto, F. Couëdo, P. Kumar, A. Dogra, R. C. Budhani, S. Caprara, M. Grilli, E. Lesne, A. Barthélémy, M. Bibes, C. Feuillet-Palma, J. Lesueur, and N. Bergeal (Jan. 2018). "Competition between electron pairing and phase coherence in superconducting interfaces". In: *Nature Communications* 9.1. DOI: 10.1038/s41467-018-02907-8 (Cited on pages 77, 85).
Singh, Vibhor, Ben H. Schneider, Sal J. Bosman, Evert P. J. Merkx, and Gary A. Steele (Dec. 2014). "Molybdenum-rhenium alloy based high-Q superconducting microwave resonators". In: *Applied Physics Letters* 105.22. DOI: 10.1063/1.4903042 (Cited on pages 124, 126).
Sonnet Software, Inc (n.d.). *Sonnet Software* (Cited on page 52).
Spiecker, Martin, Patrick Paluch, Nicolas Gosling, Niv Drucker, Shlomi Matityahu, Daria Gusenkova, Simon Günzler, Dennis Rieger, Ivan Takmakov, Francesco Valenti, Patrick Winkel, Richard Gebauer, Oliver Sander, Gianluigi Catelani, Alexander Shnirman, Alexey V. Ustinov, Wolfgang Wernsdorfer, Yonatan Cohen, and Ioan M. Pop (June 2023). "Two-level system hyperpolarization using a quantum Szilard engine". In: *Nature Physics*. DOI: 10.1038/s41567-023-02082-8 (Cited on page 123).
Stan, Gheorghe, Stuart B. Field, and John M. Martinis (Mar. 2004). "Critical Field for Complete Vortex Expulsion from Narrow Superconducting Strips". In: *Physical Review Letters* 92.9. DOI: 10.1103/physrevlett.92.097003 (Cited on pages 134, 135, 137, 138).
Stanley, H. Eugene and Paul Meakin (Sept. 1988). "Multifractal phenomena in physics and chemistry". In: *Nature* 335.6189, pp. 405–409. DOI: 10.1038/335405a0 (Cited on page 152).
Stepanov, Nikolai A. and Mikhail A. Skvortsov (Apr. 2018). "Superconducting fluctuations at arbitrary disorder strength". In: *Phys. Rev. B* 97 (14), p. 144517. DOI: 10.1103/PhysRevB.97.144517 (Cited on page 70).
Takagi, H. and Y. Kuroda (Mar. 1982). "Anderson localization and superconducting transition temperature in two-dimensional systems". In: *Solid State Communications* 41.9, pp. 643–648. DOI: 10.1016/0038-1098(82)90722-0 (Cited on page 22).
The Royal Swedish Academy of Sciences (2016). *Nobel Prize Press Release*. Accessed on February 8, 2023. DOI: https://www.nobelprize.org/prizes/physics/2016/press-release (Cited on page 8).
Thorbeck, Ted, Andrew Eddins, Isaac Lauer, Douglas T. McClure, and Malcolm Carroll (2022). *TLS Dynamics in a Superconducting Qubit Due to Background Ionizing Radiation*. DOI: 10.48550/ARXIV.2210.04780 (Cited on pages 119, 123).
Thouless, D. J. (Oct. 1977). "Maximum Metallic Resistance in Thin Wires". In: *Phys. Rev. Lett.* 39 (18), pp. 1167–1169. DOI: 10.1103/PhysRevLett.39.1167 (Cited on pages 155, 161).
– (Oct. 1974). "Electrons in disordered systems and the theory of localization". In: *Physics Reports* 13.3, pp. 93–142. DOI: 10.1016/0370-1573(74)90029-5 (Cited on pages 155, 160).
Tinkham, Michael (1975). *Introduction to superconductivity*. McGraw-Hill (Cited on pages 56, 123, 129, 181).
Turneaure, Stefan J., Aaron A. Pesetski, and Thomas R. Lemberger (Apr. 1998). "Numerical modeling and experimental considerations for a two-coil apparatus to measure the complex conductivity of superconducting films". In: *Journal of Applied Physics* 83.8, pp. 4334–4343. DOI: 10.1063/1.367193 (Cited on page 34).
Turneaure, Stefan J., Eric R. Ulm, and Thomas R. Lemberger (1996). "Numerical modeling of a two-coil apparatus for measuring the magnetic penetration depth in superconducting films

and arrays". In: *Journal of Applied Physics* 79.8, p. 4221. DOI: 10.1063/1.362657 (Cited on page 34).
Vaknin, A., Z. Ovadyahu, and M. Pollak (Mar. 2002). "Nonequilibrium field effect and memory in the electron glass". In: *Physical Review B* 65.13. DOI: 10.1103/physrevb.65.134208 (Cited on page 17).
Valenti, Francesco, Fabio Henriques, Gianluigi Catelani, Nataliya Maleeva, Lukas Grünhaupt, Uwe von Lüpke, Sebastian T. Skacel, Patrick Winkel, Alexander Bilmes, Alexey V. Ustinov, Johannes Goupy, Martino Calvo, Alain Benoit, Florence Levy-Bertrand, Alessandro Monfardini, and Ioan M. Pop (May 2019). "Interplay Between Kinetic Inductance, Nonlinearity, and Quasiparticle Dynamics in Granular Aluminum Microwave Kinetic Inductance Detectors". In: *Physical Review Applied* 11.5. DOI: 10.1103/physrevapplied.11.054087 (Cited on page 121).
van der Zant, H. S. J., W. J. Elion, L. J. Geerligs, and J. E. Mooij (Oct. 1996). "Quantum phase transitions in two dimensions: Experiments in Josephson-junction arrays". In: *Physical Review B* 54.14, pp. 10081–10093. DOI: 10.1103/physrevb.54.10081 (Cited on page 73).
Vepsäläinen, Antti P., Amir H. Karamlou, John L. Orrell, Akshunna S. Dogra, Ben Loer, Francisca Vasconcelos, David K. Kim, Alexander J. Melville, Bethany M. Niedzielski, Jonilyn L. Yoder, Simon Gustavsson, Joseph A. Formaggio, Brent A. VanDevender, and William D. Oliver (Aug. 2020). "Impact of ionizing radiation on superconducting qubit coherence". In: *Nature* 584.7822, pp. 551–556. DOI: 10.1038/s41586-020-2619-8 (Cited on page 120).
Verjauw, J., A. Potočnik, M. Mongillo, R. Acharya, F. Mohiyaddin, G. Simion, A. Pacco, Ts. Ivanov, D. Wan, A. Vanleenhove, L. Souriau, J. Jussot, A. Thiam, J. Swerts, X. Piao, S. Couet, M. Heyns, B. Govoreanu, and I. Radu (July 2021). "Investigation of Microwave Loss Induced by Oxide Regrowth in High-Q Niobium Resonators". In: *Physical Review Applied* 16.1. DOI: 10.1103/physrevapplied.16.014018 (Cited on page 124).
Visser, P. J. de, J. J. A. Baselmans, P. Diener, S. J. C. Yates, A. Endo, and T. M. Klapwijk (Apr. 2011). "Number Fluctuations of Sparse Quasiparticles in a Superconductor". In: *Physical Review Letters* 106.16. DOI: 10.1103/physrevlett.106.167004 (Cited on page 119).
Vissers, M. R., R. P. Erickson, H.-S. Ku, Leila Vale, Xian Wu, G. C. Hilton, and D. P. Pappas (Jan. 2016). "Low-noise kinetic inductance traveling-wave amplifier using three-wave mixing". In: *Applied Physics Letters* 108.1. DOI: 10.1063/1.4937922 (Cited on page 147).
Wang, C., C. Axline, Y. Y. Gao, T. Brecht, Y. Chu, L. Frunzio, M. H. Devoret, and R. J. Schoelkopf (Oct. 2015). "Surface participation and dielectric loss in superconducting qubits". In: *Applied Physics Letters* 107.16, p. 162601. DOI: 10.1063/1.4934486 (Cited on page 115).
Wei, Xing-Yu, Jia-Zheng Pan, Ya-Peng Lu, Jun-Liang Jiang, Zi-Shuo Li, Sheng Lu, Xue-Cou Tu, Qing-Yuan Zhao, Xiao-Qing Jia, Lin Kang, Jian Chen, Chun-Hai Cao, Hua-Bing Wang, Wei-Wei Xu, Guo-Zhu Sun, and Pei-Heng Wu (Dec. 2020). "Compact NbN resonators with high kinetic inductance". In: 29.12, p. 128401. DOI: 10.1088/1674-1056/abc2b8 (Cited on pages 124, 126).
Weißl, T., B. Küng, E. Dumur, A. K. Feofanov, I. Matei, C. Naud, O. Buisson, F. W. J. Hekking, and W. Guichard (Sept. 2015). "Kerr coefficients of plasma resonances in Josephson junction chains". In: *Physical Review B* 92.10. DOI: 10.1103/physrevb.92.104508 (Cited on pages 53, 179).
Weitzel, Alexander, Lea Pfaffinger, Ilaria Maccari, Klaus Kronfeldner, Thomas Huber, Lorenz Fuchs, James Mallord, Sven Linzen, Evgeni Il'ichev, Nicola Paradiso, and Christoph Strunk (Nov. 2023). "Sharpness of the Berezinskii-Kosterlitz-Thouless Transition in Disordered NbN Films". In: *Physical Review Letters* 131.18. DOI: 10.1103/physrevlett.131.186002 (Cited on page 83).

Wheeler, H.A. (1965). "Transmission-Line Properties of Parallel Strips Separated by a Dielectric Sheet". In: *IEEE Transactions on Microwave Theory and Techniques* 13.2, pp. 172–185. DOI: 10.1109/TMTT.1965.1125962 (Cited on page 44).

Wilen, C. D., S. Abdullah, N. A. Kurinsky, C. Stanford, L. Cardani, G. D'Imperio, C. Tomei, L. Faoro, L. B. Ioffe, C. H. Liu, A. Opremcak, B. G. Christensen, J. L. DuBois, and R. McDermott (June 2021). "Correlated charge noise and relaxation errors in superconducting qubits". In: *Nature* 594.7863, pp. 369–373. DOI: 10.1038/s41586-021-03557-5 (Cited on page 119).

Winkel, Patrick, Kiril Borisov, Lukas Grünhaupt, Dennis Rieger, Martin Spiecker, Francesco Valenti, Alexey V. Ustinov, Wolfgang Wernsdorfer, and Ioan M. Pop (Aug. 2020). "Implementation of a Transmon Qubit Using Superconducting Granular Aluminum". In: *Physical Review X* 10.3. DOI: 10.1103/physrevx.10.031032 (Cited on pages 147, 180).

Xu, Mingrui, Risheng Cheng, Yufeng Wu, Gangqiang Liu, and Hong X. Tang (Feb. 2023). "Magnetic Field-Resilient Quantum-Limited Parametric Amplifier". In: *PRX Quantum* 4.1. DOI: 10.1103/prxquantum.4.010322 (Cited on page 147).

Xu, Mingrui, Xu Han, Wei Fu, Chang-Ling Zou, and Hong X. Tang (May 2019). "Frequency-tunable high-Q superconducting resonators via wireless control of nonlinear kinetic inductance". In: *Applied Physics Letters* 114.19, p. 192601. DOI: 10.1063/1.5098466 (Cited on pages 124, 126, 129).

Yong, Jie, T. R. Lemberger, L. Benfatto, K. Ilin, and M. Siegel (May 2013). "Robustness of the Berezinskii-Kosterlitz-Thouless transition in ultrathin NbN films near the superconductor-insulator transition". In: *Physical Review B* 87.18. DOI: 10.1103/physrevb.87.184505 (Cited on page 34).

Yu, Cécile Xinqing, Simon Zihlmann, Gonzalo Troncoso Fernandez-Bada, Jean-Luc Thomassin, Frédéric Gustavo, Étienne Dumur, and Romain Maurand (Feb. 2021). "Magnetic field resilient high kinetic inductance superconducting niobium nitride coplanar waveguide resonators". In: *Applied Physics Letters* 118.5, p. 054001. DOI: 10.1063/5.0039945 (Cited on pages 124, 126, 129, 130).

Zaikin, Andrei D., Dmitrii S. Golubev, Anne van Otterlo, and Gergely T. Zimányi (Feb. 1997). "Quantum Phase Slips and Transport in Ultrathin Superconducting Wires". In: *Physical Review Letters* 78.8, pp. 1552–1555. DOI: 10.1103/physrevlett.78.1552 (Cited on pages 69, 99).

Zhang, Wenyuan, K. Kalashnikov, Wen-Sen Lu, P. Kamenov, T. DiNapoli, and M.E. Gershenson (Jan. 2019). "Microresonators Fabricated from High-Kinetic-Inductance Aluminum Films". In: *Physical Review Applied* 11.1. DOI: 10.1103/physrevapplied.11.011003 (Cited on pages 124, 126, 146).

Zhu, S., F. Crisa, M. Bal, A. A. Murthy, J. Lee, Z. Sung, A. Lunin, D. Frolov, R. Pilipenko, D. Bafia, A. Mitra, A. Romanenko, and A. Grassellino (2022). *High quality superconducting Nb co-planar resonators on sapphire substrate*. DOI: 10.48550/ARXIV.2207.13024 (Cited on pages 124, 126).